To the Graduate Council:

I am submitting herewith a dissertation written by Monir Hanna Sharobeam entitled "The Geometry and Deformation Functions in Ductile Fracture Mechanics and Methodologies". I have examined the final copy of this Dissertation for form and content and recommend that it be accepted in partial fulfillment of the requirements for the degree of Doctor of Philosophy, with a major in Engineering Science and Mechanics.

John D. Landes

John D. Landes, Major Professor

We have read this dissertation and recommend its acceptance:

John G. Merkle

W T Becker

Joseph A. Wilson

Jerry E. Glandt

Michael Matthews

Accepted for the Council:

Lee Minkel

Vice Provost
and Dean of The Graduate School

THE GEOMETRY AND DEFORMATION FUNCTIONS IN DUCTILE FRACTURE MECHANICS AND METHODOLOGIES

A Dissertation

Presented for the

Doctor of Philosophy

Degree

The University of Tennessee, Knoxville

Monir Hanna Sharobeam

December, 1990

Copyright © Monir Hanna Sharobeam, 1990
All rights reserved

DEDICATION

To my wife, Nahed

Without your love, patience, and encouragement
this degree would not have been achieved.

ACKNOWLEDGMENTS

In the course of thesis research, a number of scholars have assisted me generously. In particular, I am most indebted to Dr. John D. Landes, my major professor, for his invaluable direction, support, and friendship. With his assistance and guidance, I was able to achieve results otherwise impossible. I wish also to extend my appreciation to Dr. Archie Mathews for presenting me to the department of Engineering Science and Mechanics. Also as a member of my doctoral committee and a friend, he encouraged and supported me continuously. My gratitude is also expressed to Dr. Jerry Stoneking, Head of the department and member of my doctoral committee, for his friendly encouragement and guidance, also for providing me with the financial support through a graduate assistantship. I would like also to express my appreciation to the other members of my doctoral committee; Mr. John G. Merkle, Dr. William T. Becker, and Dr. J. A. M. Boulet. Their support, encouragement, and advice have been greatly appreciated. A special thanks go to Dr. Osama Soliman, and Mrs. Hinkle for their invaluable help to make my job as a teaching assistant enjoyable and productive. Finally, a sincere gratitude is expressed to the department of Engineering Science and Mechanics for the invaluable contributions to both my education and experience.

ABSTRACT

The recent evaluation of the material fracture toughness parameter J is based on load separation. Load separation is the assumption that the load can be represented as a multiplication of two separate functions: a crack geometry function and a material deformation function. Until recently, the main experimental basis for such assumption was the approximate agreement between the experimental results of the single specimen J form and the energy rate interpretation of J for blunt notched bending geometries. However, load separation has also been implied in precracked specimen test records in order to develop the R-curve analysis for bending geometries.

In this study, the assumption of load separation was examined in the test records of specimens with different crack sizes, geometries, constraints, and materials, for both stationary and growing crack cases. The study proved that load separation is a dominant criterion in material ductile fracture behavior that exists in both bending and tension geometries. Also, it illustrated the material basis for such criterion. In addition, the study developed a generalized form for the geometry function as a power law function. Also, the deformation function for the different test records was constructed. Moreover, the study proposed an approach to develop a

unified deformation function that is independent of constraint and displacement measurement.

A new reliable method for the evaluation of the η-factor was proposed. The η-factor is the multiplication factor in the single specimen J form. This method avoids most of the approximation errors in other methods.

The study proved that the geometry and deformation functions maintain their form as the crack grows far beyond the J-controlled crack growth limit, which validates using J analysis for growing cracks in different geometries.

Through the experimental development of the geometry and deformation functions, an advanced ductile fracture methodology was established that could provide accurate predictions of the fracture behavior of defective materials and structures.

TABLE OF CONTENTS

CHAPTER		PAGE
I.	AN INTRODUCTION TO DUCTILE FRACTURE MECHANICS AND METHODOLOGIES	1
	1.1 Introduction	1
	1.2 Linear Elastic Fracture Mechanics (LEFM)	2
	1.3 Elastic-Plastic Fracture Mechanics (EPFM)	6
	1.3.1 *J*-integral	7
	1.3.2 Fracture Toughness Measurement Using Crack Tip Opening Displacement (CTOD) Method	18
	1.4 Failure Predictions in Ductile Fracture	21
	1.4.1 General Approach	22
	1.4.2 Failure Prediction Methods	24
	1.4.3 An Advanced Ductile Fracture Methodology	30
	1.5 Objectives	33
II.	LOAD SEPARATION	35
	2.1 Introduction	35
	2.2 Load Separation in Stationary Crack Test Records	36
	2.2.1 Load Separation Analysis	36
	2.2.2 Experimental Results	37
	2.3 Load Separation in Precracked Specimen Test Records	47
	2.3.1 Load Separation Analysis	47
	2.3.2 Experimental Results	49
	2.4 Summary and Discussion	52

III. CRACK GEOMETRY FUNCTION AND PLASTIC ETA (η_{pl}) DEVELOPMENT 56
3.1 Introduction 56
3.2 The Geometry Function in Stationary Crack Test Records 57
3.3 The Geometry Function in Precracked Specimen Test Records 70
3.4 Plastic Eta (η_{pl}) Development 74
3.5 Summary and Conclusions 79

IV. MATERIAL DEFORMATION FUNCTION 82
4.1 Introduction 82
4.2 Development of Material Deformation Function 84
4.3 Development of the Geometry and Deformation Functions for Precracked Specimen Test Records Using Normalization Technique 88
4.4 Unified Deformation Function 90
4.5 Summary and Conclusions 93

V. SUMMARY OF RESULTS 94
5.1 Load Separation 94
5.2 Crack Geometry Function 95
5.3 Plastic Eta (η_{pl}) 96
5.4 Material Deformation Function 96
5.5 Ductile Fracture Methodology 97
5.6 Suggested Future Studies 98

REFERENCES 100

APPENDIX 109

VITA 235

LIST OF TABLES

TABLE		PAGE
2.1.	Measured compliance values for the HY130 CT set.	38
2.2.	Mechanical properties of studied materials.	40
2.3.	Computed compliance and displacement offset values.	40
2.4.	Measured compliance values for the HY130 SENB set.	41
2.5.	Measured compliance values for the HY130 CCT set.	42
2.6.	Measured compliance values for the A533B SENT set.	43
2.7.	Measured compliance values for the thin A710 SENT set.	44
2.8.	Measured compliance values for the thick A710 SENT sets.	46
2.9.	Measured and estimated crack length values.	51
2.10.	Summary of the different cases involved in the load separation study.	54
3.1.	Power law fit results in the HY130 CT set.	58
3.2.	Power law fit results in the other four CT sets.	60
3.3.	Power law fit results in the HY130 SENB set.	64
3.4.	Power law fit results in the HY130 CCT set.	65
3.5.	Power law fit results in the A533B SENT set.	67

3.6.	Power law fit results in the thin A710 SENT set.	67
3.7.	Power law fit results in the 1.0 in. thick A710 SENT sets.	69
3.8.	Power law fit results in the different A710 SENT sets for the load versus crack mouth opening displacement records.	69
3.9.	Power law fit results in the precracked specimen sets.	71
3.10.	Power law exponent values in the blunting region of the precracked specimen records.	73
3.11.	Summary of η_{pl} values in the different studied cases.	77
4.1.	Mechanical properties of A508 and A710 steels.	89
4.2.	Initial and final crack lengths in the different specimens.	90
4.3.	Coordinates scaling factors for the A710 sets.	92

LIST OF FIGURES

FIGURE		PAGE
1.1.	Crack tip field.	110
1.2.	Stress variation in the crack vicinity.	110
1.3.	*J*-integral contour.	111
1.4.	Different fields in the crack vicinity.	111
1.5.	*J*-integral evaluation using energy rate interpretation form.	112
1.6.	*J*-integral evaluation using single specimen form.	113
1.7.	Crack growth mechanism in ductile fracture mechanics.	114
1.8.	Proportional and non-proportional regions in the crack tip field.	115
1.9.	*J*-integral evaluation for growing crack test record.	116
1.10.	Stable and unstable regions in crack growth based on *J-T* analysis.	117
1.11.	Ductile fracture methodology.	118
2.1.	Load separation in blunt notched specimens test records.	119
2.2.	Schematic drawings of the different four geometries.	120
2.3.	Load versus load line displacement test records of ten identical HY130 blunt notched compact specimens of different crack sizes.	121

2.4. Separation parameters of the different test records in the HY130 compact specimens set with respect to two reference test records: (a) a_j/W=0.55, and (b) a_j/W=0.70. 122

2.5. Load versus load line displacement test records of three identical A533B blunt notched compact specimens of different crack sizes. 124

2.6. Load versus load line displacement test records of three identical HSLA80 blunt notched compact specimens of different crack sizes. 125

2.7. Load versus load line displacement test records of three identical A106 blunt notched compact specimens of different crack sizes. 126

2.8. Load versus load line displacement test records of three identical HY80 blunt notched compact specimens of different crack sizes. 127

2.9. Separation parameters of two test records of A533B compact specimens set with respect to the third test record. 128

2.10. Separation parameters of two test records of HSLA80 compact specimens set with respect to the third test record. 129

2.11. Separation parameters of two test records of A106 compact specimens set with respect to the third test record. 130

2.12. Separation parameters of two test records of HY80 compact specimens set with respect to the third test record. 131

2.13. Load versus load line displacement test records of ten identical HY130 single edge blunt notched bend specimens of different crack sizes. 132

2.14. Separation parameters of the different test records in the HY130 single edge notched bend specimens set with respect to two reference test records: (a) a_j/W=0.55, and (b) a_j/W=0.75. 133

2.15. Load versus load line displacement test records of ten identical HY130 blunt notched center cracked tension specimens of different crack sizes. 135

2.16. Separation parameters of the different test records in the HY130 center cracked tension specimens set with respect to two reference test records: (a) a_j/W=0.55, and (b) a_j/W=0.75. 136

2.17. Load versus load line displacement test records of seven identical A533B single edge blunt notched tension specimens of different crack sizes. 138

2.18. Separation parameters of the different test records in the A533B single edge blunt notched tension specimens set with respect to two reference test records: (a) a_j/W=0.40, and (b) a_j/W=0.70. 139

2.19. Load versus load line displacement test records of six identical A710 thin single edge blunt notched tension specimens of different crack sizes. 141

2.20. Separation parameters of the different test records in the A710 thin single edge blunt notched tension specimens set with respect to two reference test records: (a) a_j/W=0.20, and (b) a_j/W=0.60. 142

2.21. Load versus load line displacement test records of two A710 single edge notched tension specimens of thickness 1.0 inch. 144

2.22. Load versus load line displacement test records of three A710 single edge notched tension specimens of thickness 1.0 inch with 20% side grooving. 145

2.23. Load versus load line displacement test records of three A710 single edge notched tension specimens of thickness 1.0 inch with 50% side grooving. 146

2.24. Separation parameters of the different load-load line displacement test records of the A710 SENT non-side grooved specimens. 147

2.25. Separation parameters of the different load-load line displacement test records of the A710 SENT 20% side grooved specimens. 148

2.26. Separation parameters of the different load-load line displacement test records of the A710 SENT 50% side grooved specimens. 149

2.27. Load versus crack mouth opening displacement test records of the different A710 SENT thin specimens. 150

2.28. Load versus crack mouth opening displacement test records of the different A710 SENT 1.0 thick specimens with no side grooving. 151

2.29. Load versus crack mouth opening displacement test records of the different A710 SENT 1.0 inch thick specimens with 20% side grooving. 152

2.30. Load versus crack mouth opening displacement test records of the different A710 SENT 1.0 inch thick specimens with 50% side grooving. 153

2.31. Separation parameters of the different load-crack mouth opening displacement test records of the A710 SENT thin specimens. 154

2.32. Separation parameters of the different load-crack mouth opening displacement test records of the A710 SENT 1.0 inch thick specimens with no side grooving. 155

2.33. Separation parameters of the different load-crack mouth opening displacement test records of the A710 SENT 1.0 inch thick specimens with 20% side grooving. 156

2.34. Separation parameters of the different load-crack mouth opening displacement test records of the A710 SENT 1.0 inch thick specimens with 50% side grooving. 157

2.35. Load versus load line displacement test records of three precracked and one blunt notched A533B compact specimens. 158

2.36. Load versus load line displacement test records of four precracked and one blunt notched HSLA80 compact specimens. 159

2.37. Load versus load line displacement test records of four precracked and one blunt notched A106 compact specimens. 160

2.38. Load versus load line displacement test records of three precracked and one blunt notched HY80 compact specimens. 161

2.39. Variation of separation parameter and uncracked ligament of an A533B precracked specimen with respect to plastic displacement. 162

2.40. Variation of separation parameter and uncracked ligament of an HSLA80 precracked specimen with respect to plastic displacement. 163

2.41. Variation of separation parameter and uncracked ligament of an A106 precracked specimen with respect to plastic displacement. 164

2.42. Variation of separation parameter and uncracked ligament of an HY80 precracked specimen with respect to plastic displacement. 165

2.43. Variation of separation parameters of the different A533B precracked specimens test records with respect to uncracked ligament. 166

2.44. Variation of separation parameters of the different HSLA80 precracked specimens test records with respect to uncracked ligament. 167

2.45. Variation of separation parameters of the different A106 precracked specimens test records with respect to uncracked ligament. 168

2.46. Variation of separation parameters of the different HY80 precracked specimens test records with respect to uncracked ligament. 169

2.47. Schematic drawings of plastic pattern developed in four point bend test; (a) slightly past the yield point, (b) well past the yield point. 170

2.48. Schematic drawings of the yielded regions in bend specimen (a/W = 0.5) of non-work hardening material and the corresponding points in the load-load line displacement record. 171

2.49. Position at which load separation starts in test records of three HY130 SENB specimens. 172

3.1. Variation of the separation parameters, $\bar{S}_{i,j}$, with respect to uncracked ligament, b_i/W, on logarithmic coordinates for the HY130 CT set. 173

3.2. Power law fit of the $S_{i,j}$ versus b_i/W records for the HY130 CT set. 174

3.3. Sample of the power law fit of one of the $S_{i,j}$ versus b_i/W records in the HY130 CT set. 175

3.4. Power law fit of the $S_{i,j}$ versus b_i/W record for the A533B CT set. 176

3.5. Power law fit of the $S_{i,j}$ versus b_i/W record for the HSLA80 CT set. 177

3.6. Power law fit of the $S_{i,j}$ versus b_i/W record for the A106 CT set. 178

3.7. Power law fit of the $S_{i,j}$ versus b_i/W record for the HY80 CT set. 179

3.8. Load estimation errors using the power law geometry function and the literature geometry function. 180

3.9. Power law fit of the $S_{i,j}$ versus b_i/W record obtained using the Handbook numerical solutions for the compact geometry with plane stress constraint. 181

3.10. Power law fit of the $S_{i,j}$ versus b_i/W record obtained using the Handbook numerical solutions for the compact geometry with plane strain constraint. 182

3.11. Variation of the separation parameters, $S_{i,j}$, with respect to uncracked ligament, b_i/W, on logarithmic coordinates for the HY130 SENB set. 183

3.12. Power law fit of the $S_{i,j}$ versus b_i/W records for the HY130 SENB set. 184

3.13. Power law fit of the $S_{i,j}$ versus b_i/W records for the HY130 CCT set. 185

3.14. Power law fit of the $S_{i,j}$ versus b_i/W records for the A533B SENT set. 186

3.15. Power law fit of the $S_{i,j}$ versus b_i/W records for the A710 SENT thin specimens set. 187

3.16. Power law fit of the $S_{i,j}$ versus b_i/W records for the A710 SENT 1.0 in. thick specimens with 20% side grooving. 188

3.17. Power law fit of the $S_{i,j}$ versus b_i/W records for the A710 SENT 1.0 in. thick specimens with 50% side grooving. 189

3.18. Power law fit of the $S_{i,j}$ versus b_i/W records obtained using load versus crack mouth opening displacement records for the A710 SENT thin specimens set. 190

3.19. Power law fit of the $S_{i,j}$ versus b_i/W records obtained using the load versus crack mouth opening displacement records for the A710 SENT 1.0 in. thick specimens with no side grooving. 191

3.20. Power law fit of the $S_{i,j}$ versus b_i/W records obtained using the load versus crack mouth opening displacement records for the A710 SENT 1.0 in. thick specimens with 20% side grooving. 192

3.21. Power law fit of the $S_{i,j}$ versus b_i/W records obtained using the load versus crack mouth opening displacement records for the A710 SENT 1.0 in. thick specimens with 50% side grooving. 193

3.22. Power law fit of the $S_{i,j}$ versus b_i/W record obtained using the Handbook numerical solutions of the load versus crack mouth opening displacement relationship for the SENT geometry with plane stress constraint. 194

3.23. Power law fit of the $S_{i,j}$ versus b_i/W record obtained using the Handbook numerical solutions of the load versus crack mouth opening displacement relationship for the SENT geometry with plane strain constraint. 195

3.24. Power law fit of the $S_{i,j}$ versus b_i/W records for the A533B CT precracked specimens set. 196

3.25. Power law fit of the $S_{i,j}$ versus b_i/W records for the HSLA80 CT precracked specimens set. 197

3.26. Power law fit of the $S_{i,j}$ versus b_i/W records for the A106 CT precracked specimens set. 198

3.27. Power law fit of the $S_{i,j}$ versus b_i/W records for the HY80 CT precracked specimens set. 199

3.28. Variation of η_{pl} obtained using classical method versus plastic displacement for one of the HY130 CT test records. 200

3.29. Variation of η_{pl} obtained using classical method versus plastic displacement for one of the HY130 CCT test records. 201

3.30. η_{pl} values obtained using both classical and new methods for the HY130 CT set. 202

3.31. η_{pl} values obtained using both classical and new methods for the HY130 SENB set. 203

3.32. η_{pl} values obtained using both classical and new methods for the HY130 CCT set. 204

3.33. η_{pl} values obtained using both classical and new methods for the A533B SENT set. 205

4.1. Deformation function for the HY130 CT set developed by load normalization using a power law geometry function with a power law exponent of 2.13. 206

4.2. Deformation function for the HY130 SENB set developed by load normalization using a power law geometry function with a power law exponent of 1.96. 207

4.3. Deformation function for the HY130 CCT set developed by load normalization using a power law geometry function with a power law exponent of 0.963. 208

4.4. Deformation function for the HY130 CT set developed by load normalization using the geometry function expression given in Eq [3.7]. 209

4.5. Deformation function for the HY130 SENB set developed by load normalization using a power law geometry function with a power law exponent of 2.0. 210

4.6. Deformation function for the HY130 CCT set developed by load normalization using a power law geometry function with a power law exponent of 1.0. 211

4.7. Deformation function for the A533B SENT set developed by load normalization using a power law geometry function with a power law exponent of 2.44. 212

4.8. Deformation function for the A533B blunt notched CT specimens developed by load normalization using a power law geometry function with a power law exponent of 2.19. 213

4.9. Deformation functions for both blunt notched and precracked A533B CT specimens sets developed by load normalization using a power law geometry function with a power law exponent of 2.12. 214

4.10. Deformation function for the A106 blunt notched CT specimens developed by load normalization using a power law geometry function with a power law exponent of 2.11. 215

4.11. Deformation function for one blunt notched and four precracked A106 CT specimens developed by load normalization using a power law geometry function with a power law exponent of 2.38. 216

4.12. Deformation function for the HY80 blunt notched CT specimens developed by load normalization using a power law geometry function with a power law exponent of 2.25. 217

4.13. Deformation function for one blunt notched and three precracked HY80 CT specimens developed by load normalization using a power law geometry function with a power law exponent of 2.28. 218

4.14. Deformation function for the HSLA80 blunt notched CT specimens developed by load normalization using a power law geometry function with a power law exponent of 2.32. 219

4.15. Deformation function for one blunt notched and four precracked HSLA80 CT specimens developed by load normalization using a power law geometry function with a power law exponent of 1.87. 220

4.16. Deformation functions for both blunt notched and precracked HSLA80 CT specimens sets using different Y-axes. 221

4.17. Deformation function for the load versus load line displacement test records of the A710 SENT thin specimens. 222

4.18. Deformation function for the load versus crack mouth opening displacement test records of the A710 SENT thin specimens. 223

4.19. Deformation function for the load versus load line displacement test records of the A710 SENT specimens of 1.0 in. thickness with no side grooving. 224

4.20. Deformation function for the load versus crack mouth opening displacement test records of the A710 SENT specimens of 1.0 in. thickness with no side grooving. 225

4.21. Deformation function for the load versus load line displacement test records of the A710 SENT specimens of 1.0 in. thickness with 20% side grooving. 226

4.22. Deformation function for the load versus crack mouth opening displacement test records of the A710 SENT specimens of 1.0 in. thickness with 20% side grooving. 227

4.23. Deformation function for the load versus load line displacement test records of the A710 SENT specimens of 1.0 in. thickness with 50% side grooving. 228

4.24. Deformation function for the load versus crack mouth opening displacement test records of the A710 SENT specimens of 1.0 in. thickness with 50% side grooving. 229

4.25. Load normalization in the A508 precracked specimens using the literature geometry function expression, Eq [3.7]. 230

4.26. Load normalization in the A710 precracked specimens using the literature geometry function expression, Eq [3.7]. 231

4.27. Load normalization in the A508 precracked specimens using a power law geometry function with a power law exponent of 2.22. 232

4.28. Load normalization in the A710 precracked specimens using a power law geometry function with a power law exponent of 2.40. 233

4.29. Key curve for the different 1.0 in. thickness A710 specimens. 234

CHAPTER I

AN INTRODUCTION TO DUCTILE FRACTURE MECHANICS AND METHODOLOGIES

1.1 Introduction

The conventional engineering design of a structure is often based on the failure strength of the structural material. This approach is insufficient in many real applications, particularly when the structure contains some material defects and/or manufacturing flaws. The presence of such defects and flaws increases the probability of crack initiation and growth under normal service conditions. Environmental conditions, fluctuating loads, or accidental overloads may accelerate the initiation and growth of the cracks. The catastrophic failure of many vital structures, early in this century, illustrated a need to develop a quantitative approach that can characterize the failure in structures containing crack-like defects. The early approaches were more interested in the fracture as an event but, later on, the fracture as a process captured much interest. Different disciplines have been adopted in this matter which gave more understanding of the material's fracture behavior for different combinations of cracks, geometries, constraints, and loading conditions. These extensive studies yielded the modern approach of fracture mechanics. Fracture mechanics provides the mathematical descriptions of the relationships between the parameters which control the fracture process. These parameters are mainly the load or stress, the crack size, and the material properties. Fracture mechanics provides also the necessary tools to predict the failure behavior of defective structures. Many analytical and numerical techniques have been developed that can model the real structures and provide an

approximate prediction of their fracture behavior. Recently, a new methodology based on experimental data has been introduced. This methodology provides more accurate and reliable predictions. A primary objective of this thesis is to develop this methodology by providing mathematical descriptions of the functions that model most defective structures' ductile fracture behavior. First, however, a description will be given of the developments in fracture mechanics which led to the introduction of this new methodology.

1.2 Linear Elastic Fracture Mechanics (LEFM)

In 1921, Griffith (1)* approached the fracture problem by using the first law of thermodynamics. He introduced the first analytical approach of the linear theory of crack propagation. He postulated that an existing crack would grow by some increment if the necessary additional surface energy were supplied by the system. Using the stress analysis of Inglis for the case of an infinitely large plate containing an elliptical crack, he obtained the necessary condition for a sharp crack to grow as

$$\sigma = \sqrt{\frac{2E\gamma_s}{\pi a}} \qquad [1.1]$$

where σ is the applied stress, a is one half the crack length, E is modulus of elasticity, and γ_s is specific surface energy.

Irwin (2) chose another energy term G to replace $2\gamma_s$ in Eq [1.1]. This new term was defined as the elastic energy release rate. He (3) also used Westergaard-Airy stress functions (4) to obtain the crack tip elastic stress-strain field associated with the different modes of

---

* Numbers between ( ) denote references.

loading. Generally, the stress at any point (r,θ) in the vicinity of a crack tip, Fig. 1.1**, can be written as

$$\sigma_{ij} = \frac{K}{\sqrt{2\pi r}} f_{ij}(\theta) \qquad [1.2]$$

where K is the stress intensity factor. This factor uniquely characterizes the singularity at the crack tip. In case of elastic loading of an infinite cracked plate, K takes the form

$$K = c\,\sigma\sqrt{a} \qquad [1.3]$$

where c is a constant.

Many analytical and numerical studies (5) have been conducted to account for finite sizes and different geometries. In most cases, K can be written (6) as

$$K = \sigma\sqrt{a}\,Y \qquad [1.4]$$

where Y is a geometry factor. K and G represent the stress and energy parameters in the elastic theory of crack propagation, and they are related as

$$G = K^2 / E' \qquad [1.5]$$

where

$E' = E$ for plane stress, and
$E' = E/(1-\nu^2)$ for plane strain.

** All the figures are in the Appendix.

According to the elastic theory of crack propagation, a crack in a perfectly elastic plate will not grow unless K reaches a critical value K_{Ic} or, in other words, G reaches G_{Ic}. K_{Ic} and G_{Ic} are material constants, and they represent a lower limiting value of fracture toughness. An ASTM standard test method (7) has been established to determine K_{Ic} of metallic materials for different geometries. The K_{Ic} is technically defined as the material plane-strain fracture toughness. The validity of the test and the determined K_{Ic} value depend on the existence of a sharp crack in a specimen of adequate size to assure severe tensile constraint at the crack tip.

The elastic stress field solutions in Eq [1.2] assume a stress singularity at the crack tip. In other words, the stress becomes infinite when $r \rightarrow 0$. In practice, materials yield at specific stress values, then deform plastically. Figure 1.2 shows the stress variation at the crack tip for both linear-elastic and elastic-plastic materials. A portion of the work done is consumed in creating a plastic zone at the crack tip. Therefore, the behavior of a cracked structure is not perfectly elastic but contains some plastic contribution. This may not be ideally modeled by LEFM; however, some approximate elastic solutions with plasticity adjustments have been developed to handle such cases. These solutions can only be used for cases of contained plasticity (low-scale yielding) where the plastic region size is very small compared to the geometric dimensions and the ratio of the net section applied stress to the yield stress is much lower than 1.0.

Irwin (8) stated that plasticity makes the crack behave as if it were longer than its physical length, and he suggested the use of an effective crack length equal to the physical length plus a correction of the order of the plastic zone size. The plastic zone size, r_p, can be estimated using Eq [1.2] as

$$r_p = \frac{K^2}{2\pi\sigma_y^2} \qquad \text{for plane stress} \qquad [1.6a]$$

and

$$r_p = \frac{K^2}{6\pi\sigma_y^2} \qquad \text{for plane strain} \qquad [1.6b]$$

where σ_y is yield stress. In a different approach, Dugdale (9) proposed that the correction should be chosen such that the stress singularity disappears at a crack tip which has a plastic zone addition. His solution yielded the plastic zone correction ω as

$$\frac{a}{a+\omega} = cos\frac{\pi\sigma}{2\sigma_y} \qquad [1.7]$$

In both solutions, there are two main assumptions: the material is linear-elastic, perfect-plastic and the plasticity correction depends on K which is a linear-elastic parameter.

In case of plane stress where the plastic zone is large but still small when compared to the uncracked ligament, an energy balance criterion called the R-curve method is usually used. It assumes that there is a continuous balance between the crack driving force and the fracture resistance associated with both crack growth and plasticity zone formation. Both energies are calculated using linear analysis with a plastic zone correction. The R-curve characterizes the material's resistance to fracture during stable crack growth. Instability occurs when the released energy exceeds the material's resisting energy. This can be written mathematically as

$$G_{material} \geq G_{applied}$$

and

$$\frac{dG_{material}}{da} \geq \frac{dG_{applied}}{da}$$

The values of G and K corresponding to the instability point are G_c and K_c. The value K_c is defined as the plane stress fracture toughness. An ASTM standard practice (10) for R-curve determination has been issued under the designation E561. The practice states that "...materials tested for R-curve are not limited by strength, thickness, or toughness, so long as specimens are of sufficient size to remain predominantly elastic throughout the duration of the test." This means that K_c values obtained from the R-curve are limited to structures with the same thickness and geometry as the test specimen.

1.3 Elastic-Plastic Fracture Mechanics (EPFM)

After the increasing progress in metallurgy and manufacturing, modern structures can be loaded above the elastic limit without failure and they fail after a considerable amount of plasticity. However, most of the previously mentioned approaches to extend the linear-elastic fracture mechanics solutions into the elastic-plastic regime showed limited success, especially for large-scale yielding cases. Several attempts were made to develop new approaches that are not limited to linear behavior but can be extended to non-linear behavior without any violation of their analytical basis. These approaches introduced new parameters that can uniquely characterize the crack singularity and successfully predict the failure in both elastic and plastic regions. The two most successful methods are the J-integral method and the crack tip opening displacement (CTOD) method.

1.3.1 *J*-Integral

Formulation and Development of the *J*-Integral

The *J*-integral was formulated by Rice (11,12) in 1967. It is a path-independent integral which has the advantage that it can be evaluated sufficiently far from the crack tip and still characterize the singularity at the crack tip. The *J*-integral can be written as

$$J = \int_{\Gamma} (W dy - T_i \frac{\partial u_i}{\partial x} dS) \qquad [1.8]$$

where W is strain energy density, T_i is traction on the contour, and u_i is displacement in the direction of T_i, Fig. 1.3. The only restriction in the definition of J is that W be the strain energy density for linear or non-linear elastic behavior. Within the plastic region, this fits any stress-strain $(\sigma-\varepsilon)$ behavior in the loading process but only the "deformation theory of plasticity" in the unloading process. In practice, most materials follow the "incremental theory of plasticity" during unloading. In order to avoid any unloading, J is evaluated for stationary cracks only. J reaches its critical value J_{IC} when the crack initiates. The crack tip stress-strain field can be uniquely characterized by J for both elastic and plastic regions as long as there is no unloading.

Hutchinson (13) and Rice and Rosengren (14) indicated that for a hardening material, the product of stress and strain at the crack tip is a singularity of order $1/r$. McClintock (15) developed this fact to obtain the stress-strain field for a power law hardening material as

$$\sigma_{ij}(r,\theta) = \sigma_o \left\{\frac{J}{\sigma_o \varepsilon_o r}\right\}^{\frac{1}{n+1}} \tilde{\sigma}_{ij}(\theta,n) \qquad [1.9a]$$

$$\varepsilon_{ij}(r,\theta) = \varepsilon_o \left\{\frac{J}{\sigma_o \varepsilon_o r}\right\}^{\frac{n}{n+1}} \tilde{\varepsilon}_{ij}(\theta,n) \qquad [1.9b]$$

where

$$\frac{\varepsilon}{\varepsilon_o} = \alpha \left\{\frac{\sigma}{\sigma_o}\right\}^n$$

and (θ,r) are position coordinates of a point in the crack tip vicinity with the crack tip as the origin. σ_o is yield stress, ε_o is yield strain, α is a material constant, and n is the strain-hardening exponent. $\tilde{\sigma}_{ij}(\theta,n)$and $\tilde{\varepsilon}_{ij}(\theta,n)$ are dimensionless functions. These equations describe the stress-strain field in the plastic region (which is known as the HRR field) except for the intensively deformed non-linear zone ahead of the crack tip (16). The different crack tip fields are shown in Fig. 1.4. Equation [1.9a] is completely analogous to Eq [1.2], which represents the linear-elastic field.

Rice (11,12) obtained another alternative form to represent J as the potential energy difference between two identically loaded cracked bodies with an incremental crack size difference. This can be written as

$$J = -\frac{1}{B}\frac{\partial U}{\partial a} \qquad [1.10]$$

where U is the potential energy, and B is the thickness. This energy rate interpretation of J allowed Landes and Begley (17,18) to develop their multi-specimen experimental technique to evaluate J from the

load displacement records of identical specimens with different crack lengths. They calculated the potential energy by estimating the area under the test record. Then, they generated the U-a relationship for different displacement values. The tangent of the U-a curve represents J for the corresponding crack length and displacement. Figure 1.5 shows a schematic flow chart of their technique.

The energy rate interpretation of J, Eq [1.8], also yielded the most applied J form as

$$J = \frac{\eta}{bB} \int P\,dv \qquad [1.11]$$

where b is uncracked ligament, P is load, v is displacement, and η is a factor that may depend on the geometry, material, and/or loading conditions. This form provides the possibility of evaluating J from a single test record, Fig. 1.6. It is based on the assumption that the load can be represented as a multiplication of two separate functions (19): a crack geometry function, and a material deformation function. This single-specimen form was first introduced by Rice, Paris, and Merkle (20) for deeply cracked bend specimens. They proposed that the load-displacement relationship can be represented as

$$\theta = f(M/b^2) \qquad [1.12a]$$

where θ is the rotation due to the presence of the crack, and M is the applied moment. This form can be rearranged in a separable form as

$$M = b^2\, F(\theta)$$

or [1.12b]

$$M = G(a)\, F(\theta)$$

where $G(a)=b^2$, $G(a)$ and $F(\theta)$ are the geometry and deformation functions. Using this separable form, they wrote J as

$$J = \frac{2}{bB} \int M d\theta \qquad [1.12c]$$

where $\int M d\theta$ represents the area under the load-displacement $(M-\theta)$ record. Merkle and Corten (21) developed another analysis to find J for the compact geometry which is also a bending configuration but with a small tension component. Their analysis is based on a separable load form derived using limit load analysis. The simplest J form obtained from their analysis was

$$J = \frac{2(1+\alpha)}{1+\alpha^2} \frac{\int P dv}{Bb} \qquad [1.13a]$$

where

$$\alpha = \left[\left(\frac{2a}{b} \right)^2 + 2\left(\frac{2a}{b} \right) + 2 \right]^{1/2} - \left[\frac{2a}{b} + 1 \right] \qquad [1.13b]$$

Through Eqs [1.12c] and [1.13a], the η–factor is given as

$$\eta = 2 \qquad \text{for bend specimen} \qquad [1.14a]$$

and

$$\eta = \frac{2(1+\alpha)}{1+\alpha^2} \qquad \text{for compact specimen.} \qquad [1.14b]$$

Landes, et al. (22) conducted an experimental evaluation of J for compact specimen using both the multi-specimen technique and the single-specimen technique. They found a reasonable agreement between both techniques. Landes, et al. (23) suggested also the approximation of the η expression for the compact specimen to be

$$\eta = 2 + 0.522 \frac{b}{W} \qquad [1.15]$$

where W is specimen width. This form is the linear fit of the Merkle-Corten expression, Eq [1.14b].

Rice, et al. (20) proposed representing J as the sum of an elastic part, J_{el}, and a plastic part, J_{pl}. This was later generalized by Sumpter and Turner (24) into a new form that utilizes the single-specimen form in the elastic and plastic regions separately. This form can be written as

$$J = \eta_{el} \frac{A_{el}}{b} + \eta_{pl} \frac{A_{pl}}{b} \qquad [1.16]$$

where A_{el} and A_{pl} are the elastic and plastic parts of the area under the load displacement record.

J_{Ic} Determination

The main interest, during the early development of EPFM, was to determine the J value at crack initiation, J_{Ic}, as a measure of fracture toughness. In 1981, the ASTM issued a standard test method (E813-81) for J_{Ic} determination (25) for bending geometries. The method suggests J evaluation using the single-specimen technique as

$$J = \eta \frac{A}{Bb_o} \qquad [1.17a]$$

where for bend specimen

$$\eta = 2$$

for compact specimen [1.17b]

$$\eta = 2 + 0.522 \frac{b_o}{W}$$

and b_o is the initial uncracked ligament. The method requires testing many identical precracked specimens. The specimens should be loaded until a crack initiates, stable tearing develops, and small crack extension occurs. The crack extension is assumed to be too small to affect the area, η, and b values. An approximate linear fit can be constructed between J values and the corresponding crack extensions, Δa. Δa is defined as the difference between the final physical crack length and the original physical crack length. The intersection of the fit line and the blunting line defines J_{Ic}. The blunting line is an approximate estimate of the crack's artificial growth as the crack tip stretches before any tearing takes place. The blunting line can be obtained from the flow properties of the material as

$$J_{blunting} = 2\sigma_y \, (\Delta a)_{blunting}$$

Figure 1.7 shows a schematic drawing of the crack growth mechanism in both $J_{blunting}$ and $J_{tearing}$ regions.

In 1987, the ASTM proposed some modifications in the test method (26). The J can be evaluated as the sum of J_{el} and J_{pl} where J_{el} can be obtained from LEFM as

$$J_{el} = \frac{K^2(1-\nu^2)}{E} \qquad [1.17c]$$

and J_{pl} is evaluated using the single-specimen form as

$$J_{pl} = \eta_{pl} \frac{A_{pl}}{Bb_o} \qquad [1.17c]$$

where η_{pl} is considered the same as the overall η, Eq [1.17b]. Also, the method suggested using a power law fit for J versus Δa instead of a linear fit, and J_{Ic} became the intersection point between the power

law fit and a line drawn parallel to the blunting line with an offset of Δa = 0.2 mm.

J-R Curve

In ductile fracture, structures do not fail by crack initiation. The complete failure usually occurs after some stable crack growth. Therefore, J_{Ic} may represent a very conservative limit for ductile failure. Complete fracture analysis will require a crack growth resistance curve while J-integral analysis is limited to stationary cracks. However, crack growth usually involves elastic unloading and non-proportional plastic deformation near the crack tip which may not be accurately modeled by the "deformation theory of plasticity." Nevertheless, Hutchinson and Paris (27) argued some theoretical basis for using the "deformation theory of plasticity" J-integral in crack growth analysis. They stated that a J-controlled crack growth can exist if nearly proportional plastic deformation occurs everywhere but in a small neighborhood of the crack tip. Then, the necessary conditions for J-controlled crack growth are as follows.

1- The crack growth, Δa, must be of the order of the non-proportional plastic region, which is very small compared to the proportional plastic region, R, as shown in Fig. 1.8. This can be written as

$$\Delta a \ll R \qquad [1.18a]$$

2- The proportional part in the incremental strain must be dominant compared to the non-proportional part $(d\varepsilon_{ij} \sim \varepsilon_{ij})$. Using Eq [1.9b], one can write this condition as

$$\frac{dJ}{da} \gg \frac{J}{r} \qquad [1.18b]$$

where r is the polar coordinate of any point in the proportional region $(b>\rho>r)$. Therefore condition [1.18b] can be rewritten as

$$b \gg \rho \gg \frac{J}{dJ/da} \qquad [1.18c]$$

where ρ is the size of the intensive deformation zone where the "deformation theory of plasticity" is not applicable.

Shih, et al. (28) conducted some numerical studies to check the validity of the "deformation theory" J-integral as the crack grows, using the contour integral form, Eq [1.8]. They found that the J-integral maintains its path independence for crack growth up to 6% of the original uncracked ligament.

Both theoretical and numerical studies suggested the possibility of using the "deformation theory" J as a crack growth parameter within certain limits. Ernst, Paris, and Landes (29) developed a technique to construct a J_R-Δa curve with J updated for crack growth. Their analysis is primarily based on the assumption of load separation. They suggested that the load for a predominant bending configuration can be represented as

$$P = \frac{b^2}{W}\, g(\frac{a}{W})\, H(\frac{v}{W}) \qquad [1.19]$$

where $g(a/W)$ is a weak function of the crack length. The factors $\frac{b^2}{W}g(\frac{a}{W})$ and $H(\frac{v}{W})$ are the crack geometry and material deformation functions, respectively. Substituting Eq [1.19] in the single-specimen J form, they obtained an incremental J expression as

$$dJ = \left\{(-\gamma)\frac{\eta g}{W}\int_{o}^{v} H\,dv\right\}da + \left\{\frac{\eta b}{W}\,g\;H\right\}dv \qquad [1.20]$$

where

$$\gamma = \eta - 1 - \frac{b\eta'}{W\eta}$$

and

$$\eta' = \frac{d\eta}{d(a/W)}$$

Then, for a stationary crack, Eq [1.20] can be written as

$$\Delta J = \int_{v}^{v+\Delta v} \frac{\eta b}{W}\,gH\;dv\Big|_{a=const.}$$

$$= \frac{\eta}{b}\int_{v}^{v+\Delta v} P\,dv \qquad [1.21a]$$

and for a crack growth at constant displacement

$$\Delta J = \int_{a}^{a+\Delta a} -\gamma\frac{J}{b}\,da \approx -\gamma\frac{J}{b}\Delta a \qquad [1.21b]$$

Using Eqs [1.21a] and [1.21b], one can write a continuous incremental evaluation of J for a growing crack load-displacement record. As shown in Fig. 1.9, J for the growing crack record OAC can be obtained as the sum of J at point A and ΔJ evaluated on the path ABC.

$$J_C = J_A + \Delta J_{AB} + \Delta J_{BC}$$

$$\approx J_A + \frac{\eta}{b}(\text{Area ABDE}) - \gamma \frac{J_B}{b} \Delta a$$

$$\approx \left[J_A + \frac{\eta}{b}(\text{Area ABDE}) \right] \left[1 - \frac{\gamma}{b} \Delta a \right] \qquad [1.22a]$$

Area ABDE is almost equal to area ACDE for small Δa and Δv, so that Eq [1.22a] can be rewritten as

$$J_C \approx \left[J_A + \frac{\eta}{b}(\text{Area ACDE}) \right] \left[1 - \frac{\gamma}{b} \Delta a \right] \qquad [1.22b]$$

Following this process, one can update J over the whole test record and construct a complete J-R curve.

Recently the ASTM published a J-Resistance test method (E1152) based on this technique (30). The test method suggests a crack growth limit of 10% of the original uncracked ligament. Crack growth can be calculated using the elastic unloading compliance method which requires unloading and reloading the specimen at fixed intervals during the test. Also, the method suggests some size requirements to maintain "deformation theory" J-controlled crack growth conditions and to provide thickness independence. The J-R curve is constructed from a power law fit of the data points (J versus Δa).

As mentioned before, The crack grows first in the form of crack tip blunting until conditions of crack initiation develop ($J = J_{Ic}$), then stable tearing extension proceeds until a sudden instability may occur. Instability for ductile fracture can be defined on the J-R curve by the following two conditions:

$$J_{applied} \geq J_{material}$$

and [1.23]

$$T_{applied} \geq T_{material}$$

where T is the tearing modulus proposed by Paris, et al. (31,32) as

$$T = \frac{E}{\sigma_o^2} \frac{dJ}{da} \qquad [1.24]$$

$J_{material}$ and $T_{material}$ can be evaluated from the J-R curve for any specific crack extension. $T_{material}$ is the normalized form of the tangent to the J-R curve. $J_{applied}$ and $T_{applied}$ can be evaluated experimentally or numerically for the defective structure being analyzed as will be shown later. Then, the stable and unstable regions of the defective structure's fracture behavior can be determined from a J-T diagram as shown in Fig. 1.10.

The J-R curve, with a crack extension limit of 10% of the original uncracked ligament, may not provide the complete fracture behavior of many materials, especially if the instability occurs after this limit. In this case, the use of the "deformation theory" J may not be appropriate. A new modified J form, J_m, has been introduced by Ernst (33) as

$$J_m = J - \int_{a_o}^{a} \left. \frac{\partial J_{pl}}{\partial a} \right|_{v_{pl}} da \qquad [1.25]$$

where a_o is the original crack length. This form is based on subtracting the crack growth dependence from the "deformation theory" J. A J_m-R curve (34,35) may show better geometry and thickness independence than a "deformation theory" J-R curve up to 30% of the original uncracked ligament, but it shows worse dependence after that. The geometry and thickness independence in J-R curve and J_m-R curve are the subject of many recent studies on

fracture behavior and instability beyond the J-controlled crack growth limit.

1.3.2 Fracture Toughness Measurement Using Crack Tip Opening Displacement (CTOD) Method

The CTOD (δ) represents an average measure of the strain field in the vicinity of the crack tip. It is based on the plasticity model proposed by Dugdale. It was first used as a fracture parameter by Wells (36) in 1961. Since then, it has been widely used experimentally to characterize the fracture behavior of metals and weldments. After the J development, numerical and analytical studies showed that there is a linear relationship between CTOD and J. This gives an analytical basis to use the CTOD as a fracture parameter. The British Standard Institution issued a CTOD test method (37) in 1979, and then published a document PD6493 as a CTOD practice code (38) in 1980. Also, in 1989, ASTM issued a standard, CTOD fracture toughness measurement (39), under the designation E1290. The main objective of this method (as well as the British test method) is to determine critical CTOD values at different crack extension events. These values are: δ_c, the CTOD value at the onset of unstable crack extension (cleavage) with $\Delta a < 0.2$ mm; δ_i, the CTOD value at crack initiation and onset of stable tearing ($\Delta a = 0.2$ mm); δ_u, the CTOD value at the onset of unstable crack growth after stable tearing; and δ_m, the CTOD value at the maximum load. There are many controversial approaches for CTOD (40) evaluations and measurements, especially, for growing cracks. The ASTM recommends using

$$\delta = \delta_{el} + \delta_{pl} \qquad [1.26a]$$

where

$$\delta_{el} = \frac{K^2(1-\nu^2)}{2\,\sigma_y\,E} \qquad [1.26b]$$

$$\delta_{pl} = \frac{r_p\,(W-a_o)\,v_p}{r_p\,(W-a_o) + a_o + z} \qquad [1.26c]$$

$$K = \frac{Y\;P}{B\,\sqrt{W}} \qquad [1.26d]$$

P is the applied load, σ_y is the yield or 0.2% offset yield strength, v_p is the plastic component of crack mouth opening displacement measured as close as possible to the front face, z is the distance of the displacement measurement point from the front face on a single-edge notched bend (SENB) specimen or from load line in compact (CT) specimen, and r_p is a plastic rotation factor given as

$$r_p = 0.4\,(1+\alpha) \qquad [1.27a]$$

where for SENB

$$\alpha = 0.1 \qquad [1.27b]$$

and for CT

$$\alpha = \left[\left(\frac{2a}{b}\right)^2 + 2\left(\frac{2a}{b}\right) + 2\right]^{1/2} - \left[\frac{2a}{b} + 1\right] \qquad [1.27c]$$

The test method recommends using only SENB or CT specimens. Also, the original crack length should be within the range

$$0.45 \geq \frac{a_o}{W} \geq 0.55$$

There is no thickness requirement in the test method; however, there are some recommended geometric proportions for the specimens.

While the values δ_c, δ_u, and δ_m can be determined from a single load-CTOD record, δ_i determination may require a CTOD-Δa curve. The CTOD-Δa curve can be developed by either of two methods. The first is to test several identical specimens up to different stable crack extensions, then heat tint or fatigue crack them to mark the crack growth before breaking them. The second method is to test a single specimen with periodic unloading and reloading cycles, and obtain the crack length using the compliance method. The CTOD-Δa curve can be constructed using the following fit

$$\delta = C_1(C_2 + \Delta a)^{C_3} \qquad [1.28]$$

where Δa is the physical crack growth. The method suggests that only the data points with $\Delta a \leq 1.5$ mm can be included in the fit. δ_i is the intersection point of the fit curve and the vertical offset line at $\Delta a = 0.2$ mm. The critical CTOD values δ_c, δ_i, and δ_u are valid if they are equal or less than δ_m.

The CTOD critical values can be used in fracture analysis of defective structures using the CTOD design curve proposed by Burdekin (41). This curve can be represented mathematically (42,43) as

$$\phi = \left(\frac{\varepsilon}{\varepsilon_y}\right)^2 \qquad \text{for } \frac{\varepsilon}{\varepsilon_y} \leq 0.5 \qquad [1.29a]$$

$$\phi = \frac{\varepsilon}{\varepsilon_y} - 0.25 \qquad \text{for } \frac{\varepsilon}{\varepsilon_y} > 0.5 \qquad [1.29b]$$

where

$$\phi = \frac{\delta}{2\pi\ \varepsilon_y\ a} \qquad [1.29c]$$

δ is any of the critical CTOD values. ε is the strain value at the defective location to be analyzed, and can be obtained using any analytical approach. For example, using mechanics of materials, one can write ε at a crack tip as

$$\varepsilon = k\frac{\sigma_{design}}{E} \qquad [1.30]$$

where k is a concentration factor and σ_{design} is the design stress for this area. By substituting for ε in Eq [1.29a] or [1.29b], ϕ can be obtained, and hence the critical crack length values corresponding to the critical CTOD values can be calculated. Similarly, for a given crack length, the design stress (or load) values corresponding to the different critical CTOD values can be calculated.

The design curve can not provide a continuous estimation of the ductile fracture behavior of a defective structure but only very approximate design values at certain events in the failure process. Also, there is (44) a built-in safety factor in the CTOD design curve of about 1 to 5, which sometimes makes the predicted values unrealistic. There is currently much interest in using the CTOD-Δa as an R-curve, in analogy to the J-R curve, to obtain more details about the ductile failure behavior of a defective structure.

1.4 Failure Predictions in Ductile Fracture

The primary objective of ductile fracture mechanics is to predict the behavior of defective structures: how the structure responds to an applied load, when a crack may initiate, and how long it may grow in a stable manner before its growth becomes unstable. Apparently, if a defective structure's original crack length, geometry, thickness, and material are the same as those of an already tested specimen, the structure's fracture behavior is expected to be similar

to that of the tested specimen. But if the structure is different in any of these parameters, its fracture behavior can not be directly predicted. In this case, a successful ductile fracture methodology should be applied to obtain the predicted fracture behavior without testing the structure itself.

1.4.1 General Approach

There are two basic sets of information that must be available to conduct any failure prediction methodology: the applied input behavior (calibration functions) and the material's fracture behavior. These two sets should be combined to predict the required defective structure's behavior. It is useful to discuss first the sources of both sets, and the difficulties associated with conducting any fracture methodology, before introducing some of the available methodologies.

Calibration Functions

Calibration functions represent the applied input to the cracked loaded structure. They can be defined as the mathematical relationships that exist between the main parameters associated with any failure, namely, load P, displacement v, crack length a, and J-integral (or CTOD). They can be written as

$$v = v(P, a)$$

and

$$J = J(P, a) \qquad [1.31]$$

or

$$\delta = \delta(P, a)$$

The calibration functions can be developed by either estimation methods or experimental methods. Estimation methods, such as the finite element method, or limit load analysis, may provide numerical or analytical expressions for the calibration functions. However, the accuracy of such expressions is dependent on the analytical assumptions used to model the specimen or defective structure. The calibration functions can also be developed experimentally by testing several identical specimens with different stationary crack sizes. But the developed functions, in this case, are limited to the tested crack size range, constraint, geometry, and material, that is, to specimen-like structures.

Fracture Behavior

Fracture behavior can be provided as either a J-R curve or a CTOD-R curve. The R-curves represent the material output or response to the loading conditions. Both must be developed experimentally, and it is believed that they are independent of crack length, geometry, and thickness within certain crack extension limits. However, these limits are sometimes inadequate to handle cases of moderate or large crack extension. Moreover, the R-curves may show geometry and thickness dependence even before such proposed limits.

The final product of any fracture methodology should be complete information about the crack initiation and instability points. If possible, the method should also produce the expected load-displacement record of the structure, or at least some specific points on this record such as the maximum load point. Figure 1.11 shows a schematic flow chart of a typical fracture methodology. The procedure is simple if both the calibration curves and the J-R curve (or CTOD-R curve) match the required structure, which is not likely the case. Ductile fracture methodology has to deal with two main

problems: first, how to provide accurate estimated calibration curves for the structure or how to use the available experimental calibration curves to develop those of the structure (which will be of main concern in this thesis); and second, how to handle the thickness and geometry dependence of the R-curves after (and sometimes before) the proposed limit if the structure is expected to fail beyond this limit.

1.4.2 Failure Prediction Methods

Different approaches have been proposed to predict the fracture behavior of defective structures. These approaches are based on different assumptions, such as that the material is elastic-perfectly plastic in the limit load analysis approach, or that the post-yield stress-strain behavior is a power law in the engineering treatment model. Such assumptions may limit these approaches to specific applications. The following is a discussion of the main failure prediction approaches, their theoretical bases, and their limitations.

Limit Load Analysis

For an elastic-perfectly (non-hardening) plastic material, the applied input in the plastic region can be given as

$$P_L = A\, P(a) \qquad [1.32]$$

where P_L is the limit load, $P(a)$ is a function of the crack length, and A is a constant that depends on the geometry, structure proportions, and material flow stress. A and $P(a)$ can be obtained using slip line field analysis. As an example, the limit load for a three point bend specimen (with $\frac{a}{W} \geq 0.32$) can be given (45) as

$$P_L = \frac{1.4\ \sigma_o\ B\ b^2}{S} \qquad [1.33]$$

where S is the span and σ_o is the flow stress. The flow stress, σ_o, can be taken as yield stress, ultimate stress, or an average of both, depending on the material's work-hardening behavior.

J_{pl} can be obtained from Eq [1.32] using either the single-specimen form or the energy rate interpretation form, and can be written as

$$J_{pl} = C\ v_{pl}\ f(a) \qquad [1.34]$$

where C is a constant and $f(a)$ is a function of the crack length. J_{el} can be obtained from the linear-elastic solutions.

The material's fracture behavior can be represented by either the CTOD-R curve or the J-R curve. Combining Eq [1.32] with the CTOD-R curve provides the predicted load-CTOD fracture behavior of the required structure. Also, Eq [1.34] can be used with the J-R curve to obtain the load and displacement at the crack initiation point, J_{Ic}, and instability point, J_{ins}. The J-R curve can be used also to obtain the predicted P-v_{pl} record for the required structure.

Despite the simplicity of the limit load analysis, the solutions are very approximate, especially for highly work-hardening materials.

Engineering Treatment Model (ETM)

The ETM (46,47,48) is based on the assumption that the post yield behavior of a material can be represented by a power law as

$$\frac{\sigma}{\sigma_y} = \left(\frac{\varepsilon}{\varepsilon_y}\right)^N \qquad [1.35]$$

where N is the inverse of the strain hardening exponent, n. (σ_y,ε_y) represents a reference point in the stress-strain curve, and can be taken as the 0.2% offset yield strength ($\sigma_y = \sigma_{0.2}$). In analogy to this, the post yield behavior of a cracked body can be represented as

$$\frac{P}{P_y} = \left(\frac{\delta_5}{\delta_y}\right)^N \qquad [1.36]$$

where P_y is the load at which the net section reaches the yield conditions at each point, δ_5 is the CTOD measured over a gage length of 5 mm, and δ_y is equal to δ_5 at the net section yield condition, $P=P_y$. Both Eqs [1.35], and [1.36] can be represented as straight lines on logarithmic coordinates with (σ_y,ε_y) and (P_y,δ_y) as the origin and n as the slope. The net section yield load, P_y, can be obtained by the limit load analysis. For the purpose of this approach, the following P_y expressions (49) have been chosen:

$$P_y = A\ \sigma_y\ \frac{BW2}{S}\left(1 - \frac{a}{W}\right)^2 \qquad [1.37a]$$

for single-edge notched bend (SENB) geometry, and

$$P_y = \sigma_y\ B\ W \qquad [1.37b]$$

for compact (CT) geometry. A is a function of a/W that depends on geometric proportions and the constraints. For center-cracked tension (CCT) and double-edge notched tension (DENT) geometries, P_y is represented by the simple form

$$P_y = B\ \sigma_y\ (W-2a) \qquad [1.37c]$$

and δ_y can be obtained using the small-scale yielding solution

$$\delta = \frac{K^2}{E\ \sigma_y} \qquad \text{at } P = P_y \qquad [1.38]$$

where K can be calculated using the linear-elastic solution but with some modifications to adjust the solution for plasticity. In the method, the following K solution adjustments are suggested:

$$K = K(a_e) \qquad \text{for tension configurations,}$$

and [1.39]

$$K = \frac{1}{2}\,[K(a) + K(a_e)] \qquad \text{for bending configurations.}$$

Using Eq [1.36] and the δ_5-R curve as the material's fracture behavior, one can obtain a full prediction of the required structure. The load at the crack initiation point (δ_i or $\delta_{0.2}$) can be written as

$$P_{0.2} = P_y \left(\frac{\delta_{0.2}}{\delta_y}\right)^N \qquad [1.40]$$

Also, the load-controlled instability point can be obtained by constructing different δ_5-a curves for different load values. The curve that is tangent to the δ_5-R curve defines the maximum load and the tangential point defines the corresponding δ_5 value. Some approximate expressions are proposed to obtain the different displacements values using δ_5 for CCT geometry.

The ETM is a more advanced procedure than the limit load analysis, but many difficulties have been found using it: many materials do not follow a hardening power law, especially after the early hardening; some materials show a different hardening exponent in cracked body fracture behavior than in the regular

tensile specimen; also it is often difficult to relate the CTOD to the global displacement of the structure.

The EPRI Handbook

The EPRI handbook (50,51) provides load-displacement and J-integral solutions for five different geometries: compact specimen, center-cracked plate in tension, single-edge cracked plate in three point bending, single-edge cracked plate in uniform tension, double-edge cracked plate in tension. These solutions have been developed using the finite element method (two-dimensional code) for materials that follow a Ramberg-Osgood stress-strain relationship

$$\frac{\varepsilon}{\varepsilon_o} = \frac{\sigma}{\sigma_o} + \alpha\left(\frac{\sigma}{\sigma_o}\right)^n \qquad [1.41]$$

where ε_o is yield strain, σ_o is yield stress, α is a material constant, and n is the strain-hardening exponent. The J-integral and load line displacement solutions are given as the sum of an effective elastic part and a fully plastic part by

$$J = J_{el}\,(a_e) + J_{pl}\,(a,n) \qquad [1.42a]$$

$$v = v^c + v^{nc} \qquad [1.42b]$$

$$v^c = v^c_{el}\,(a_e) + v^c_{pl}\,(a,n) \qquad [1.42c]$$

where v^c is load line displacement due to the crack's presence, and v^{nc} is load line displacement if there is no crack. For the compact specimen, v is usually measured on the crack surfaces, so that $v = v^c$ and $v^{nc} = 0$. For other geometries, v^{nc} can be obtained from

analytical or numerical solutions of uncracked bodies. The effective crack length a_e is given as

$$a_e = a + \phi r_y \qquad [1.43a]$$

where

$$r_y = \frac{1}{\beta\pi}\left[\frac{n-1}{n+1}\right]\left(\frac{K_I}{\sigma_o}\right)^2 \qquad [1.43b]$$

$$\phi = \frac{1}{1+P/P_o} \qquad [1.43c]$$

and

$$\beta = 2 \quad \text{for plane stress}$$
$$\beta = 6 \quad \text{for plane strain} \qquad [1.43d]$$

where P is the applied load per unit thickness. P_o is a limit or reference load per unit thickness and can be given as

$$P_o = \Lambda\, b\, \sigma_o \qquad [1.43e]$$

where Λ is a constraint factor which may depend on geometry, structure proportions, and constraints (plane stress or plane strain).

The effective elastic part in the solutions, Eqs [1.42a,c], can be obtained from small-scale yielding solutions (available in several LEFM handbooks) using the given adjusted crack length expression, Eq [1.43a], instead of the physical crack length. On the other hand, the EPRI handbook provides the fully plastic region solutions. As an example, the fully plastic solutions for single-edge cracked plate in three-point bending are given as

$$J_{pl} = \alpha\, \sigma_o\, \varepsilon_o\, b\; h_1(a/W,n) \left\{\frac{P}{P_o}\right\}^{n+1} \qquad [1.44a]$$

$$v_{pl}^{c}(a,n) = \alpha\, \varepsilon_o\, a\; h_3(a/W,n) \left\{\frac{P}{P_o}\right\}^n \qquad [1.44b]$$

The handbook provides tables for h_1 and h_3 values for different a/W, and n values for different geometries, and both plane stress and plane strain constraints. The handbook also provides similar solutions for other displacement forms such as: crack tip opening displacement (CTOD), and crack mouth opening displacement (CMOD). These displacements, CTOD and CMOD, are due to the crack's presence only and there is no non-crack contribution in their values.

The EPRI handbook suggests using the J-R curve as the material's fracture behavior. The crack initiation point can be obtained from handbook solutions using J_{Ic} value given by the material J-R curve. The instability can be represented by the tangential point of the J-integral solutions to the J-R curve for the specific loading conditions.

Many difficulties and deficiencies have been found using the handbook solutions. These include the following.

1- The solutions are good only for either plane stress or plane strain case.
2- It is difficult for the average engineer to use the handbook.
3- Many materials do not follow a Ramberg-Osgood relationship.
4- The J-integral calculations using both the J expression and the energy rate interpretation of J obtained by area integration in the load-displacement expression are not compatible.
5- The solutions do not fit the experimental data (52) in many cases. The experimental load-displacement record usually lies between the plane stress and plane strain solutions.

1.4.3 An Advanced Ductile Fracture Methodology

As mentioned before, the single-specimen J form is based on the assumption that the load can be represented as a multiplication of two separate functions: a crack geometry function and a material deformation function. Mathematically, the load for a certain geometry, thickness, and material can be written as

$$P = G\left(\frac{a}{W}\right) H\left(\frac{v}{W}\right) \qquad [1.45]$$

where $G(a/W)$ and $H(v/W)$ are the crack geometry and material deformation functions, respectively. In linear-elastic behavior, the geometry and deformation functions are simply the compliance inverse $[1/C(a/W)]$ and the elastic displacement $[v_{el}]$, respectively. In the plastic region, they are much different because they are related to the non-linear region in the material's behavior. However, defining both functions for different geometries and materials may yield the most reliable ductile fracture methodology.

Based on some analytical and experimental studies, approximate $G(a/W)$ expressions for different geometries have been introduced as

$$G\left(\frac{a}{W}\right) = \left(\frac{b}{W}\right)^2 \qquad \text{for SENB}$$

$$G\left(\frac{a}{W}\right) = \left(\frac{b}{W}\right)^2 e^{0.522\frac{b}{W}} \qquad \text{for CT} \qquad [1.46]$$

and

$$G\left(\frac{a}{W}\right) = 2\frac{b}{W} \qquad \text{for CCT and DENT}$$

Knowing the geometry function for different geometries, one can write a normalized load-plastic displacement P-v_{pl} form as

$$P_N = H(v_{pl}/W) \qquad [1.47a]$$

where

$$P_N = \frac{P/BW}{(b/W)^2} \qquad \text{for SENB}$$

$$P_N = \frac{P/BW}{(b/W)^2\ e^{0.522b/W}} \qquad \text{for CT} \qquad [1.47b]$$

$$P_N = \frac{P/BW}{2\,b/W} \qquad \text{for CCT and DENT}$$

Then, the relation P_N-v_{pl}, which is an alternative expression to the deformation function, can be obtained by testing one stationary crack specimen of the required geometry, material, and thickness. Using the J-R curve, together with the geometry and deformation functions of the defective structure, one can obtain its fracture behavior.

The proposed method is simple and reliable and can be further developed, especially if the deformation function of the defective structure can be obtained by testing a specimen other than a structure-like specimen which is sometimes difficult to obtain. This specimen may be of different geometry, thickness, or material (of similar mechanical properties as the required material) than the defective structure-like specimen.

It had been thought that the deformation function could be a power law function with an exponent equal to the material tensile strain hardening exponent but experimental studies (53) showed that, even if the deformation function is a power law function, it has a different exponent than the material hardening exponent. Moreover, the deformation function may follow a power law

behavior in the early plastic regime, but it changes to a more flattened behavior as plasticity increases. Recently, another fit (LMN function) has been used (54) and it showed better representation of the deformation function.

Defining a generalized form for the deformation function is of primary interest, especially if the effect of geometry, material properties, and thickness can be included in the coefficients and constants of this form. In this case, knowing the material, geometry, and thickness of the defective structure, one can obtain both the geometry and deformation functions and, consequently, construct the structure's calibration curves.

1.5 Objectives

There are four main objectives in this thesis. The first objective is to study the assumption of load separation. Load separation has been previously proposed in bending geometries after the approximate agreement in J values between the single-specimen J form and the energy rate interpretation of J form. In this study, a new approach, not based on the J results agreement, is adopted in studying the load separation assumption in both bending and tension geometries. Load separation is studied in many load versus load line displacement test records of specimens of different crack lengths, geometries, materials, and constraints. It is also studied in both stationary and growing cracks records. The study investigates load separation in other forms of test records such as load versus crack mouth opening displacement test records. Also, a brief discussion about the material basis for the separable behavior is given.

The second objective is to develop the crack geometry function for the different geometries. The effect of the geometry, material, and constraint on the developed functions is discussed in detail. Also,

the study compares the developed forms with those proposed in the literature, when they are available. The geometry functions are also developed from the load versus crack mouth opening displacement records, then compared to those obtained from load versus load line displacement records of the same specimens. The study investigates the agreement of the numerical solutions provided in the EPRI handbook with the developed forms. The study also develops the geometry functions in precracked specimen test records and studies whether they are the same as those obtained from the stationary crack test records of specimens of the same geometry, material, and constraint.

The third objective is a direct result of the first and second objectives' implementation. New experimental methods for η_{pl} development, one using stationary crack test records and the other using growing crack test records, are proposed. These methods are based on load separation. The developed η_{pl} values in the different geometries are discussed in detail, and also compared to those proposed in the literature and obtained using theoretical analyses or experimental methods.

Fourth, the material deformation functions for the different materials involved in the study are constructed. The effects of the geometry and constraint on the constructed function will be discussed. The study discusses whether the deformation function maintains its form as the crack grows.

These objectives are of great importance in ductile fracture mechanics and, especially, in the development of an advanced ductile fracture methodology. The impact of the study's results on the development of such advanced methodology is discussed, and some additional steps to improve the methodology are proposed.

CHAPTER II

LOAD SEPARATION

2.1 Introduction

Load separation is the assumption that the load can be represented as a multiplication of two separate functions: a crack geometry function and a material deformation function. This assumption was first introduced by Rice (20) for the deeply cracked bend specimen in order to evaluate the J-integral using a single specimen. Then, it was used in the Merkle-Corten analysis (21) to obtain another single-specimen J form that can be applied to compact geometry. Since then, the load separation assumption and the single-specimen J form developed for both bend and compact geometries have been widely used, especially after the reasonable agreement found (22) between the energy rate interpretation of J and the single-specimen J form. Although this agreement was found in stationary crack experimental results only, the assumption of load separation was also extended to growing crack analysis. Hence it is the basis for the incremental evaluation of the J-R and J_m-R curves. Thus, as a result, these R-curves are limited only to bend and compact geometries.

In ASTM standard test methods for both J_{Ic} and J-R curve determinations in compact and bend geometries, load separation is assumed to be valid over the whole plastic region and for a recommended range of crack length.

In this chapter, load separation is investigated experimentally in different geometries, materials, and constraints. The study examines the load separation assumption itself, not the developed J

values, in order to verify the validity and to obtain the limitations of such assumption. Also, the study investigates the extension of load separation to precracked specimen test records. Eighty different test records in sixteen different sets will be used in this study. The sets will be grouped on the basis of the specimen geometry and the crack type (a stationary crack or a growing crack).

2.2 Load Separation in Stationary Crack Test Records

In this section, load separation is discussed in the stationary crack test records. First, a load separation analysis is developed; then it is used to study load separation in the experimental test records.

2.2.1 Load Separation Analysis

If the load, for given material, geometry, and constraint, can be represented in a separable form as

$$P = G(a/W)\ H(v_{pl}/W) \qquad [2.1]$$

then, for two test records (P-v_{pl}) of different stationary crack lengths a_i and a_j, as those shown in Fig. 2.1, a parameter $S_{i,j}$ defined as the ratio $P(a_i)/P(a_j)$ at a constant v_{pl} will have a constant value over the whole domain of the plastic displacement. This can be written mathematically as

$$S_{i,j} = \left.\frac{P(a_i)}{P(a_j)}\right|_{v_{pl}} \qquad [2.2]$$

$$= \frac{G(a_i/W)\ H(v_{pl}/W)}{G(a_j/W)\ H(v_{pl}/W)}\Bigg|_{v_{pl}}$$

$$= \frac{G(a_i/W)}{G(a_j/W)} = \text{constant} \qquad [2.3]$$

This also implies that if $S_{i,j}$ maintains a constant value all over the plastic region, then the load can be represented by a separable form, Eq [2.1].

2.2.2 Experimental Results

In this section, the separation parameter is used to investigate load separation in the four main geometries shown in Fig. 2.2: compact (CT), single-edge notched bend (SENB), center-cracked tension (CCT), and single-edge notched tension (SENT) geometries. The SENB is a pure bending geometry while the CCT is a pure tension geometry. The CT is basically a bending geometry but with a small tension component that depends on the ratio a/W, and the SENT is basically a tension geometry with a bending component that depends, also, on the ratio a/W.

Compact Geometry (CT)

Five sets of test records for five different materials are used in studying load separation in compact geometry. The first set includes ten blunt-notched specimens with a crack length to width ratio varying from 0.4 to 0.85. The specimens were machined from HY130 steel with 22.86 mm (0.9 in.) thickness and 50.8 mm (2.0 in.) width. The tests had been conducted by Westinghouse, and the test records were originally reported in Ref. (22). Figure 2.3 shows the different

load versus load line displacement test records. These records were obtained by digitizing those published in the mentioned reference. The elastic displacement, at any point of the test record, can be evaluated as

$$v_{el} = C\,P \qquad [2.4a]$$

where C is the effective compliance measured from the initial linear part of the test record. Table 2.1 lists the compliance measured values for the different test records in this set. The plastic displacement at any point of the record can be obtained as

$$v_{pl} = v_{total} - C\,P \qquad [2.4b]$$

where v_{total} is the total load line displacement. Thus the load versus load line plastic displacement can be developed and, consequently, the separation parameter $S_{i,j}$ for any record a_i/W with respect to any other record a_j/W can be calculated at the different plastic displacement values as discussed in section 2.2.1. A simple computer program was developed to implement the whole procedure and calculate the separation parameters for the different combinations of

Table 2.1: Measured compliance values for the HY130 CT set.

$\frac{a}{W}$	Compliance (10^{-3}in/Kips)	Compliance (10^{-3}mm/KN)	$\frac{a}{W}$	Compliance (10^{-3}in/Kips)	Compliance (10^{-3}mm/KN)
0.40	1.030	5.881	0.65	3.360	19.19
0.45	1.510	8.622	0.70	4.930	28.15
0.50	1.540	8.793	0.75	7.460	42.6
0.55	1.955	11.16	0.80	12.50	71.38
0.60	2.490	14.22	0.85	22.20	126.8

a_i/W and a_j/W records. Figures 2.4a and 2.4b show the separation parameters of the different test records with respect to two reference records, a_j/W=0.55 and 0.70. The separation parameters maintain almost constant values over the whole range of the plastic displacement except for a limited region at the early plastic behavior. This indicates that load separation is a valid assumption in compact geometry for such wide range of crack length (a/W = 0.40 to 0.85) and over the whole plastic region except for this limited region at the beginning.

HY130 steel is a high strength, low work-hardening material and it might be interesting to explore the existence of such load separation in the test records of other materials with different combinations of strength and work-hardening. This can be implemented by studying the test records of other four sets of different materials: A533B, HSLA80, A106, and HY80 steels. The mechanical properties of all the materials used in this study are given in Table 2.2. The hardening exponents of the different materials listed in this table are obtained using an approximate formula proposed by Bloom (55) and based on the engineering ε_y, σ_y, and σ_u values. All the specimens in these sets are of 50.8 mm (2.0 in.) width and 25.4 mm (1.0 in.) thickness with 20% side grooving. Each set includes three specimens. The crack length to width ratio, a/W, is varying between 0.641 to 0.806 in the different sets. These tests records were originally reported in Ref. (56) and were provided for this study as data records on diskettes. The different load versus load line displacement test records for the different sets are shown in Figs. 2.5, 2.6, 2.7, and 2.8. A computer program was developed to obtain the compliance of the initial linear part of the records and the displacement measurement offset at zero load. A least square fit method (57) was used to construct the best linear fit for the data points of the initial linear part. Table 2.3 lists the compliance values and the displacement offsets for the different test records. The program also develops the P versus v_{pl} record and calculates the

Table 2.2: Mechanical properties of studied materials.

Material	Yield Strength (Ksi)	(MPa)	Ultimate Strength (Ksi)	(MPa)	*n*
HY130	141	972	151	1040	18.4
A533B[1]	65	448	90.1	621	7.6
HSLA80	75	517	87.7	604	12.4
A106	44	303	80	551	5.1
HY80	82	565	91	627	15.8
A533B[2]	68	469	90	620	8.4
A710	82.7	570	97	669	12.04

1- The yield and ultimate strength values were reported for the CT set material
2- The yield and ultimate strength values were reported for the SENT set material

Table 2.3: Computed compliance and displacement offset values.

Material	$\frac{a}{W}$	Compliance (10^{-3}in/Kips)	(10^{-3}mm/KN)	Disp. Offset (10^{-4}in)	(10^{-2}mm)
A533B	0.6410	3.221	18.39	2.24	0.569
	0.6965	4.649	26.55	8.22	2.088
	0.7290	6.225	35.54	10.6	2.692
HSLA80	0.6500	3.393	19.37	4.78	1.214
	0.7035	5.048	28.82	23.3	5.918
	0.7580	8.354	47.70	64.1	16.28
A106	0.7000	4.817	27.51	-8.39	-2.131
	0.7530	8.095	46.22	-12.6	-3.200
	0.8055	12.204	69.68	-20.8	-5.283
HY80	0.6565	3.526	20.13	7.89	2.004
	0.7055	4.938	28.20	8.09	2.055
	0.7565	7.858	44.87	-16.7	-4.242

separation parameters. Figures 2.9, 2.10, 2.11, and 2.12 show the separation results for the different sets. The results demonstrate, again, the validity of the load separation assumption in compact geometry and also indicate that such separation is not limited to any specific material.

Single-Edge Notched Bend Geometry (SENB)

A set of ten blunt-notched specimens with a crack length to width ratio, a/W, varying from 0.40 to 0.85 is used in studying load separation in bend geometry. This set is similar to the first set used in the compact geometry study and it was also reported in the same reference. The specimens were machined from HY130 steel with 22.86 mm (0.9 in.) thickness, 50.8 mm (2.0 in.) width, and span to width ratio of 4.0. Figure 2.13 shows the different load versus load line displacement test records obtained by digitizing those published in Ref. (22). Also, Table 2.4 lists the compliance measured values for the different test records. The separation parameters for the different combinations of a_i/W and a_j/W records were calculated using the same computer program previously used for the HY130 CT set. Figures 2.14a and 2.14b show the separation parameters of the

Table 2.4: Measured compliance values for the HY130 SENB set.

$\frac{a}{W}$	Compliance (10^{-3}in/Kips)	Compliance (10^{-3}mm/KN)	$\frac{a}{W}$	Compliance (10^{-3}in/Kips)	Compliance (10^{-3}mm/KN)
0.40	1.367	7.806	0.65	5.000	28.55
0.45	1.483	8.468	0.70	6.628	37.85
0.50	2.140	12.22	0.75	9.320	53.22
0.55	2.486	14.20	0.80	15.81	90.28
0.60	3.290	18.79	0.85	26.41	150.8

different test records with respect to two reference records, a_j/W = 0.55 and 0.75. These results verify that load separation exists also in SENB specimen test records for such wide range of crack length (0.45 $\leq a/W \leq$ 0.85) and over the whole plastic region except for a limited region at the early plastic behavior.

Center-Cracked Tension Geometry (CCT)

Another HY130 set of ten blunt-notched specimens is used in studying load separation in center-cracked tension geometry. The specimens are 22.86 mm (0.9 in.) thick, 50.8 mm (2.0 in) wide and prepared with a crack length to width ratio, $2a/W$, varying from 0.40 to 0.85. Figure 2.15 shows the load versus load line displacement test records obtained by digitizing those originally reported in Ref. (22). Table 2.5 lists the compliance measured values for the different test records. Also, Figs 2.16a, 2.16b show load separation results for this set. The separation parameters maintain constant values over the whole plastic region except, again, for a limited region at the early plastic behavior. This simply means that load separation is not limited to bending (SENB and CT) geometries only but may also exist in tension geometries.

Table 2.5: Measured compliance values for the HY130 CCT set.

$\frac{2a}{W}$	Compliance (10^{-4}in/Kips)	Compliance (10^{-4}mm/KN)	$\frac{2a}{W}$	Compliance (10^{-4}in/Kips)	Compliance (10^{-4}mm/KN)
0.40	1.019	5.818	0.65	1.389	7.931
0.45	1.111	6.344	0.70	1.484	8.474
0.50	1.176	6.715	0.75	1.586	9.056
0.55	1.243	7.098	0.80	1.786	10.20
0.60	1.314	7.503	0.85	2.039	11.64

Load separation in the CCT geometry yields the interesting result that the single-specimen J form can be used in tension geometries as well as bending geometries.

Single-Edge Notched Tension Geometry (SENT)

Five different sets of two different materials, A533B steel and A710 steel, were used to study load separation in single-edge notched tension geometry. These five sets, which include twenty two blunt-notched specimen test records, were provided by Westinghouse. They were originally used in calibration curves and J-evaluation studies in Refs. (58) and (59). For the purpose of this study, the original test records were digitized to develop the data points required to implement the load separation study.

The first set includes seven specimens with crack length to width ratio, a/W, varying from 0.2 to 0.8. The specimens were machined from A533B steel with 2.5 mm (0.1 in.) thickness and 76 mm (3.0 in.) width. Figure 2.17 shows the digitized load versus load line displacement test records for the different test specimens while Table 2.6 lists the compliance measured values for the different test

Table 2.6: Measured compliance values for the A533B SENT set.

$\frac{a}{W}$	Compliance (10^{-4}in/Kips)	Compliance (10^{-3}mm/KN)	$\frac{a}{W}$	Compliance (10^{-4}in/Kips)	Compliance (10^{-3}mm/KN)
0.20	2.9150	1.664	0.60	24.540	14.01
0.30	4.0130	2.291	0.70	59.524	33.99
0.40	6.5810	3.758	0.80	193.80	110.66
0.50	12.195	6.963			

records. Figures 2.18a and 2.18b show two examples of the load separation results for this set.

The second set includes six specimens with crack length to width ratio, a/W, varying from 0.2 to 0.7. The specimens were machined from A710 steel with 2.5 mm (0.1 in.) thickness and 152 mm (6.0 in.) width. Figures 2.19, 2.20a, and 2.20b show the digitized load versus load line displacement test records and two examples of the separation results in this set. The compliance measured values for the different test records are given in Table 2.7.

The separation results in both sets indicate the existence of load separation in single-edge notched tension specimen test records no matter how much bending component is included in the specimen loading. Theoretically, the bending component increases as the ratio a/W increases. Also, the results show that load separation dominates the whole plastic region except for a limited region in the early plastic behavior which is typical of what was previously found in other geometries.

Table 2.7: Measured compliance values for the thin A710 SENT set.

$\frac{a}{W}$	Compliance (in P-v_{ll} records)[1]		Compliance (in P-v_{ff} records)[2]	
	(10^{-4}in/Kips)	(10^{-3}mm/KN)	(10^{-4} in/Kips)	(10^{-3}mm/KN)
0.20	3.68	2.101	4.30	2.455
0.30	4.60	2.627	8.69	4.962
0.40	7.00	3.997	15.4	8.793
0.50	13.5	7.709	33.3	19.01
0.60	27.5	15.70	69.3	39.57
0.70	53.0	30.26	148.0	84.51

1- v_{ll}: load line displacement

2- v_{ff}: crack mouth opening displacement

The specimens in the previous two sets were very thin section specimens with thickness of 2.5 mm (0.1 in.) and no side grooving which may represent a pure plane stress case. The other three sets include nine specimens (three specimens in each set) that are machined also from A710 steel with 152 mm (6.0 in) width but with 25.4 mm (1.0 in) thickness and even with a 20% or 50% side grooving which intensifies the plane strain conditions. The crack length to width ratio, a/W, in the nine specimens is varying from 0.3 to 0.7. Figures 2.21, 2.22, and 2.23 show the digitized load versus load line displacement records for the three sets; no side-grooved specimens set, 20% side-grooved specimens set, and 50% side-grooved specimens set, respectively. The load versus load line displacement test record for one of the specimens with no side grooves is missing, but its load versus crack mouth opening displacement test record is available and will be used, later on, in another load separation study. Table 2.8 lists the compliance measured values for the load versus load line displacement test records in these sets. Figures 2.24, 2.25, and 2.26 show the load separation results in the different sets. These results, together with those of the other two sets, not only verify that the load is separable in this geometry, but also indicate that load separation exists in plane stress cases as well as plane strain cases.

In most test records, load line displacement is the common type of displacement to be measured because it is the one that is always used in J evaluation. However, the load versus crack mouth opening displacement test records for the four A710 steel sets are also provided which allows studying load separation in different form of plastic displacement other than the load line plastic displacement.

Figures 2.27, 2.28, 2.29, and 2.30 show the digitized load versus crack mouth opening displacement test records for the different four sets, and the corresponding compliance measured values are given in Tables 2.7 and 2.8. The load versus crack mouth

Table 2.8: Measured compliance values for the thick A710 SENT sets.

Set	$\frac{a}{W}$	Compliance (in P-v_{ll} records)[1] (10^{-4}in/Kips)	(10^{-4}mm/KN)	Compliance (in P-v_{ff} records)[2] (10^{-4}in/Kips)	(10^{-4}mm/KN)
50% side-grooved	0.30	0.495	2.826	1.177	6.721
	0.50	1.390	7.937	4.30	24.55
	0.70	6.710	38.31	19.70	112.49
20% side-grooved	0.40	0.62	3.540	1.66	9.479
	0.50	1.11	6.338	3.676	20.99
	0.70	5.97	34.09	16.32	93.19
Non side-Grooved	0.50	1.35	7.709	3.57	20.38
	0.60	2.18	12.45	7.30	41.68
	0.70	(missing)		16.16	92.27

1- v_{ll}: load line displacement

2- v_{ff}: crack mouth opening displacement

opening plastic displacement record can be developed using same procedure explained in section 2.2.1. Then, the separation parameters can be evaluated at the different crack mouth opening plastic displacement values. Figures 2.31, 2.32, 2.33, and 2.34 show the load separation results for the different sets. The separation parameters maintain constant values over the whole range of the crack mouth opening plastic displacement except for a limited region at the early plastic behavior. This is exactly what was previously found in the load versus load line plastic displacement records. This indicates that load separation may also exist in other forms of load-plastic displacement records such as load versus crack mouth opening plastic displacement records.

2.3 Load Separation in Precracked Specimen Test Records

In this section, load separation is studied in precracked specimen test records. A new approach is developed first, then an experimental verification follows.

2.3.1 Load Separation Analysis

For precracked specimen test records, we can begin the analysis by assuming that, for same material, geometry, and constraint, the load may be represented as

$$P = G_p(b_p/W)\ H_p(v_{pl}/W) \qquad [2.5]$$

where $G_p(b_p/W)$ and $H_p(v_{pl}/W)$ are proposed geometry and deformation functions for precracked specimen test records. These proposed functions are assumed to be different than those previously proposed for stationary crack specimen test records. The load form in Eq [2.5] can be normalized by the load separable form proposed for stationary crack case assuming that the specimens in both cases have same material, geometry, and constraint. This normalized form can be written as

$$\frac{P_p}{P_b} = \frac{G_p(b_p/W)}{G_b(b_b/W)}\ \frac{H_p(v_{pl}/W)}{H_b(v_{pl}/W)} \qquad [2.6]$$

where the subscripts p, b denote precracked specimen and blunt-notched specimen, respectively. $G_b(b_b/W)$ is constant because the crack is stationary. The ratio P_p/P_b at constant plastic displacement represents a proposed separation parameter for the precracked specimen test record with respect to the blunt-notched specimen test record as

$$S_{p,b} = \left.\frac{P_p}{P_b}\right|_{v_{pl}} \qquad [2.7]$$

Hence

$$S_{p,b} = A\ G_p(b_p/W)\ \left.\frac{H_p(v_{pl}/W)}{H_b(v_{pl}/W)}\right|_{v_{pl}}$$

$$= A\ G_p(b_p/W)\ h_{p,b}(v_{pl}/W) \qquad [2.8]$$

where A is a constant equal to $1/G_b(b_b/W)$, and $h_{p,b}(v_{pl}/W)$ is a function of plastic displacement. The proposed separation parameter, $S_{p,b}$, can be evaluated for different growing crack test records with respect to the same blunt-notched specimen test record as

$$S^i_{p,b} = A\ G^i_p(b_p/W)\ h^i_{p,b}(v_{pl}/W) \qquad [2.9]$$

where $i=1,\ldots,n$ denotes precracked specimens. The different precracked specimen $S^i_{p,b}$-b_p/W records can be constructed together on one graph to check the plastic displacement contribution in the separation parameters. If the data show a wide scatter, this indicates that the separation parameters are dependent on the plastic displacement. Rather, if all the records $S^i_{p,b}$-b_p/W collapse together into one record so that

$$S^1_{p,b} = S^2_{p,b} = \ldots\ldots = S^n_{p,b} \qquad \text{at same } b_p/W \text{ value}$$

then $S_{p,b}$ is a function of b_p/W only and the plastic displacement has no contribution in the separation parameter, hence the plastic displacement corresponding term $h_{p,b}(v_{pl}/W)$ can be dropped, and Eq [2.8] can be rewritten as

$$S_{p,b} = A\ G_p(b_p/W) \qquad [2.10]$$

An experimental verification of Eq [2.10] indicates that the load in precracked specimen test records is separable and can be represented as a multiplication of two separate functions: a crack geometry function and a material deformation function. A more detailed discussion will be presented in chapter three and four about these functions and whether they are the same as those for stationary crack test records.

Much caution is required in studying load separation in precracked specimen records. There are two regions in crack growth mechanism in precracked specimen: blunting region and stable tearing region. Also, there are two regions in load separation: non-separable region and separable region. All these regions must be identified before interpreting the results. It is also worth noting that the current crack length in precracked specimens is estimated, usually using the compliance method, while the stationary crack is usually measured. This may slightly affect load separation results.

2.3.2 Experimental Results

Four sets of test records for four different materials (A533B, HSLA80, A106, and HY80 steels) will be studied in this section. Each set includes three or four precracked specimen test records. The specimens are of the compact geometry with 50.8 mm (2.0 in.) width and 25.4 mm (1.0 in.) thickness with 20% side grooving. These test records have been originally used in Ref. (56), and they are provided as data records on diskettes. The specimens in these four sets are of similar geometry, constraint, and machined from same materials as four compact tension sets previously used in studying load separation in compact geometry. One of the blunt-notched specimen test records of each material will be used as a reference record in studying the load separation in the precracked specimen test records. The current crack length in the precracked specimens was estimated

using the compliance method while the initial and final crack lengths were both estimated and physically measured. Also, the crack lengths in the blunt-notched specimens were both measured and estimated. Table 2.9 lists a summary of the crack lengths measured and estimated values for the different specimens. Figures 2.35, 2.36, 2.37, and 2.38 show the test records of the different precracked specimens and the reference blunt-notched specimen in the different sets. The elastic displacement at any point of the record can be evaluated using current compliance. Then, the load-plastic displacement can be developed. The separation parameters can be obtained using Eq [2.7]. Figure 2.39 shows the variation of the separation parameter, $S_{p,b}$, of an A533B precracked specimen with respect to the plastic displacement. Also, the figure shows the variation of the uncracked ligament, b_p/W, for the same record with respect to the plastic displacement. In the $S_{p,b}$-v_{pl} record, there is a small region at the early plastic behavior where $S_{p,b}$ varies significantly and this can be regarded as the non-separable region as discussed before in stationary crack test records. After this region, the separation parameter maintains almost a constant value for a while, then it starts to decrease. During both the non-separable region and the constant separation parameter region, the crack length shows little or almost no change if compared to the measured initial crack length value. Hence this region in b_p/W-v_{pl} record can be considered as the crack blunting region. The blunting region is followed by the stable tearing region. Figures 2.40, 2.41, and 2.42 show a similar behavior in HSLA80, A106, and HY80 precracked specimens. In v_{pl}-R curve study using same records, Joyce (60) described the slow crack growth region as initial blunting which agrees with the observation found by this study using load separation.

The nearly constant separation parameter in the crack blunting region indicates that load separation is maintained for this region in

Table 2.9: Measured and estimated crack length values.

Material	Specimen	Estimated		Measured	
		a_o/W	a_f/W	a_o/W	a_f/W
A533B Steel	Precrack E71	0.6045	0.6560	0.6080	0.6673
	Precrack E75	0.6045	0.7060	0.6070	0.7115
	Precrack E76	0.6030	0.7360	0.6070	0.7440
	Blunt E73	0.7410		0.7290	
HSLA80 Steel	Precrack GFFJ11	0.6075	0.6590	0.6150	0.6650
	Precrack GFFJ10	0.6045	0.7065	0.6150	0.7185
	Precrack GFFJ9	0.6140	0.7500	0.6240	0.7730
	Precrack GFFJ5	0.6125	0.7920	0.6225	0.8160
	Blunt GFFJ12	0.7730		0.7580	
A106 Steel	Precrack GAF34	0.6000	0.6530	0.6135	0.6673
	Precrack GAF19	0.6003	0.6740	0.6182	0.6955
	Precrack GAF17	0.5990	0.7300	0.6120	0.7510
	Precrack GAF18	0.6065	0.7835	0.6140	0.7980
	Blunt GAF22	0.753 (average)		0.7530	
HY80 Steel	Precrack FYBA12	0.6030	0.6550	0.6030	0.6565
	Precrack FYBA11	0.6005	0.7015	0.6020	0.7055
	Precrack FYBA10	0.6005	0.7515	0.6050	0.7565
	Blunt FYBA12	0.7140		0.7055	

the precracked specimen test records as if it were a stationary crack case, despite the difference in the crack nature in both cases.

To check explicitly the load separation in the entire test records for the different materials sets, the different $S_{p,b}$-b_p/W records for the different precracked specimens of each material set will be constructed together on one graph. If these records collapse together into almost one record, this indicates that the load is separable. Figures 2.43, 2.44, 2.45, and 2.46 show the different $S_{p,b}$-b_p/W records for A533B, HSLA80, A106, and HY80 sets, respectively. It is clear that the records collapse together in the stable tearing region no matter what plastic displacement is associated with the crack length at this point of the test. This indicates that the load in precracked specimen test records is separable and can be represented as a multiplication of two separate functions as proposed by Eq [2.5]. It is also clear in the figures that load separation is maintained over the whole crack extension which is sometimes far beyond the J-controlled crack growth limit. Also, the trend of the $S_{p,b}$-b_p/W record for large crack extension records is the same as that for short crack extension records. The blunting region can also be distinguished in these figures. The data points in the blunting region of an $S_{p,b}$-b_p/W record show almost vertical line in the non-separable region, then a cluster of points when load separation starts.

The load separation results in precracked specimen test records imply that using the single-specimen J form in J-R curve analysis is very appropriate.

2.4 Summary and Discussion

This experimental study shows that load separation exists in both pure bending and pure tension geometries, and also in those geometries with varied tension to bending ratio. Also, load separation

is not limited to a specific crack size, material, or constraint. Different test records of blunt-notched specimens that are machined from different materials with wide range of crack lengths and different variety of thickness and side grooving were studied and all of them, with no exception, shows load separation. Table 2.10 lists a summary of all the geometries, materials, constraints, crack length ranges involved in this study. It is also found that load separation may exist in other test records in which other forms of displacement, such as crack mouth opening displacement, are used instead of the commonly used load line displacement. Finally, load separation also exists in growing crack test records and this separation is maintained far beyond the J-controlled crack growth limit. Generally, it can be concluded that load separation is a dominant criterion in ductile fracture of cracked bodies. This provides a solid basis for the single-specimen J form which can be, then, considered as a generalized form for J-integral evaluation in ductile fracture mechanics.

Another important observation in all of the studied test records is that there is always a limited non-separable region at the early plastic behavior. The existence of such non-separable region before load separation may have a special significance. In an experimental study, Green and Hundy (45) noticed that a unique plastic pattern develops all over the uncracked ligament of slowly tested blunt-notched bend specimens just slightly past the yield point. They also found that as loading increases, yielded areas grow; yet the overall developed plastic region maintains roughly the same pattern. This observation was found in four-point bending, slow Izod and slow Charpy tests. Fig. 2.47 shows schematic drawings of the plastic pattern they noticed in V-notched plate under pure bending slightly past the yield point and well past the yield point.

On the other hand, in a numerical study, Sumpter (61, 62) evaluated the yielded regions that develop in a three-point bending

Table 2.10: Summary of the different cases involved in the load separation study.

Geom.	Mat.	Crack Type	Dimensions and Constraints	No. of Specs	$\frac{a}{W}$	test record
CT	HY130	Blunt	B=1 in., W=2 in. No side grooves	10	0.40 to 0.85	P-v_{ll}[1]
	A533B	Blunt	B=1 in., W=2 in. 20% side grooves	3	0.641 to 0.729	P-v_{ll}
		Precrack	B=1 in., W=2 in. 20% side grooves	3	0.607 to 0.744	P-v_{ll}
	HSLA80	Blunt	B=1 in., W=2 in. 20% side grooves	3	0.65 to 0.758	P-v_{ll}
		Precrack	B=1 in., W=2 in. 20% side grooves	4	0.615 to 0.816	P-v_{ll}
	A106	Blunt	B=1 in., W=2 in. 20% side grooves	3	0.70 to 0.806	P-v_{ll}
		Precrack	B=1 in., W=2 in. 20% side grooves	4	0.612 to 0.798	P-v_{ll}
	HY80	Blunt	B=1 in., W=2 in. 20% side grooves	3	0.657 to 0.757	P-v_{ll}
		Precrack	B=1 in., W=2 in. 20% side grooves	3	0.602 to 0.757	P-v_{ll}
SENB	HY130	Blunt	B=1 in., W=2 in., S=4W No side grooves	10	0.40 to 0.85	P-v_{ll}
CCT	HY130	Blunt	B=1 in., W=2 in. No side grooves	10	0.40 to 0.85	P-v_{ll}
SENT	A533B	Blunt	B=0.1 in., W=3 in. No side grooves	7	0.20 to 0.80	P-v_{ll}
	A710	Blunt	B=0.1 in., W=6 in. No side grooves	6	0.20 to 0.70	P-v_{ll} and P-v_{ff}[2]
		Blunt	B=1 in., W=6 in. No side grooves	3	0.50 to 0.70	P-v_{ll} and P-v_{ff}
		Blunt	B=1 in., W=6 in. 20% side grooves	3	0.40 to 0.70	P-v_{ll} and P-v_{ff}
		Blunt	B=1 in., W=6 in. 50% side grooves	3	0.30 to 0.70	P-v_{ll} and P-v_{ff}

1- P-v_{ll}: load versus load line displacement test record

2- P-v_{ff}: load versus crack mouth opening displacement test record

specimen. His results indicated that yield usually spreads across the uncracked ligament within the "elbow" region of the load-deflection record. Figure 2.48 shows schematic drawings of the yielded areas in the bend specimen and the corresponding points of loading on the load versus load line displacement record. This agrees with Green and Hundy's experimental observations.

Through the load separation study in this chapter, it seems that the position at which the behavior changes from non-separable to separable is also slightly past the yield point and almost within the elbow region. Figure 2.49 shows where load separation starts in three different test records of the HY130 SENB set. This indicates that load separation exists as soon as the plastic pattern develops across the uncracked ligament. Also, the non-separable region is the region where yielded areas start to develop and spread but are not yet fully connected across the uncracked ligament.

Within the non-separable region, J evaluation using the single-specimen form may not be appropriate; however, a recent study by Sharobeam and Landes (63) showed that the percentage errors due to the inclusion of such limited region in J evaluation are small, especially in bending geometries. The study also showed that these errors become much smaller when a considerable plastic behavior is included in the evaluation.

CHAPTER III

CRACK GEOMETRY FUNCTION AND PLASTIC ETA (η_{pl}) DEVELOPMENT

3.1 Introduction

It is demonstrated in chapter two that, in the test records of specimens of the same geometry, material, and constraint, the load can be represented as a multiplication of two functions: a crack geometry function and a material deformation function. The crack geometry function represents the effect of the crack length on the load value. Some expressions have been already proposed in the literature for the geometry function in compact, single-edge notched bend, and center-cracked tension geometries. These expressions were generally developed using limit load analysis.

In this chapter, the geometry function is constructed for the different test record sets using the load separation parameters developed in Chapter II. Then, the constructed functions are compared to those reported in the literature. Also, we discuss whether the geometry functions developed for growing crack test records are the same as those developed for stationary crack test records for specimens machined of the same material with the same geometry and constraint.

We also discuss the development of the multiplication factor in the single-specimen J form, namely η_{pl}. This factor only exists if the load is separable, and it is directly related to the geometry function.

Therefore, if the geometry function can be developed, η_{pl} can be obtained.

3.2 The Geometry Functions in Stationary Crack Test Records

The separation parameter $S_{i,j}$ for any test record a_i/W with respect to another test record a_j/W was written before as

$$S_{i,j} = \frac{G(a_i/W)}{G(a_j/W)} \qquad [3.1]$$

Then, for a set of n test records, a_1/W to a_n/W, the different $S_{i,j}$ values for the different test records, a_i/W, with respect to a certain reference record, a_j/W, can be written as

$$S_{i,j}(a_i/W) = A\ G(a_i/W) \qquad [3.2]$$

or

$$S_{i,j}(b_i/W) = A\ G(b_i/W) \qquad [3.3]$$

where i varies from 1 to n and j is fixed. A is a constant that is equal to $1/G(a_j/W)$. Therefore, b_i/W is the only variable in Eq [3.3]. Based on Eq [3.3], as the relationship $S_{i,j}$-b_i/W is constructed for the different test records in each set, the corresponding geometry function $G(b_i/W)$ can be developed.

Compact Geometry

Figure 3.1 shows the variation of the separation parameter $S_{i,j}$ versus b_i/W for the HY130 compact specimens set on logarithmic coordinates. All the test records have been alternately used as reference records in order to construct all the possible $S_{i,j}$-b_i/W

records. It is obvious that the power law fit is the best candidate for the $S_{i,j}$-b_i/W relationship. Figure 3.2 shows the power law fit for all the $S_{i,j}$-b_i/W records on logarithmic coordinates and Fig. 3.3 shows a sample of the power law fit for one of these records on linear coordinates. Hence $S_{i,j}$ can be written as

$$S_{i,j} = A_1 (b_i/W)^m \qquad [3.4]$$

where m is the power law exponent and A_1 is a constant. Table 3.1 lists the values of the power law exponent m and the constant A_1 for the power law fit of the different $S_{i,j}$-b_i/W records. The power law exponent is almost the same ($m \approx 2.13$) for all records. This also can be seen in Fig. 3.2, where all the fit lines are parallel. This indicates that the power law fit is consistent no matter which record is used as a reference record.

Table 3.1: Power law fit results in the HY130 CT set.

b_j/W	m	A_1	$A_1.(b_j/W)^m$
0.60	2.135	3.038	1.021
0.55	2.134	3.587	1.002
0.50	2.129	4.341	0.992
0.45	2.127	5.445	0.996
0.40	2.126	6.972	0.994
0.35	2.117	9.241	1.001
0.30	2.118	12.763	0.997
0.25	2.125	19.112	1.005
0.20	2.124	30.534	1.001
0.15	2.146	58.047	0.991

Comparing Eq [3.4] to Eq [3.3], one can obtain

$$G(b_i/W) = c\ (b_i/W)^m \qquad [3.5]$$

and

$$A = A_1/c \qquad [3.6]$$

where c is a constant. Thus (A_1/c) is equal to $1/G(b_j/W)$. Based on Eq [3.5], $G(b_j/W)$ is also a power law function of b_j/W; therefore A_1 must be equal to $1/(b_j/W)^m$ or, in other words, $\{A_1.(b_j/W)^m\}$ must be equal to 1.0. Table 3.1 lists the $\{A_1.(b_j/W)^m\}$ values for the different records. They are very close to 1.0 which emphasizes the validity of the power law form as the best candidate for the geometry function.

In the four other compact specimen sets, the power law fit shows reasonable results despite the fact that the crack length range is relatively small in these sets, which may not help in constructing a very reliable fit. Figures 3.4, 3.5, 3.6, and 3.7 show the power law fit of the $S_{i,j}$-b_i/W records for the different sets. Also, Table 3.2 lists a summary of the power law fit results (m, A_1, and $\{A_1.(b_j/W)^m\}$) in the different sets. The fit results are reasonable in the different sets except in the A106 steel set. One of the three test records in this set might have been over- or under-estimated.

In the literature, the geometry function for the compact geometry is presented as

$$G\left(\frac{b}{W}\right) = \left(\frac{b}{W}\right)^2 e^{0.522\frac{b}{W}} \qquad [3.7]$$

This form is based on the η-expression given in Eq [1.15] which is a linear approximation of the Merkle-Corten η-expression, Eq [1.14b], obtained also through an approximate theoretical analysis (limit load analysis). Limit load analysis is based on the assumption that the

Table 3.2: Power law fit results in the other four CT sets.

Set	b_j/W	m	A_1	$A_1.(b_j/W)^m$
A533B	0.271	2.187	17.534	1.0088
HSLA80	0.242	2.316	26.772	1.0014
A106	0.247	2.106	20.050	1.055
HY80	0.2435	2.251	24.025	0.9991

material is non-hardening (elastic-perfectly plastic). Therefore, the geometry function expression in Eq [3.7] is developed through a series of theoretical and numerical approximations.

Using the G-expression given in the literature, Eq [3.7], may result a significant error in load estimation which is of main concern in any ductile fracture methodology. This can be explained through the following procedure.

Based on load separation, Eq [3.1] can be written as

$$\left.\frac{P(a_i)}{P(a_j)}\right|_{v_{pl}} = \frac{G(b_i/W)}{G(b_j/W)}$$

Then, if the load $P(a_j)$ value at certain plastic displacement is given from experimental data, $P(a_i)$ value at the same plastic displacement can be estimated as

$$\{P(a_i)\}_{\text{est.}} = \frac{G(b_i/W)}{G(b_j/W)} \{P(a_j)\}_{\text{exp.}}$$

By dividing both sides by $\{P(a_i)\}_{exp.}$ at the same plastic displacement, one gets

$$\left.\frac{\{P(a_i)\}_{est.}}{\{P(a_i)\}_{exp.}}\right|_{v_{pl}} = \frac{G(b_i/W)}{G(b_j/W)} \Big/ \left.\frac{\{P(a_i)\}_{exp.}}{\{P(a_j)\}_{exp.}}\right|_{v_{pl}}$$

$$= \frac{G(b_i/W)}{G(b_j/W)} \Big/ \{S_{i,j}\}_{exp.} \qquad [3.8a]$$

The right side of Eq [3.8a] is constant for stationary cracks over the whole plastic region except for the limited non-separable region at the early plastic behavior. Thus the ratio of the load's estimated value to the load's experimental value for a certain test record a_i/W is the same for almost the whole plastic region, then Eq [3.8a] can be rewritten as

$$\frac{\{P(a_i)\}_{est.}}{\{P(a_i)\}_{exp.}} = \frac{G(b_i/W)}{G(b_j/W)} \Big/ \{S_{i,j}\}_{exp.} \qquad [3.8b]$$

Using any proposed geometry function expression in Eq [3.8], one can calculate the error in the load estimation for the different test records. Figure 3.8 shows the errors in the estimated load values for the different test records with respect to a reference record in the HY130 steel set when the geometry function expression in Eq [3.7] is used. The errors are varying from 0% to 10% and they are bigger when the difference between b_i/W and b_j/W is bigger. The figure shows also how small the errors are when the power law geometry function is used.

The validity of the power law geometry function expression in the compact geometry can also be verified through the numerical solutions provided in the EPRI handbook (50). The handbook

suggests a separable form to represent the load versus load line plastic displacement relationship in the compact geometry for a Ramberg-Osgood material as

$$v_{pl} = \alpha\, \varepsilon_o\, a\, h_3(a/W,n)\ (P/P_o)^n \qquad [3.9]$$

and

$$P_o = 1.455\ \mu\, b\, \sigma_o \qquad \text{for plane strain, and}$$
$$P_o = 1.071\ \mu\, b\, \sigma_o \qquad \text{for plane stress.}$$

where σ_o is yield stress, ε_o is yield strain, α is a material constant, n is strain-hardening exponent in Ramberg-Osgood relationship, Eq [1.41], μ is the α-expression given in Eq [1.13b], and h_3 is a function of a/W and n. The handbook provides numerical tables for $h_3(a/W,n)$ values at specific a/W and n values for both plane stress and plane strain cases. Equation [3.9] can be rewritten as

$$P = \{f_1(a/W,n)\ f_2(\alpha,\sigma_o,\varepsilon_o)\}\ (v_{pl}/W)^{1/n} \qquad [3.10]$$

which, for same material, yields

$$P = \{G(b/W)\}_{HB}\ (v_{pl}/W)^{1/n} \qquad [3.11]$$

where $\{G(b/W)\}_{HB}$ can be regarded as a geometry function that is proposed by the handbook. The handbook does not provide a specific form for $h_3(a/W,n)$ function, therefore $[G(b/W)]_{HB}$ can only be calculated at certain a/W and n values. An $[S_{i,j}]_{HB}$-b_i/W record for a certain material (n = constant) can be constructed, then checked whether it agrees with a power law fit. The parameter $[S_{i,j}]_{HB}$ can be defined as the ratio of the handbook geometry function for the different crack lengths, a_i/W, to that for a reference crack length, a_j/W, and it is material independent except for n because the term $f_2(\alpha,\sigma_o,\varepsilon_o)$ is dropped in this case. Figures 3.9 and 3.10 show the $[S_{i,j}]_{HB}$-b_i/W records for both plane stress and plane strain

constraints on logarithmic coordinates for a material with n=10 . The figures show how the records agree very well with the power law fit except for the shallow crack case (a/W=0.25) in plane strain constraint. The power law exponent, m, values for the plane stress and plane strain cases for the given n value are found to be 2.234 and 2.280, respectively. Other n values (n=3 to 20) showed m values very close to these.

Briefly, one can conclude that the power law function is an appropriate form for the geometry function in compact geometry.

Single-Edge Notched Bend Geometry

The geometry function in the single-edge notched bend geometry can be similarly developed by constructing the appropriate fit of the experimental $S_{i,j}$-b_i/W records. Figure 3.11 show the different $S_{i,j}$-b_i/W records developed for the different b_j/W reference records on logarithmic coordinates. It is clear that the power law fit, again, is the best candidate for these records for the different b_i/W values except for two test records: b_i/W=0.20 and b_i/W=0.15. The data of these records are a little bit higher than the fit lines of all the other data as shown in Fig. 3.12. These two records might have been over-estimated. Table 3.3 lists the different power law exponent m, constant A_1, and $\{A_1.(b_j/W)^m\}$ values associated with the different reference records except the two bad records, b_i/W=0.20 and b_i/W=0.15. The power law exponent maintains almost the same value ($m \approx 1.94$). Also, $\{A_1.(b_j/W)^m\}$ is almost equal to (1.0) no matter what reference record is used. Hence the geometry function in single-edge notched bend geometry is a power law function and can be written as shown in Eq [3.5].

Table 3.3: Power law fit results in the HY130 SENB set.

b_j/W	m	A_1	$A_1.(b_j/W)^m$
0.60	1.940	2.725	1.011
0.55	1.943	3.178	0.995
0.50	1.941	3.833	0.998
0.45	1.937	4.654	0.991
0.40	1.942	5.936	1.002
0.35	1.939	7.737	1.010
0.30	1.946	10.346	1.003
0.25	1.943	14.836	1.003

The widely used geometry function form for this geometry in the literature is also a power law form but with a power law exponent equal to 2.0. This form is based on limit load analysis with the assumption that the material is non-hardening (elastic-perfectly plastic). The HY130 steel is not an elastic-perfectly plastic material which may be the reason that the power law exponent obtained from the experimental results fit is slightly different from 2.0. Unfortunately, there are no other data sets to examine such assumption and investigate the power law exponent variation (if there is any) with the material mechanical properties and also to check whether it converges to 2.0 for non-hardening materials, as proposed by limit load analysis.

Center-Cracked Tension Geometry

Figure 3.13 show the different $S_{i,j}$-b_i/W records developed for the different reference b_j/W records in the HY130 CCT set on logarithmic coordinates. The figure shows also the power law fit lines of the different records, and Table 3.4 lists the different power law

Table 3.4: Power law fit results in the HY130 CCT set.

b_j/W	m	A_1	$A_1.(b_j/W)^m$
0.60	0.963	1.640	1.003
0.55	0.963	1.772	0.996
0.50	0.964	1.954	1.002
0.45	0.962	2.148	0.996
0.40	0.962	2.436	1.009
0.35	0.963	2.729	0.993
0.30	0.963	3.200	1.004
0.25	0.963	3.794	0.998
0.20	0.962	4.686	0.996
0.15	0.962	6.225	1.004

exponent m, constant A_1, and $\{A_1.(b_j/W)^m\}$ values associated with the different reference records. These results show that the power law fit is also the best candidate for the geometry function in the center-cracked tension geometry. The power law exponent in this set almost maintains a constant value of 0.963 for the different reference records.

The CCT geometry function proposed in the literature is based on limit load analysis and can be written as

$$G(2b/W) = 2b/W \qquad [3.12]$$

This G-expression is also a power law function with a power law exponent of 1.0. As previously discussed, the difference in the power law exponent between the limit load analysis form and the experimental form might result from the fact that the HY130 steel is

not an elastic-perfectly plastic material as proposed by limit load analysis.

Single-Edge Notched Tension Geometry

No specific geometry function expression has been proposed in the literature for the single-edge notched tension geometry. This geometry is basically a tension geometry but with a bending component; therefore it may be interesting to investigate the possibility that the geometry function in such case is also a power law function as in the other studied cases.

Figure 3.14 shows the power law fit of the different $S_{i,j}$-b_i/W records of the A533B SENT set on logarithmic coordinates. The power law fit agrees very well with the data in this set. Table 3.5 lists the different power law exponent m, constant A_1, and $\{A_1.(b_j/W)^m\}$ values associated with the different reference records. The power law exponent almost maintains a constant value of 2.44 for all the reference records.

Another example of the power law fit in single-edge notched tension geometry is shown in Fig. 3.15 for the A710 SENT set. Table 3.6 lists a summary of the corresponding power law fit results. The power law fit in the A710 set is not as good as in the A533B set; however, the fit results are reasonably consistent. The problem of this set is that the specimens were very wide (6.0 in. wide) and very thin (0.1 in thick) at the same time, which may create some problems in maintaining the stability of the specimens during the test.

The other A710 thick specimens (1.0 in thick) sets show a nice power law fit as shown in Figs. 3.16 and 3.17 for sets with 20% and 50% side grooving. In the no side-grooved specimens set, there are only two load versus load line displacement records, which is not

Table 3.5: Power law fit results in the A533B SENT set.

b_j/W	m	A_1	$A_1.(b_j/W)^m$
0.80	2.441	1.756	1.019
0.70	2.451	2.385	0.995
0.60	2.442	3.473	0.997
0.50	2.434	5.272	0.975
0.40	2.442	9.430	1.006
0.30	2.439	19.213	1.019
0.20	2.449	51.092	0.992

Table 3.6: Power law fit results in the thin A710 SENT set.

b_j/W	m	A_1	$A_1.(b_j/W)^m$
0.80	2.363	1.768	1.043
0.70	2.368	2.352	1.011
0.60	2.366	3.182	0.950
0.50	2.370	4.958	0.960
0.40	2.360	8.888	1.023
0.30	2.378	17.743	1.013

sufficient for constructing the fit. Table 3.7 lists a summary of the power law fit results for the sets with 20% and 50% side grooving.

The different A710 sets have also shown load separation in the load versus crack mouth opening displacement records. Therefore, the geometry functions for these sets can also be developed using the $S_{i,j}$-b_i/W records obtained from the load versus crack mouth opening displacement test records. Figures 3.18, 3.19, 3.20, and 3.21 show the power law fit of the different $S_{i,j}$-b_i/W records developed in each set and Table 3.8 lists a summary of the fit results. The power law exponents obtained for the load versus crack mouth opening displacement records are almost the same as those obtained for the load versus load line displacement records.

The EPRI handbook solutions for the load versus crack mouth opening displacement relationships are represented in a separable forms that can be written as Eq [3.11]. This allows the development of the $[S_{i,j}]_{HB}$-b_i/W record for the SENT geometry for any specific material (n=constant). This record can be checked for whether it agrees with the power law fit. Figures 3.22 and 3.23 show the $[S_{i,j}]_{HB}$-b_i/W records on logarithmic coordinates for a material with n=10 for both plane stress and plane strain constraints. The power law fit is the best candidate for these records except for the very shallow crack case (a/W=1/8) in the plane strain constraint. The power law exponents for the given n value are found to be 2.345 and 2.359 for plane stress and plane strain cases, respectively.

Briefly, the power law fit is an appropriate candidate for the geometry function in the single-edge notched tension geometry. Also, the power law exponent maintains almost the same value when another displacement form is used in the test record instead of the load line displacement. The results also show that the constraint, provided by thickness and side grooving, may have a slight effect on the power law exponent values.

Table 3.7: Power law fit results in the 1.0 in. thick A710 SENT sets.

Set	b_j/W	m	A_1	$A_1.(b_j/W)^m$
20% side groove	0.60	2.317	3.277	1.003
	0.50	2.316	4.952	0.994
	0.30	2.316	16.269	1.001
50% side groove	0.70	2.437	2.394	1.004
	0.50	2.392	5.255	1.001
	0.30	2.432	18.587	0.995

Table 3.8: Power law fit results in the different A710 SENT sets for the load versus crack mouth opening displacement records.

Set	b_j/W	m	A_1	$A_1.(b_j/W)^m$
B=0.1 in., W=6.0 in No side groove	0.80	2.402	1.754	1.026
	0.70	2.399	2.406	1.022
	0.60	2.393	3.250	0.957
	0.50	2.389	5.057	0.966
	0.40	2.389	9.134	1.023
	0.30	2.404	18.198	1.006
B=1.0 in., W=6.0 in No side groove	0.50	2.324	4.996	0.998
	0.40	2.325	8.452	1.004
	0.30	2.319	16.285	0.999
B=1.0 in., W=6.0 in 20% side groove	0.60	2.325	3.263	0.995
	0.50	2.341	5.100	1.007
	0.30	2.328	16.451	0.998
B=1.0 in., W=6.0 in 50% side groove	0.70	2.382	2.345	1.003
	0.50	2.374	5.164	0.997
	0.30	2.383	17.644	1.001

3.3 The Geometry Function in Precracked Specimen Test Records

In precracked specimen test records, the geometry function can be obtained by constructing the best fit for the $S_{p,b}$-b_p/W data in the stable tearing region. In the load separation study of the four precracked compact specimen sets in section 2.3, the stable tearing region in the different $S_{p,b}$-b_p/W records of each set collapsed together into one record creating almost a line on logarithmic coordinates (see Figs. 2.43, 2.44, 2.45, and 2.46). This implies that the power law fit is the best candidate for the stable tearing region in these $S_{p,b}$-b_p/W records. The power law fit in the stable tearing region is shown again, but more explicitly, in Figs. 3.24, 3.25, 3.26, and 3.27 on linear coordinates. Therefore, $S_{p,b}$ can be written as

$$S_{p,b} = A_1 \, (b_p/W)^m \qquad [3.13]$$

where A_1 is the fit constant and m is the power law exponent. Comparing Eq [3.13] with Eq [2.10], one gets

$$G(b_p/W) = c \, (b_p/W)^m \qquad [3.14]$$

and

$$A = A_1/c \qquad [3.15]$$

Table 3.9 lists a summary of the power law exponent m and the constant A_1 values in the different sets. The table lists also the $\{A_1.(b_b/W)^m\}$ values, in analogy to the stationary crack case, however the estimated b_b/W values are used instead of the measured values because the power law fit was developed using the b_p/W estimated values. The power law exponent, m, values for the precracked specimen sets are very close to those obtained for the corresponding blunt-notched specimen sets for the A533B and HY80 sets. Also, the $\{A_1.(b_b/W)^m\}$ values are very close to 1.0 in these two

Table 3.9: Power law fit results in the precracked specimen sets.

Set	b_b/W	m	A_1	$A_1.(b_b/W)^m$
A533B	0.259	2.12	17.37	0.991
HSLA80	0.227	1.87	18.58	1.161
A106	0.247	2.38	27.85	0.999
HY80	0.286	2.28	16.97	0.978

sets. This indicates that the geometry function, in such cases, maintains its form and power law exponent value as the crack grows. The power law exponent values in the A106 and HSLA80 precracked specimen sets are different than those obtained from the blunt-notched specimen sets; however, the $\{A_1.(b_b/W)^m\}$ value for the A106 precracked specimens set is very close to (1.0). On the other hand, the A106 blunt-notched specimens set showed an unreliable fit. This may imply that the geometry function for the A106 steel showed a different power law exponent in the precracked specimens than in the blunt-notched specimens only because one of the blunt-notched specimen records (most probably that of the specimen with a/W=0.8055) was under-estimated, or its crack length value was not carefully measured. The value of the power law exponent in the HSLA80 precracked specimens is relatively surprising because the power law fit in compact geometries is expected to be higher than 2.0.

The effect of the crack length measurment (or estimations) on the geometry function fit can be shown by studying the constant A_1. The crack length of the reference blunt-notched specimen can be evaluated from the constant A_1 as

$$b_b/W = \frac{-\ln(A_1)}{m} \qquad [3.16]$$

Using Eq [3.16] with m as the power law exponent obtained from the precracked specimens' fit, one obtains the estimated crack length values for the A533B, HY80, and A106 blunt-notched specimens used in the precracked specimen study as: 1.48, 1.422, and 1.506, respectively. These values are between the physically measured values and the estimated values using the compliance method, see Table 2.9. This may indicate that if there was no difference between the crack length measured and estimated values, we might get the the same power law exponent in both cases.

The blunting region in the precracked specimen test records may be also handled as a stationary crack case. Using Eqs [3.1] and [3.5], one can obtain the power law exponent m for the blunting region in each precracked specimen as

$$S_{p,b} = \frac{\{G_p(b_b/W)\}_{blunt.\ region}}{G(b_b/w)}$$

$$= [\{b_b\}_{blunt.\ region}/b_b]^m$$

then

$$m = ln(S_{p,b}) \ / \ ln[\{b_b\}_{blunt.\ region}/b_b] \qquad [3.17]$$

where b_p can be considered as the average estimated uncracked ligament in the precracked specimen during the blunting region and b_b is the estimated uncracked ligament of the reference blunt-notched specimen. Table 3.10 shows the different m values obtained using Eq [3.17] for the different precracked specimens in each set. The m values are very close to those obtained from the stable tearing region, and consequently to the blunt-notched specimen results, except in the HSLA80 steel set. The calculated m values for the HSLA80 set are between the blunt-notched specimens and the precracked specimens results. This may imply that either the geometry function for the HSLA80 steel changes its power law exponent as the crack grows or there are some measurement errors

Table 3.10: Power law exponent values in the blunting region of the precracked specimen records.

Set	Specimen	Blunting region b_p/W	$S_{p,b}$	m
A533B	E71	0.395	2.424	2.10
	E75	0.393	2.391	2.09
	E76	0.396	2.436	2.10
HSLA80	GFFJ11	0.391	3.132	2.10
	GFFJ10	0.389	3.072	2.086
	GFFJ9	0.384	3.064	2.127
	GFFJ5	0.384	3.013	2.103
A106	GAF34	0.396	3.005	2.33
	GAF19	0.394	2.980	2.338
	GAF17	0.400	3.140	2.374
	GAF18	0.390	3.047	2.44
HY80	FYBA12	0.393	2.063	2.28
	FYBA11	0.392	2.063	2.293
	FYBA10	0.395	2.074	2.27

involved in the precracked specimen test records. However, we can generally conclude that the geometry function in the growing crack test records is a power law function and is identical, in most cases, to the one obtained in the stationary crack test records.

3.4 Plastic Eta (η_{pl}) Development

The use of a separable form to represent the load, in the early 1970's, created a new factor η. This factor appears in the single-specimen J form and exists only if the load is separable. It represents a coefficient that modifies the area under the load versus load line displacement record per unit length of the uncracked ligament to represent J, Eq [1.11]. The present η-expressions evolved through series of approximate analyses and experimental results, and they are available for single-edge notched bend and compact geometries only, Eqs [1.14a] and [1.15].

As previously mentioned, the single-specimen J form is more appropriate for the experimental evaluation of the plastic part of J (J_{pl}) only and not the overall J, where J_{pl} can be written as

$$J_{pl} = \eta_{pl} \frac{A_{pl}}{Bb} \qquad [3.18]$$

This form is a direct result of the load separation in the plastic region. The η_{pl}-factor in Eq [3.18] is assumed to maintain the same expressions used for the overall η. Such assumption may require additional study. On the other hand, a numerical study showed that η_{pl} is independent of the plastic displacement for only a small range of configurations, such as deeply notched bending configurations or similar cases, while the overall η is independent of the plastic displacement for a much wider range of cases. This may suggest that

using the overall η and, consequently the overall J, is more appropriate. To settle this dispute about η_{pl}, it may be very useful to find a reliable method to develop η_{pl} experimentally, then discuss the effect of the different variables on η_{pl} values.

If η_{pl} can be evaluated experimentally by comparing the single-specimen J_{pl} form, Eq [3.18] with the energy rate interpretation form written for the plastic region as

$$J_{pl} = -\frac{1}{B}\frac{\partial U_{pl}}{\partial a} \qquad [3.19]$$

where U_{pl} is the plastic potential energy, and if it can be represented as the area A_{pl} under the load versus load line plastic displacement record, then η_{pl} can be written as

$$\eta_{pl} = \frac{\{-\partial U_{pl}/\partial a\}}{\{A_{pl}/b\}} \qquad [3.20]$$

For a separable behavior, U_{pl} (or A_{pl}) can be written as

$$A_{pl} = \int G(a/W)\, H(v_{pl}/W)\, dv_{pl}$$

$$= G(a/W) \int H(v_{pl}/W)\, dv_{pl}$$

$$= U_{pl}$$

Thus Eq [3.20] can be written as

$$\eta_{pl} = -b\frac{dG(a/W)/da}{G(a/W)} \qquad [3.21]$$

The first derivative of $G(a/W)$ with respect to a can be written as

$$\frac{dG(a/W)}{da} = \frac{1}{W}\frac{dG(a/W)}{d(a/W)}$$

$$= -\frac{1}{W}\frac{dG(b/W)}{d(b/W)} \qquad [3.22]$$

Substituting Eq [3.22] into Eq [3.21], we get

$$\eta_{pl} = \frac{b}{W}\frac{dG(b/W)/d(b/W)}{G(b/W)} \qquad [3.23]$$

Equation [3.23] represents the direct relationship between η_{pl} and the crack geometry function, $G(b/W)$. Then, if $G(b/W)$ is defined, η_{pl} can be obtained. Based on the results of the previous two sections that the geometry function is a power law function, then η_{pl} is equal to the power law exponent and can be written as

$$\eta_{pl} = m \qquad [3.24]$$

Table 3.11 lists a summary of η_{pl} values for all the studied sets. In this study, η_{pl} for the compact geometry is not dependent on the crack length as predicted by Eq [3.17]. On the other hand, it shows a slight material dependence. Also, η_{pl} is neither equal to two for the studied SENB set nor equal to 1.0 for the CCT set which may point, again, to the material dependence. The η_{pl}values developed in this study for the CCT and SENT geometries are the first experimental values ever obtained for these geometries.

Equation [3.24] indicates that η_{pl} is entirely independent of the plastic displacement. This does not agree with the previously mentioned numerical study which showed that η_{pl} is dependent on

Table 3.11: Summary of η_{pl} values in the different studied cases.

Geom.	Mat.	Crack Type	Dimensions and Constraints	$\frac{a}{W}$	test record	η_{pl} (m)
CT	HY130	Blunt	B=1 in., W=2 in. No side grooves	0.40 to 0.85	P-v_{ll}[1]	2.13
	A533B	Blunt	B=1 in., W=2 in. 20% side grooves	0.641 to 0.729	P-v_{ll}	2.19
		Precrack	B=1 in., W=2 in. 20% side grooves	0.607 to 0.744	P-v_{ll}	2.12
	HSLA80	Blunt	B=1 in., W=2 in. 20% side grooves	0.65 to 0.758	P-v_{ll}	2.32
		Precrack	B=1 in., W=2 in. 20% side grooves	0.615 to 0.816	P-v_{ll}	1.87 low value
	A106	Blunt	B=1 in., W=2 in. 20% side grooves	0.70 to 0.806	P-v_{ll}	2.11 bad fit
		Precrack	B=1 in., W=2 in. 20% side grooves	0.612 to 0.798	P-v_{ll}	2.38
	HY80	Blunt	B=1 in., W=2 in. 20% side grooves	0.657 to 0.757	P-v_{ll}	2.25
		Precrack	B=1 in., W=2 in. 20% side grooves	0.602 to 0.757	P-v_{ll}	2.28
SENB	HY130	Blunt	B=1 in., W=2 in., S=4W No side grooves	0.40 to 0.85	P-v_{ll}	1.94
CCT	HY130	Blunt	B=1 in., W=2 in. No side grooves	0.40 to 0.85	P-v_{ll}	0.963
SENT	A533B	Blunt	B=0.1 in., W=3 in. No side grooves	0.20 to 0.80	P-v_{ll}	2.44
	A710	Blunt	B=0.1 in., W=6 in. No side grooves	0.20 to 0.70	P-v_{ll} P-v_{ff}[2]	2.368 2.396
		Blunt	B=1 in., W=6 in. No side grooves	0.50 to 0.70	P-v_{ll} P-v_{ff}	2.40[3] 2.324
		Blunt	B=1 in., W=6 in. 20% side grooves	0.40 to 0.70	P-v_{ll} P-v_{ff}	2.316 2.331
		Blunt	B=1 in., W=6 in. 50% side grooves	0.30 to 0.70	P-v_{ll} P-v_{ff}	2.42 2.38

1- P-v_{ll}: load versus load line displacement test record

2- P-v_{ff}: load versus crack mouth opening displacement test record

3- This value is obtained assuming that the geometry function is a power law function.

the plastic displacement for a wide range of configurations. η_{pl} dependence on v_{pl} might result from the inclusion of the non-separable region in the evaluation process. Any analysis that does not distinguish between the separable region and the non-separable region in the plastic regime, such as the one used to develop Eq [2.20], may lead to such an incorrect conclusion. For example, the classical method for η_{pl} experimental evaluation is based on Eq [3.20], and the developed values usually show η_{pl} dependence on v_{pl}.

In the classical method, the areas A_{pl} under the test records of many identical specimens with different crack lengths are evaluated at different plastic displacement, and the A_{pl}-a (or U_{pl}-a) fit is developed. Hence the slopes dU_{pl}/da at different crack lengths and plastic displacements can be calculated. Then, by substituting the slopes and the corresponding areas into Eq [3.20], one can obtain η_{pl} values at the different crack lengths and displacements. The development of dU_{pl}/da is based on Landes and Begley's multi-specimen technique (see Fig. 1.5). The classical method includes the whole plastic regime, both the separable and non-separable regions, which results in some errors in the developed values.

A computer program has been developed to evaluate η_{pl} using the classical method for the different studied sets of blunt-notched specimens. Figures 3.28 and 3.29 show, as examples of the results, the variation of η_{pl} with the plastic displacement for two test records of the HY130 CT and CCT sets. Also, the figures show the $S_{i,j}$-v_{pl} records for these test records. η_{pl} varies considerably with v_{pl} at the beginning of the plastic behavior before it converges slowly to a constant value far beyond the start of the load separation. This variation is the reason of the misinterpretation of η_{pl} dependence on v_{pl}, and results solely from the inclusion of the non-separable region

in the area calculation. As the ratio of the separable region to the non-separable region increases, η_{pl} converges.

It may be also interesting to look at the converged η_{pl} values developed by the classical method and compare them with those obtained using the load separation method proposed here. Figures 3.30, 3.31, 3.32 and 3.33 show the classical method converged η_{pl} values for the different test records of the three HY130 sets and the A533B set as examples of the different geometries. The values obtained by the classical method are not consistent, as are those obtained by load separation because, in addition to the error evolved from the non-separable region, there are some errors resulting from the successive approximation of the areas. Also, fitting the data to evaluate the slope and dividing by the area again may add additional errors.

The classical method can only be used for stationary crack specimen test records, while the new method can also be used for precracked specimen test records as long as there is an additional stationary crack test record of a similar specimen. In the new method, three blunt-notched specimens (sometimes only two if the geometry function is assumed to be a power law function) or one precracked specimen together with a blunt-notched specimen are required to evaluate η_{pl}.

3.5 Summary and Conclusions

The following observations can be made in evaluating the crack geometry function and the related η_{pl} factor.

* Generally the power law fit is the best candidate for the crack geometry function in the different studied geometries, materials, and constraints.

* The power law exponent in the power law geometry function (within the same geometry) may show a little material dependence.

* The constraints show very little effect on the power law exponent value.

* The geometry function developed from load versus load line displacement records is almost the same as that developed from load versus crack mouth opening displacement records.

* In most cases, the geometry function maintains its form and power law exponent value as the crack grows and up to a crack growth even far beyond J or J_m limits. However, the nature of the crack length measurment or estimation may result in a little difference in the developed power law exponent value. These differences can be minimized if both measurment and estimation methods provide the same crack length value.

* A new method for experimentally determining the η_{pl} factor based on load separation is proposed. The method can be applied for both blunt-notched or precracked specimen test records. By evaluating the different $S_{i,j}$ for set of blunt-notched specimen test records and then constructing the $S_{i,j}$- b_i/W record, the geometry function can be developed and η_{pl} can be obtained. Also, using a set of (or only one) precracked specimen test records with the test record of a similar blunt-notched specimen, one can develop the Sp,b-b_p/W fit for the stable tearing region and, consequently, obtain the geometry function and η_{pl}. If the geometry function is a power law function, which

seems very likely from these results, then η_{pl} is equal to the power law exponent.

* The developed η_{pl} values are consistent and accurate because the new method avoids most of the errors associated with the classical method.

* The study shows that η_{pl} is independent of the plastic displacement and the previous misinterpretation of its dependence on the plastic displacement resulted solely from the inclusion of the non-separable region in the calculation.

* The new η_{pl} method can be used with any geometry and η_{pl} can be developed using either three (or two if the geometry function is assumed to be a power law) blunt-notched specimen test records or one blunt-notched specimen test record together with a precracked specimen test record. The later is very appropriate for use with J-R determination because only one additional specimen test record is required; however, a longer crack growth may be required in the precracked specimen test record to assure a reasonable fit.

CHAPTER IV

MATERIAL DEFORMATION FUNCTION

4.1 Introduction

The material deformation function can be written as a normalized function of plastic displacement, and, based on the load separation principle, it is completely independent of crack length. In this chapter, the deformation functions for all the different sets are constructed by normalizing the different test records in each set by the corresponding geometry function developed before for this set. Hence it can be written as

$$H(v_{pl}/W) = \frac{P}{G(b/W)} \qquad [4.1]$$

The geometry function was found to be well represented as a power law function in the different studied cases, therefore Eq [4.1] can be rewritten as

$$H(v_{pl}/W) = \frac{P}{[c\ (b/W)^m]} \qquad [4.2]$$

The constant c is independent of both the crack length and the plastic displacement; however, it may differ from one set to another based on the material, constraint, and geometry of the set.

An alternative expression for Eq [4.2] can be given as

$$P_N = \frac{P}{BW(b/W)^m} \qquad [4.3]$$

P_N is the normalized load. It represents an alternative form for the deformation function but in stress dimensions. The constant c is included in the P_N term. B is the specimen thickness and, for side-grooved specimens, B can be taken as the net thickness as recommended by the ASTM standard test methods for the plastic region evaluation; however, the whole thickness or an effective thickness value can be also used as long as all the specimens in a given set have the same side grooving. Equation [4.3] will be used to construct the deformation function for the different sets. Based on the assumption of load separation, the different P_N versus v_{pl} records in each set should collapse together into one curve that is the deformation function for this set.

The study also discusses the normalization using the geometry functions given in the literature and compares the scatters in the developed deformation functions to those obtained using the geometry functions from the separation analysis.

There are some implications in the literature, especially the EPRI handbook, that the deformation function is an analogous form to the stress versus strain relationship. This may imply that the deformation function is independent of the geometry and constraints. This study discusses the effects of the geometry, constraints, also the type of displacement measurement on the developed deformation functions. The study also discusses whether the deformation function maintains its form as crack grows and the limitations, if there are any, on such behavior. This can be done by comparing the constructed deformation functions for the precracked specimens with those obtained from the blunt-notched specimens of same geometry, constraint, and material.

The data collapse, as a unique observation in the development of the deformation function, is also utilized to obtain both the geometry and deformation functions for sets with only precracked

specimen test records and no blunt-notched specimen test record. An additional blunt-notched specimen record is usually required to conduct the separation analysis for precracked specimen records.

4.2 Development of Material Deformation Function

Because the material deformation function is a material based function that depends mainly on the flow properties of the material, the constructed functions will be studied on a material basis. Hence, the different sets of specimens machined from the same material will be grouped together in order to study the geometry and constraint effects on the developed deformation functions.

HY130 Steel

Three different sets of three different geometries have been studied in Chapters II and III. The specimens in the three sets have the same thickness and width, which may imply that they have the same constraint. Using Eq [4.3] with m as the power law exponent developed for these geometries and given in Table 3.11, one can construct the P_N versus v_{pl} records for the different test records in each set. Figures 4.1, 4.2, and 4.3 show how the data points collapse into one record in each set creating almost solid curves with a very limited scatter. The data points represent ten test records in each of the CT and CCT sets and eight test records in the SENB set. When the geometry functions given in the literature for these geometries are used to develop the deformation functions for these sets, the data points show much wider scatter as shown in Figs 4.4, 4.5, and 4.6. The geometry function expression given in the literature for the CT geometry was previously given in Eq [3.7], while those for the CCT and SENB geometries are power law functions developed using the

separation analysis but with power law exponents of 1.0 and 2.0, respectively.

The deformation function curves for both the CT and SENB sets are similar and by using proper scaling factors for one or both coordinates, a unified deformation function may be obtained. The deformation function for the CCT set is different and coordinate scaling may not help to unify it with those for the bending geometries. This may not agree with the EPRI handbook implications that the deformation function is analogous to the stress versus strain relationship in the plastic region because this requires the deformation function to be geometry independent which has not been yet proved in this study.

A533B Steel

A SENT set and two CT sets; one with stationary cracks and the other with growing cracks, are studied in this thesis. The material properties are slightly different in the two geometries because the specimens' records for each geometry were obtained from different sources. Also the constraint is different because the SENT specimens are of thickness 0.1 inch (2.54 mm) while the the CT specimens are of thickness 1.0 inch (25.4 mm) and with 20% side grooving.

The deformation function, obtained by load normalization, for both the SENT set and the CT set with stationary crack test records are shown in Figs. 4.7 and 4.8. The power law exponents are 2.44 for the SENT set and 2.19 for the CT set. The data points collapse very well in both cases with a small scatter. Despite the difference in the geometry and constraint in both sets, the developed functions show similar trends.

The geometry function for the A533B CT set with growing crack test records is also a power law function with a power law exponent value of 2.12, which is very close to that of the stationary crack CT set. As the different test records in both sets are normalized by a power law geometry function with a power law exponent of 2.12, the data points collapsed together into one curve. This indicates that the deformation function in both sets is the same. In other words, the deformation function maintains its form as the crack grows and up to a considerable crack growth of about 35% of the initially uncracked ligament, which is far beyond the J-controlled 10% crack growth limit.

A106 Steel

Figure 4.10 shows the normalized test records of the A106 CT set with stationary crack specimens. The data points of two test records collapsed together into one curve while the data points of the third test record, a/W=0.753, created a new curve that is almost identical to the first one but slightly shifted down. This may indicate that either there was load-offset error during the test or the crack length was not accurately measured.

On the other hand, the data points of the different normalized test records of the precracked specimens set collapsed very well into one record together with the normalized blunt-notched specimen record used before in the separation analysis of this set, see Fig. 4.11. This, again, indicates that the deformation function is the same for both the stationary crack and growing crack sets for the whole region of the crack growth, which is about 45% of the initial uncracked ligament.

HY80 Steel

Figure 4.12 shows the normalized test records for the stationary crack CT set while Fig. 4.13 shows the normalized test records for the growing crack CT set, together with one of the stationary crack normalized records. The power law exponents used in load normalization, Eq [4.3], are very close: 2.25 and 2.28, respectively. The data points collapsed very well into one curve in both cases, also with agreement between the growing cracks and the stationary crack data points, as shown in Fig. 4.13. The crack growth in this set is about 38% of the initially uncracked ligament.

General observation in the deformation functions developed for the different precracked specimen sets is that there is no discontinuity in the initial part of the records where the crack growth changes its mechanism from blunting into tearing. This supports the hypothesis that the deformation function maintain its form as the crack grows.

HSLA80 Steel

The data points collapse together very well into one curve in the stationary crack specimens set as shown in Fig. 4.14. Also, the data points of the growing crack test records collapse together into one curve, Fig. 4.15, but it does not agree with the data points of the blunt-notched specimen test record normalized with the same power law geometry function. However, the trend of the deformation function for the precracked specimens set in Fig. 4.15, is similar to that of the blunt-notched specimens set in Fig. 4.14. Figure 4.16 shows how both functions coincide with each other when different y-axes are used. This may indicate that the deformation function as a function of the plastic displacement for both sets is the same and the difference resulted from a multiplication error in P_N. The ratio

between P_N for the precracked specimens set to P_N for blunt-notched specimens set is equal to 0.692. This may result from an error in recording the load or from inaccurate estimation of the crack growth during the test.

A710 Steel

In the four different A710 SENT sets, the data points collapse very well together for both the load versus load line displacement and load versus crack mouth opening displacement records as shown in Figs. 4.17 to 4.24. There is some scatter for the 0.1 inch thickness set, especially for load versus load line displacement record. This is expected because this set did not show as good a fit for the separation parameters as all of the other sets.

The interesting observation in all the developed deformation curves is that they are very similar. This means that they can be scaled together into one curve that represents a unified deformation function for the different cases. This will be discussed in detail in Section 4.4.

4.3 Development of the Geometry and Deformation Functions for Precracked Specimen Test Records Using Normalization Technique

The geometry function for the precracked specimen test records has been evaluated in Chapter III using load separation analysis, which requires an additional test record of blunt-notched specimen of same geometry, material, and constraint. In this section a new approach will be used to develop the geometry function and, consequently, the deformation function using the precracked specimen test records only. This approach is based on three

assumptions: first, the load is separable; second, the geometry function is well represented by a power law function; third, using the right geometry function yields the least scatter in the developed deformation function. Hence, by varying the power law exponent in Eq [4.3] until the normalized precracked specimen test records show the least scatter, the most appropriate power law geometry can be obtained. The deformation function is the corresponding normalized records.

Two new sets of precracked specimen test records will be used to demonstrate the approach suggested above. These test records were originally reported in Refs (58, 65). The specimens in both sets are compact specimens of 2.0 inches (50.8 mm) width and 1.0 inch (25.4 mm) thickness with 20% side grooving. The specimens in the first set (3 specimens) were machined from A508 steel while the specimens in the other set (4 specimens) were machined from A710 steel. Table 4.1 lists the mechanical properties reported for these materials and Table 4.2 lists the specimens codes and both initial and final crack lengths. The crack growth was monitored using the compliance method. Figures 4.25 and 4.26 show the data scatters obtained by normalizing the test records in both sets by the CT geometry function given in the literature, Eq [3.7]. Figures 4.27 and 4.28 show, again, the scatter in both sets but using a power law geometry function after a few trials to obtain the best power law exponent values. The scatter has been much improved by using the power law geometry function. The corresponding power law exponent

Table 4.1: Mechanical properties of A508 and A710 steels.

Material	Yield Strength		Ultimate Strength	
A508	56 Ksi	(386 MPa)	79 Ksi	(545 MPa)
A710	80 Ksi	(552 MPa)	97 Ksi	(669 MPa)

Table 4.2: Initial and final crack lengths in the different specimens.

Material	Specimen	Initial a/W	Final a/W
A508	A508-24	0.5155	0.6520
	A508-25	0.5200	0.6115
	A508-28	0.7680	0.8170
A710	A710-4	0.5310	0.5835
	A710-5	0.5420	0.6125
	A710-9	0.6240	0.7730
	A710-10	0.6150	0.7185

values for the A508 and A710 sets are 2.22 and 2.4, respectively.

This demonstrates how simple this approach is and how easily it can be applied to precracked test records to obtain both the geometry and deformation functions in one process. However, in some cases, the scatter in the normalized data points may not converge by varying the power law exponent of the geometry function. This may result from non-separable behavior, inaccurate crack measurement, or shifted test records. In this case, it is better to use the separation analysis to find out the reason for such non-convergent scatter.

4.4 Unified Deformation Function

One of the main objectives of fracture mechanics is to provide accurate predictions of the fracture behavior of materials and structures in service. These structures can not, of course, be destructively tested, but they can be approximately modeled by specimens that can be tested. However, these specimens may be

different in their geometry, crack length, crack tip, constraint, and displacement measurement point. Also, the mechanical properties of the specimen material could be different than those of the structure material even if both materials have the same composition and have been prepared with the same process. Therefore, the specimen results may not be directly used to obtain the expected fracture behavior of the modeled structure. A modified analysis has to be used to correlate the specimen fracture behavior to the structure's fracture behavior. Load separation represents a very promising and simple analysis that can provide such correlation. The geometry function handles the differences in the crack length between the structure and the specimen. Constraints and displacement measurement have little effect on the geometry function as shown in the different A710 sets. Therefore, each geometry should have a specific power law geometry function no matter what constraint is applied or where the displacement is measured. Even slight differences in material properties are not likely to show any effect on the geometry function. The crack tip type, blunt or sharp, has not shown any effect on either the geometry or deformation functions. Although the developed deformation functions showed a dependence on constraint and displacement measurement, the trends of the constructed curves are very similar so that these curves can be brought together into one curve by linearly scaling the coordinates. In this case, test records for specimens of the same material and geometry but with different constraints and displacement point measurements are represented by a unified deformation curve (key curve). For example, the three one inch thickness A710 SENT sets have almost the same power law geometry function An average power law exponent of 2.36 can be used for all of three sets for both load versus load line displacement and load versus crack mouth opening displacement test records. Hence a unified deformation function (key curve) can be constructed as P_N versus v_{pl}/L_{eff} where

$$P_N = \frac{P}{B_{eff} W \; G(b/W)} \qquad [4.4]$$

and B_{eff} and L_{eff} are the coordinates' scaling factors and can be defined as effective thickness and effective gage length, respectively. B_{eff} is a function of the constraint, net thickness and whole thickness and L_{eff} is function of the width and gage length. Figure 4.29 shows the six deformation functions given in Figs. 4.19 to 4.24 after scaling them together into a unified deformation function. The corresponding B_{eff} and L_{eff} values are listed in Table 4.3. The 0.1 inch A710 SENT set can be also scaled into this curve with specific B_{eff} and L_{eff} values; however, the wide scatter in this set may confuse the unique trend shown in the developed curve. This key curve uniquely represents any A710 SENT specimen and, by providing the right B_{eff} and L_{eff} values, one can develop the specimen's expected deformation function. Consequently, for any specific crack length, the expected test record can then be developed.

The key curve analysis can be further improved if the geometric effects are included. For example, if an appropriate function can be used to fit deformation functions developed for different geometries by changing only the coefficients and not the form, a more generalized key curve can be developed.

Table 4.3: Coordinates scaling factors for the A710 sets.

Set	Type of Displacement	B_{eff}	L_{eff}
No side-grooved	Load line displacement	1.0	$W/2.4$
	Crack mouth open. disp.	1.0	W
20% side-grooved	Load line displacement	0.944	$W/2.4$
	Crack mouth open. disp.	0.944	W
50% side-grooved	Load line displacement	0.708	$W/2.4$
	Crack mouth open. disp.	0.708	W

4.5 Summary and Conclusions

Following is a summary of the different observations found in studying the material deformation function.

* A deformation function can be developed by normalizing the test records with the geometry function. This developed function can be represented as P_N versus v_{pl} relationship.

* The deformation function maintains its form as the crack grows up to about 45% of initial uncracked ligament, which is far beyond the J-controlled 10% crack growth limit.

* A new method to develop the geometry and deformation function for precracked specimen test records has been introduced. This method does not require an additional blunt-notched specimen test record.

* The deformation function is dependent on the material, geometry, and constraint. It also depends on the type of the measured displacement. However, the developed functions show the same trend for sets of the same material and geometry but different constraints and displacement measurement. These functions can be scaled together into a key curve that uniquely represents the deformation function for any specimen of the same material and geometry.

* The dependence of the material deformation function on the tested specimen geometry may not agree with the EPRI handbook assumption that the deformation function is a curve analogous to the material's stress-strain curve because, based on this assumption, the developed deformation functions for the different geometry should be the same.

CHAPTER V

SUMMARY OF RESULTS

5.1 Load Separation

Load separation is the assumption that the load can be represented as a multiplication of two separate functions: a crack geometry function and a material deformation function, Eq [2.1]. Through the study of the test records of 78 specimens of different crack sizes, geometries, materials, and constraints, such assumption is proved to be a predominantly valid criterion in fracture mechanics. The different test records show load separation over all of the plastic region except for a limited region at the early plastic behavior. It is also proved that this criterion exists in stationary crack test records as well as growing crack test records and such load separation is maintained up to crack growth of 45% of the uncracked ligament, which is far beyond the J-controlled crack growth limit (10% of the uncracked ligament). The study also shows that load separation may exist in test records other than the load versus load line displacement record such as the load versus crack mouth opening displacement record.

The limited non-separable region at the early plastic behavior is the region associated with the plasticity's spreading over the uncracked ligament. As the yielded areas become fully connected across the uncracked ligament, the load separation in the plastic region of the test record starts. Such yielded areas are usually developed in a unique pattern that grows as the load increases but maintains its form, which leads us to believe that such plastic pattern is the reason for load separation in the material ductile fracture behavior.

5.2 Crack Geometry Function

The crack geometry function $G(b/W)$ for the different sets of test records are developed using the load separation analysis. The power law form well represents the geometry function in all the studied cases. This is a rather unexpected result for the compact (CT) geometry. The CT geometry function's form in the literature is a multiplication of a power law term and an exponential term, Eq[3.7]. Also, the power law exponent in the developed CT geometry functions shows a little material dependence which does not agree with the material-independent geometry function's form found in the literature. The geometry functions for the center-cracked tension (CCT) and single-edge notched bend (SENB) geometries are also found to be power law functions and this agrees with those proposed in the literature. However, the developed power law exponents are different than those proposed in the literature. The reason is that the literature forms are based on limit load analysis which assumes elastic-perfectly plastic material's behavior. Also, the developed geometry functions for different single-edge notched tension sets are power law functions.

The study also shows that the geometry function maintains its form as the crack grows over the entire range of crack growth records which is far beyond the J-controlled crack growth limit.

Constraint shows very little effect on the power law exponent values. Also, the geometry functions developed from load versus load line displacement records are almost the same as those developed from load versus crack mouth opening displacement records for specimens in the same set.

5.3 Plastic Eta (η_{pl})

η_{pl} exists only if the load is separable and there is a unique relationship between η_{pl} and the crack geometry function, Eq[3.23]. Therefore, if the geometry function can be developed η_{pl} can be obtained. For example, for a power law geometry function, η_{pl} is equal to the power law exponent. Using load separation analysis to develop the geometry function provides a simple and reliable method for determining η_{pl}. This new method avoids most of the errors in the classical approaches for η_{pl} evaluation. It also avoids the inclusion of the non-separable region in η_{pl} evaluation. Including this region contradicts the basis of η_{pl} existence. Such contradiction was ignored in the classical approaches and resulted in significant errors, especially in the early region of the plastic behavior.

Based on the new method, η_{pl} can be evaluated either using the test records of three (or more) identical blunt-notched specimens with different crack lengths or one (or more) precracked specimen test record together with a test record of a blunt-notched specimen of the same geometry, material, and constraint.

5.4 Material Deformation Function

The material deformation function, $H(v_{pl}/W)$, for any set of test records can be developed by normalizing the test records by the corresponding geometry function. The normalized test records should collapse into one curve which is the material deformation function. For the different studied sets, the data points of the normalized test records in each set collapse very well into one record that represents the deformation function for this set.

The study shows that the deformation function depends on the material, geometry, and constraint. It also depends on the displacement point measurement. However, the developed deformation functions for specimens of the same material and geometry but different constraints and displacement measurements show similar trends. But it is possible to bring them together into one curve by linearly scaling the coordinates. This curve can be defined as a key curve that uniquely represents such material's fracture behavior, and the test records of any specimen of the same material and geometry can be developed using this curve.

Also, the study shows that the deformation function maintains its form as the crack grows over the entire range of crack growth records included in this study (about 45% of the uncracked ligament).

5.5 Ductile Fracture Methodology

The optimum objective of any ductile fracture methodology is to provide accurate predictions of the fracture behavior of a defective structure. These predictions, as discussed in Chapter I, are based on two sets of information: the calibration functions, and the material's fracture behavior (J-R). Load separation provides a unique approach that represents the calibration functions in a generalized form. A key curve (or a unified deformation function) can simply represent the calibration curves of all specimens and structures that have the same geometry and are manufactured from the same material. Such a key curve can be developed experimentally by testing a few specimens. On the other hand, defining the proper scaling factors to develop a constraint independent key curve can also be utilized in the development of a constraint independent J-R curve.

Ductile fracture methodology can be further developed if the key curves for specimens of the same material but different geometries can be represented by a single generalized function.

5.6 Suggested Future Studies

The methodology presented in this dissertation has been completely developed in principle; however, there are some details which can be improved by future studies.

The effects of the different parameters on the values of the scaling factors, used before to develop a key curve independent of constraint and displacement measurement, require additional studies. Also, as implied by the previous section, it is of main interest to develop a key curve form that represents the deformation function and handles geometric effects. These may require testing more specimens of different combinations of crack sizes, constraints, and geometries. Or rather, a computational finite element model can be developed to provide such information. But a few specimens, still, have to be tested to verify the computational results.

Load separation and the development of geometry and deformation functions and, also, η_{pl} can be explored in other geometries such as double-edge notched tension, disk compact, arc tension, arc bend, and others. η_{pl} sensitivity to material properties can also be studied.

Load separation and the geometry and deformation functions are proved to be of global nature, that is, they are independent of the crack tip vicinity details. This may qualify this approach to be used with man-made materials such as polymers and composite materials. However, experimental study is required to verify such assumption.

A study to modify the load separation approach to handle fatigue and creep problems will be of great importance. Also, extending the methodology to 3-D cases will provide a simple approach that can handle very complicated problems.

REFERENCES

(1) Griffith, A. A., "The Phenomena of Rupture and Flaw in Solids," Phil. Trans. Roy. Soc. London, A221, 1921, pp. 163-197.

(2) Hertzberg, R. W., *The Deformation and Fracture Mechanics of Engineering Materials*, 2nd Ed., Wiley, 1983.

(3) Irwin, G. R., "Fracture I," *Handbuch der Physik VI*, Flugge Ed., pp. 558-590, Springer, 1958.

(4) Westergaard, H. M., "Bearing Pressures and Cracks," J. Appl. Mech., Vol. 61, 1939, pp. A49-A53.

(5) Irwin, G. R., Paris, P. C., and Tada, H., *The Stress Analysis of Cracks Handbook*, DEL Research Corp., 1973.

(6) Broek, D., *Elementary Engineering Fracture Mechanics*, 4th. Ed., Martinus Nijhoff, Dordrecht, 1986.

(7) Standard Test Method for, "Plane-Strain Fracture Toughness of Metallic Materials," ASTM Standards E399-83.

(8) Irwin, G. R., "Plastic Zone Near a Crack and Fracture Toughness," Proc. 7th. Sagamore Conf., 1960, p. IV-63.

(9) Dugdale, D. S., "Yielding of Steel Sheets Containing Slits," J. Mech. Phys. Sol., Vol. 8, 1960, pp. 100-108.

(10) Standard Test Method for, "R-Curve Determination," ASTM Standards, E561-81.

(11) Rice, J. R., "A Path-Independent Integral and the Approximate Analysis of Strain Concentration by Notches and Cracks," J. Appl. Mech., 1968, pp. 379-386.

(12) Rice, J. R., "Mathematical Analysis in the Mechanics of Fracture," Ch. 3, Vol. 2, *Fracture, an Advanced Treatise*, Liebowitz, H., Ed., Academic Press, 1968.

(13) Hutchinson, J. W., "Plastic Stress and Strain Fields at a Crack Tip," J. Mech. Phys. Sol., Vol. 16, 1968, pp. 337-347.

(14) Rice, J. R., and Rosengren, G. F., "Plane Strain Deformation Near a Crack Tip," J. Mech. Phys. Sol., Vol. 16, 1968, pp. 1-12.

(15) McClintock, F. A., "Plasticity Aspects of Fracture," Vol. 3, *Fracture, an Advanced Treatise*, Liebowitz, H., Ed., Academic Press, 1971.

(16) Paris, P. C., "Fracture Mechanics in the Elastic-Plastic Regime," *Flow Growth and Fracture*, ASTM STP 631, American Society for Testing and Materials, 1977, pp. 3-27.

(17) Begley, J. A., and Landes, J. D., "The J-Integral as a Fracture Criterion," *Fracture Toughness Proceedings of the 1971 National Symposium on Fracture Mechanics*, Part II, ASTM STP 514, American Society of Testing and Materials, 1972, pp. 1-20.

(18) Landes, J. D., and Begley, J. A., "The Effect of Specimen Geometry on J_{Ic}," *Fracture Toughness Proceedings of the 1971 National Symposium on Fracture Mechanics*, Part II, ASTM STP 514, American Society of Testing and Materials, 1972, pp. 24-39.

(19) Ernst, H. A., and Paris, P. C., "Techniques of Analysis of Load-Displacement Records by J-Integral Methods," NUREG/CR-1222, Jan. 1980.

(20) Rice, J. R., Paris, P. C., and Merkle, J. G., "Some Further Results of J-Integral Analysis and Estimates," *Progress in Flaw Growth and Fracture Toughness Testing*, ASTM STP 536, American Society of Testing and Materials, 1973, pp. 231-245.

(21) Merkle, J. G., and Corten, H. T., "A J-Integral Analysis for the Compact Specimen, Considering Axial Force as well as Bending Effects," J. Pressure Vessel Technology, Trans. of the ASME, 1974, pp. 286-292.

(22) Landes, J. D., Walker, H., and Clarke, G. A, "Evaluation of Estimation Procedures Used in J-Integral Testing,"*Elastic-Plastic Fracture*, ASTM STP 668, American Society of Testing and Materials, 1979, pp. 266-287.

(23) Clarke, G. A., and Landes, J. D., "Evaluation of the J-Integral for the Compact Specimen," J. of Testing and Evaluation, Vol. 7, No. 5, Sept. 1979, pp. 264-269.

(24) Sumpter, J. D. G., and Turner, C. E., "Method for Laboratory Determination of J_{Ic},"*Cracks and Fracture*, ASTM STP 601, American Society of Testing and Materials, 1976, pp. 3-18.

(25) Standard Test Method for, "J_{Ic}, A Measure of Fracture Toughness," ASTM Standards, E813-81.

(26) Standard Test Method for, "J_{Ic}, A Measure of Fracture Toughness," ASTM Standards, E813-87.

(27) Hutchinson, J. W., and Paris, P. C.,"Stability Analysis of J-Controlled Crack Growth," *Elastic-Plastic Fracture*, ASTM STP 668, American Society of Testing and Materials, 1979, pp. 37-64.

(28) Shih, C. F., deLorenzi, H. G., and Anderson, W. R., "Studies on Crack Initiation and Stable Crack Growth," *Elastic-Plastic Fracture*, ASTM STP 668, American Society of Testing and Materials, 1979, pp. 65-120.

(29) Ernst, H. A., Paris, P. C., and Landes, J. D.," Estimation on J-Integral and Tearing Modulus T from A Single Specimen Test Record," ASTM STP 743, American Society of Testing and Materials, pp. 476-502.

(30) Standard Test Method for, "Determining J-R Curves" ASTM Standards, E1152-87.

(31) Paris, P. C., Tada, H., Zahoor, A., and Ernst, H.,"The Theory of Instability of the Tearing Mode of Elastic Plastic Crack Growth," *Elastic-Plastic Fracture*, ASTM STP 668, American Society of Testing and Materials, 1979, pp. 5-36.

(32) Paris, P. C., Tada, H., Ernst, H., and Zahoor, A., "Initial Experimental Investigation of Tearing Instability Theory," *Elastic-Plastic Fracture*, ASTM STP 668, American Society of Testing and Materials, 1979, pp. 251-265.

(33) Ernst, H. A., "Material Resistance and Instability Beyond J-Controlled Crack Growth," *Elastic-Plastic Fracture: Second Symposium, Volume I - Inelastic Crack Analysis*, ASTM STP803, American Society for Testing and Materials, 1983, pp. I-191 to I-213..

(34) Ernst, H. A., and Landes, J. D., "Elastic-Plastic Fracture Mechanics Methodolgy Using the Modified J, J_M, Resistance Curve Approach," Journal of Pressure Vessels Technology, Vol. 108, Feb. 1986, pp.50-56.

(35) Ernst, H. A., and Landes, J. D., "Predictions of Instability Using the Modified J, J_M, Resistance Curve Approach," Scientific Paper 83-ID7-METEN-P8, Westinghouse Research and Development Center, Sept. 1983.

(36) Wells, A. A., "Unstable Crack Propagation in Metals - Cleavage and Fast Fracture," Cranfield Crack Prop. Symp., 1961, pp. 210-230.

(37) "Methods of Crack Tip Opening Displacement (CTOD) Testing," British Standards Institution, BS5762, 1979.

(38) "Guidance on Some Methods for the Derivation of Acceptance Levels for Defects in Fusion Welded Joints," British Standards Institution, PD6493, 1980.

(39) Standard Test Method for, "Crack-Tip Opening Displacement (CTOD) Fracture Toughness Measurement," ASTM Standards, E1290-89.

(40) Schwalbe, K. H., Heerens, D. H., and Cornec, A., "Relationships Between Various Definitions of the Crack Tip Opening Displacement," The Crack Tip Opening Displacement in Elastic-plastic Fracture Mechanics, Proceedings of the Workshop on the CTOD Methodology, GKSS-Forschungszentrum Geesthacht, Gmbh, Geesthacht, Germany, April 1985.

(41) Burdekin, F. M., and Stone, D. E. W., "The Crack Opening Displacement Approach to Fracture Mechanics in Yielding Materials," Journal of Strain analysis, Vol. I, No. 2, 1966, pp. 145-153.

(42) Harison, J. D., "The State of Art in Crack Tip Opening Displacement (CTOD), Testing and Analysis," The Welding Institute, Abington, England, Rep. 7302.10/80/210.2

(43) Harrison, J. D., Archer, G. L., and Kamath, M. S., "The COD Approach and Its Application to Welded Structure," *Elastic-Plastic Fracture*, ASTM STP 668, American Society of Testing and Materials, 1979, pp. 606-631.

(44) Barsom, J. M., and Rolfe, S. T., *Fracture and Fatigue in Structures*, 2nd Ed., Prentice-Hall, Inc., 1987.

(45) Green, A. P., and Hundy, B. B., "Initial Plastic Yielding in Notch Bend Tests," J. Mech. Phys. Sol., Vol. 4, 1956, pp. 128-144.

(46) Schwalbe, K. H., "A Simple Engineering Treatment of Center-cracked Tension Panels in the Regime of Non-Linear Fracture Mechanics Under Plane Stress Conditions," GKSS 84/E/38, GKSS Research Center, Geethacht, 1984.

(47) Schwalbe, K. H., "The Prediction of Failure Situations Using the CTOD Concept Based on the Engineering Treatment Model (ETM)," GKSS 85/E/61, GKSS Research Center, Geethacht, 1985.

(48) Schwalbe, K. H., "Extension of the Engineering Treatment Model (ETM) to Bending Configurations under Plane Stress," GKSS 87/E/51, GKSS Research Center, Geethacht, 1987.

(49) Royer, J., Tissot, J. M., Pelissier-Tanon, A., Le Poac, P., and Mianny, D., "J-Integral Determination and Analysis for Small Test Specimens and Their Usefulness for Estimating Fracture Toughness," *Elastic-Plastic Fracture*, ASTM STP 668, American Society of Testing and Materials, 1979, pp. 334-357.

(50) Kumar, V., German, M. D., and Shih, C. F., "An Engineering Approach for Elastic-Plastic Fracture Analysis," Electric Power Research Institute, NP 1931, Topical Report, July 1981.

(51) Kumar, V., and Shih, C. F., "Fully Plastic Crack Solutions, Estimation Scheme, and Stability Analyses for Compact Specimen," *Fracture Mechanics: Twelfth Conference*, ASTM STP 700, American Society for Testing and Materials, 1980, pp. 406-438.

(52) Landes, J. D., "Analysis of HY130 Steel Fracture Data," AWI88-0109, American Welding Institute, 1988.

(53) Herrera, R., and Landes, J. D., "Direct J-R Curve Analysis: A Guide to the Methodology,"*Fracture Mechanics: Twenty-First Symposium*, ASTM STP 1074, American Society for Testing and Materials, Philadelphia, 1990, pp. 24-43.

(54) Zhou, Z., Herrera, R., Lee, K., and Landes, J. D., "Normalization: An Experimental Method for Developing J-R Curves," presented in the ASTM Second Symposium on User Experience with Elastic-Plastic Fracture Test Methods, Lake Buena Vista, Florida, Nov. 1989.

(55) Bloom, J. M., and Malik, S. N., "Procedure for the Assessment of Integrity of Nuclear Pressure Vessels and Piping Containing Defects," EPRI Final Report NP-2431, June 1982.

(56) Joyce, J. A., Davis, D. A., Hackett, E. M., and Hayes, R. A., "Application of the J-Integral and the Modified J-Integral to Cases of Large Crack Extension," NUREG CR_5143, Feb. 1989.

(57) Dorn, William S., and McCracken, Daniel D., *Numerical Methods with Fortran IV, Case Studies*, John Wiley & Sons, Inc., 1972.

(58) Landes, J. D., McCabe, D. E., and Ernst, H. A., "Fracture Testing of Ductile Steels," Electric Power Research Institute, NP 5014, Final Report of Research Project 1238-2, Jan. 1987.

(59) McCabe, D. E., Ernst, H. A., and Landes, J. D., "Development of an Elastic-Plastic Methodology to Assess Structural Reliability and Material Selection for Navy Applications," Annual Report, Contract No. NOO 167-83-C-0121, Westinghouse Research and Development center, 1983.

(60) Joyce, J. A., "Extension of J-R Curve Validity limits," ASTM Committee Meeting, Atlanta, GA, Nov. 1988.

(61) Sumpter, J. D. G., "Elastic-Plastic Fracture Analysis and Design Using the Finite-Element Method," Ph.D. thesis, University of London, 1973.

(62) Latzko, D. G. H., Turner, C. E., Landes, J. D., McCabe, D. E., and Hellen, T. K., *Post Yield Fracture Mechanics*, 2nd Ed., Elsevier Applied Science Publishers, 1984.

(63) Sharobeam, M. H., and Landes, J. D., "The Non-separable Region in Ductile Material's Fracture Behavior," presented in the 22nd National Symposium on Fracture Mechanics, June 1990, Atlanta, GA.

(64) Turner, C. E., "The Ubiquitous η Factor," *Fracture Mechanics: Twelfth Conference*, ASTM STP 700, American Society for Testing and Materials, 1980, pp. 314-337.

(65) McCabe, D. E., unpublished results.

APPENDIX

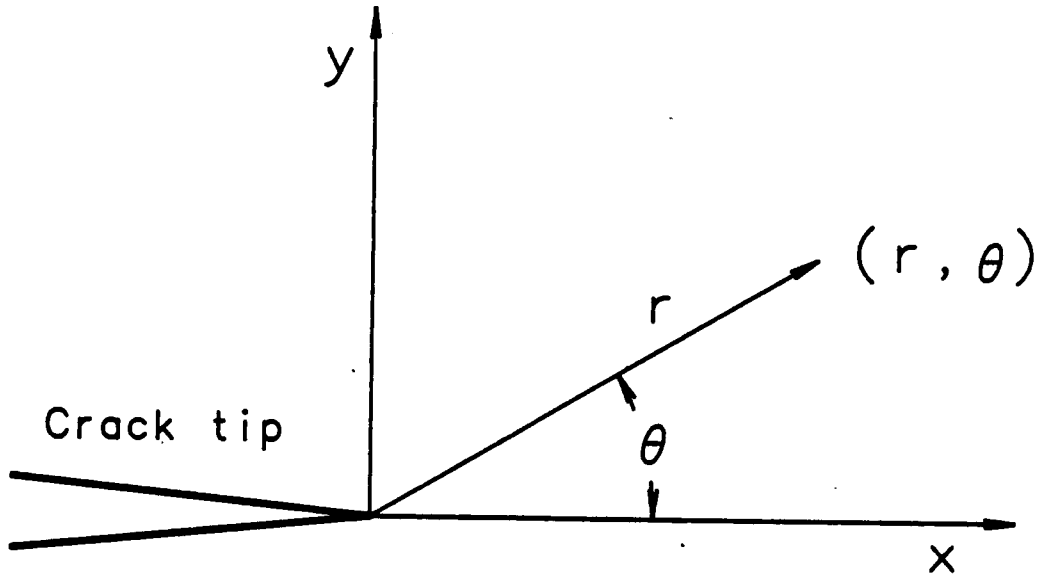
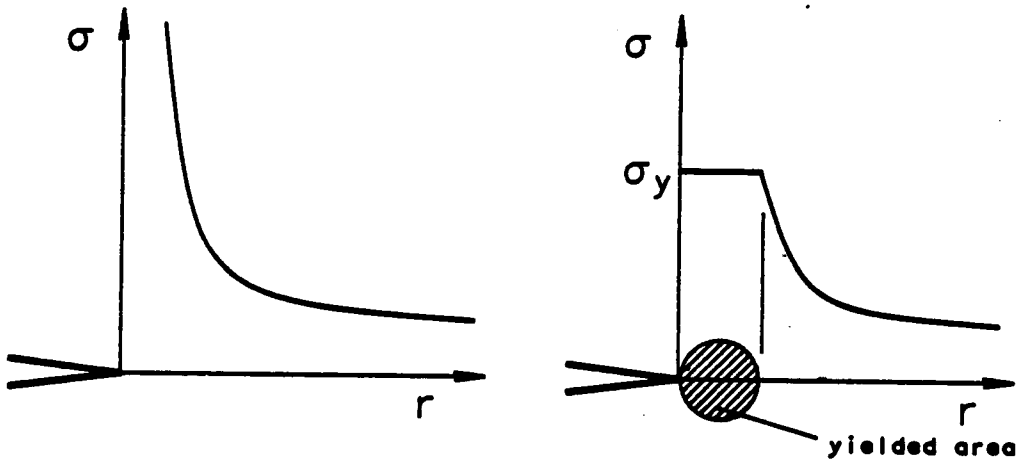


Fig. 1.1 - Crack tip field.



Stress variation in linear-elastic material

Stress variation in elastic-plastic material

Fig. 1.2 - Stress variation in the crack vicinity.

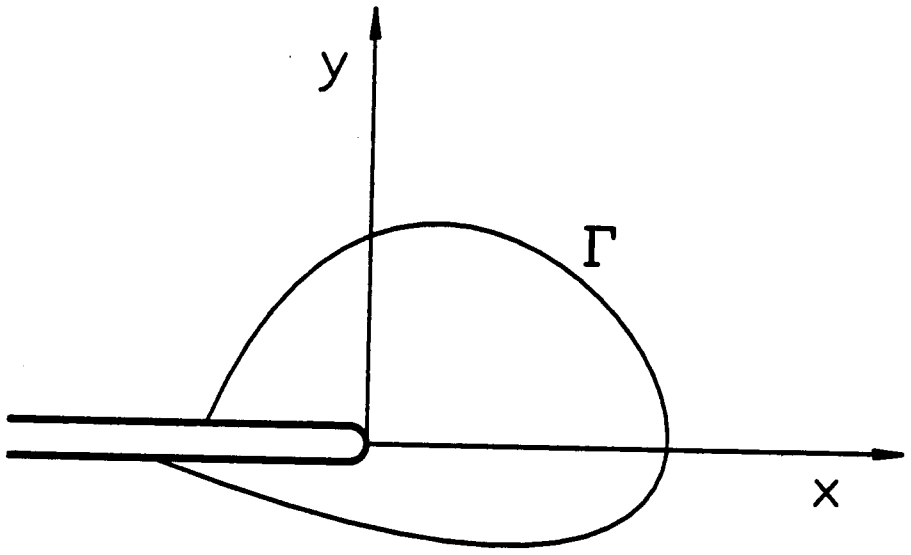


Fig. 1.3 - *J*-integral contour.

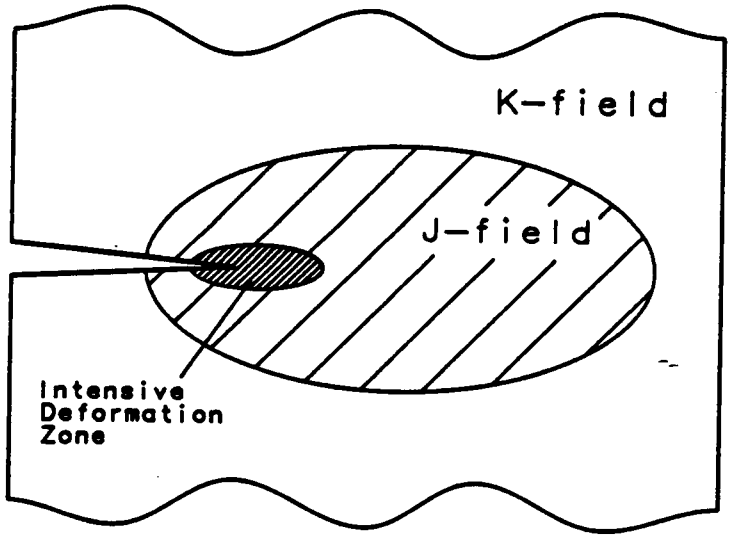


Fig. 1.4 - Different fields in the crack vicinity.

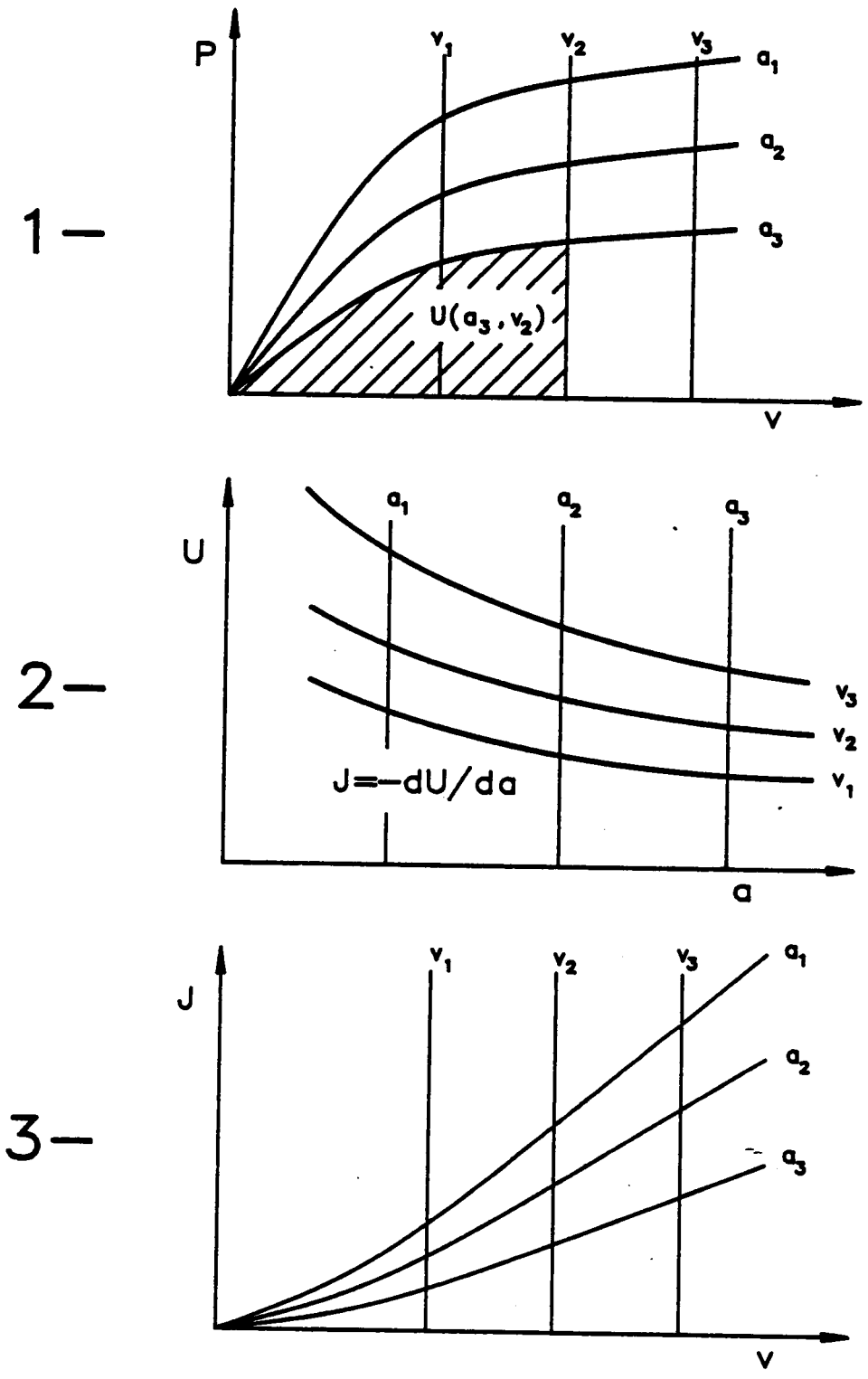


Fig. 1.5 - *J*-integral evaluation using energy rate interpretation form.

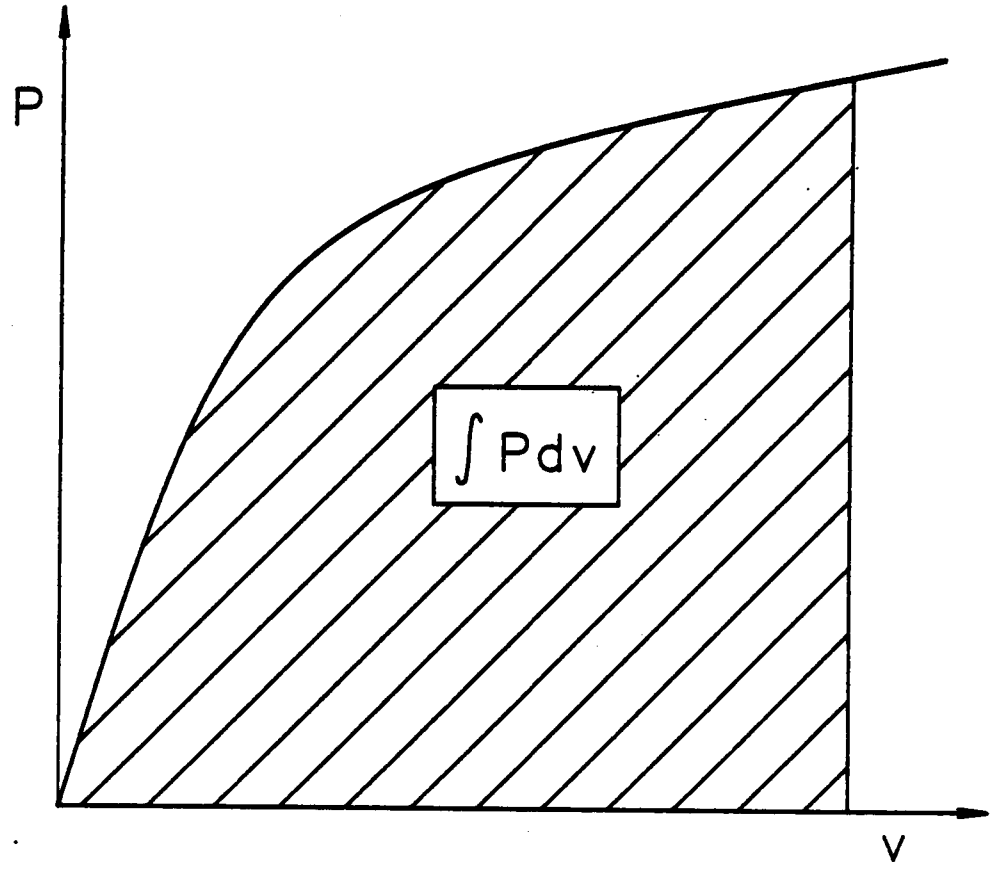


Fig. 1.6 - *J*-integral evaluation using single specimen form.

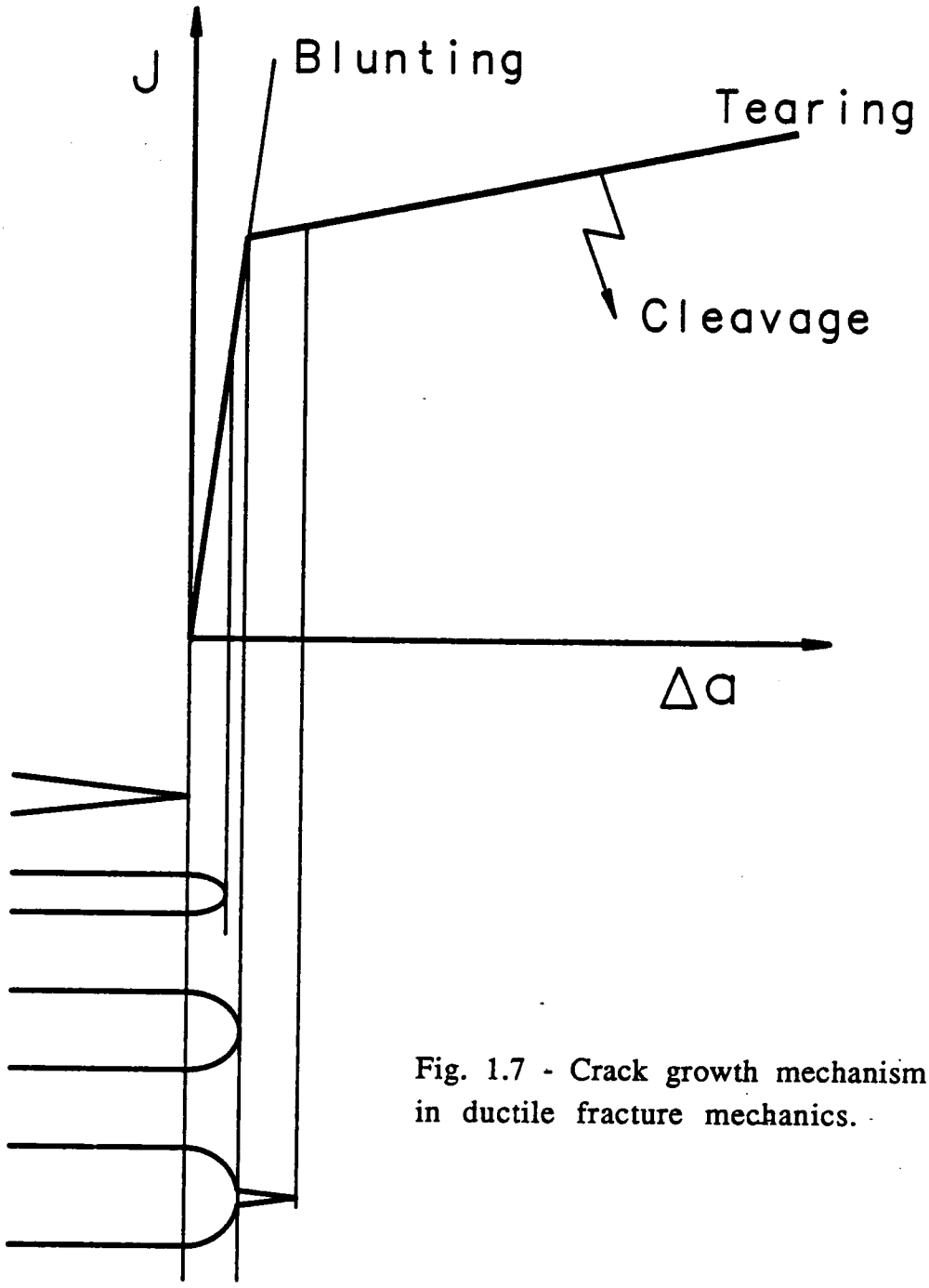


Fig. 1.7 - Crack growth mechanism in ductile fracture mechanics.

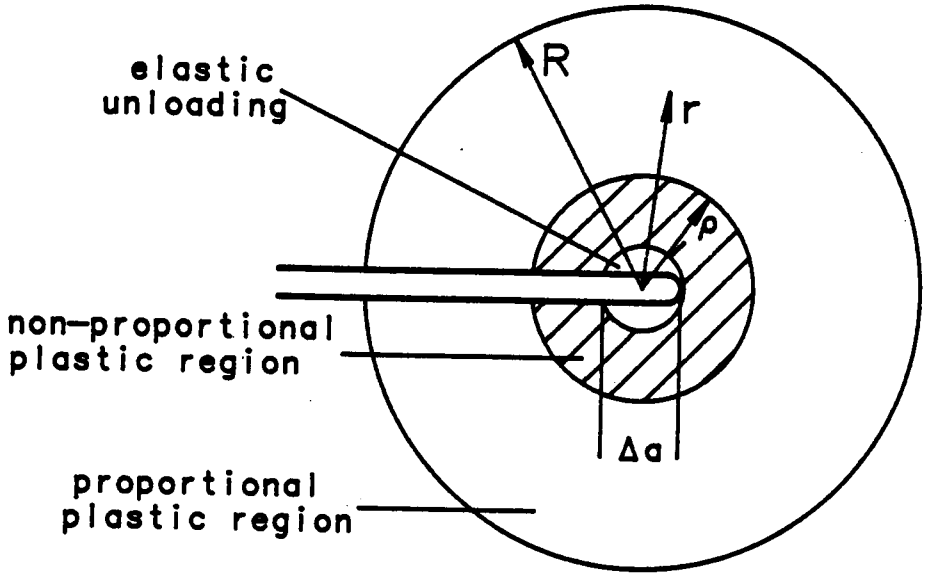


Fig. 1.8 - Proportional and non-proportional regions in the crack tip field.

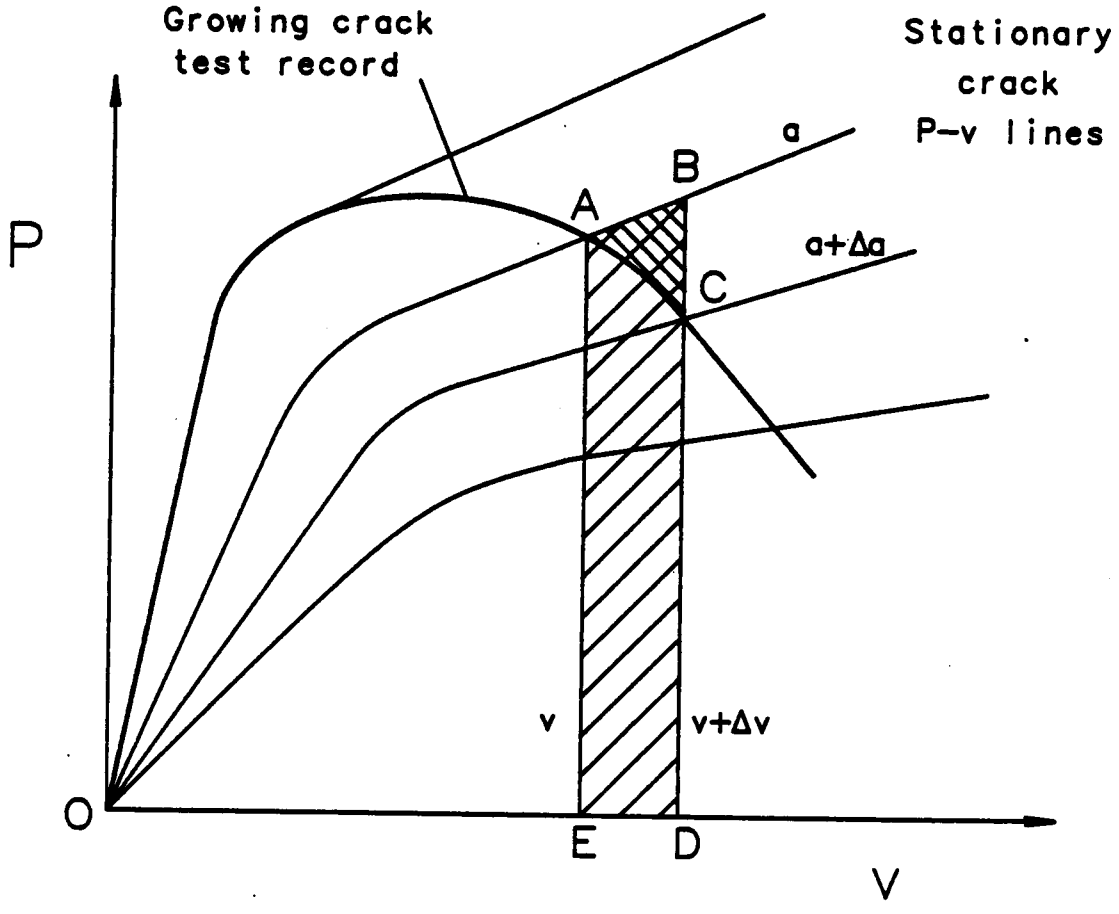


Fig. 1.9 - *J*-integral evaluation for growing crack test record.

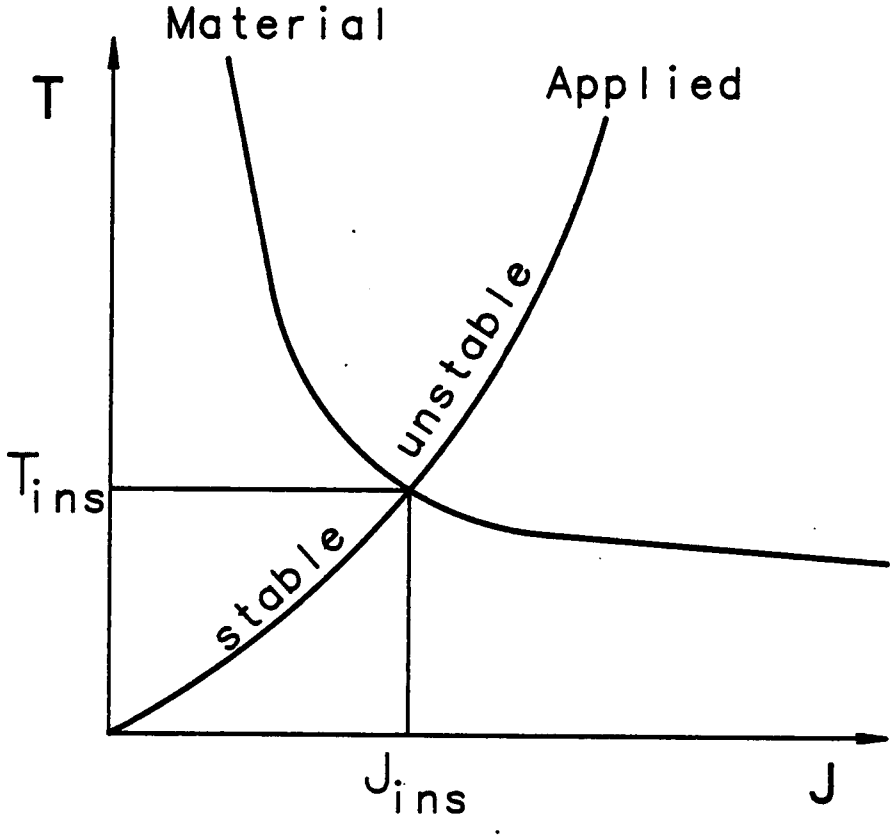


Fig. 1.10 - Stable and unstable regions in crack growth based on J-T analysis.

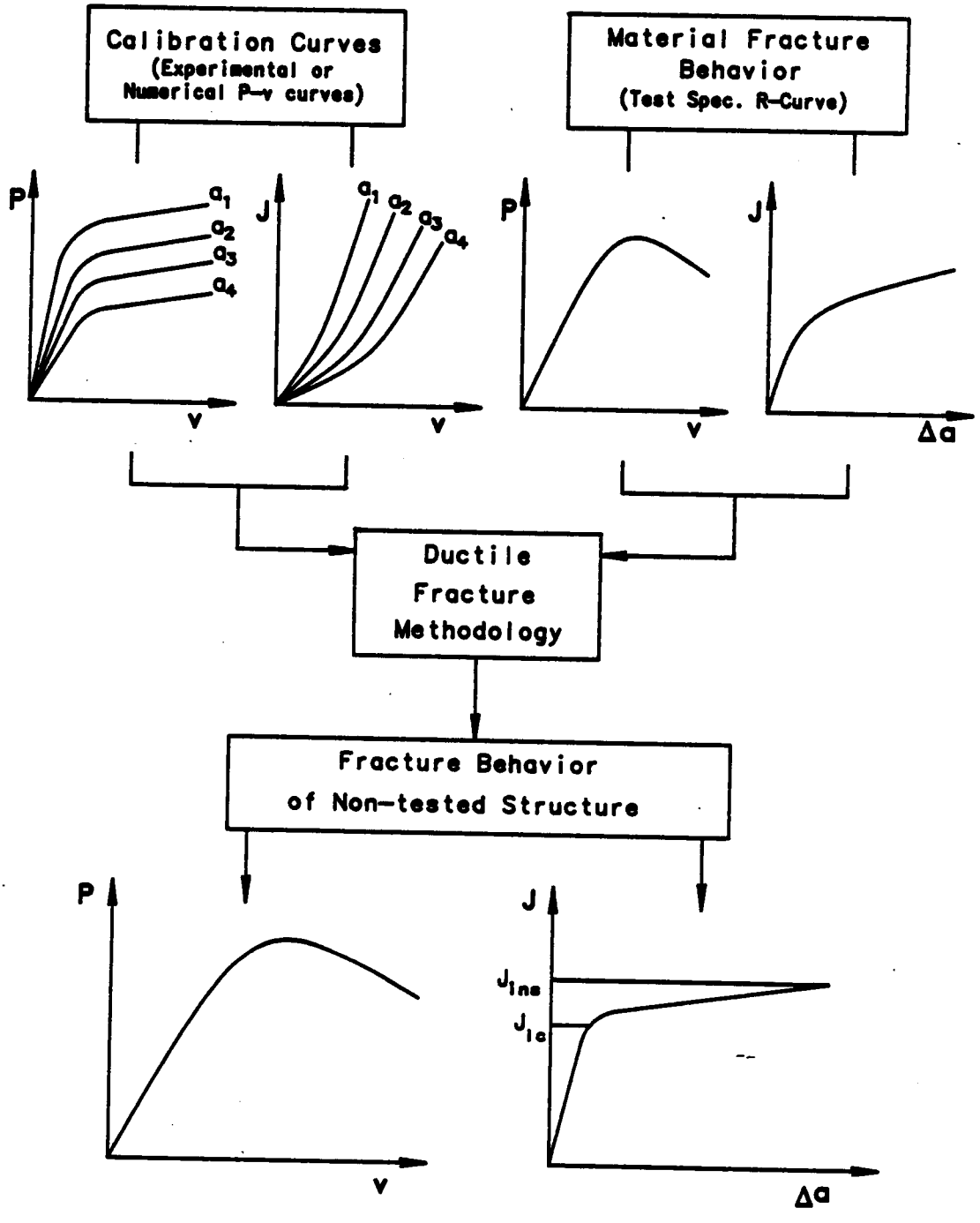


Fig. 1.11 - Ductile fracture methodology.

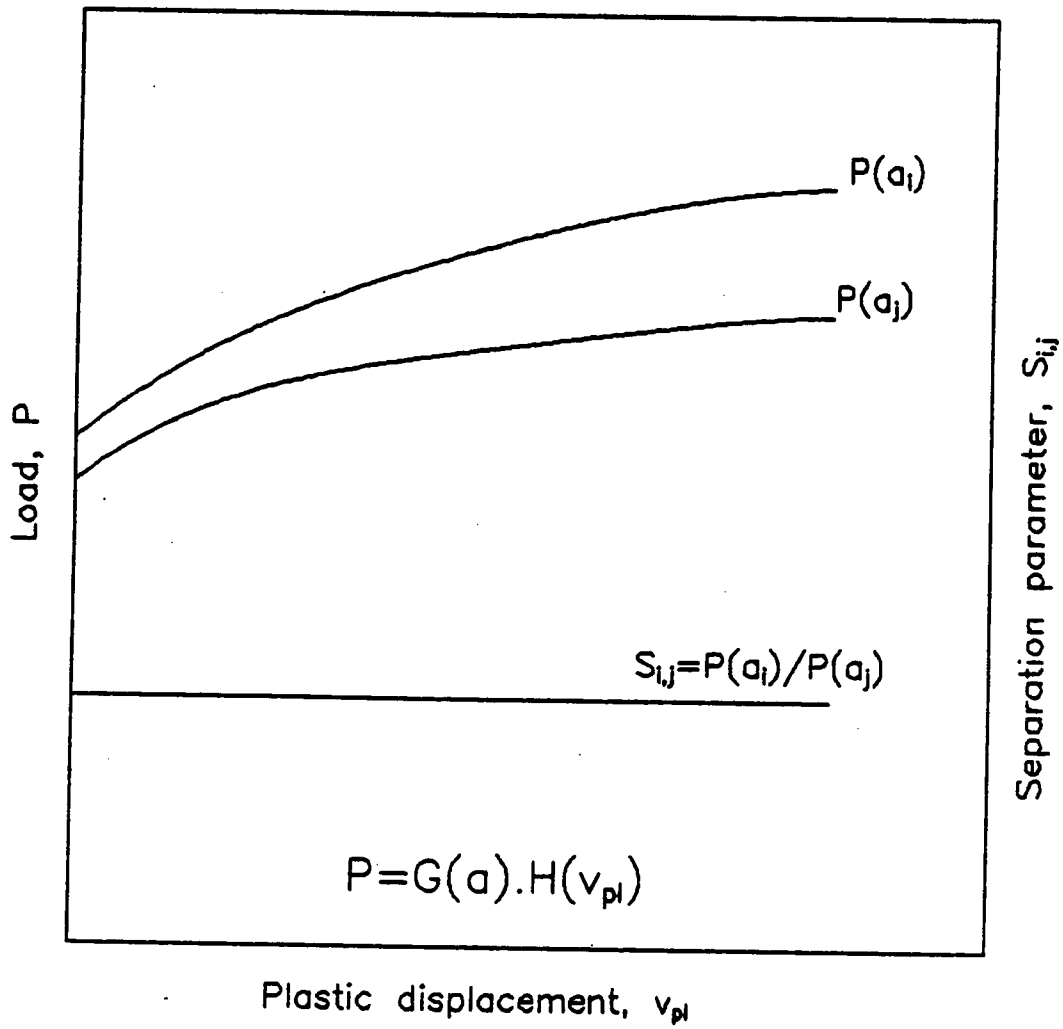


Fig. 2.1 - Load separation in blunt notched specimens test records.

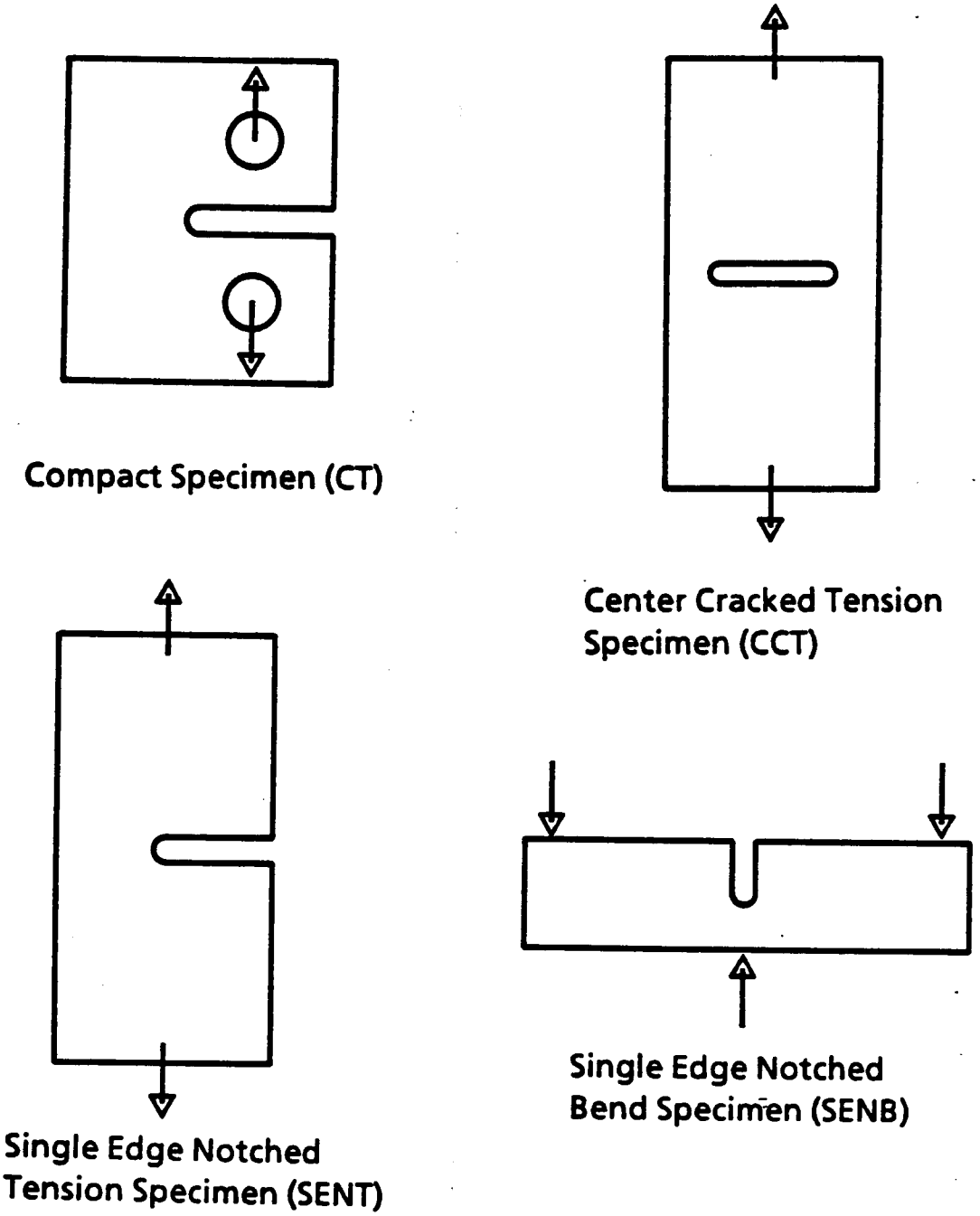


Fig. 2.2 - Schematic drawings of the different four geometries.

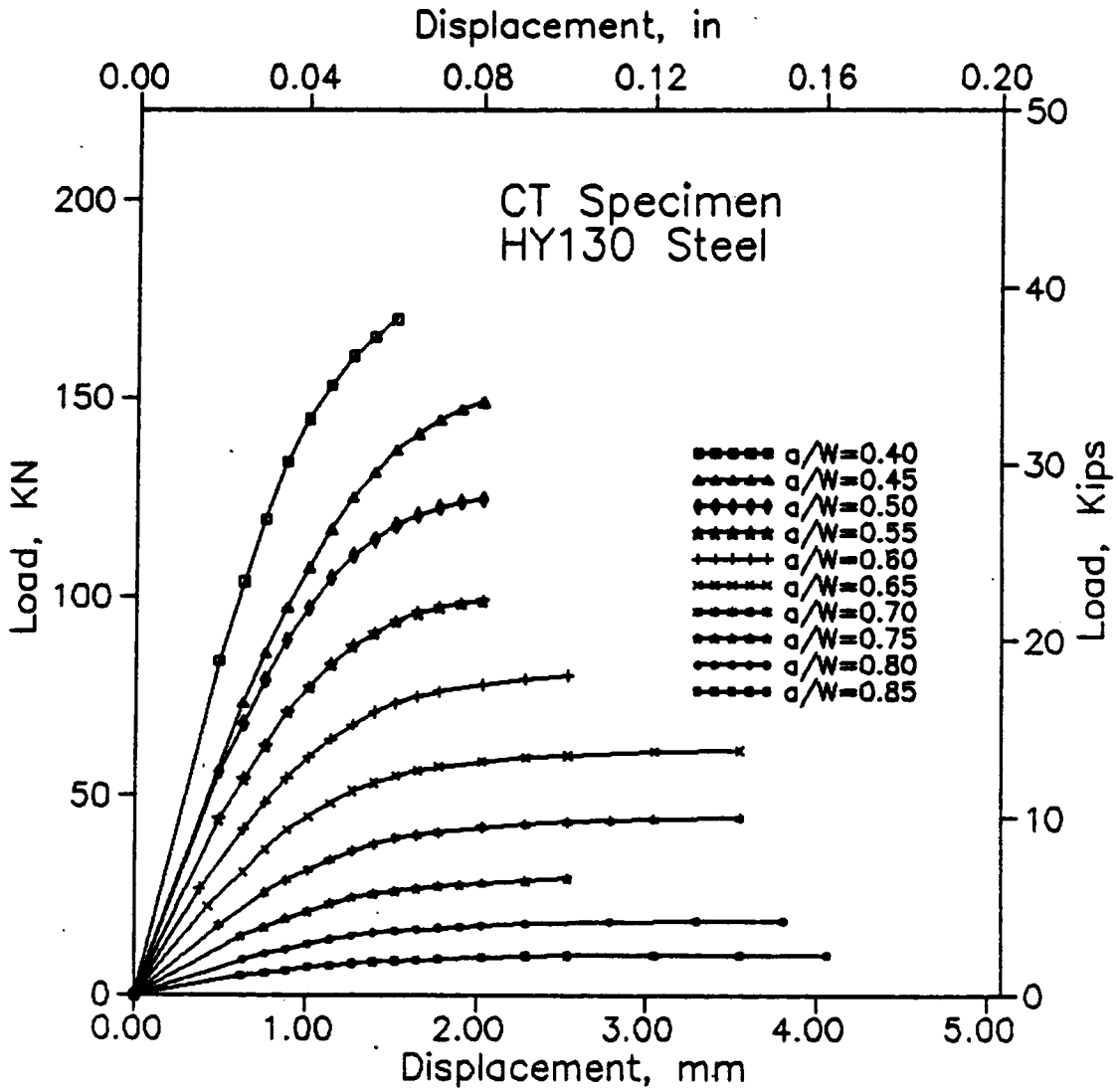
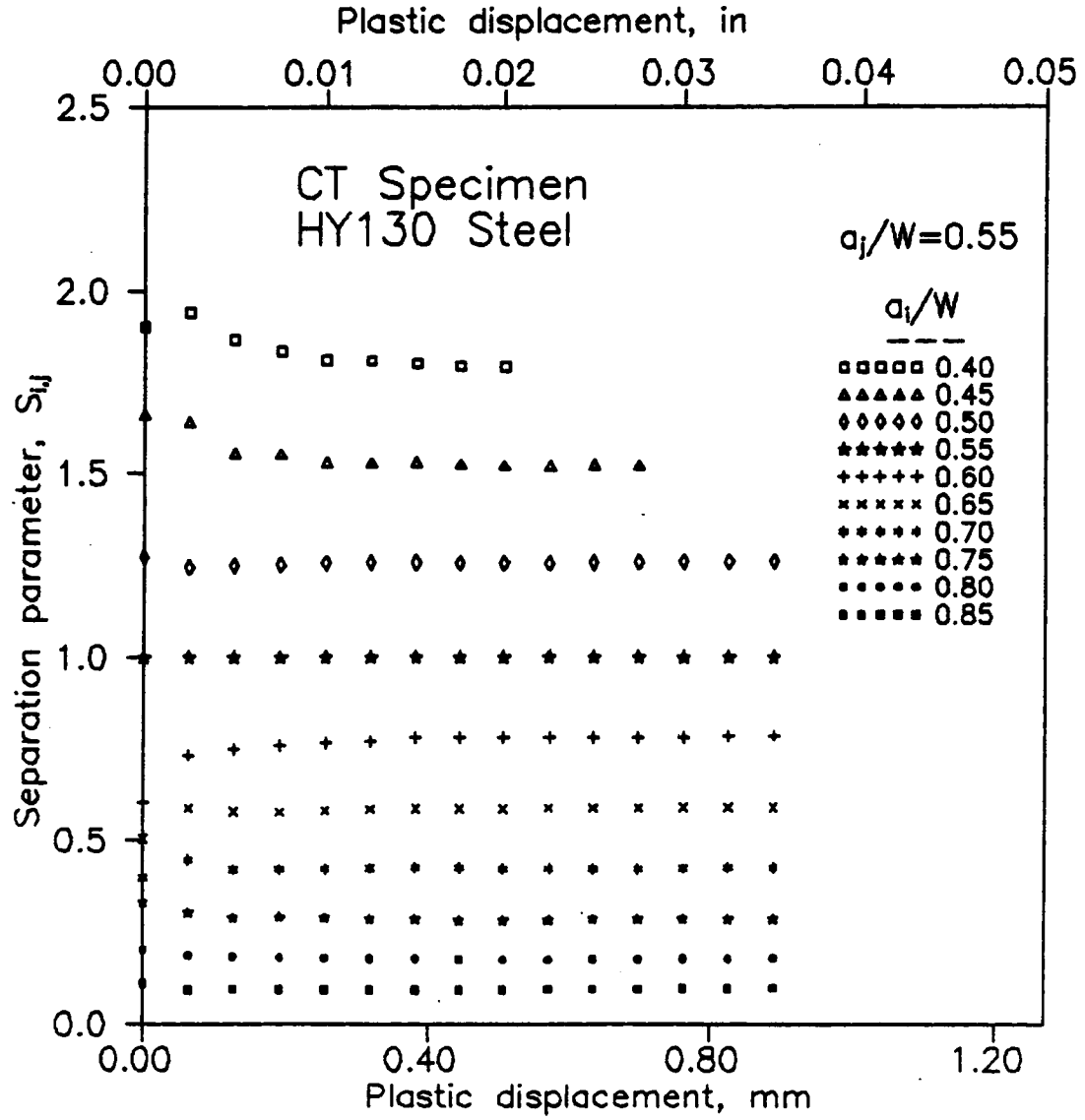
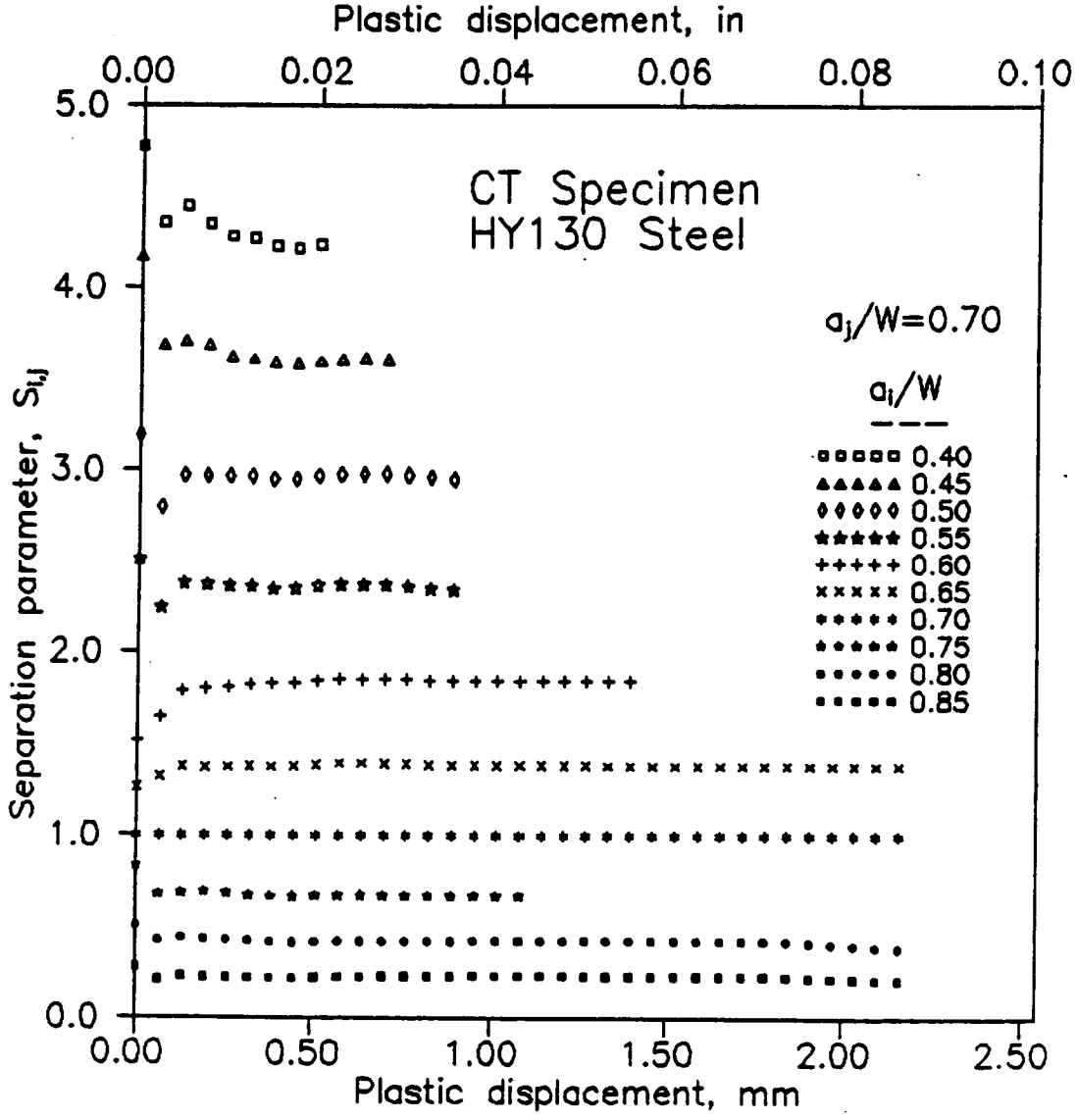


Fig. 2.3 - Load versus load line displacement test records of ten identical HY130 blunt notched compact specimens of different crack sizes.



(a)

Fig. 2.4 - Separation parameters of the different test records in the HY130 compact specimens set with respect to two reference test records: (a) a_j/W=0.55, and (b) a_j/W=0.70.



(b)

Fig. 2.4 - (continued)

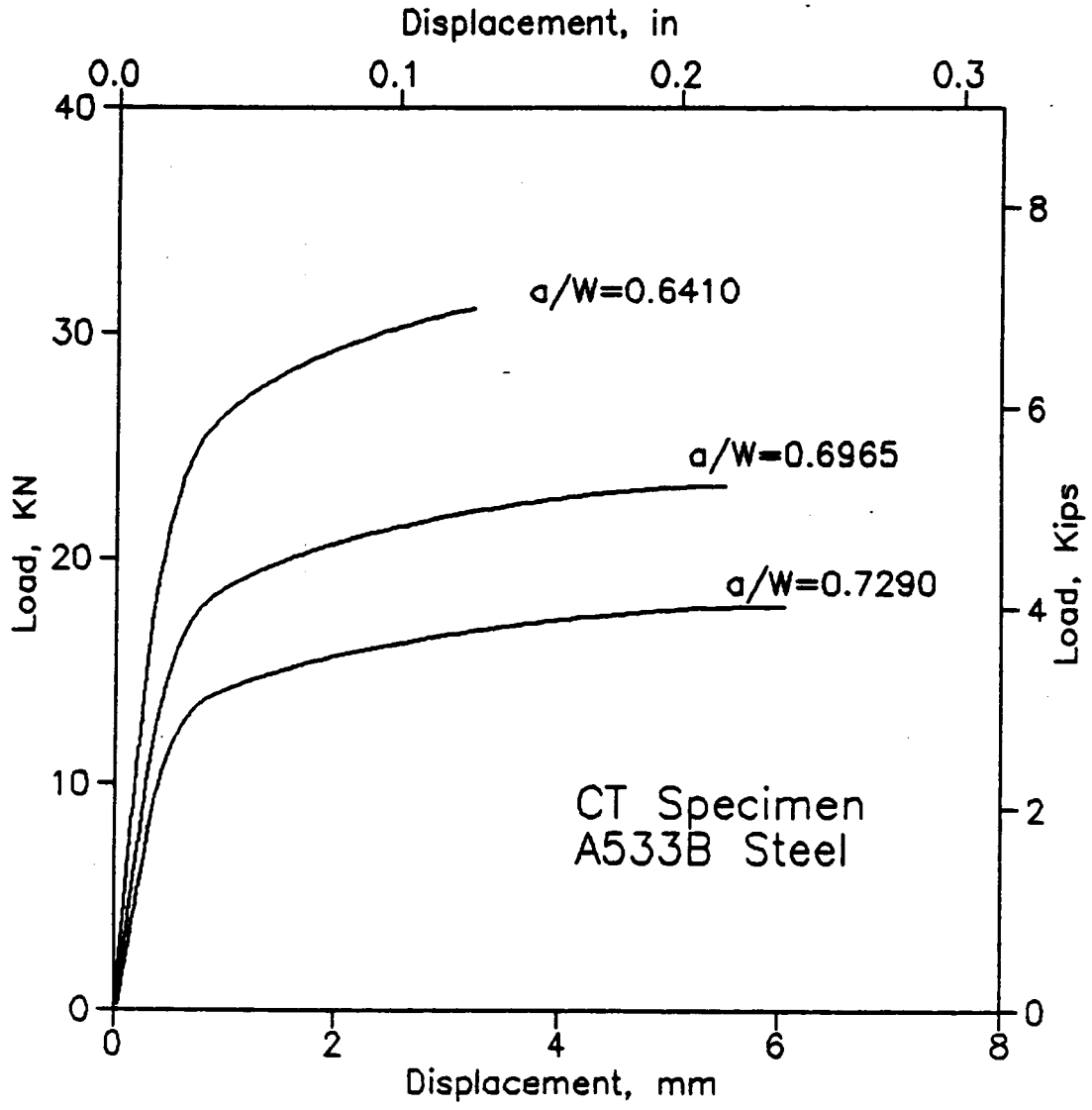


Fig. 2.5 - Load versus load line displacement test records of three identical A533B blunt notched compact specimens of different crack sizes.

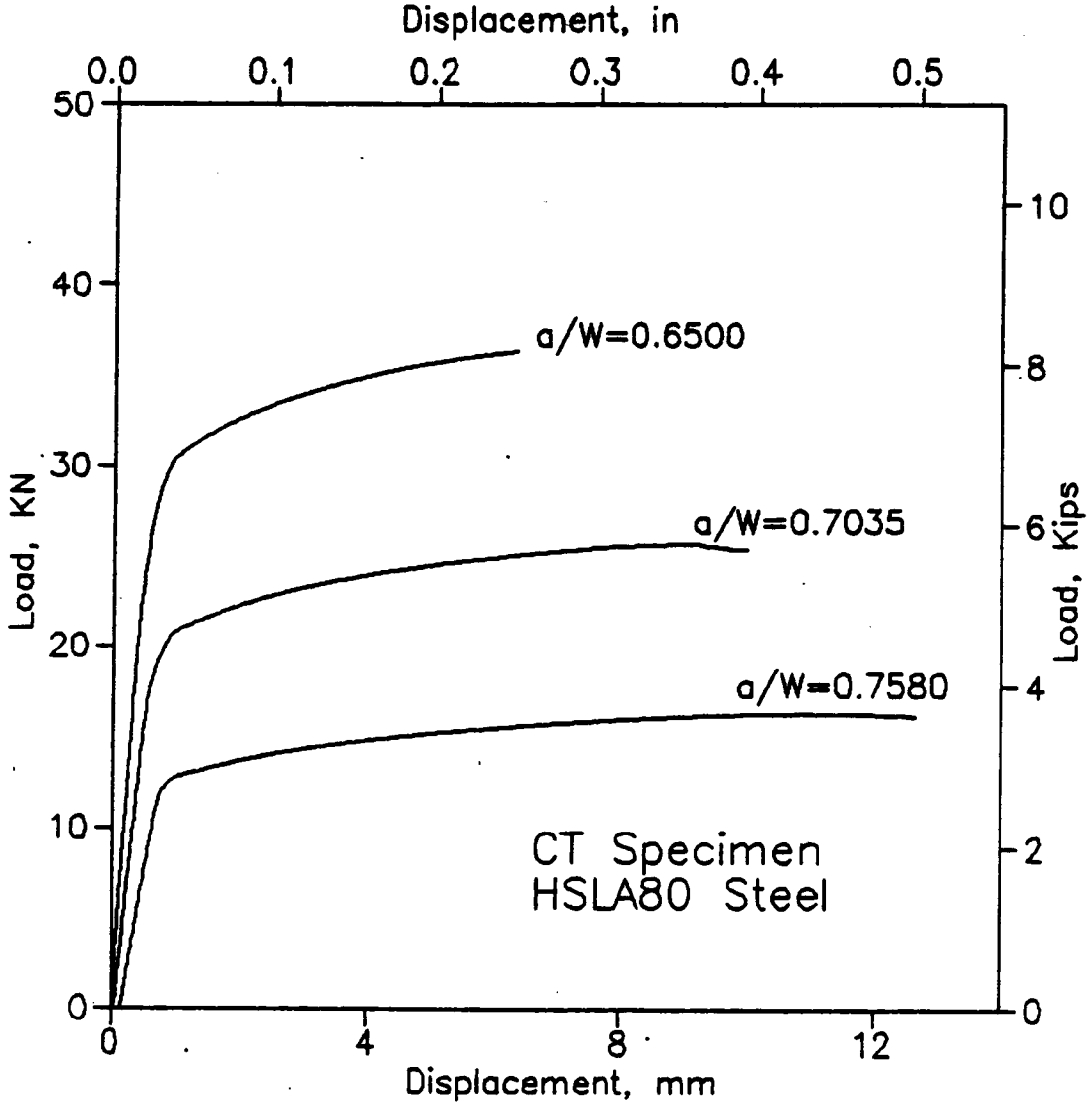


Fig. 2.6 - Load versus load line displacement test records of three identical HSLA80 blunt notched compact specimens of different crack sizes.

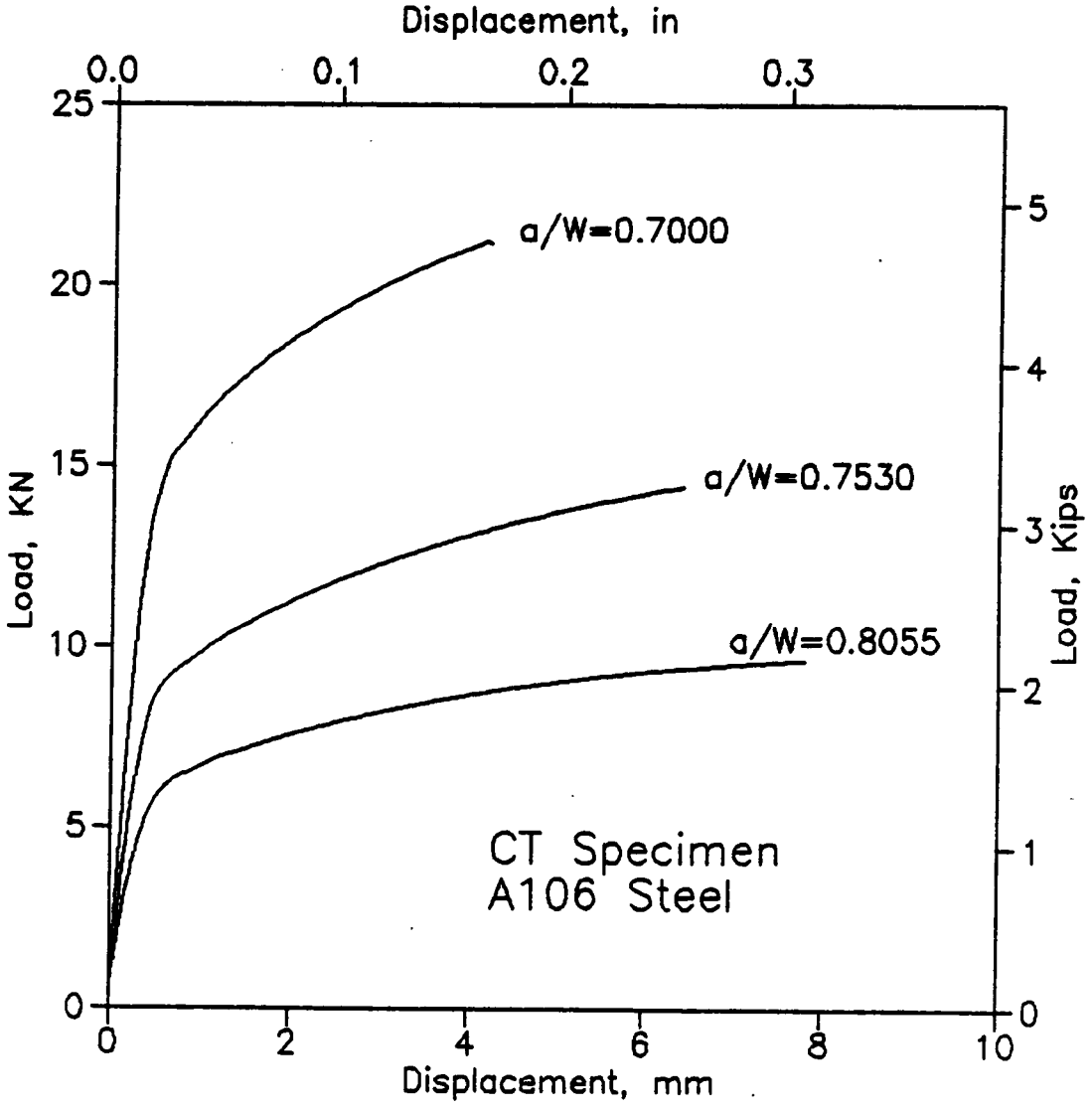


Fig. 2.7 - Load versus load line displacement test records of three identical A106 blunt notched compact specimens of different crack sizes.

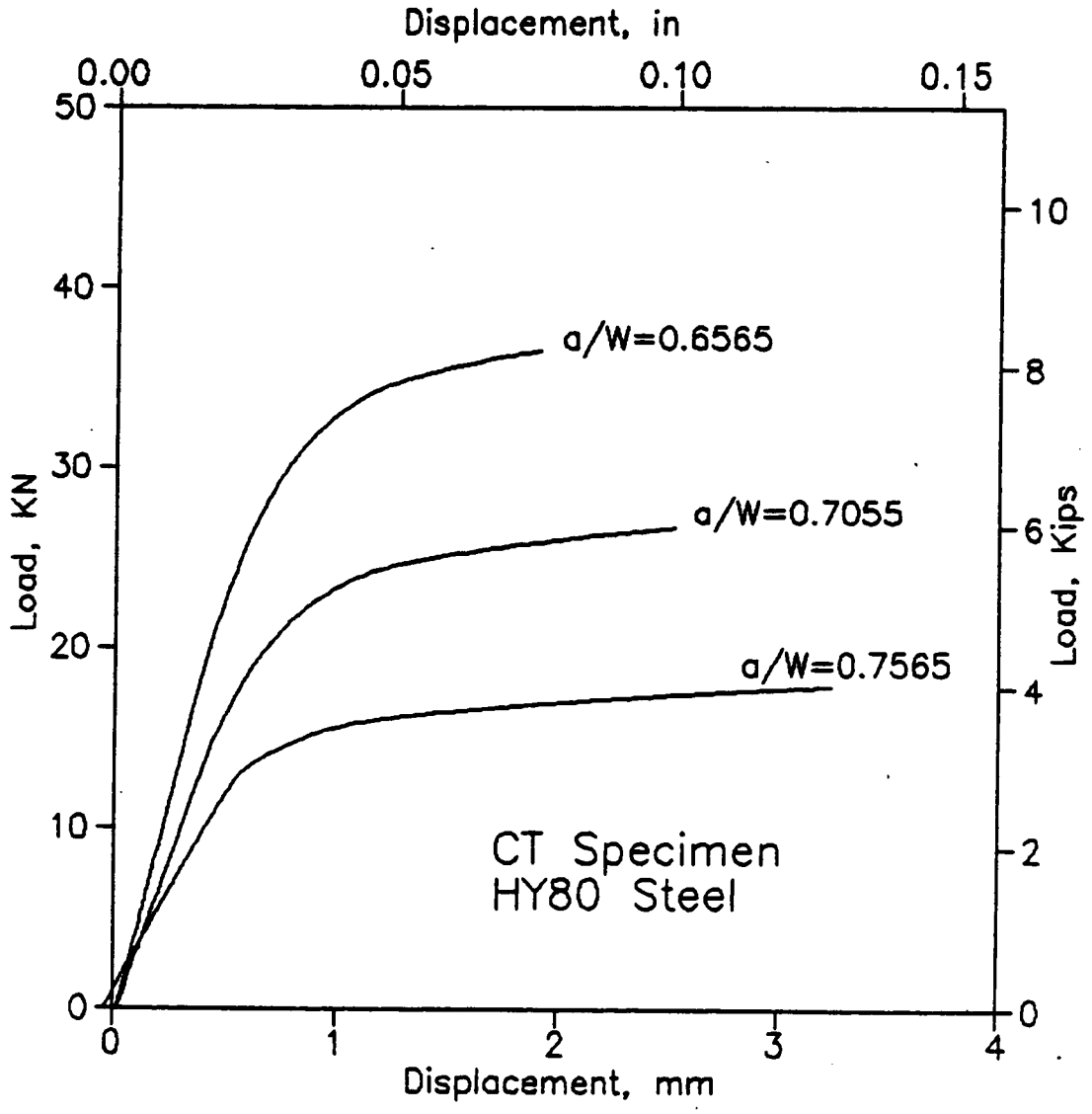


Fig. 2.8 - Load versus load line displacement test records of three identical HY80 blunt notched compact specimens of different crack sizes.

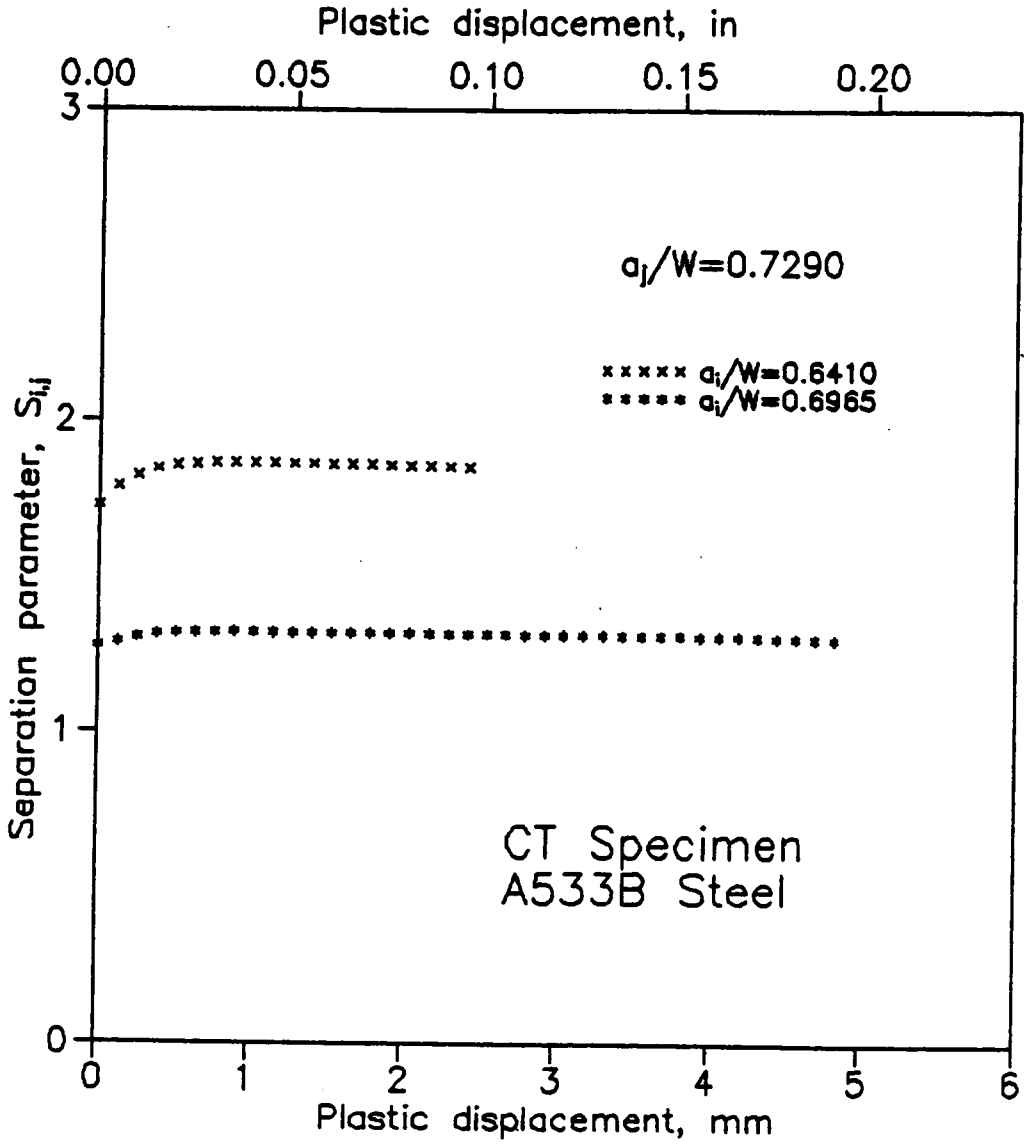


Fig. 2.9 - Separation parameters of two test records of A533B compact specimens set with respect to the third test record.

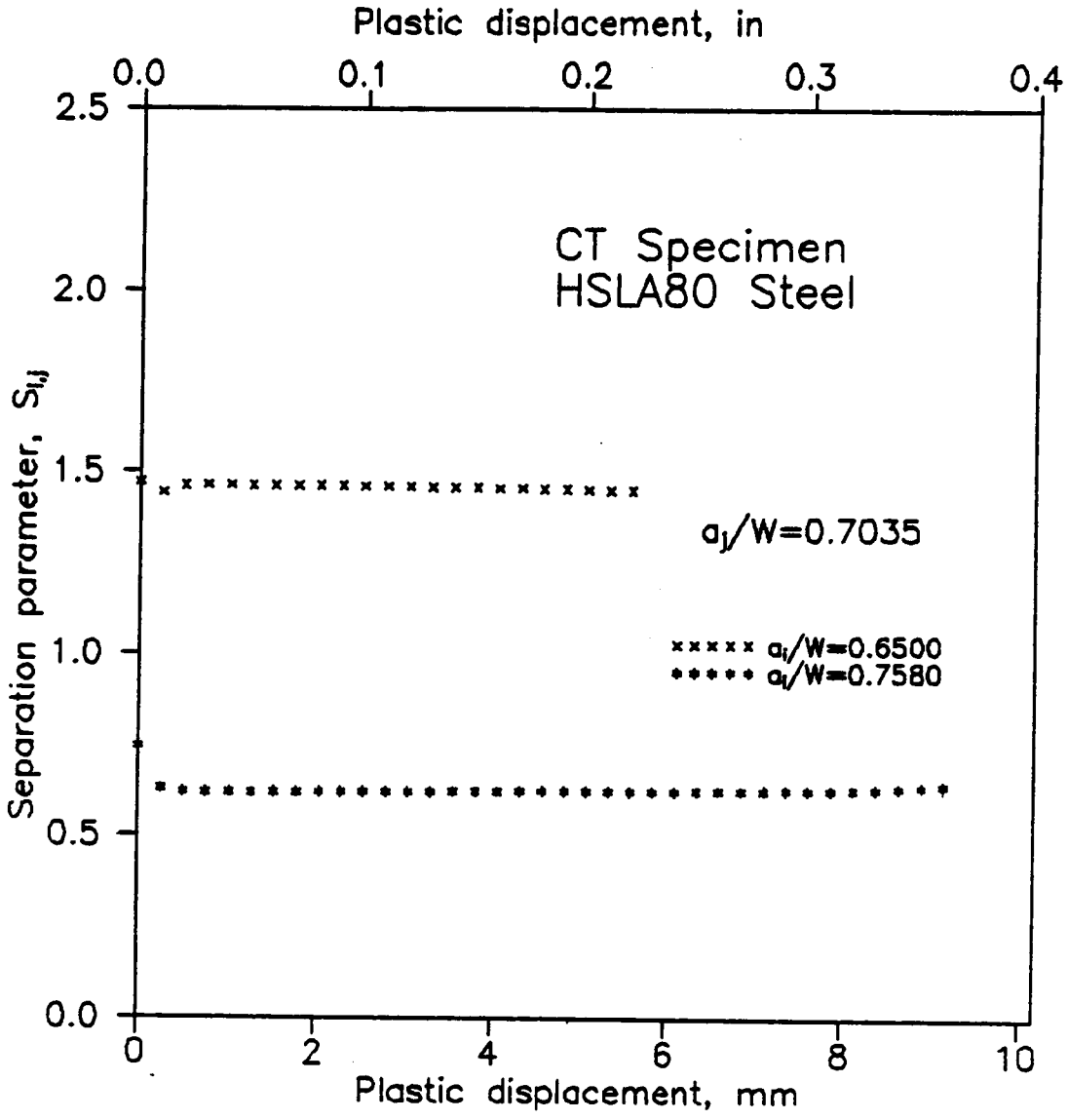


Fig. 2.10 - Separation parameters of two test records of HSLA80 compact specimens set with respect to the third test record.

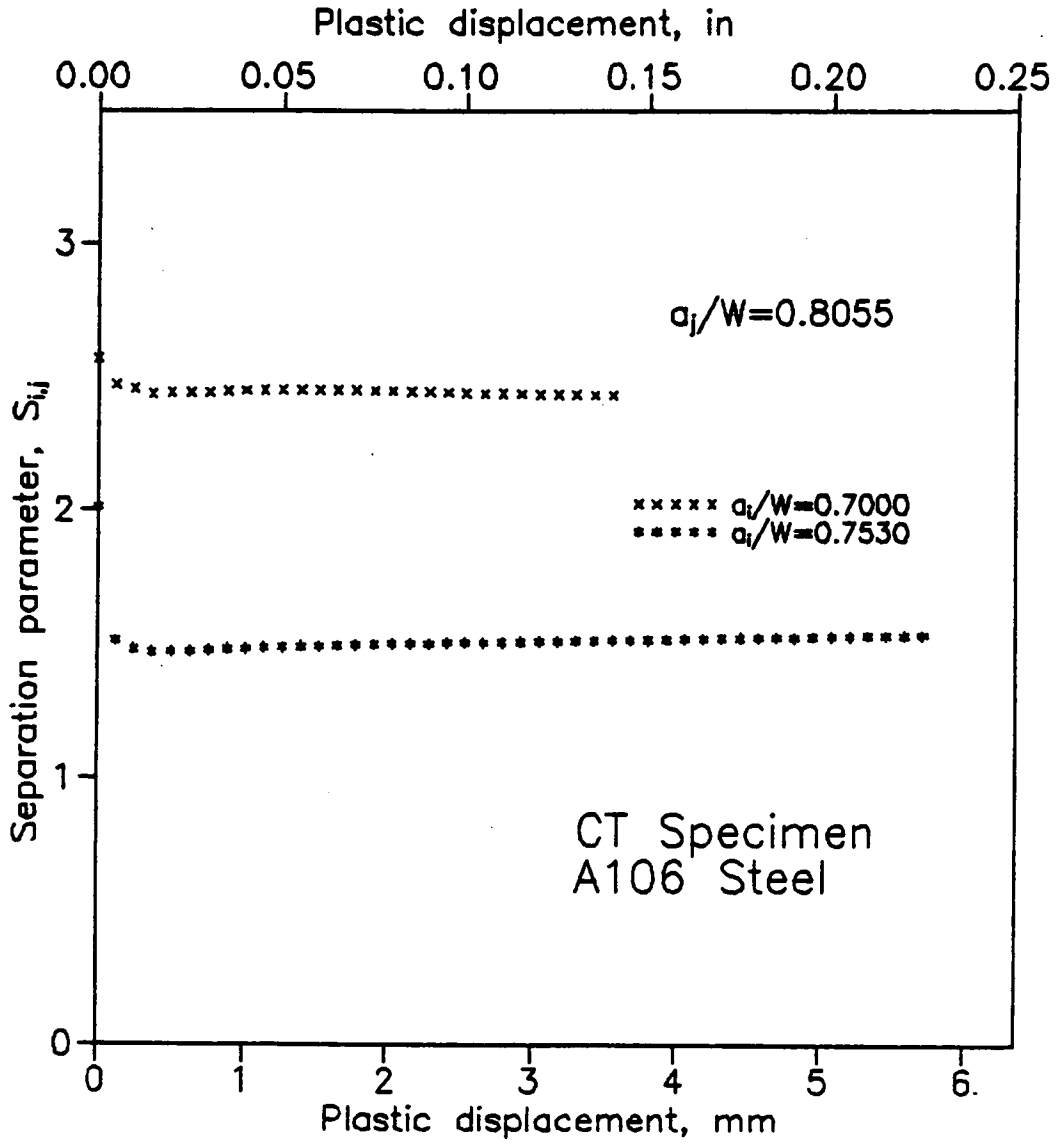


Fig. 2.11 - Separation parameters of two test records of A106 compact specimens set with respect to the third test record.

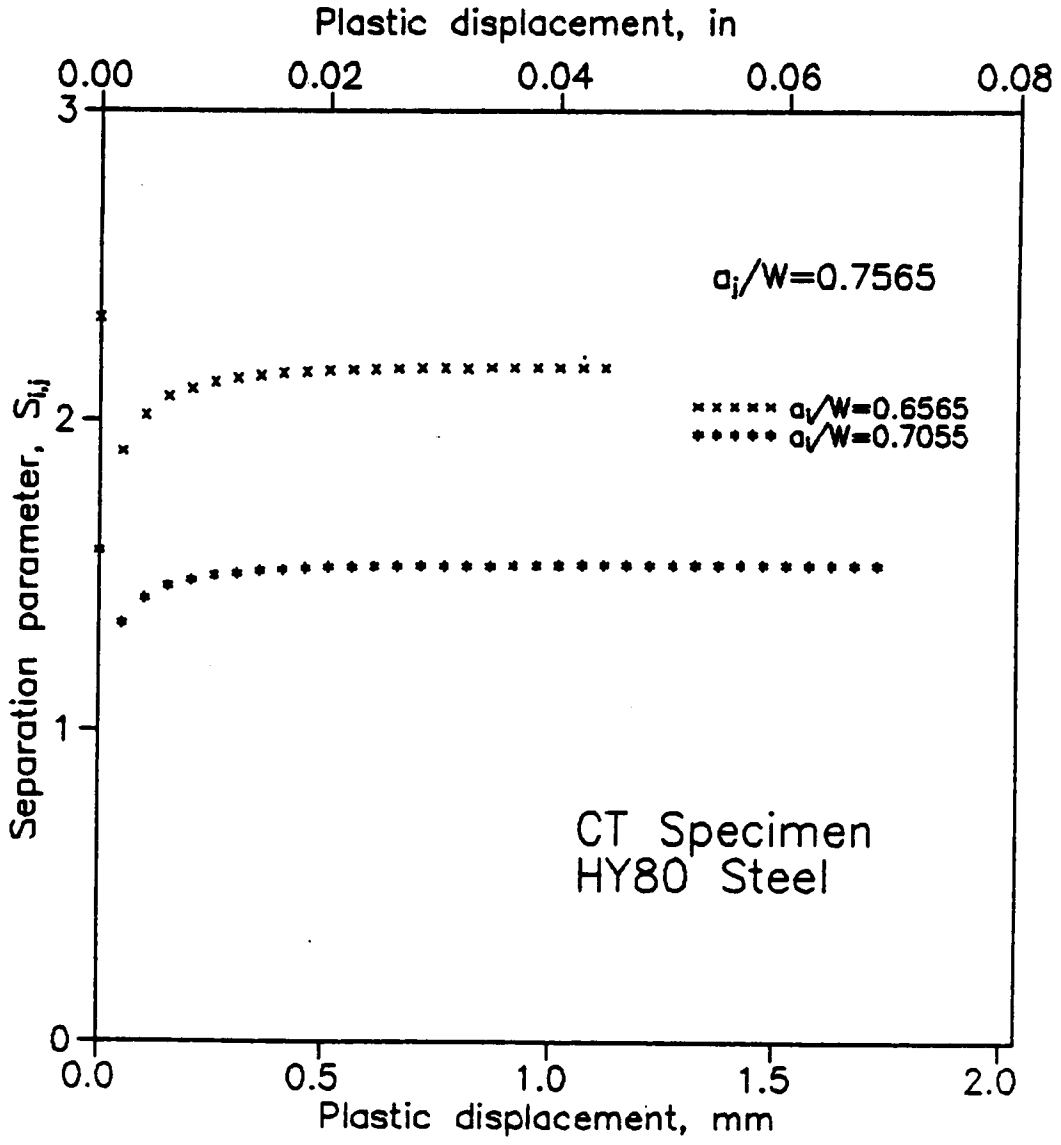


Fig. 2.12 - Separation parameters of two test records of HY80 compact specimens set with respect to the third test record.

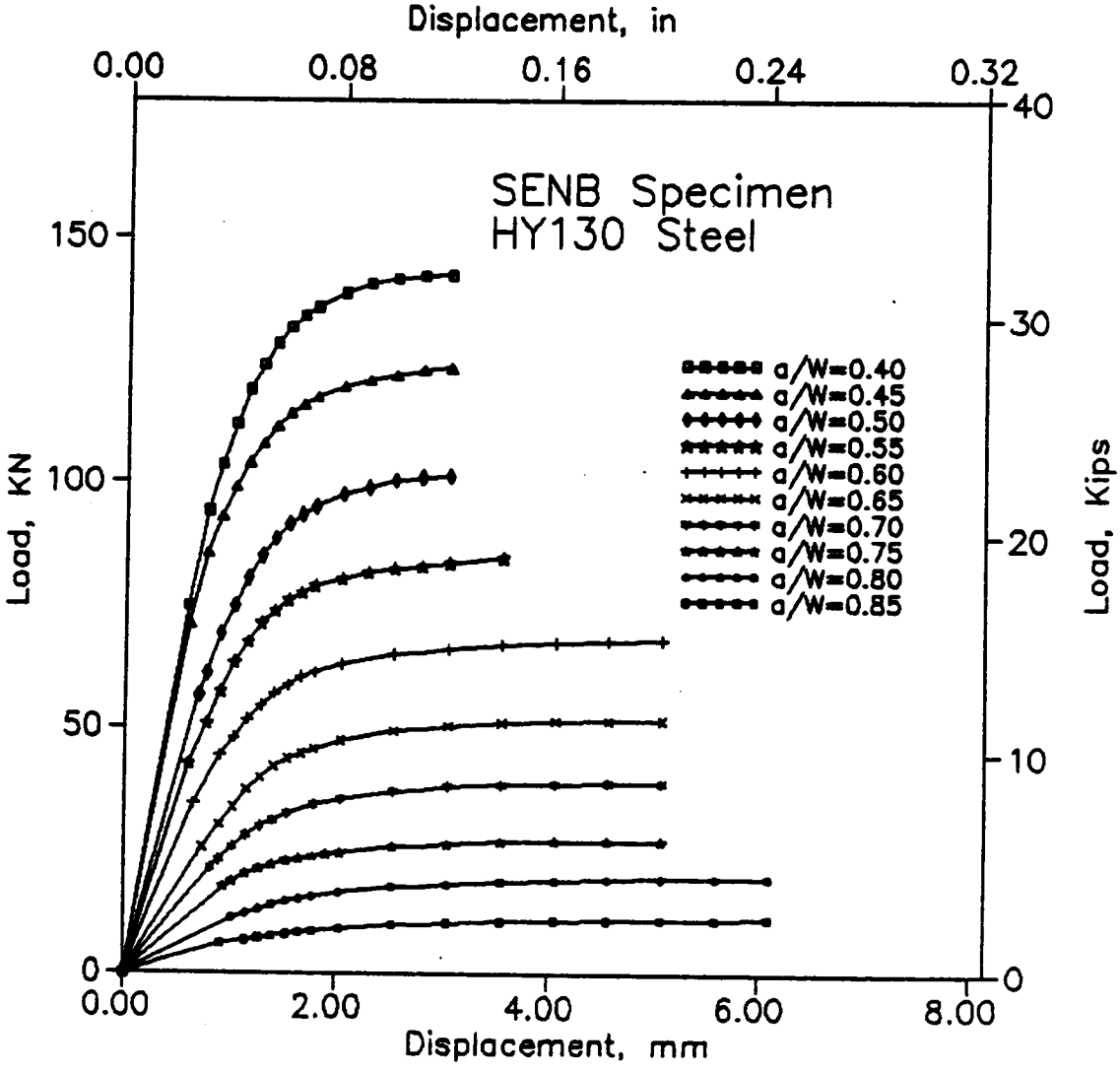
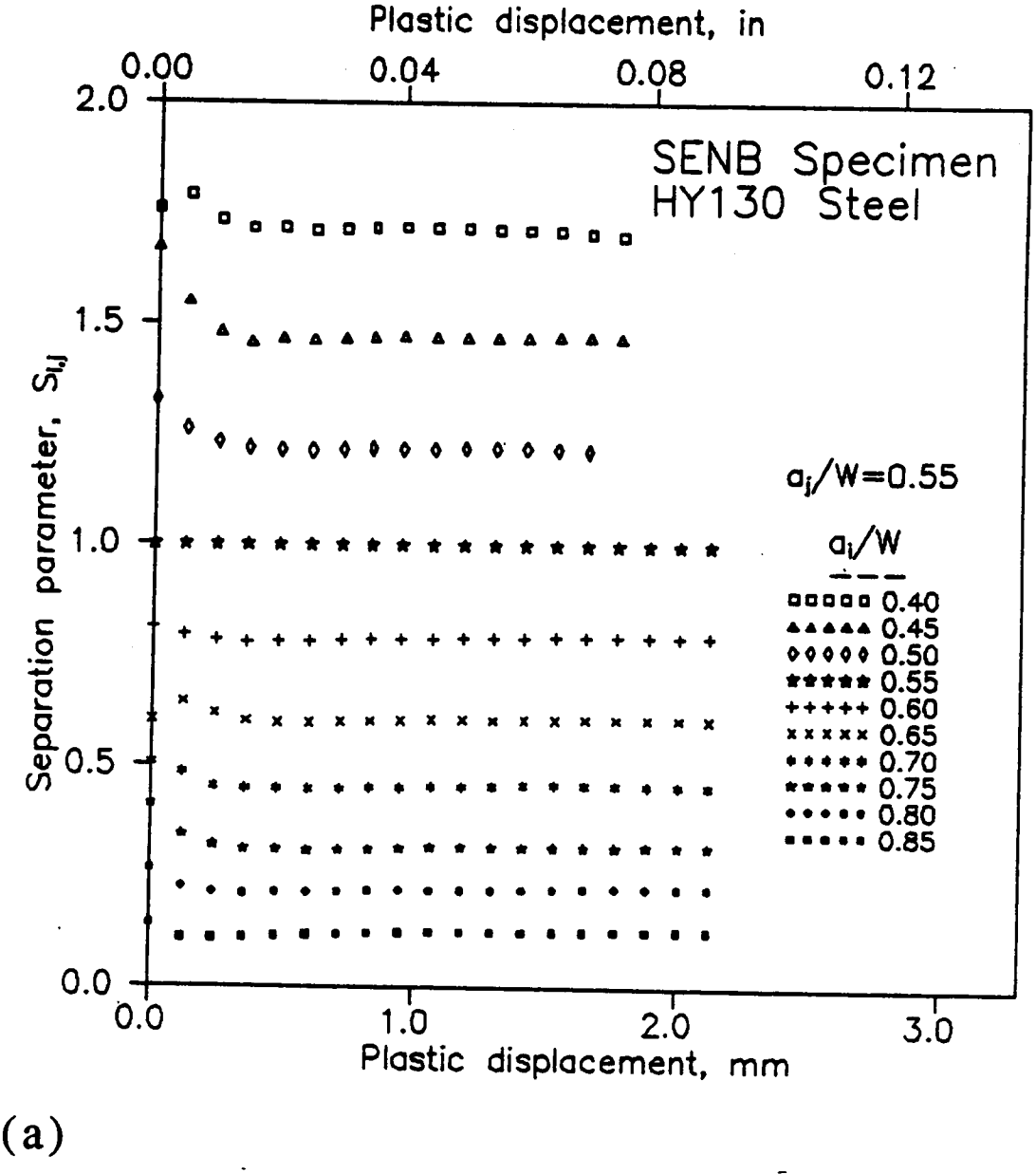
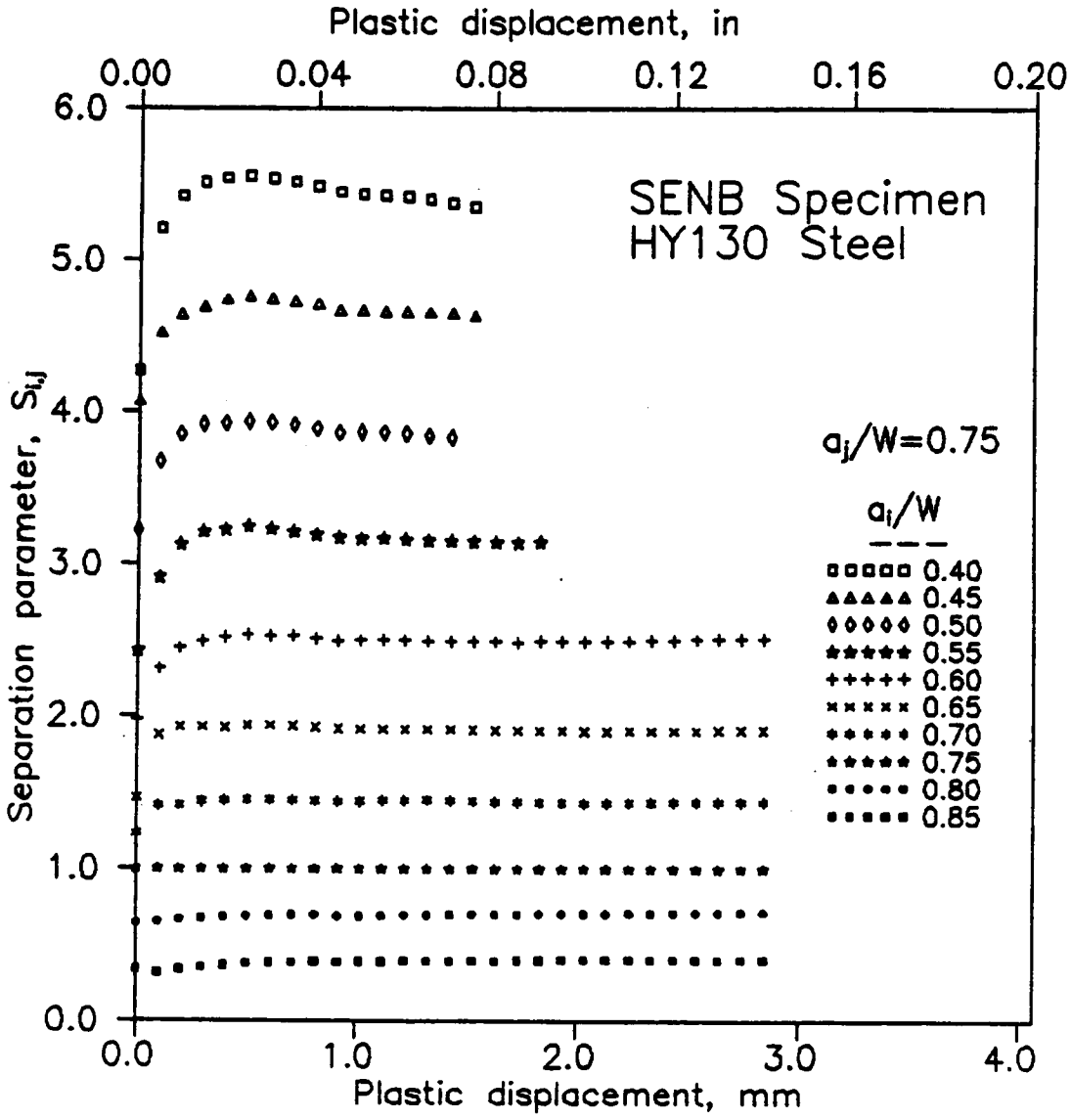


Fig. 2.13 - Load versus load line displacement test records of ten identical HY130 single edge blunt notched bend specimens of different crack sizes.



(a)

Fig. 2.14 - Separation parameters of the different test records in the HY130 single edge notched bend specimens set with respect to two reference test records: (a) a_j/W=0.55, and (b) a_j/W=0.75.



(b)

Fig. 2.14 - (continued).

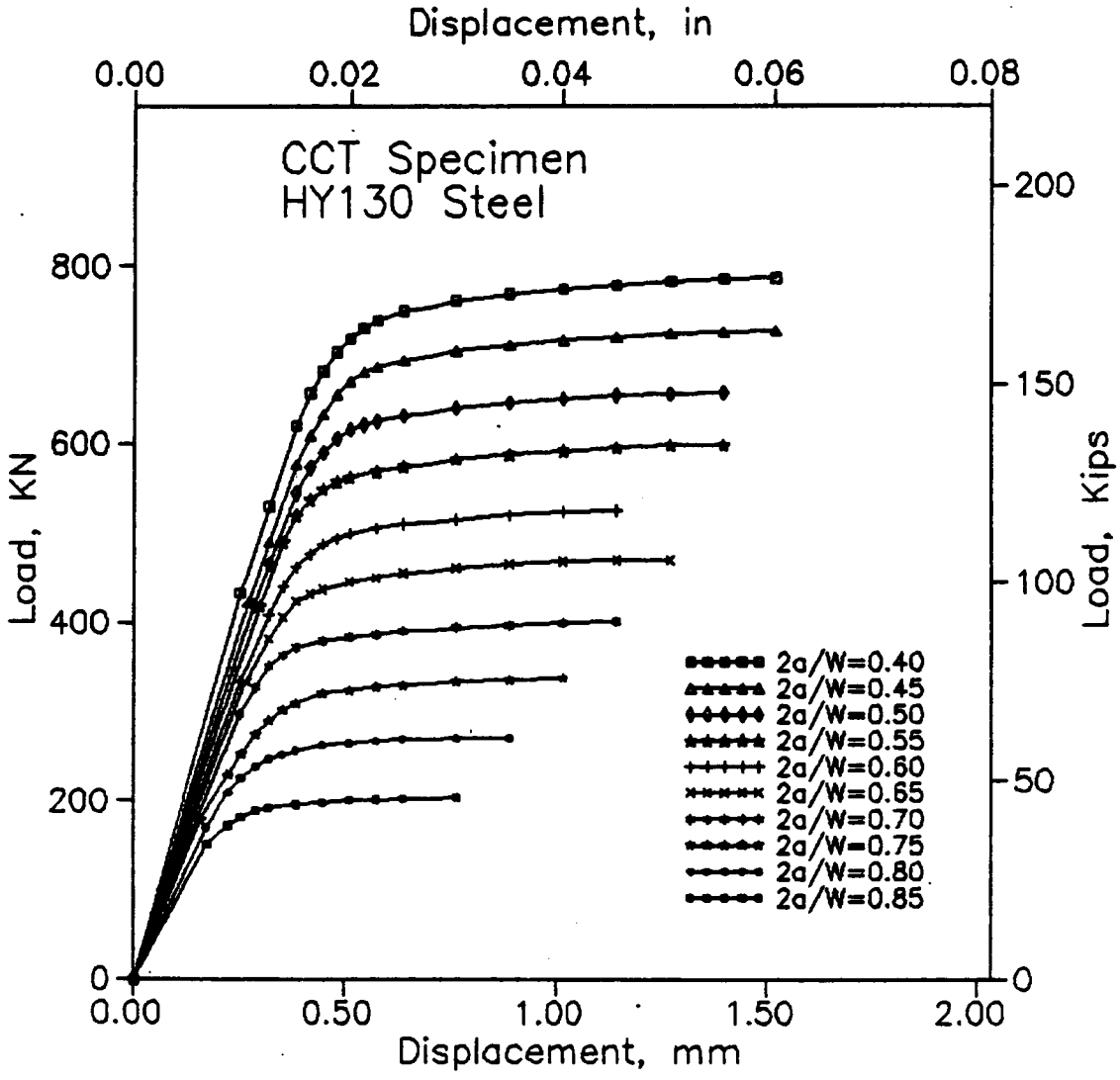
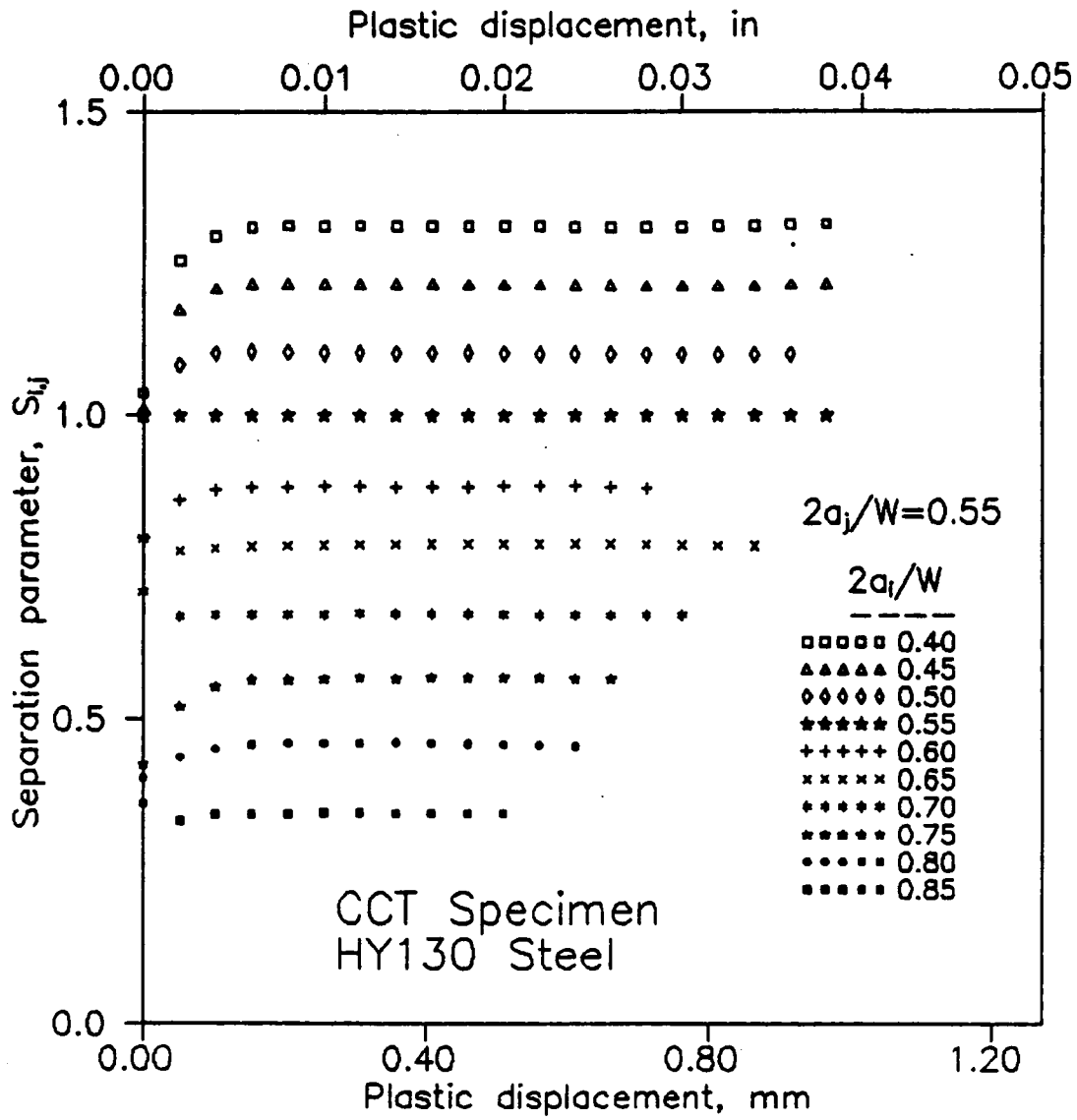
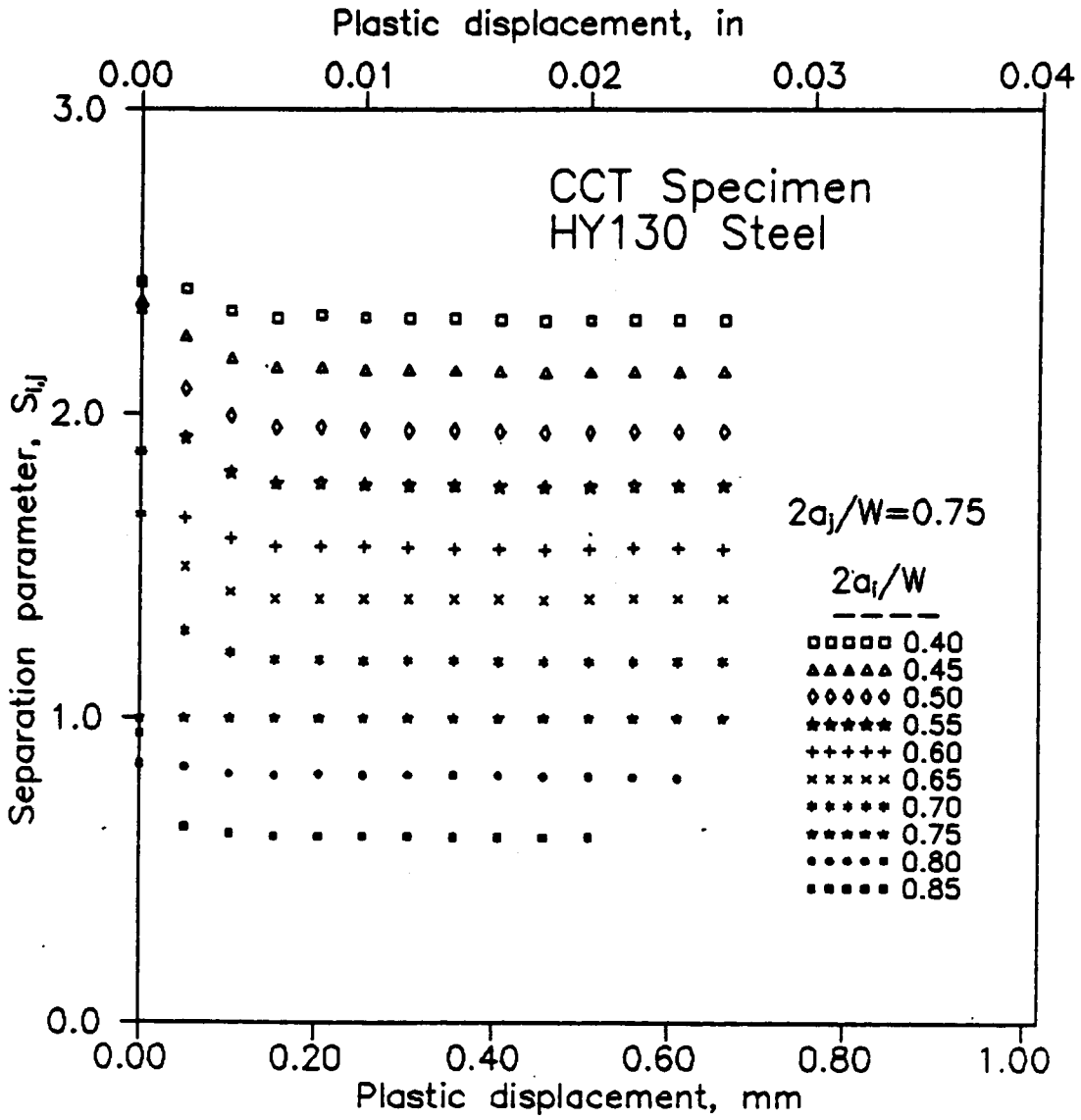


Fig. 2.15 - Load versus load line displacement test records of ten identical HY130 blunt notched center cracked tension specimens of different crack sizes.



(a)

Fig. 2.16 - Separation parameters of the different test records in the HY130 center cracked tension specimens set with respect to two reference test records: (a) a_j/W=0.55, and (b) a_j/W=0.75.



(b)

Fig. 2.16 - (continued).

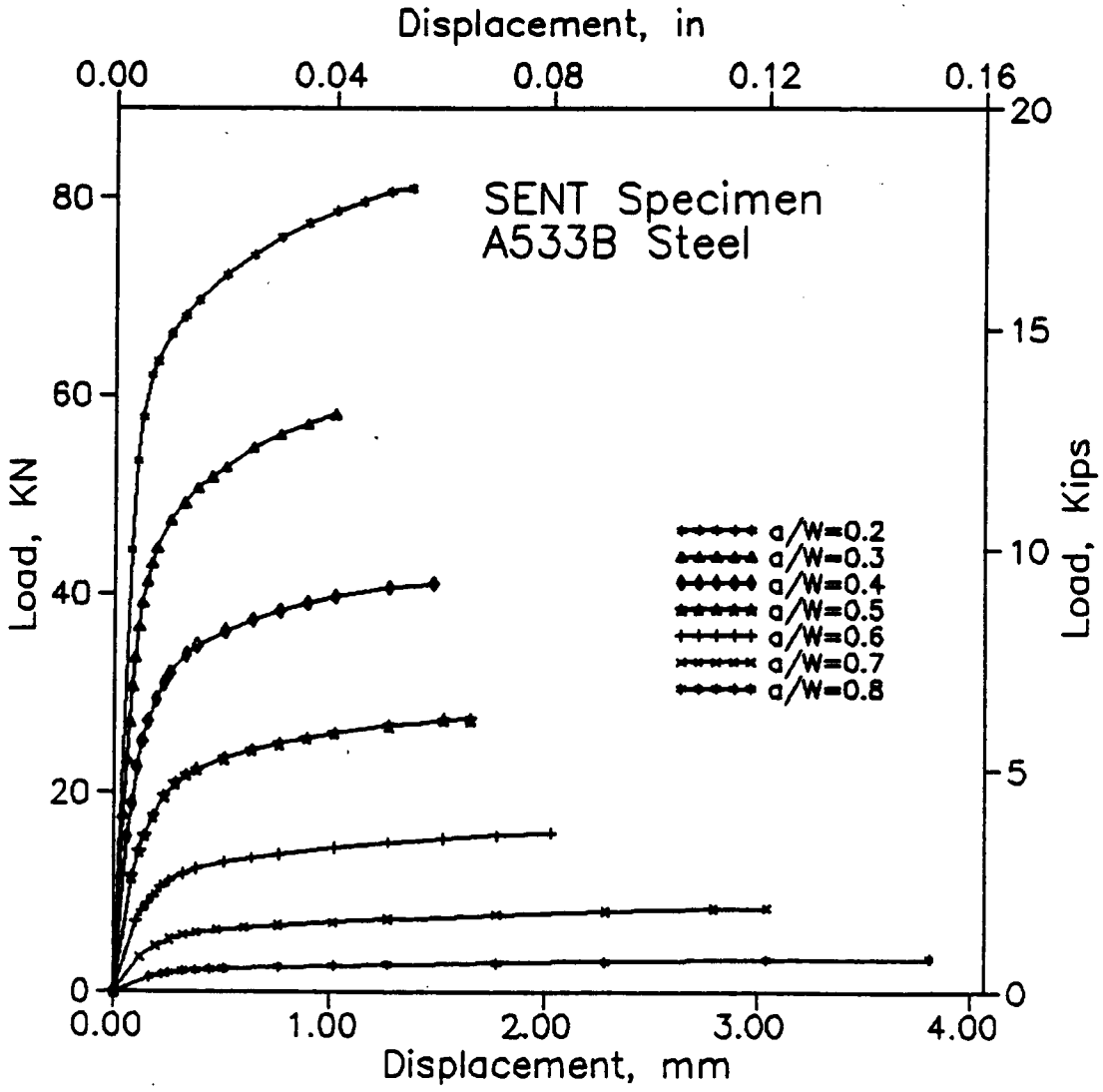
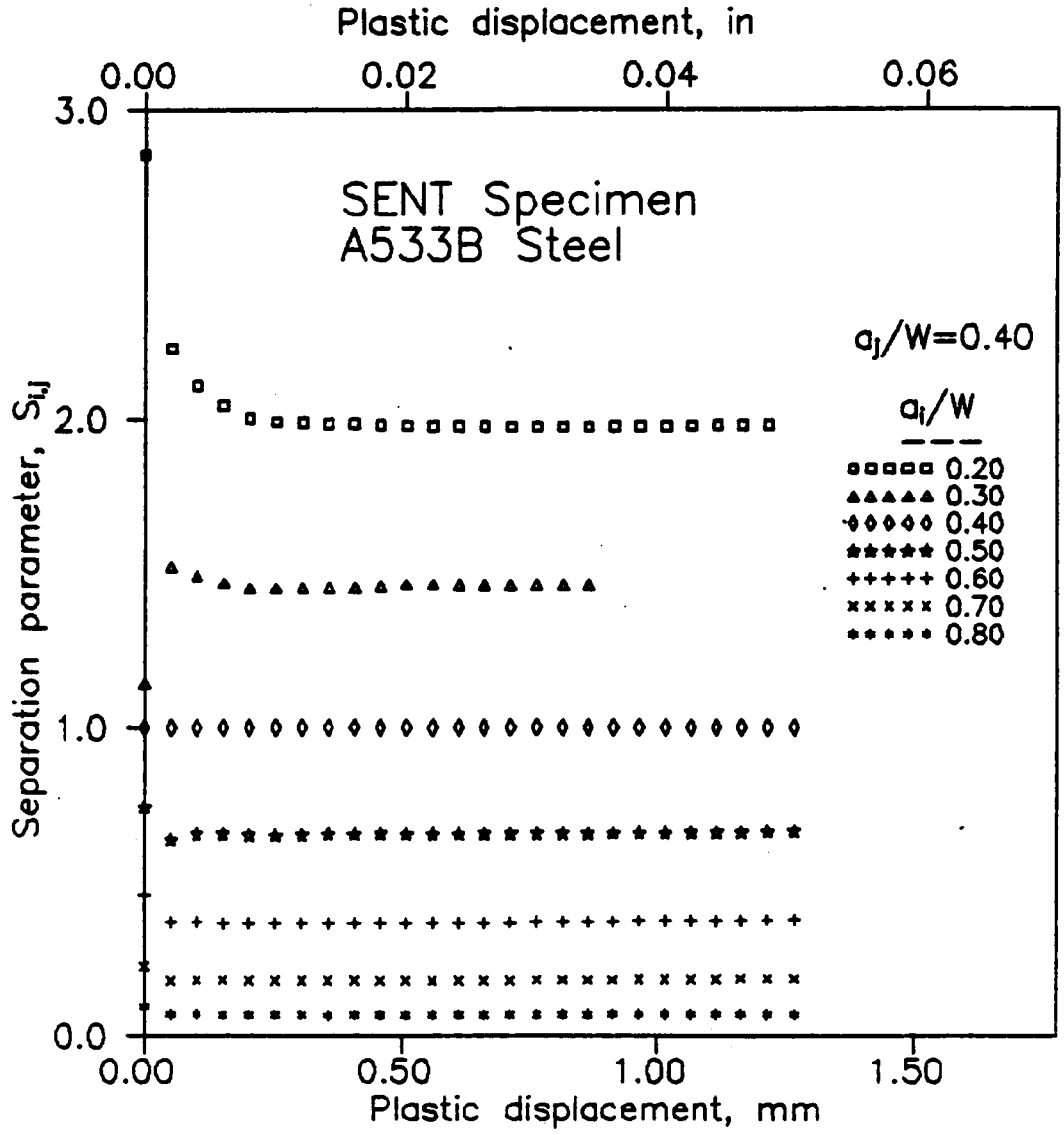
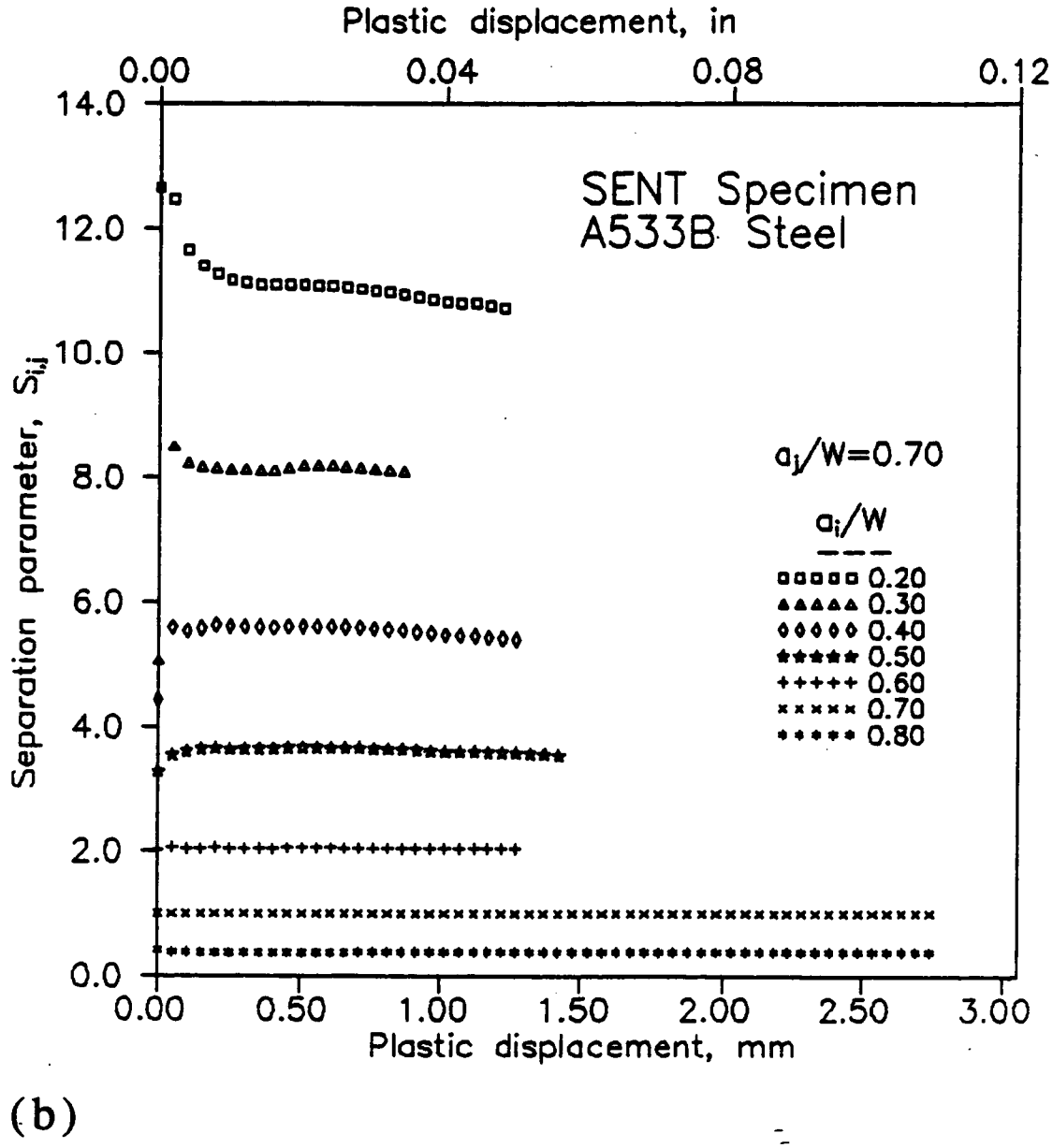


Fig. 2.17 - Load versus load line displacement test records of seven identical A533B single edge blunt notched tension specimens of different crack sizes.



(a)

Fig. 2.18 - Separation parameters of the different test records in the A533B single edge blunt notched tension specimens set with respect to two reference test records: (a) a_j/W=0.40, and (b) a_j/W=0.70.



(b)

Fig. 2.18 - (continued).

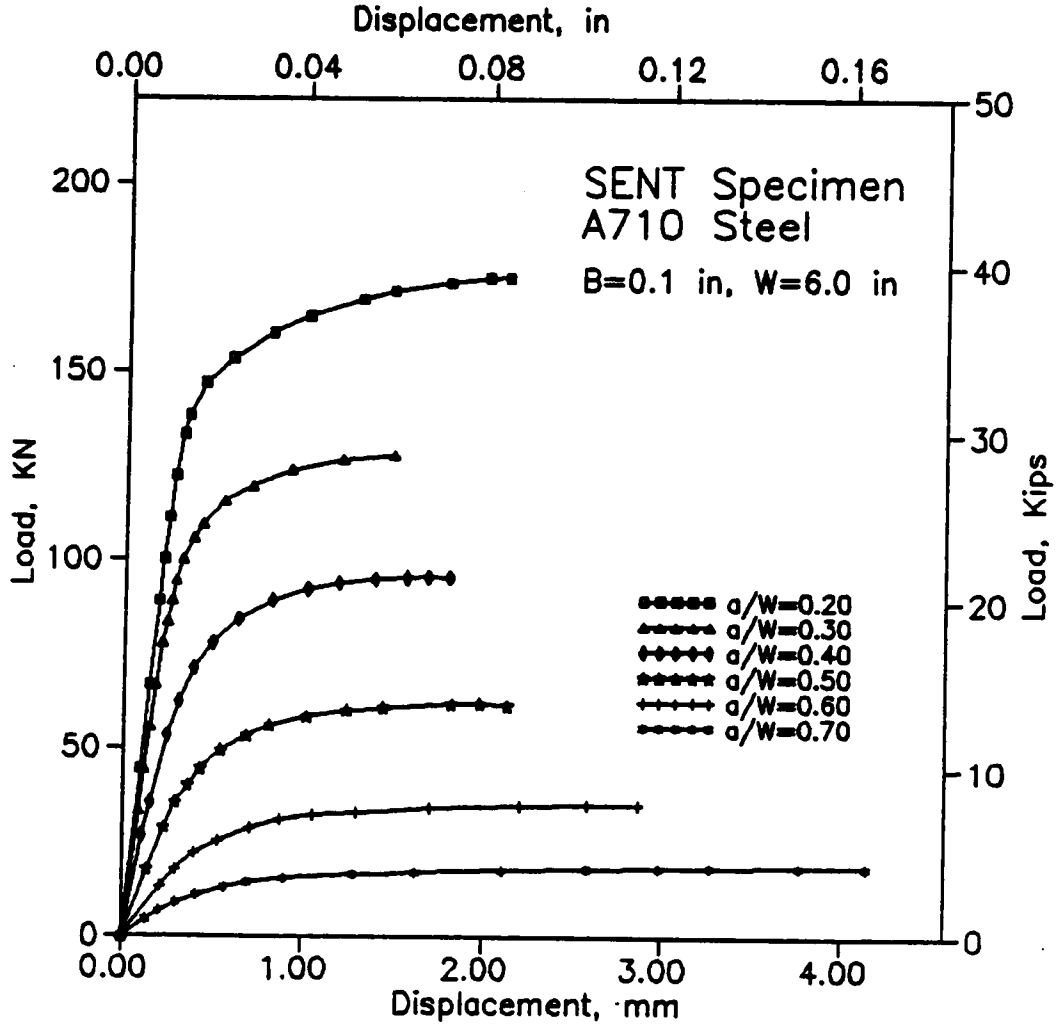
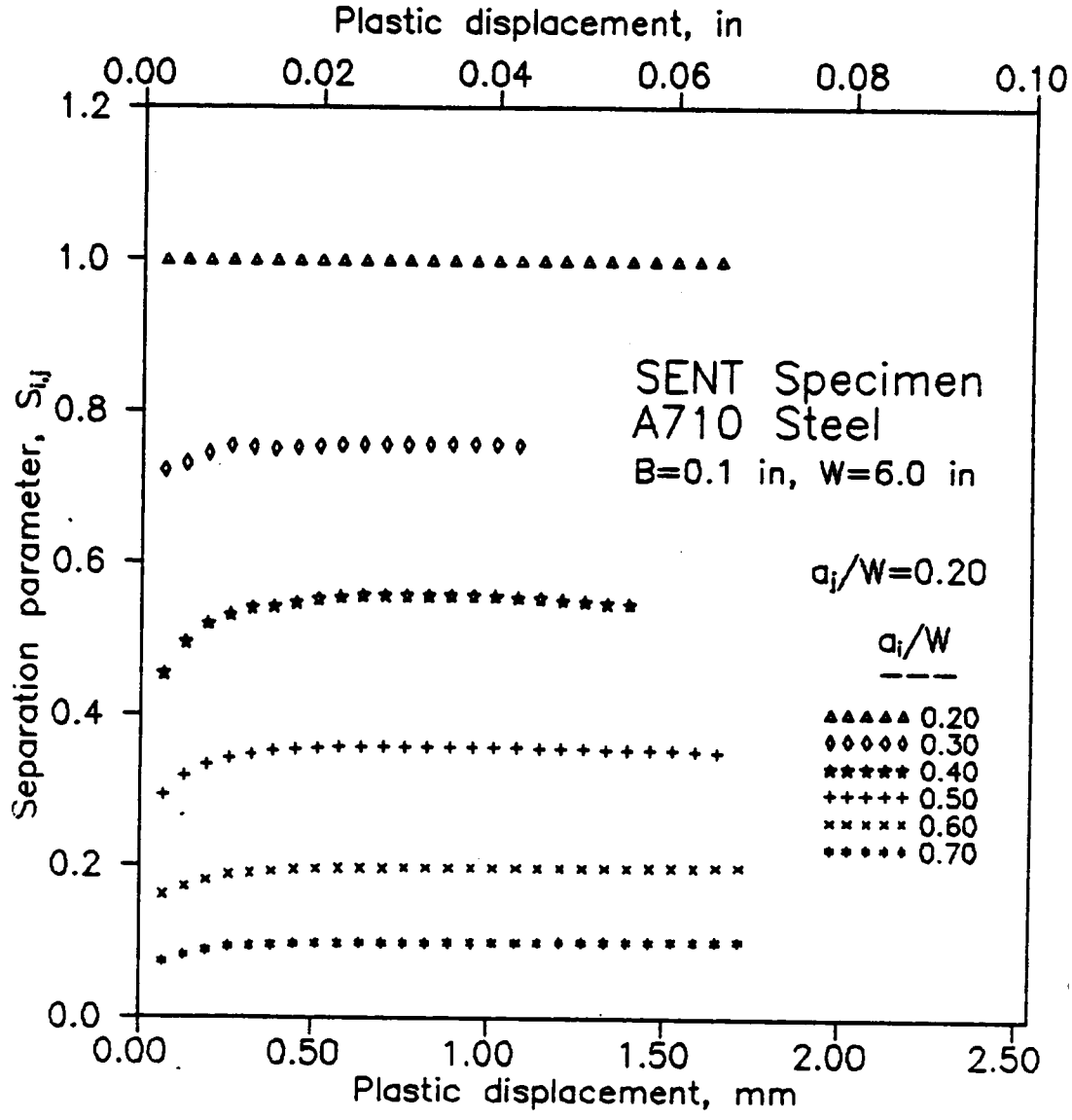
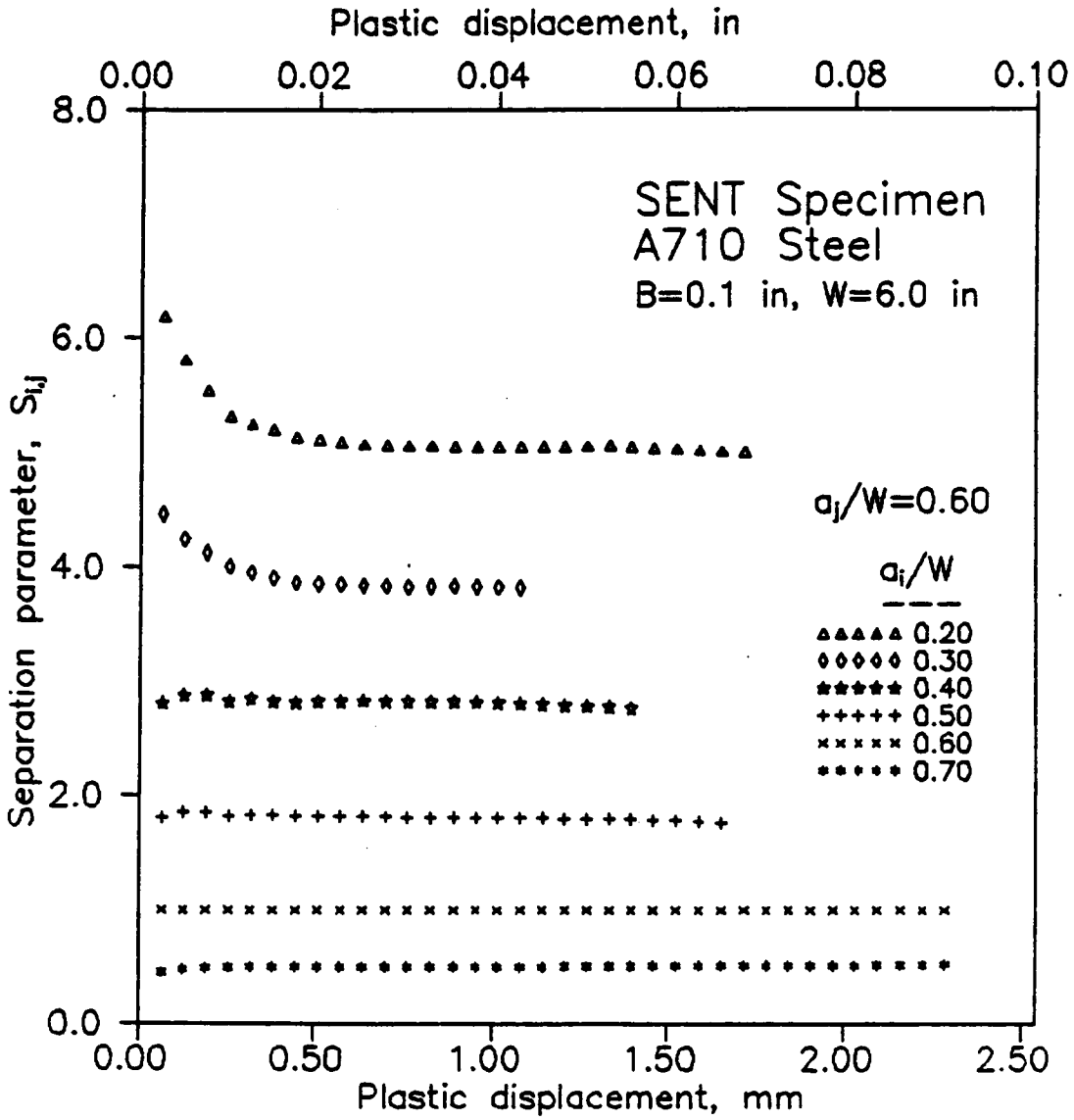


Fig. 2.19 - Load versus load line displacement test records of six identical A710 thin single edge blunt notched tension specimens of different crack sizes.



(a)

Fig. 2.20 - Separation parameters of the different test records in the A710 thin single edge blunt notched tension specimens set with respect to two reference test records: (a) a_j/W=0.20, and (b) a_j/W=0.60.



(b)

Fig. 2.20 - (continued).

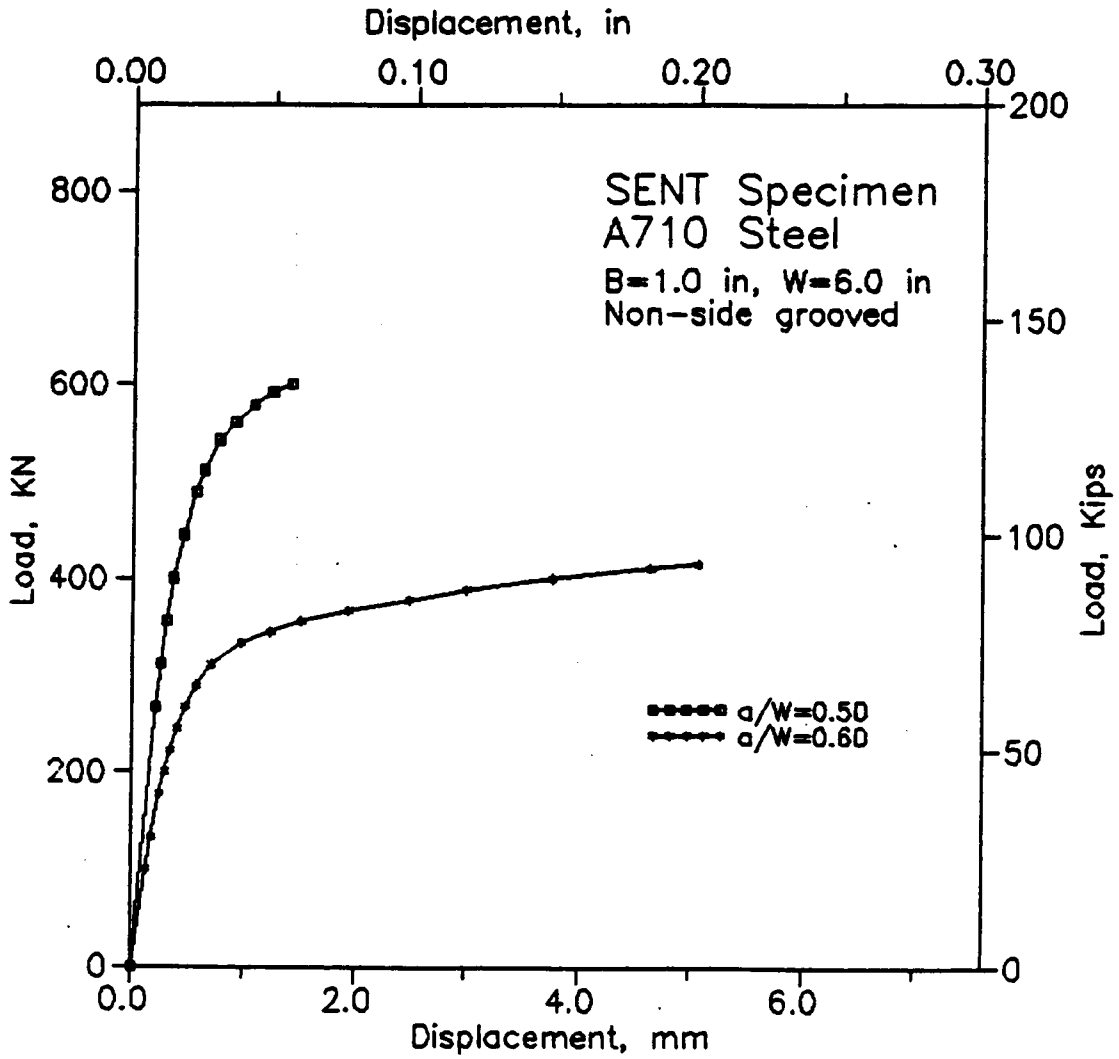


Fig. 2.21 - Load-load line displacement test records of two A710 single edge notched tension specimens of thickness 1.0 inch.

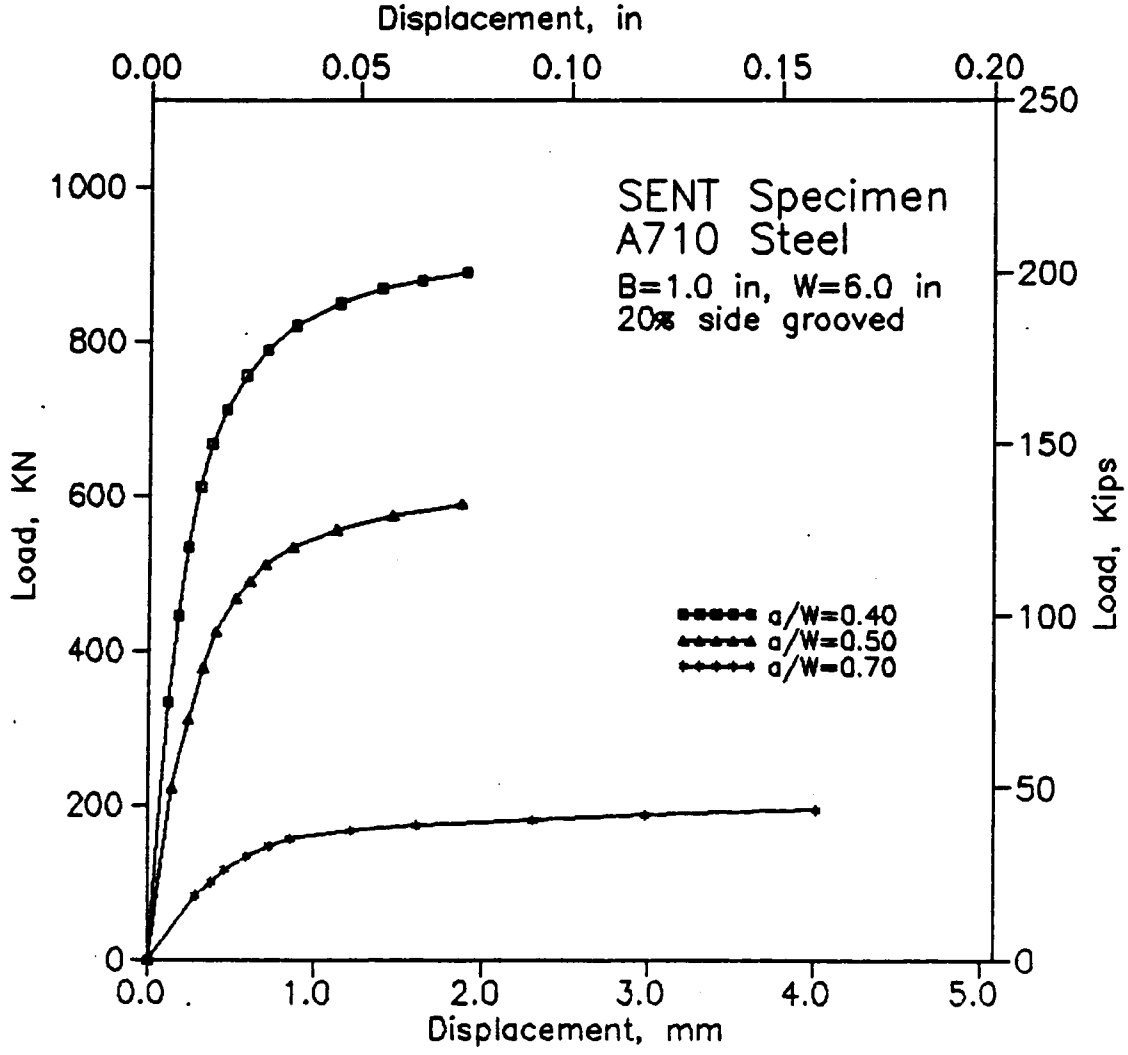


Fig. 2.22 - Load versus load line displacement test records of three A710 single edge notched tension specimens of thickness 1.0 inch with 20% side grooving.

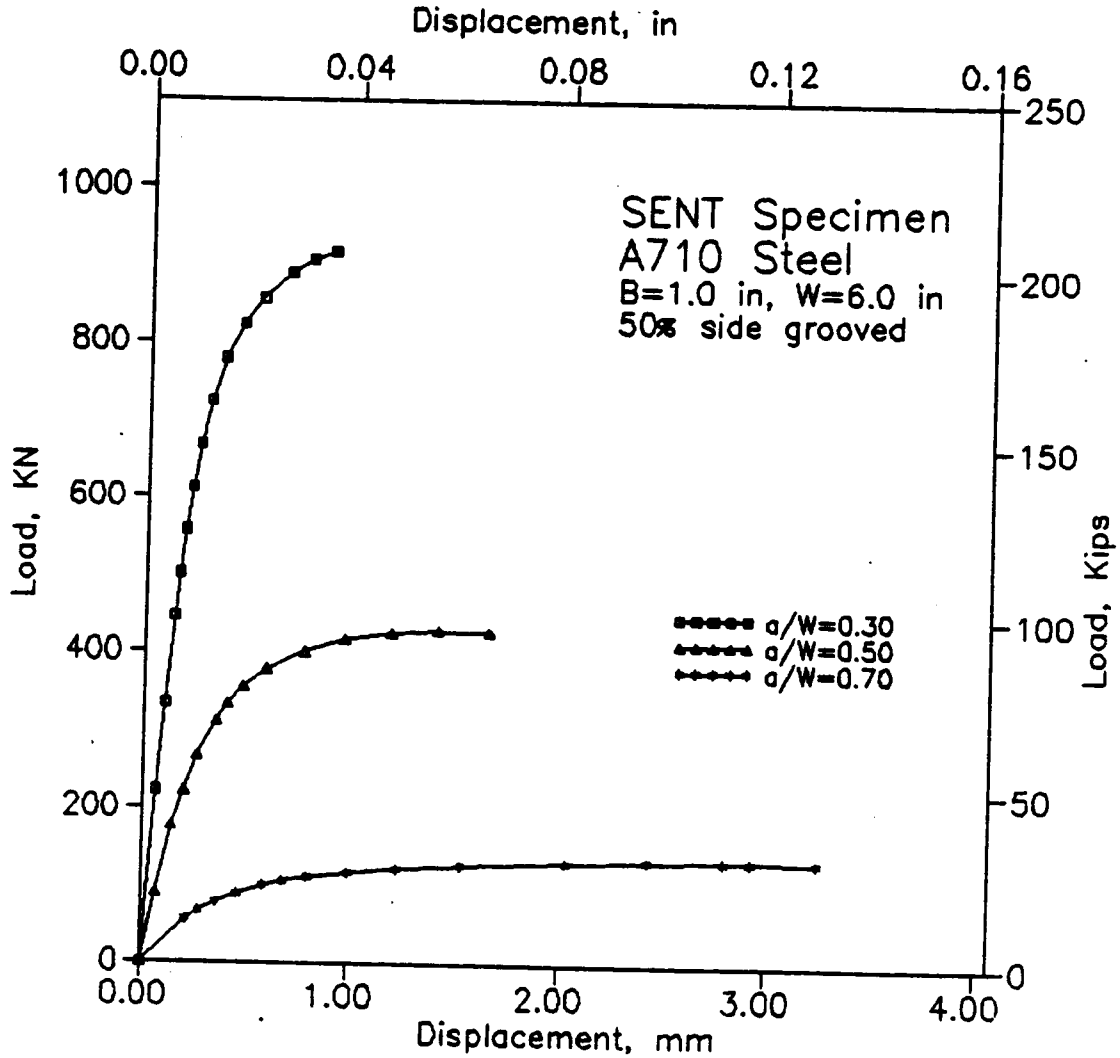


Fig. 2.23 - Load versus load line displacement test records of three A710 single edge notched tension specimens of thickness 1.0 inch with 50% side grooving.

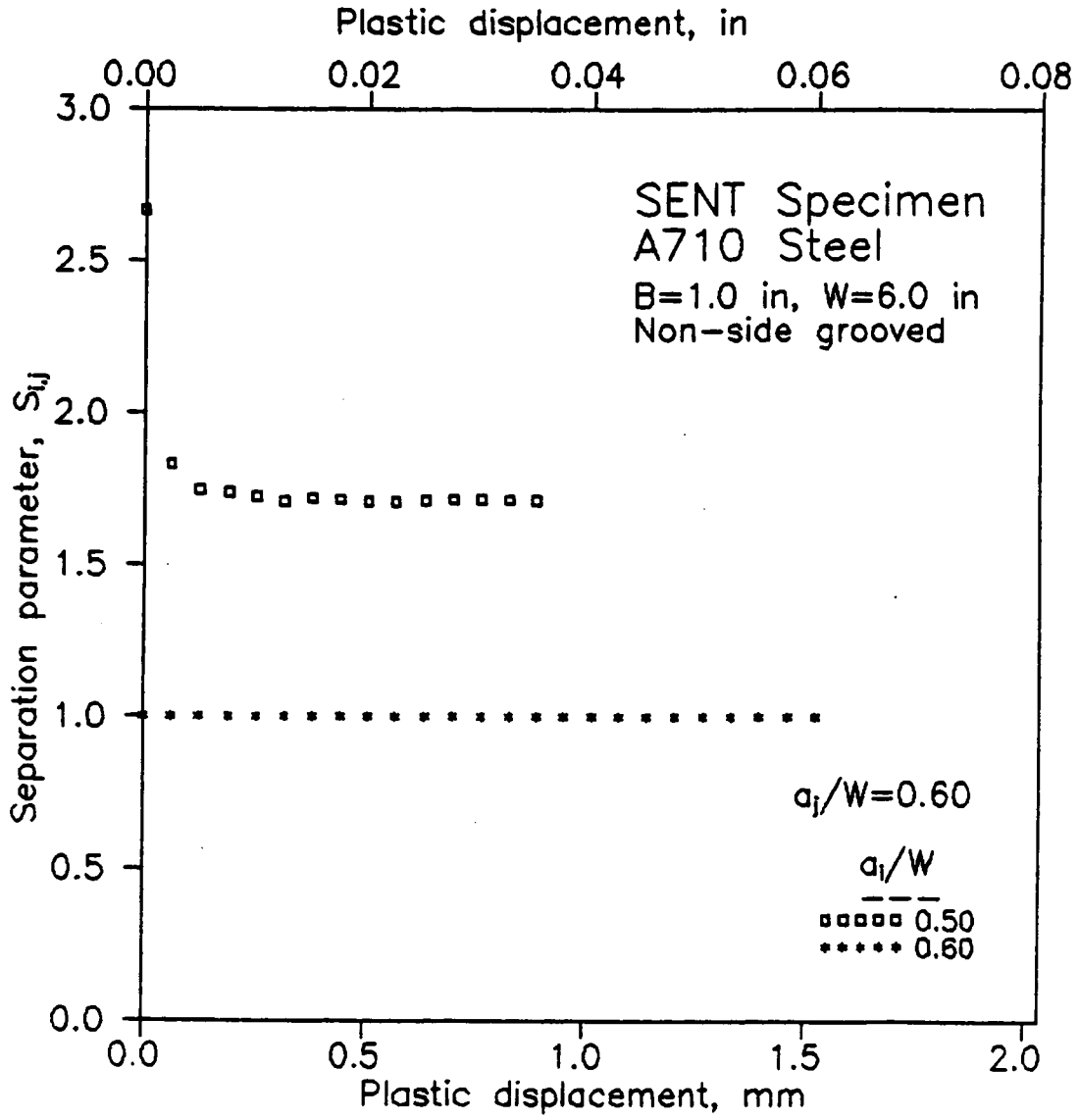


Fig. 2.24 - Separation parameters of the different load-load line displacement test records of the A710 SENT non-side grooved specimens.

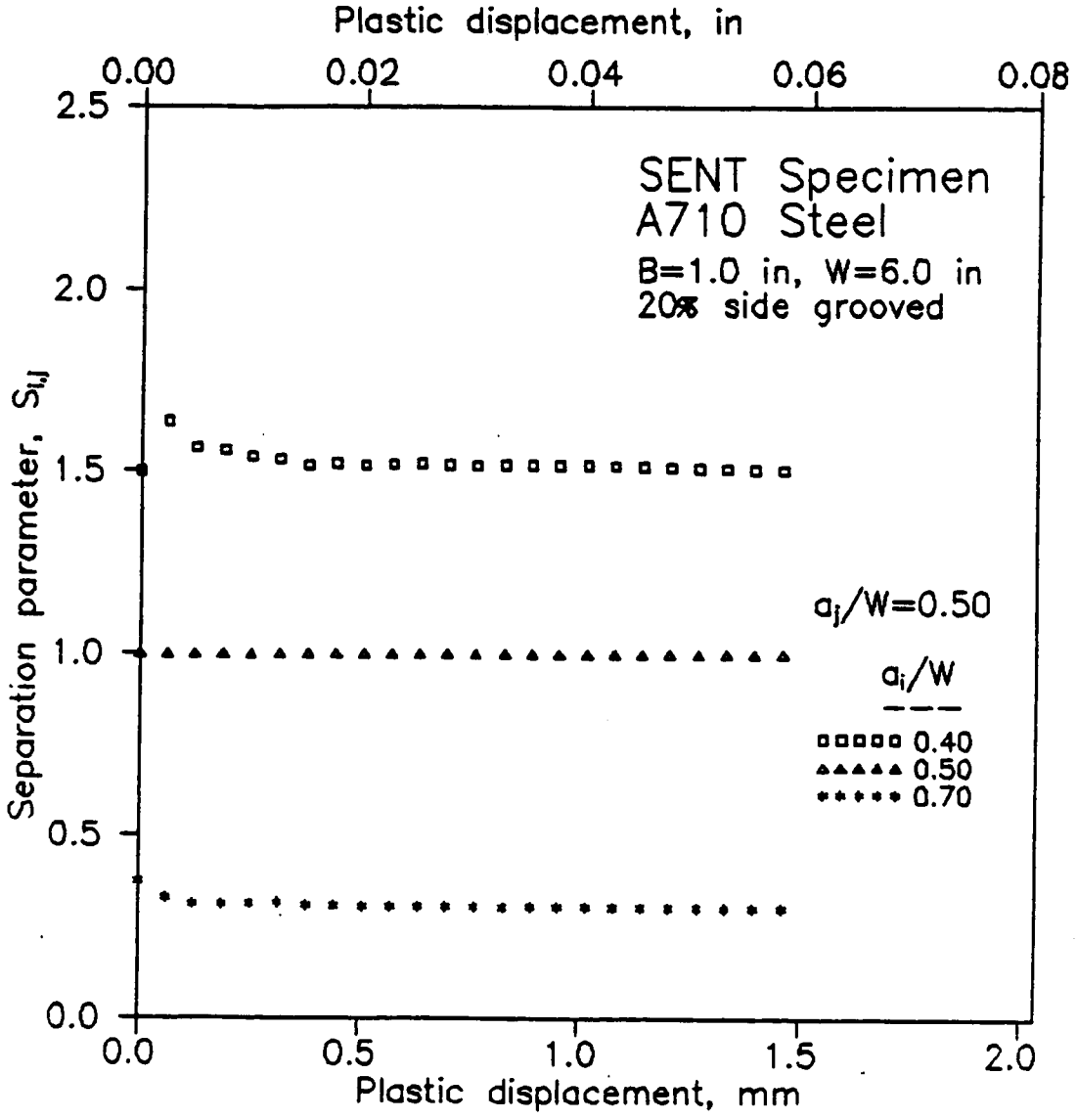


Fig. 2.25 - Separation parameters of the different load-load line displacement test records of the A710 SENT 20% side grooved specimens.

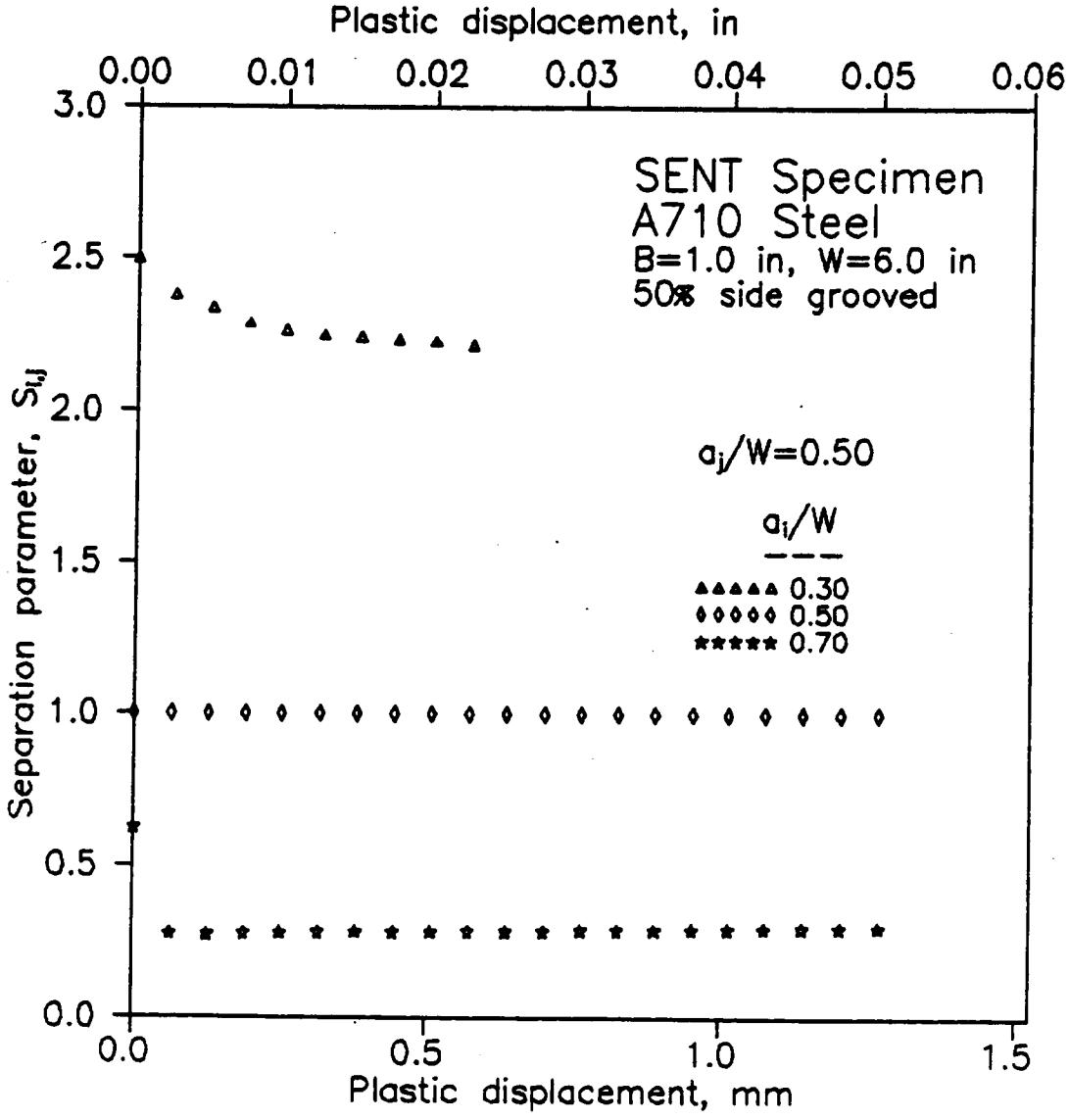


Fig. 2.26 - Separation parameters of the different load-load line displacement test records of the A710 SENT 50% side grooved specimens.

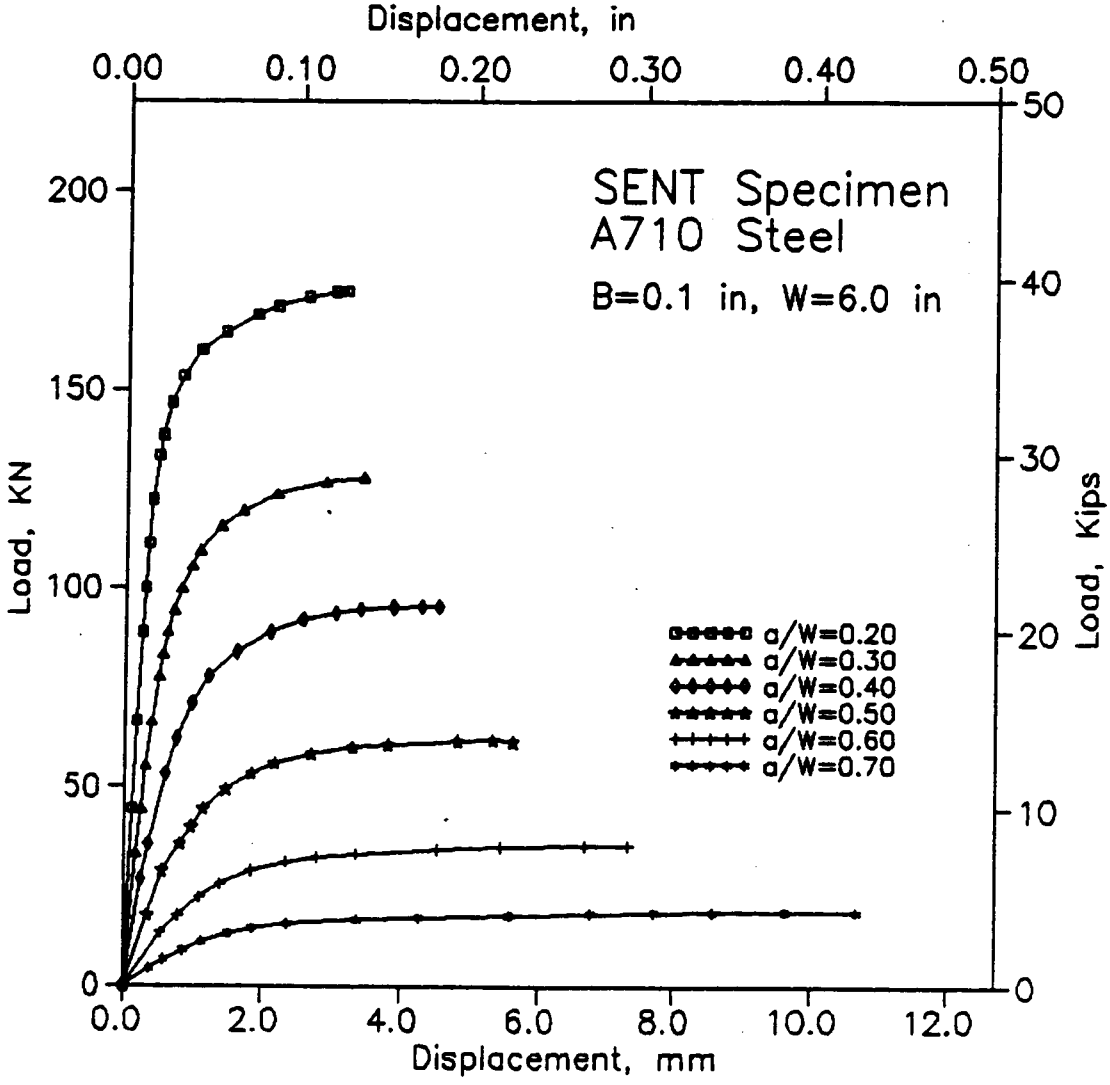


Fig. 2.27 - Load versus crack mouth opening displacement test records of the different A710 SENT thin specimens.

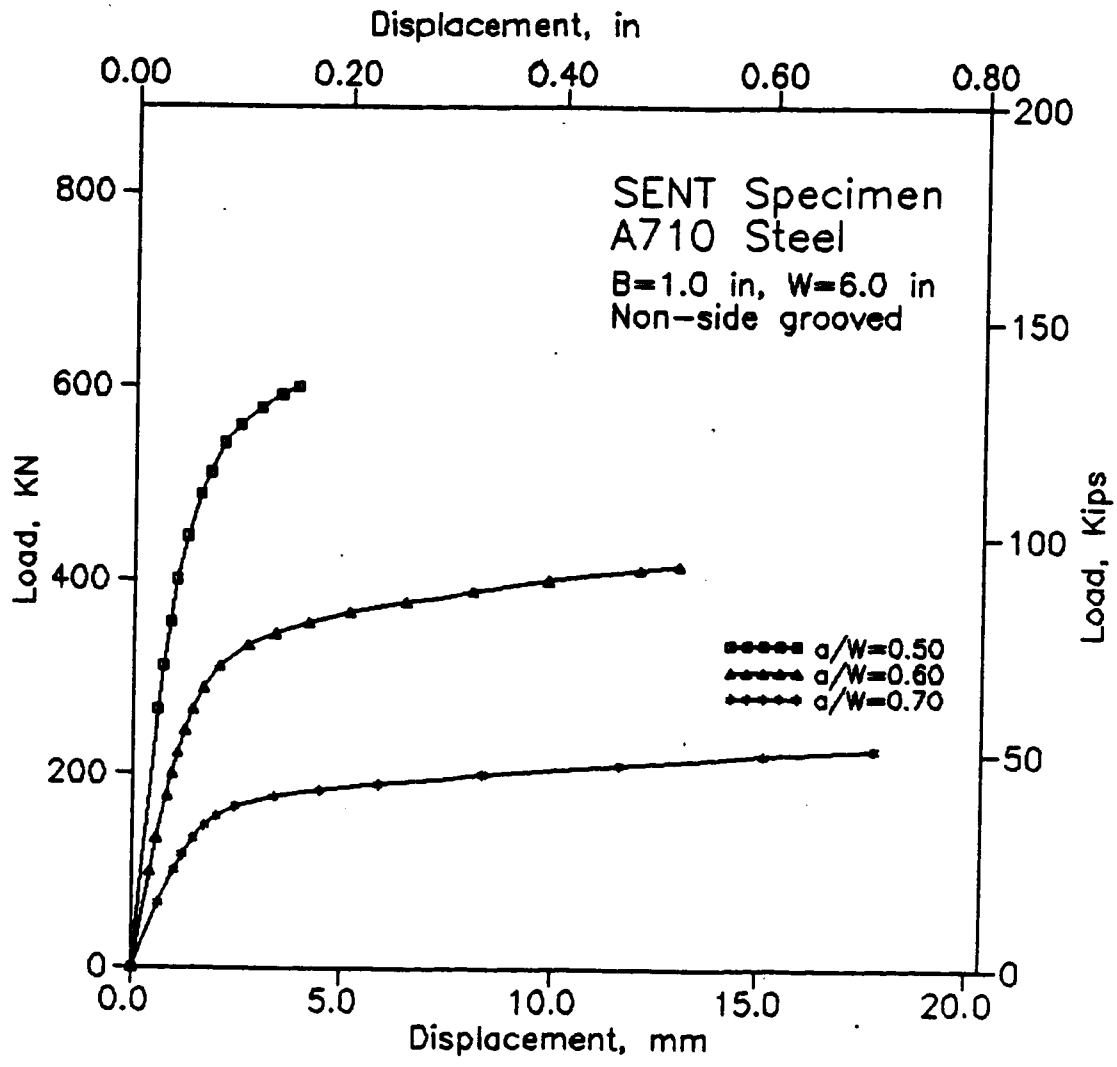


Fig. 2.28 - Load versus crack mouth opening displacement test records of the different A710 SENT 1.0 thick specimens with no side grooving.

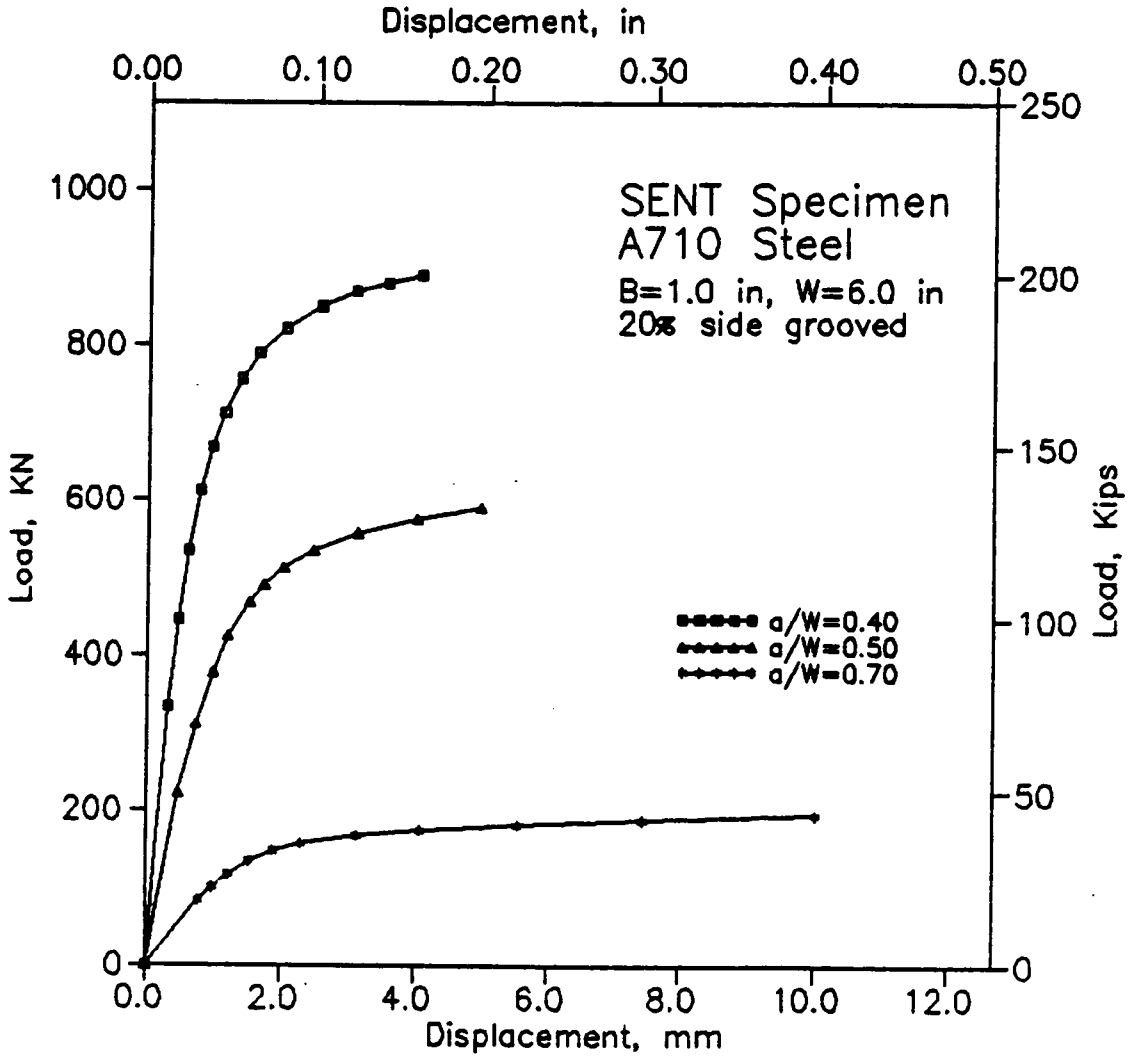


Fig. 2.29 - Load versus crack mouth opening displacement test records of the different A710 SENT 1.0 inch thick specimens with 20% side grooving.

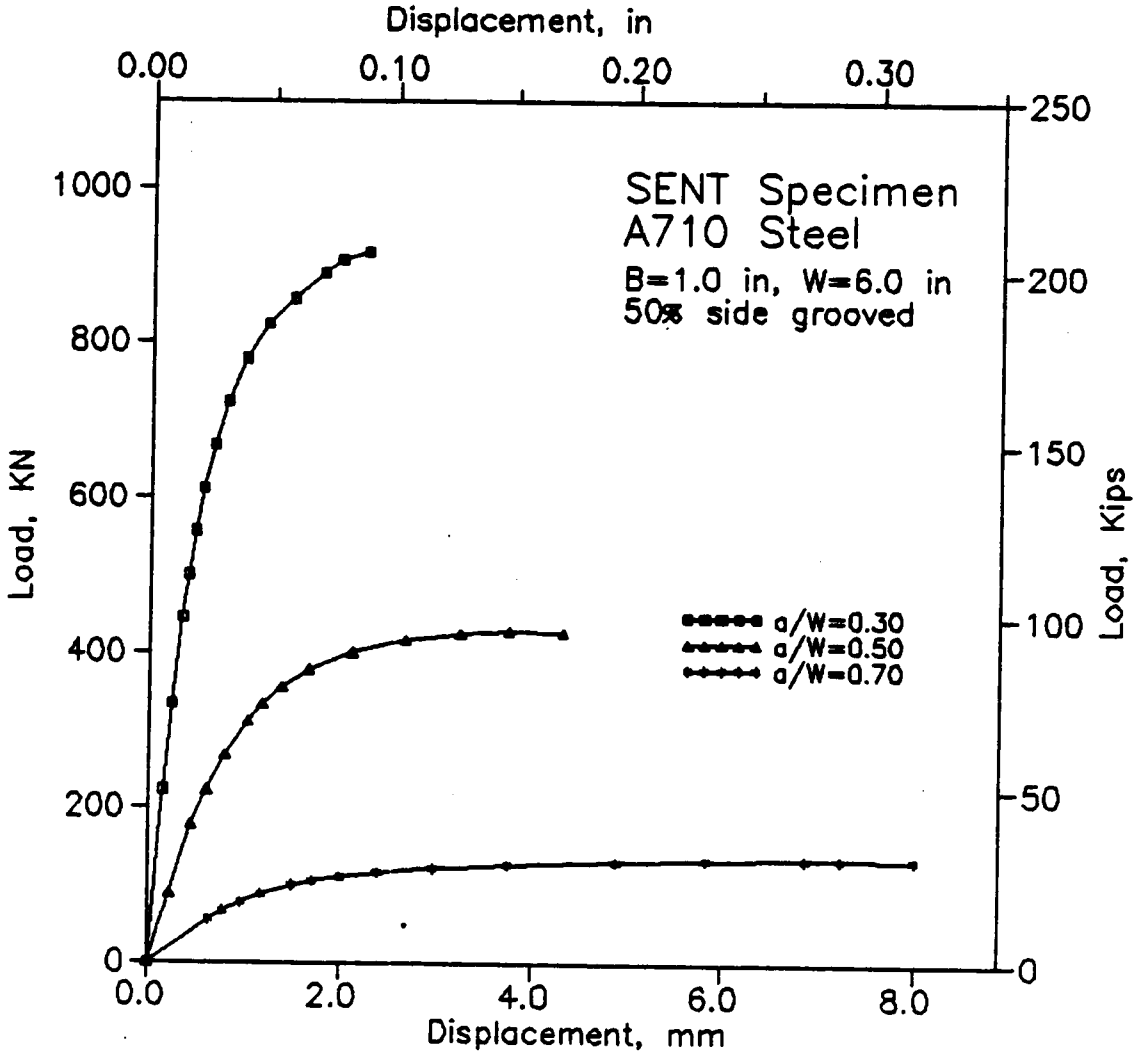


Fig. 2.30 - Load versus crack mouth opening displacement test records of the different A710 SENT 1.0 inch thick specimens with 50% side grooving.

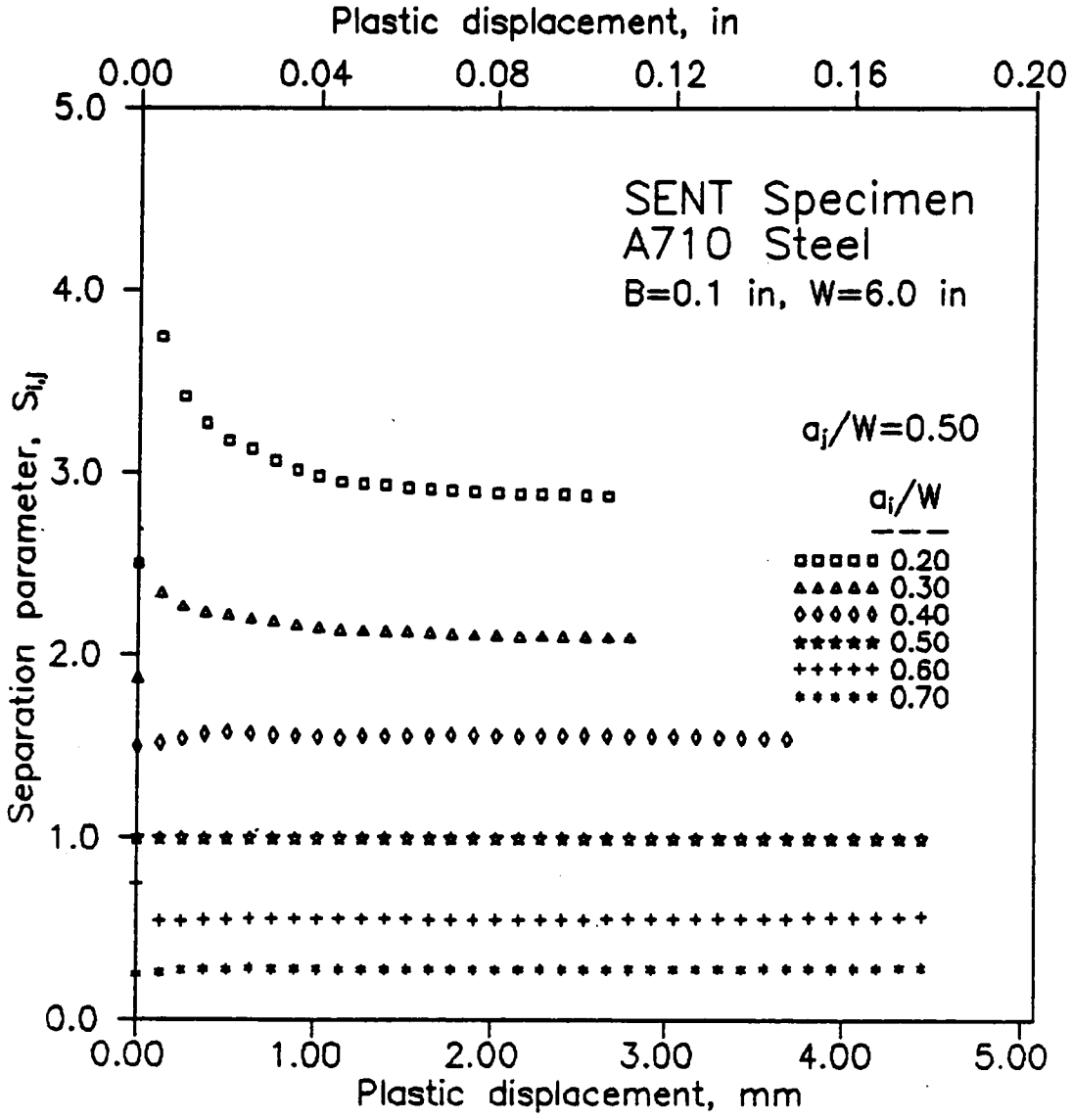


Fig. 2.31 - Separation parameters of the different load-crack mouth opening displacement test records of the A710 SENT thin specimens.

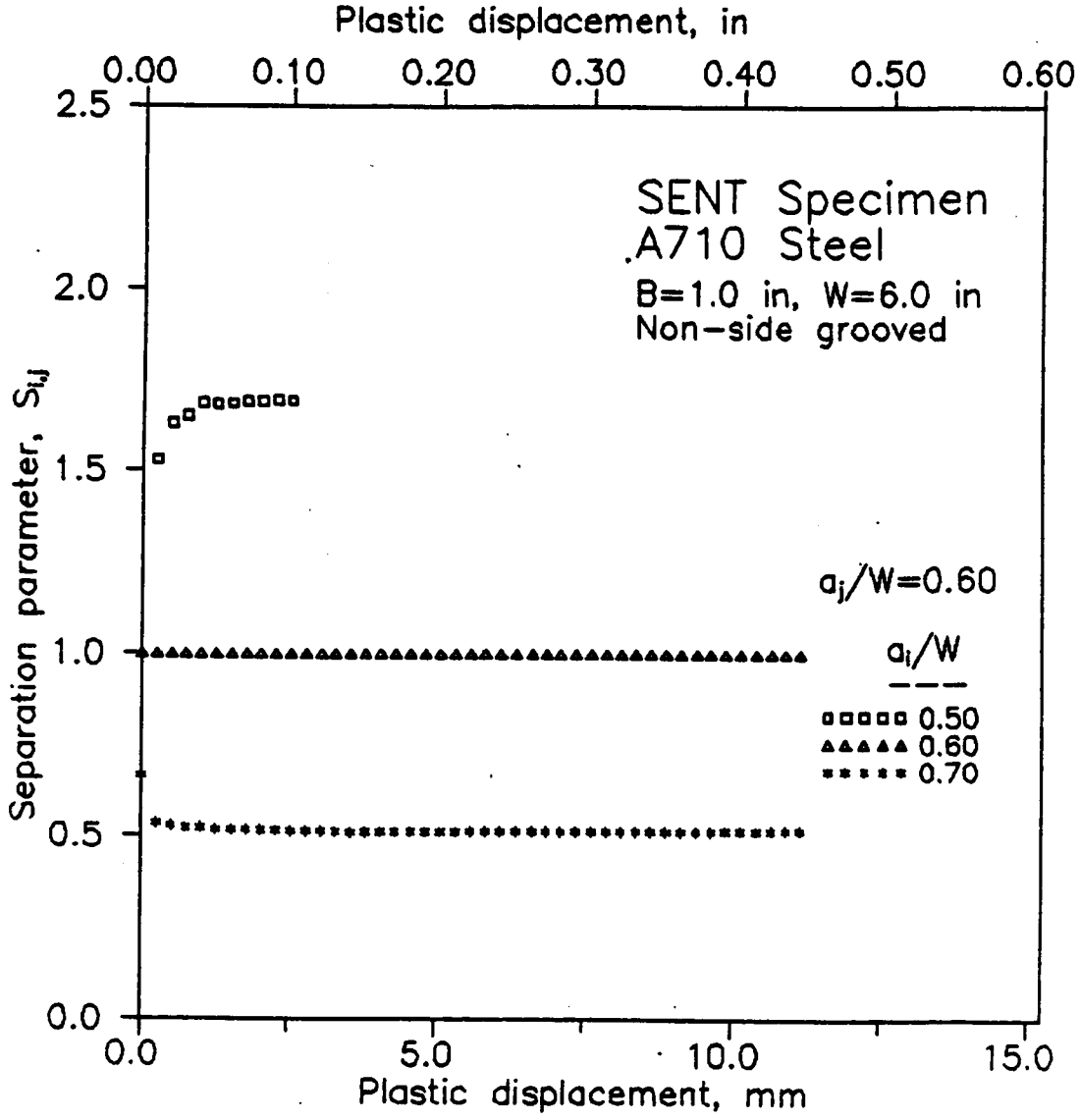


Fig. 2.32 - Separation parameters of the different load-crack mouth opening displacement test records of the A710 SENT 1.0 inch thick specimens with no side grooving.

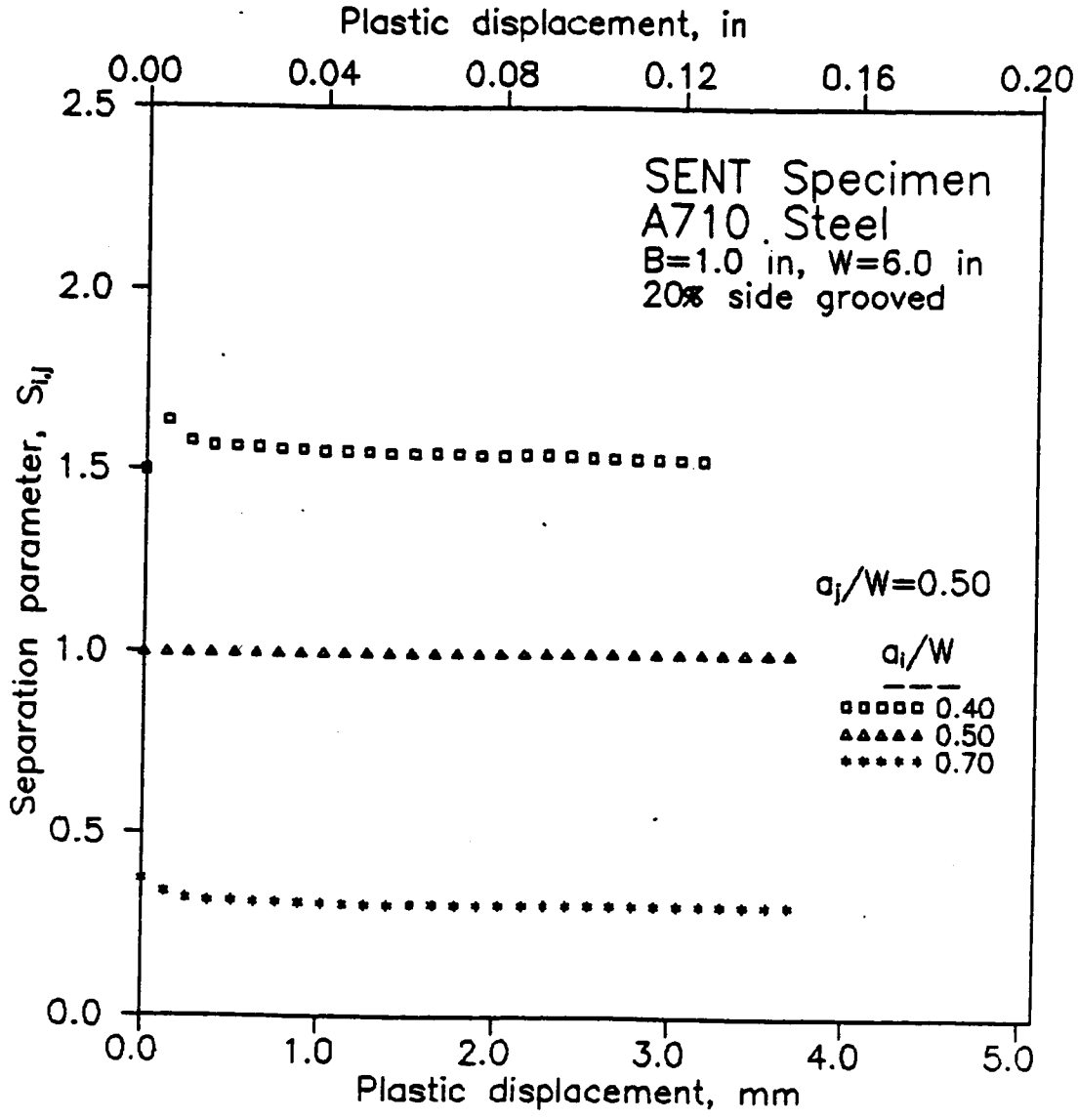


Fig. 2.33 - Separation parameters of the different load-crack mouth opening displacement test records of the A710 SENT 1.0 inch thick specimens with 20% side grooving.

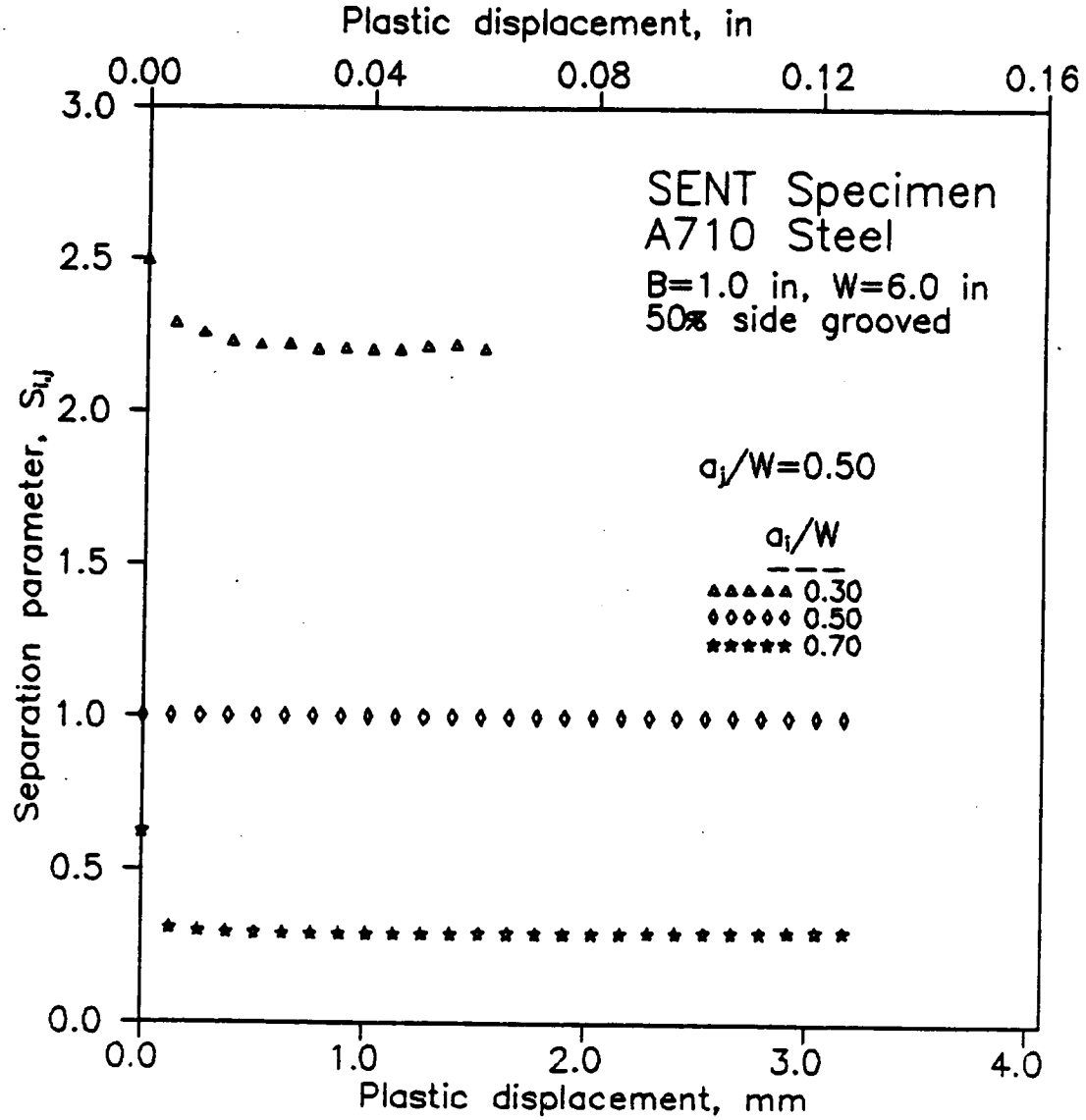


Fig. 2.34 - Separation parameters of the different load-crack mouth opening displacement test records of the A710 SENT 1.0 inch thick specimens with 50% side grooving.

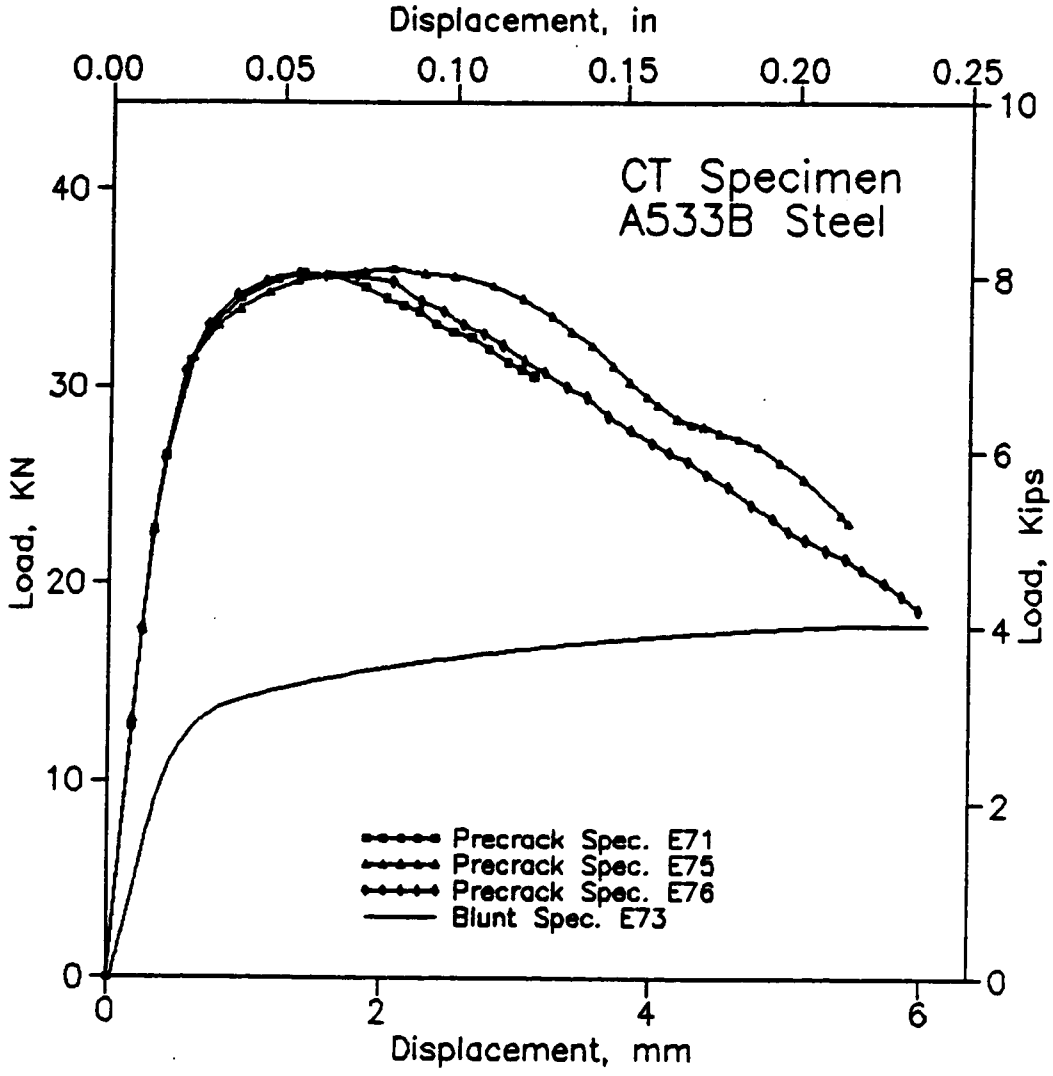


Fig. 2.35 - Load versus load line displacement test records of three precracked and one blunt notched A533B compact specimens.

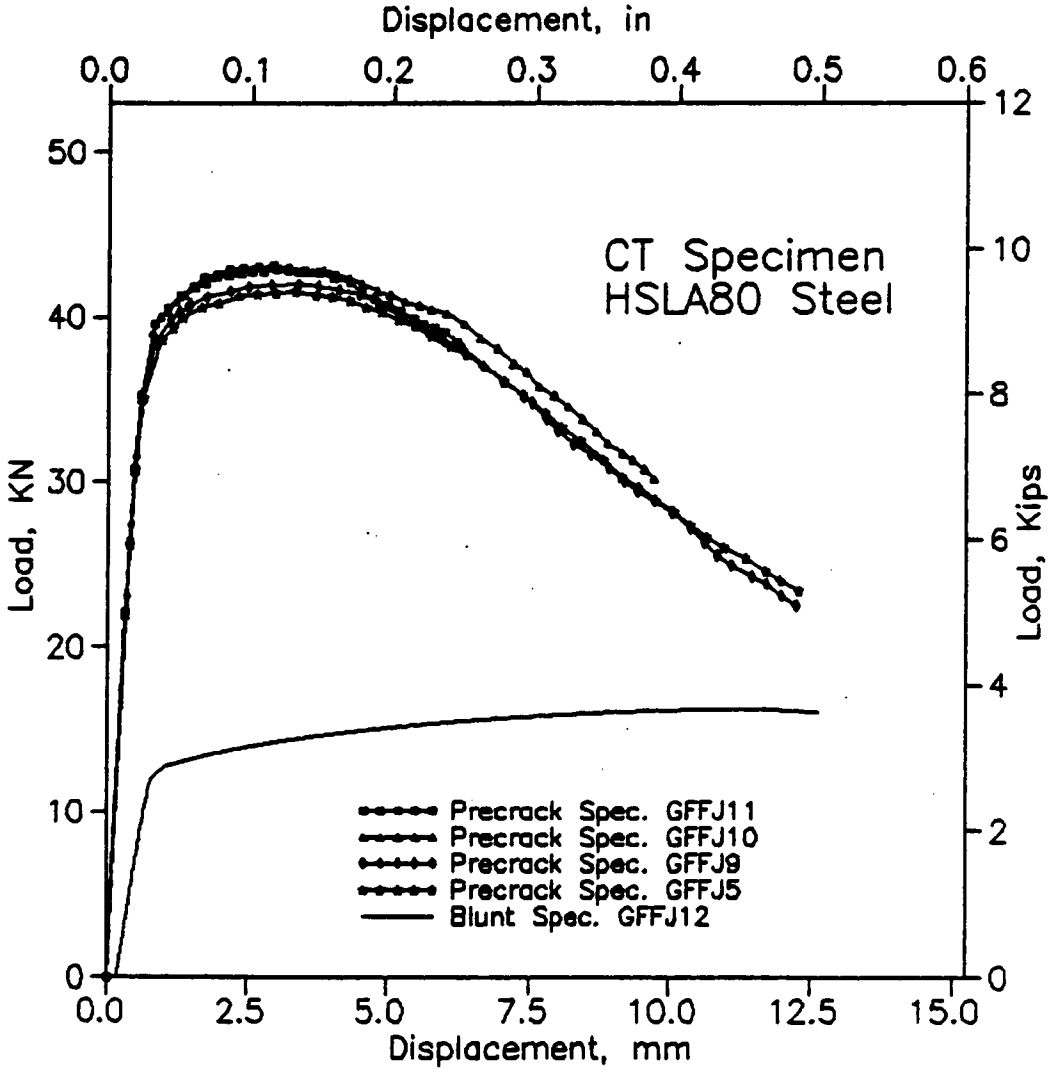


Fig. 2.36 - Load versus load line displacement test records of four precracked and one blunt notched HSLA80 compact specimens.

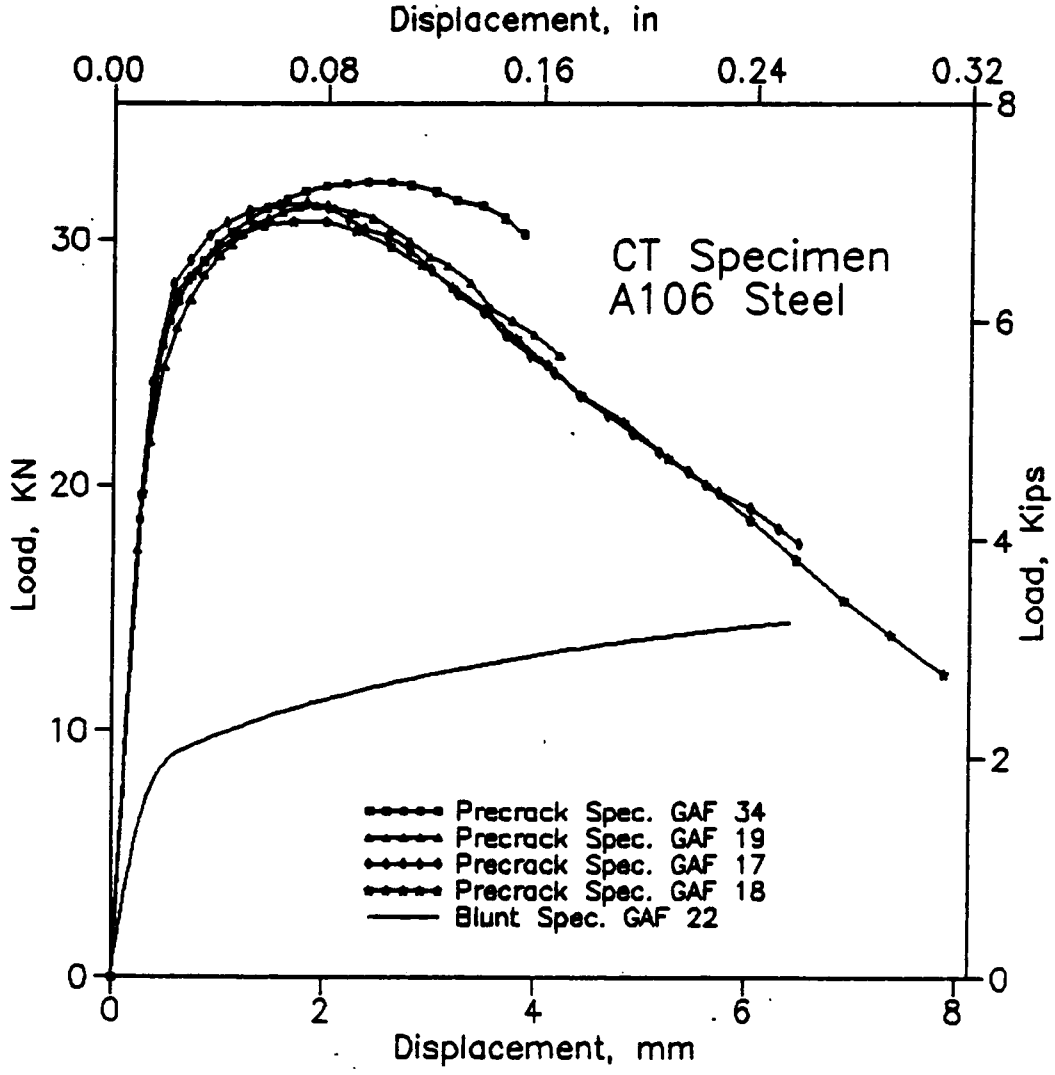


Fig. 2.37 - Load versus load line displacement test records of four precracked and one blunt notched A106 compact specimens.

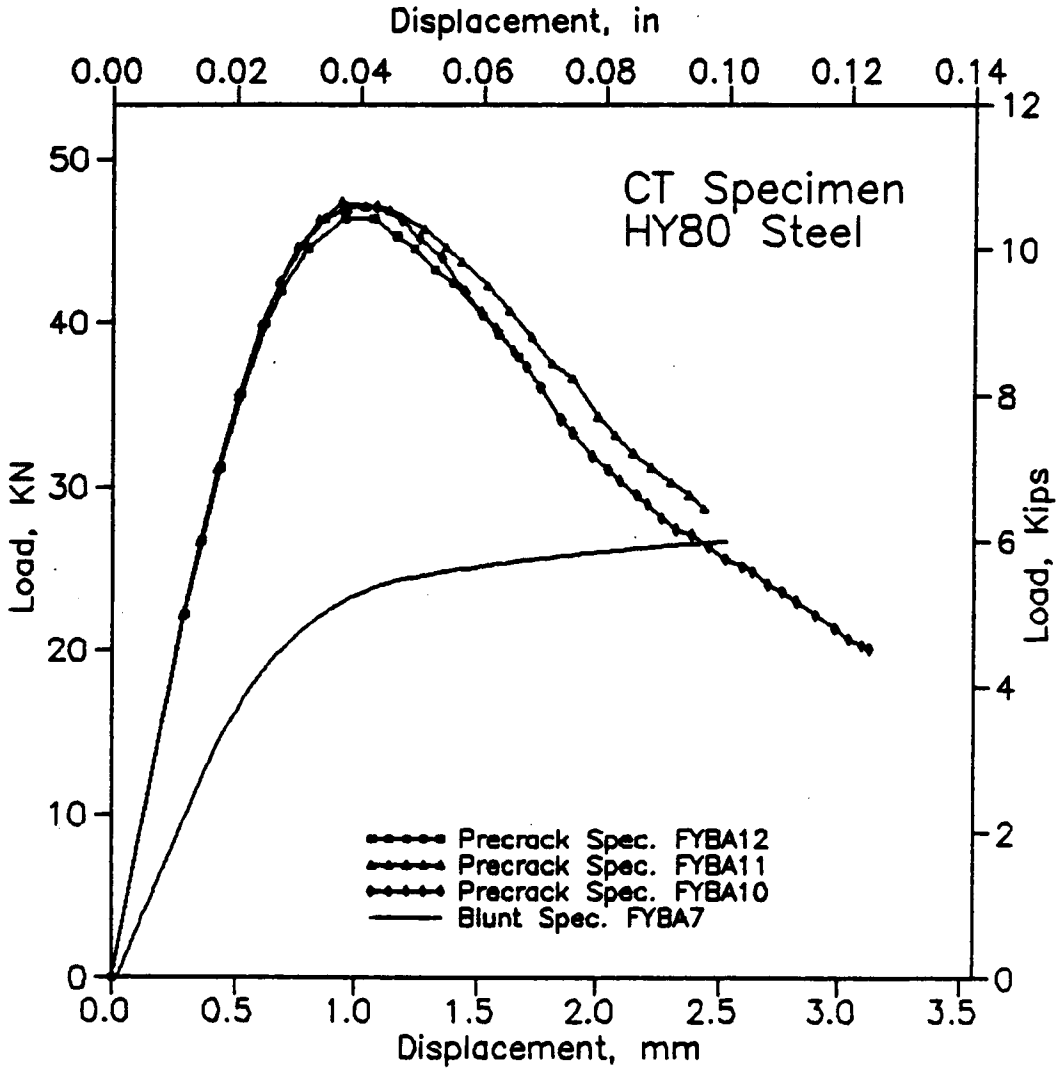


Fig. 2.38 - Load versus load line displacement test records of three precracked and one blunt notched HY80 compact specimens.

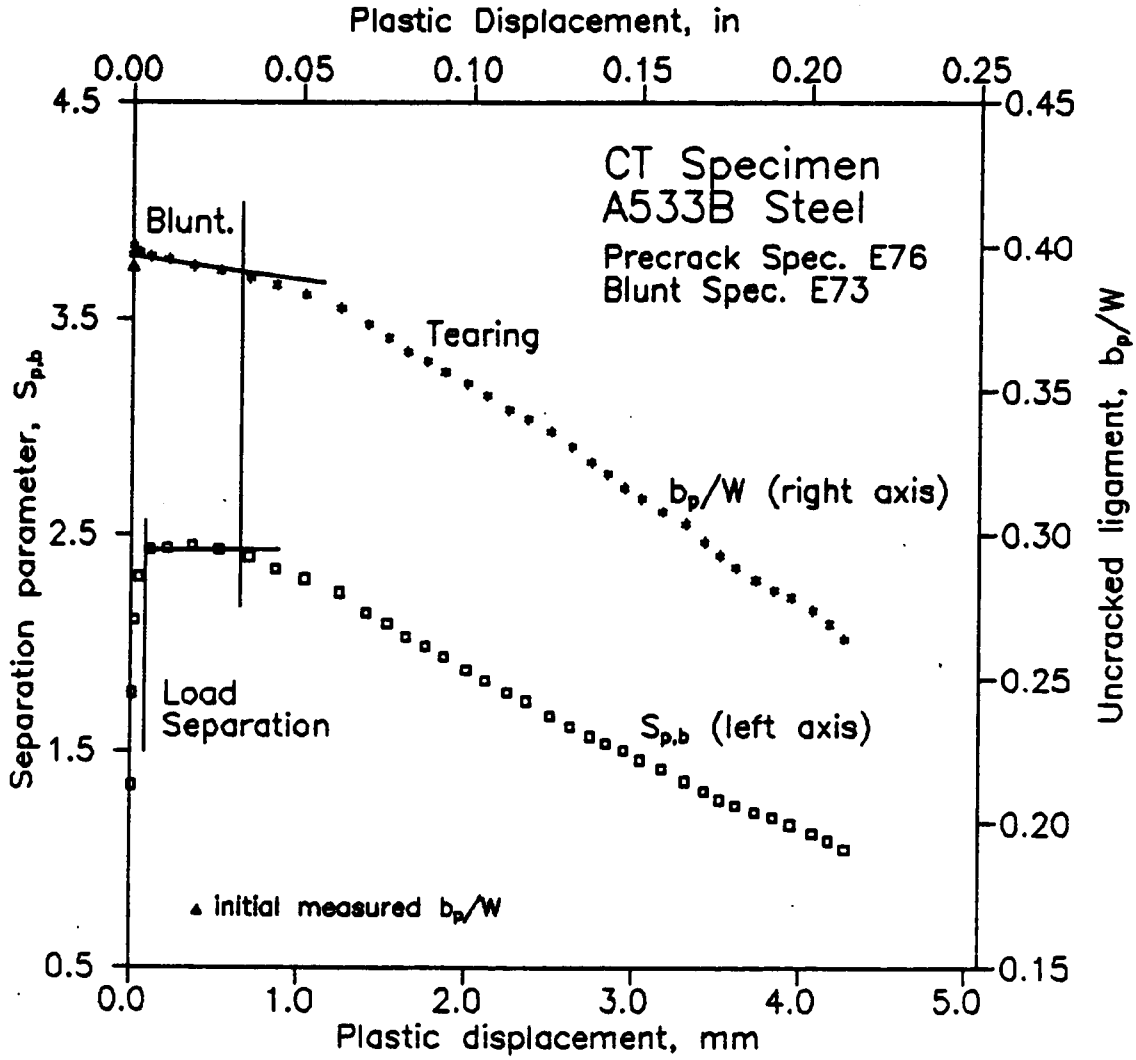


Fig. 2.39 - Variation of separation parameter and uncracked ligament of an A533B precracked specimen with respect to plastic displacement.

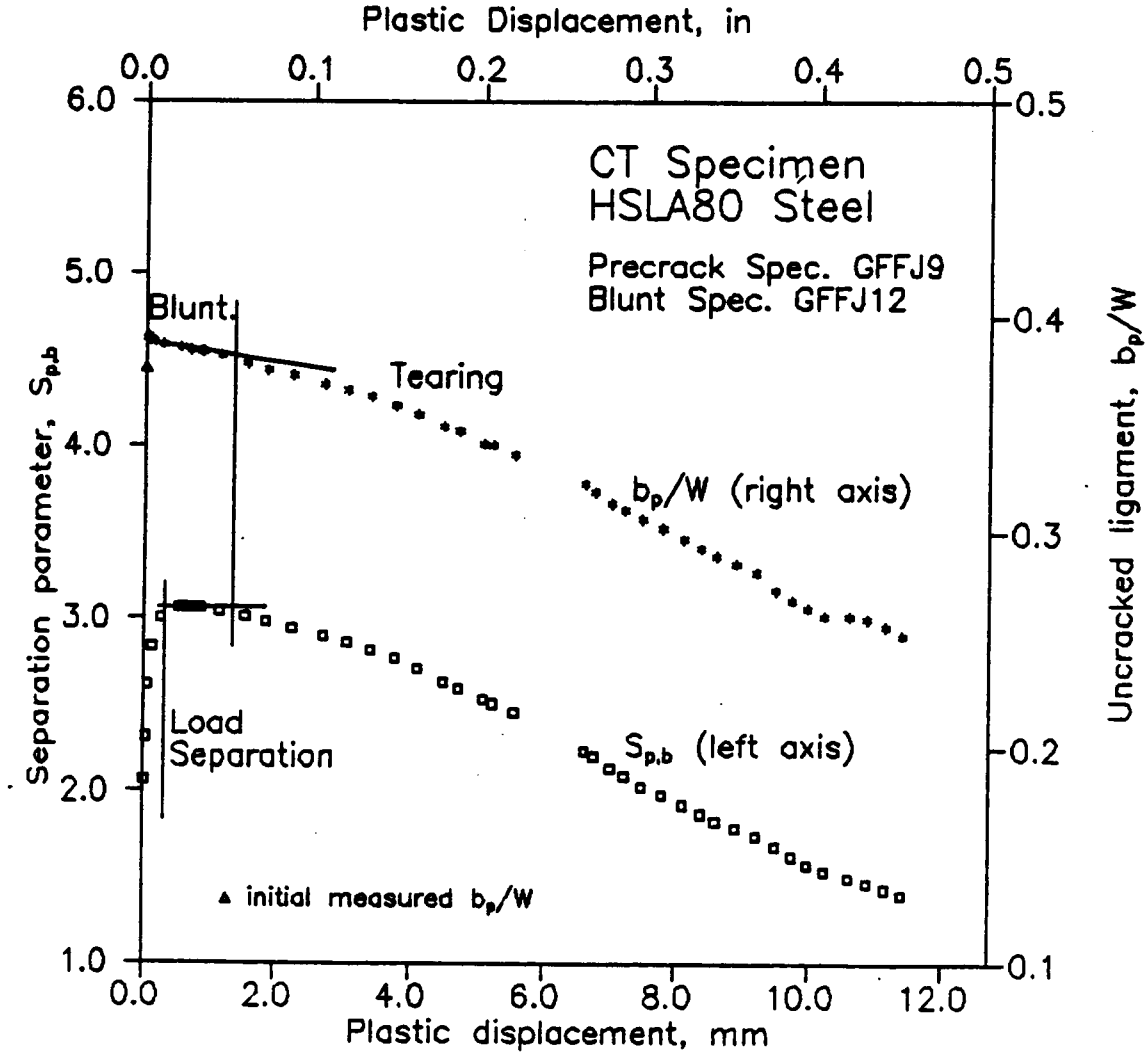


Fig. 2.40 - Variation of separation parameter and uncracked ligament of an HSLA80 precracked specimen with respect to plastic displacement.

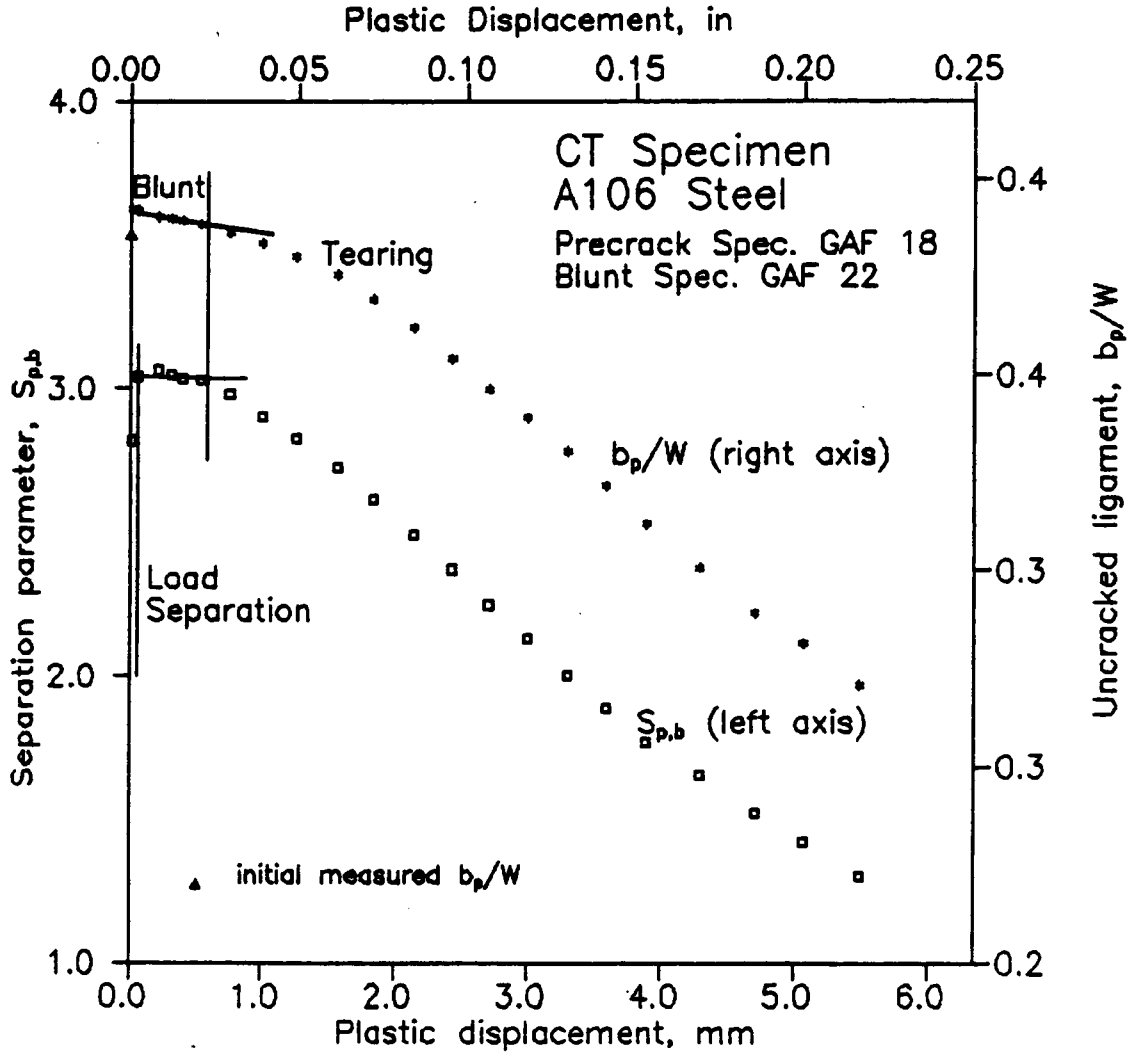


Fig. 2.41 - Variation of separation parameter and uncracked ligament of an A106 precracked specimen with respect to plastic displacement.

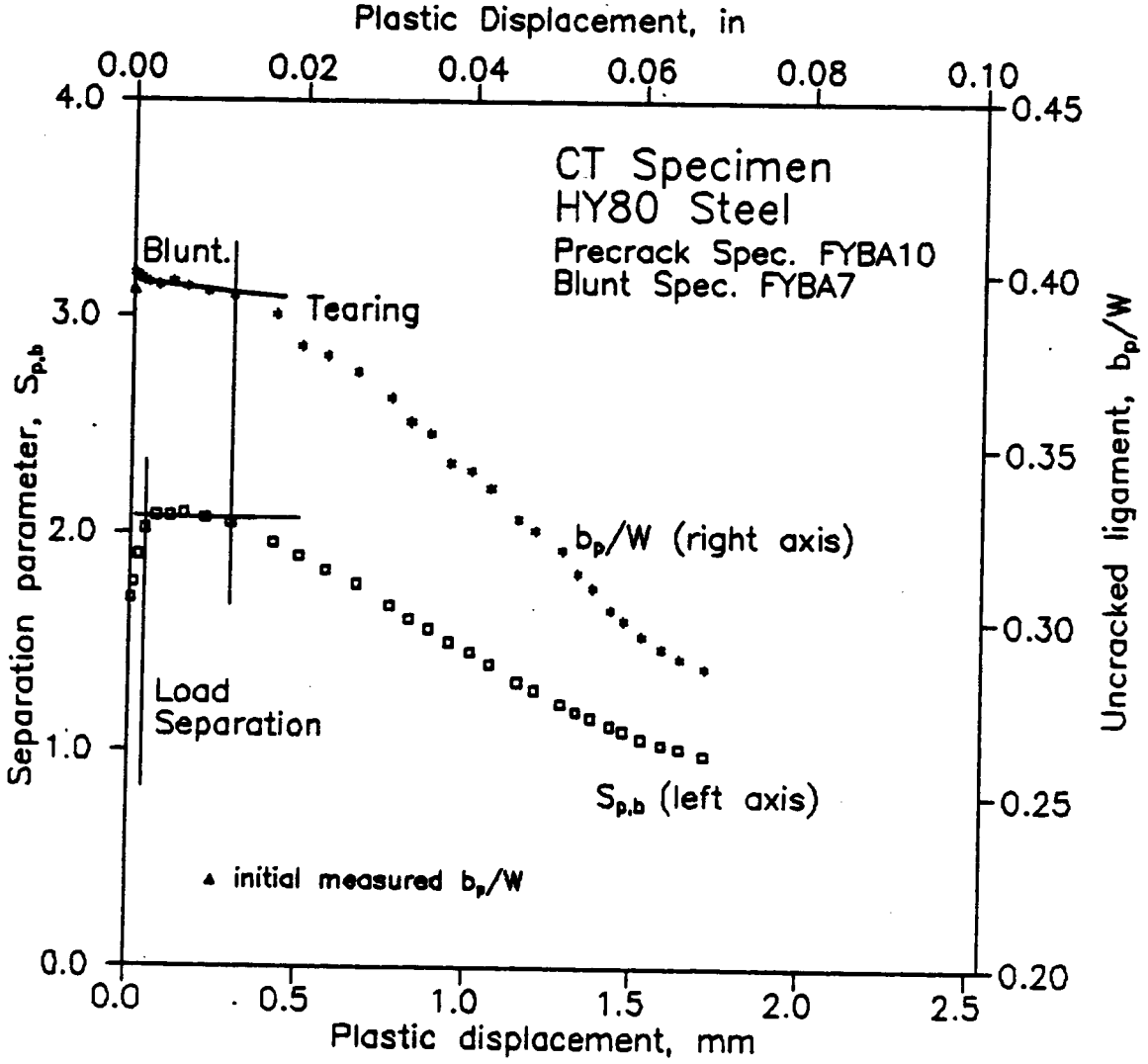


Fig. 2.42 - Variation of separation parameter and uncracked ligament of an HY80 precracked specimen with respect to plastic displacement.

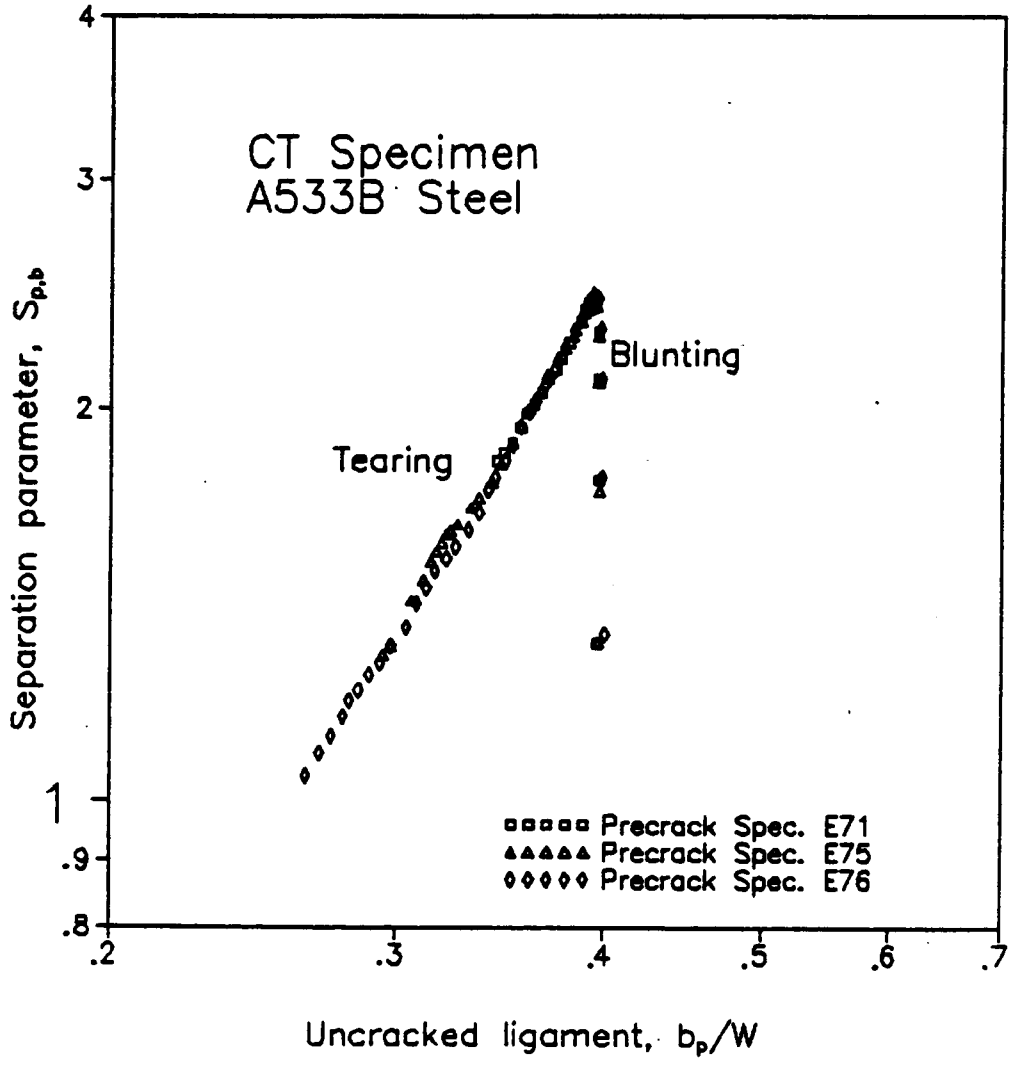


Fig. 2.43 - Variation of separation parameters of the different A533B precracked specimens test records with respect to uncracked ligament.

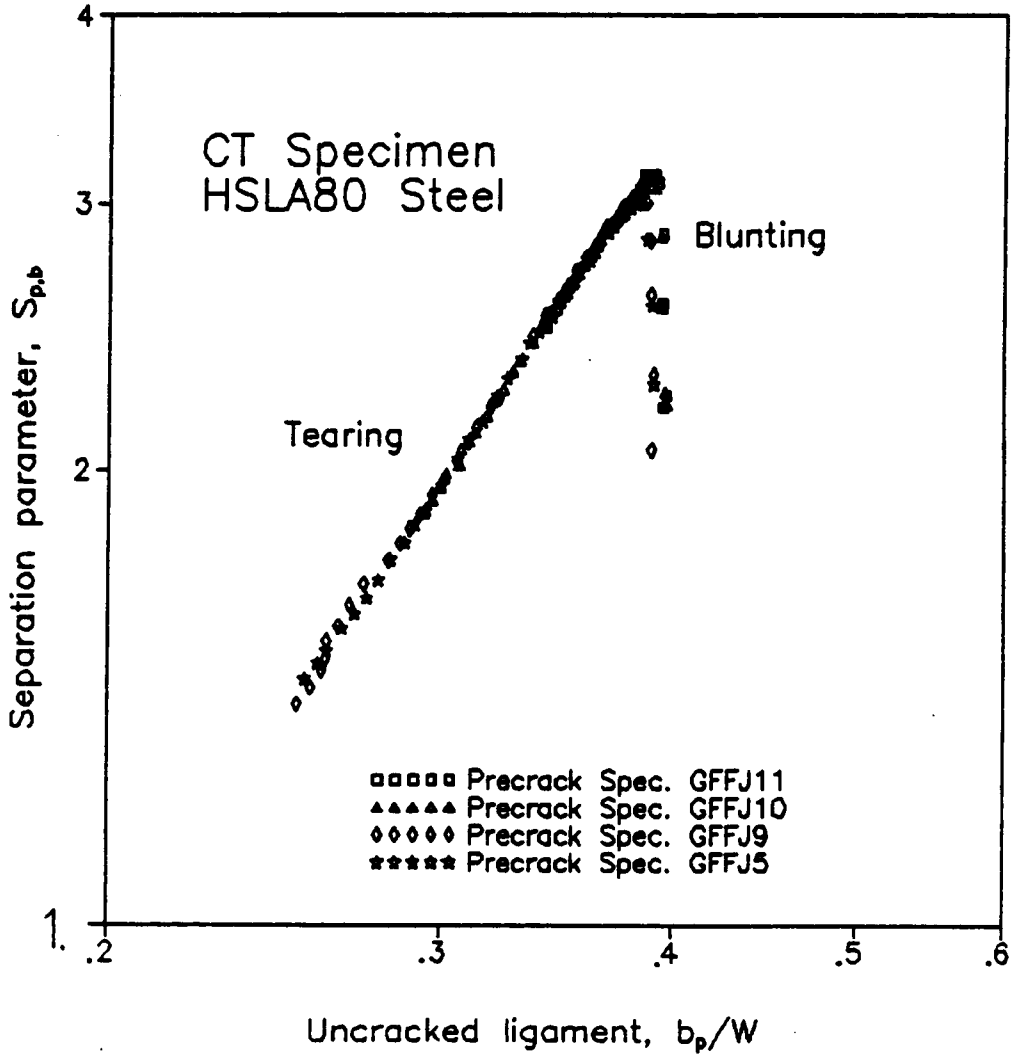


Fig. 2.44 - Variation of separation parameters of the different HSLA80 precracked specimens test records with respect to uncracked ligament.

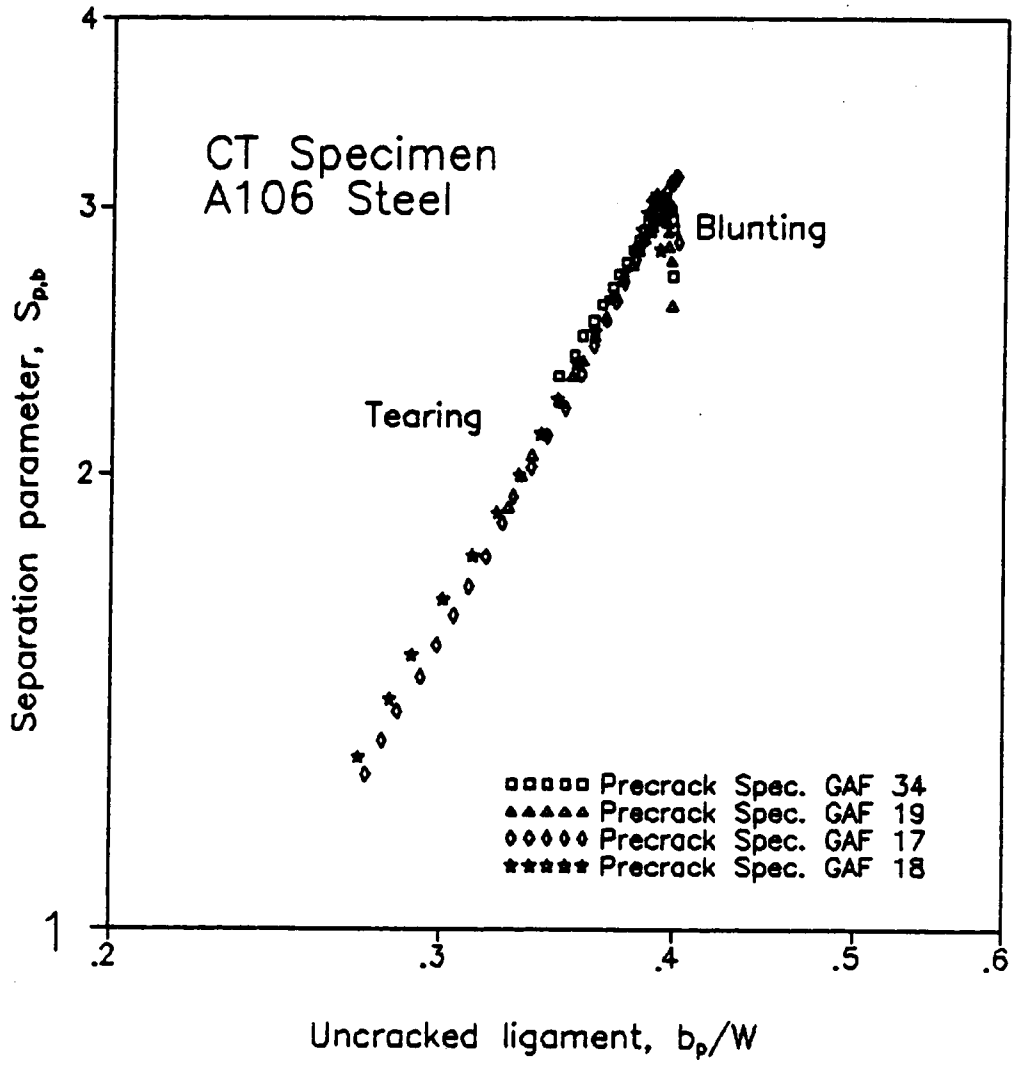


Fig. 2.45 - Variation of separation parameters of the different A106 precracked specimens test records with respect to uncracked ligament.

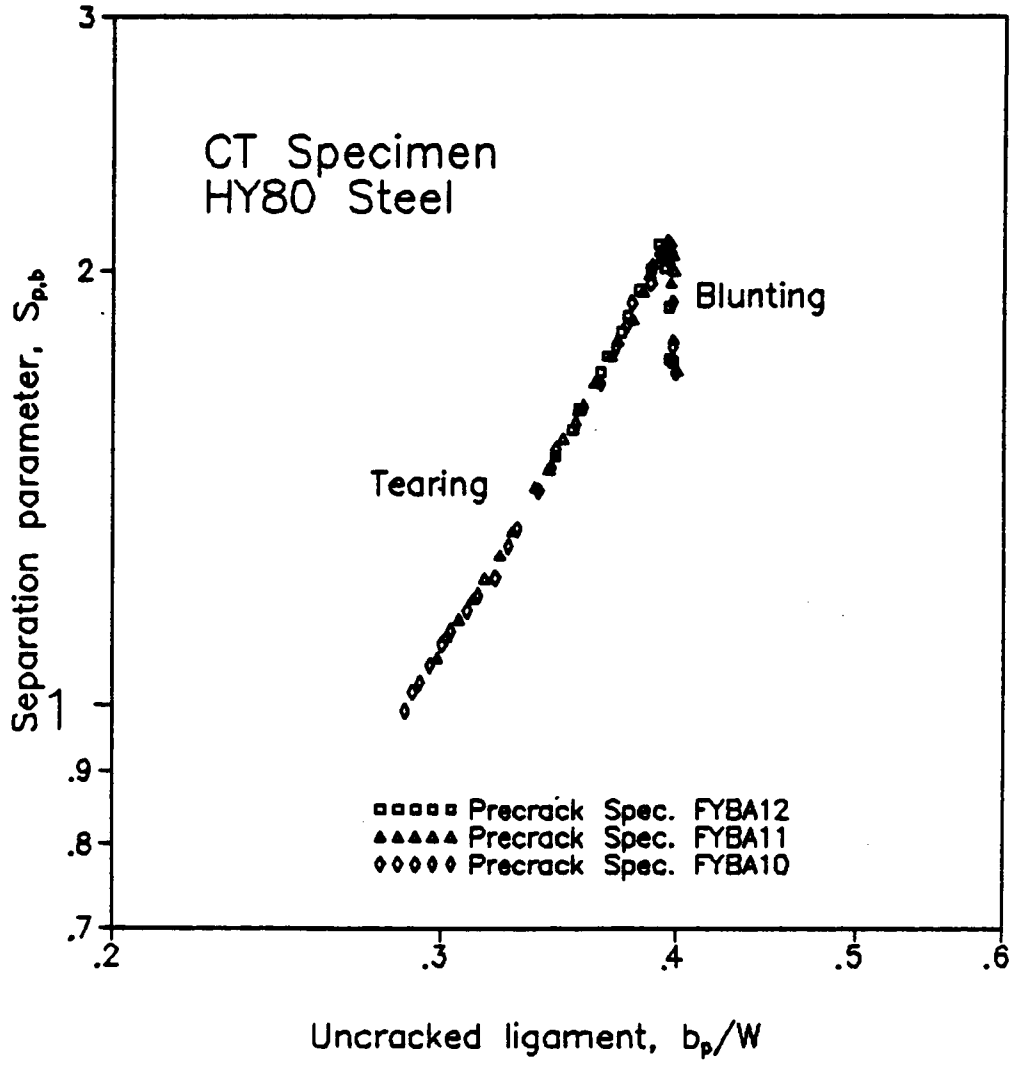


Fig. 2.46 - Variation of separation parameters of the different HY80 precracked specimens test records with respect to uncracked ligament.

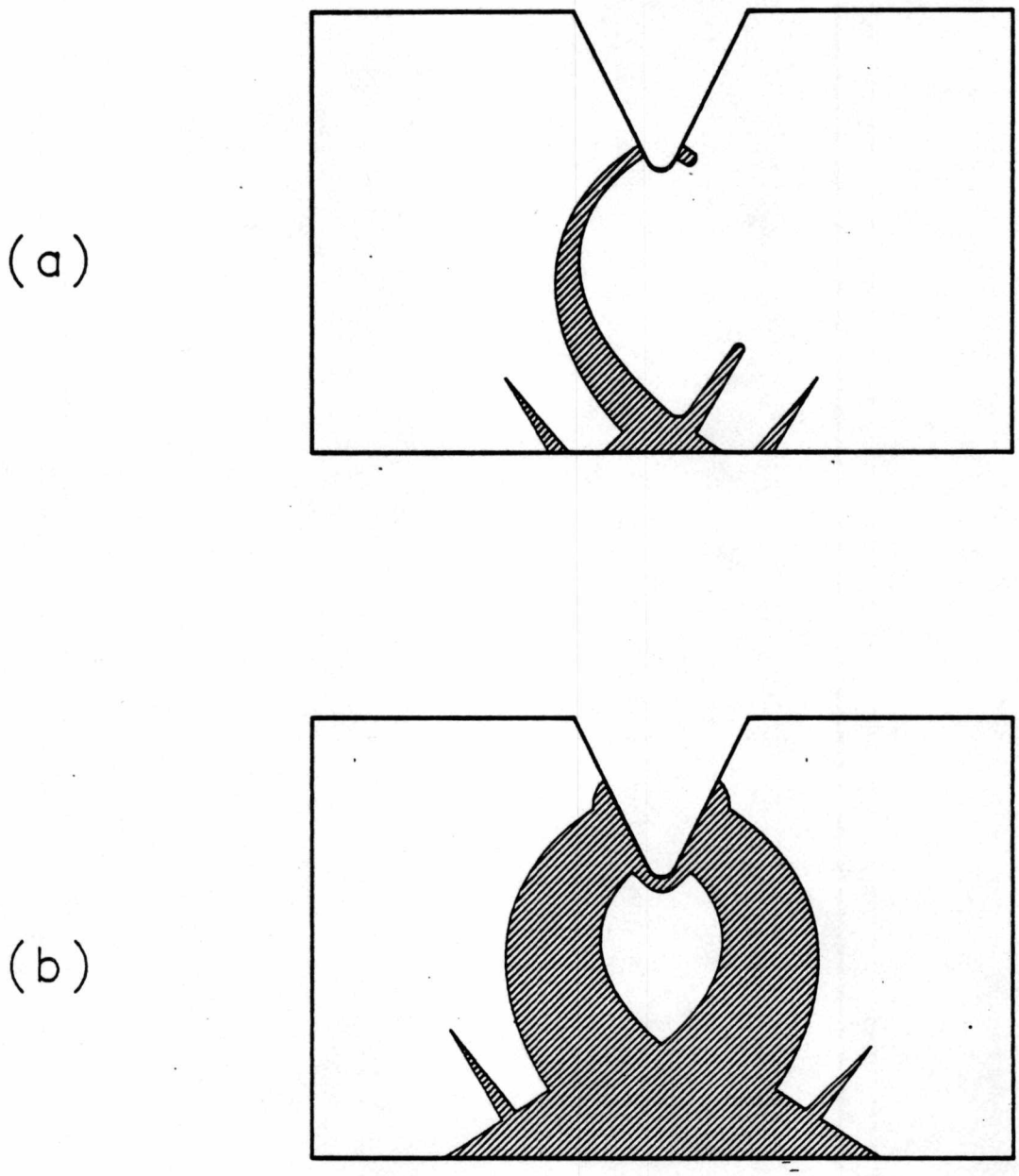


Fig. 2.47 - Schematic drawings of plastic pattern developed in four point bend test; (a) slightly past the yield point, (b) well past the yield point.

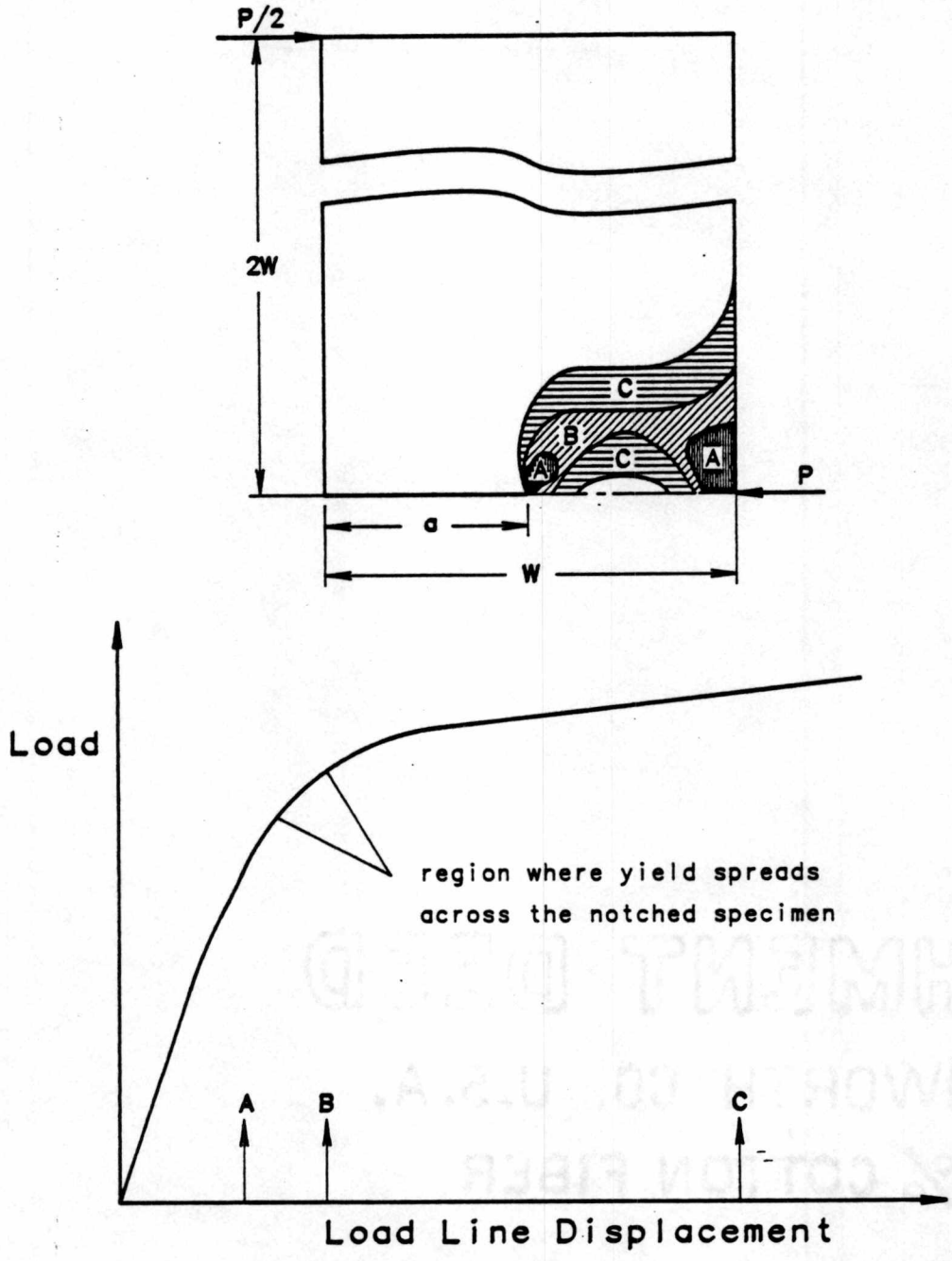


Fig. 2.48 - Schematic drawings of the yielded regions in bend specimen (a/W = 0.5) of non-work hardening material and the corresponding points in the load-load line displacement record.

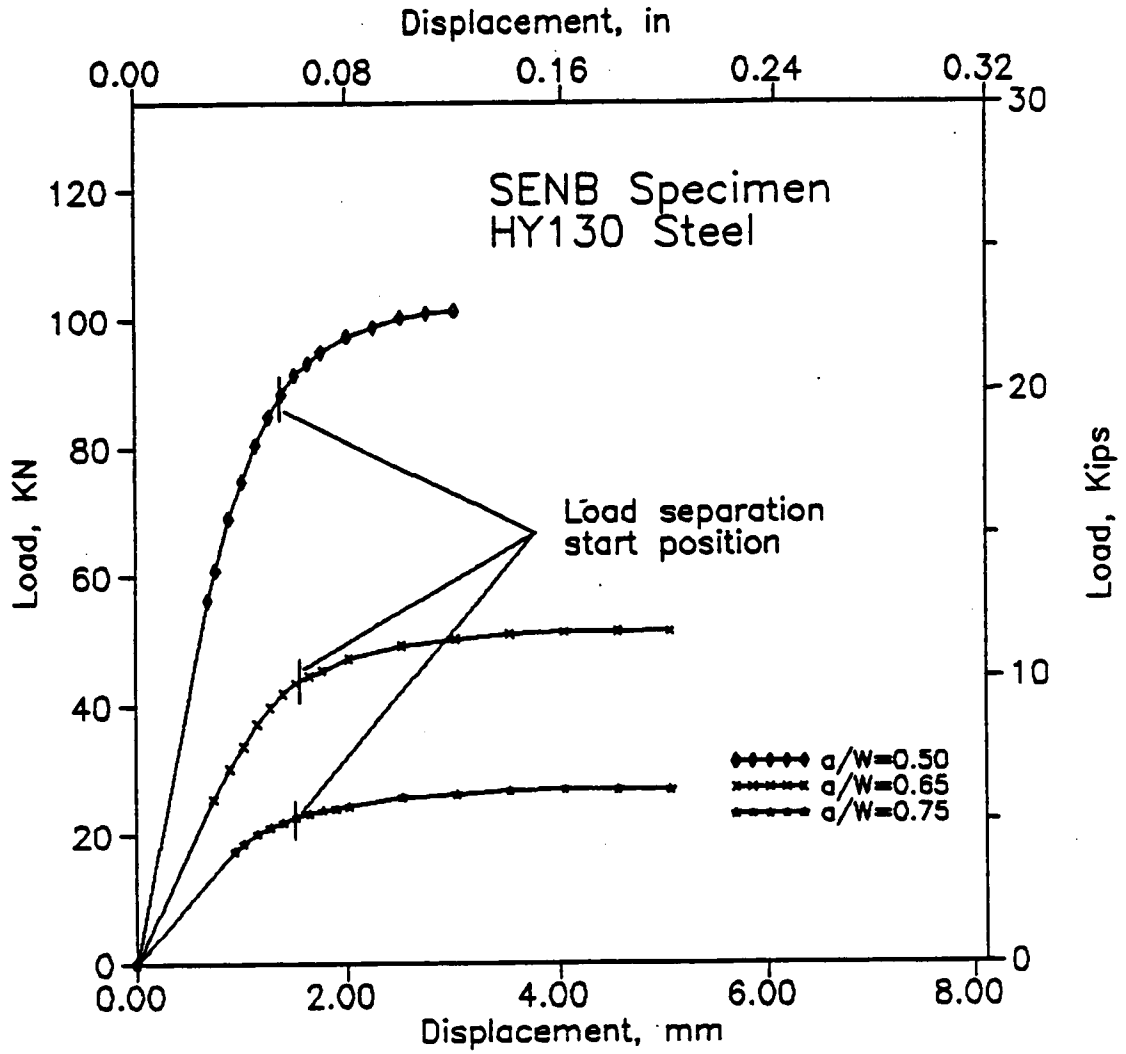


Fig. 2.49 - Position at which load separation starts in test records of three HY130 SENB specimens.

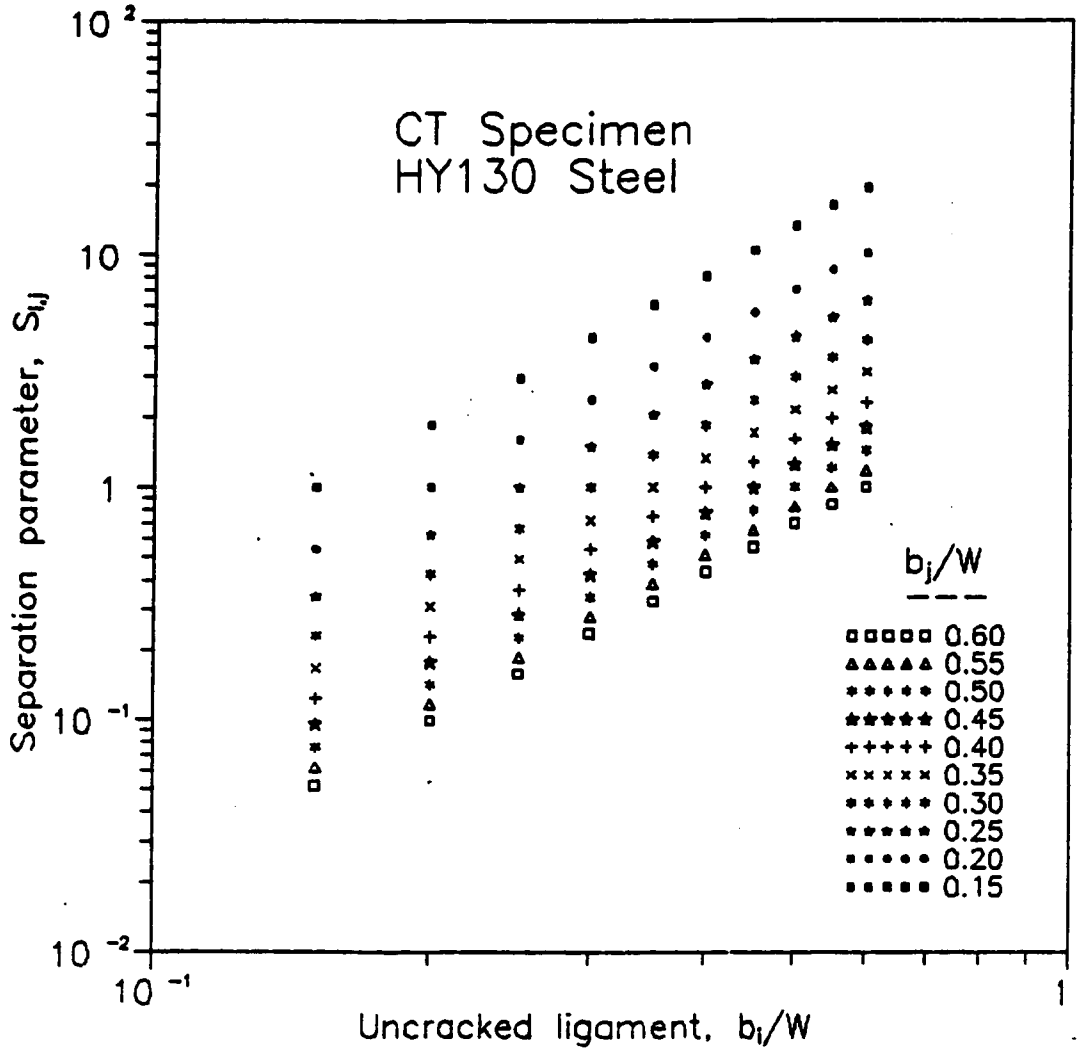


Fig. 3.1 - Variation of the separation parameters, $S_{i,j}$, with respect to uncracked ligament, b_i/W, on logarithmic coordinates for the HY130 CT set.

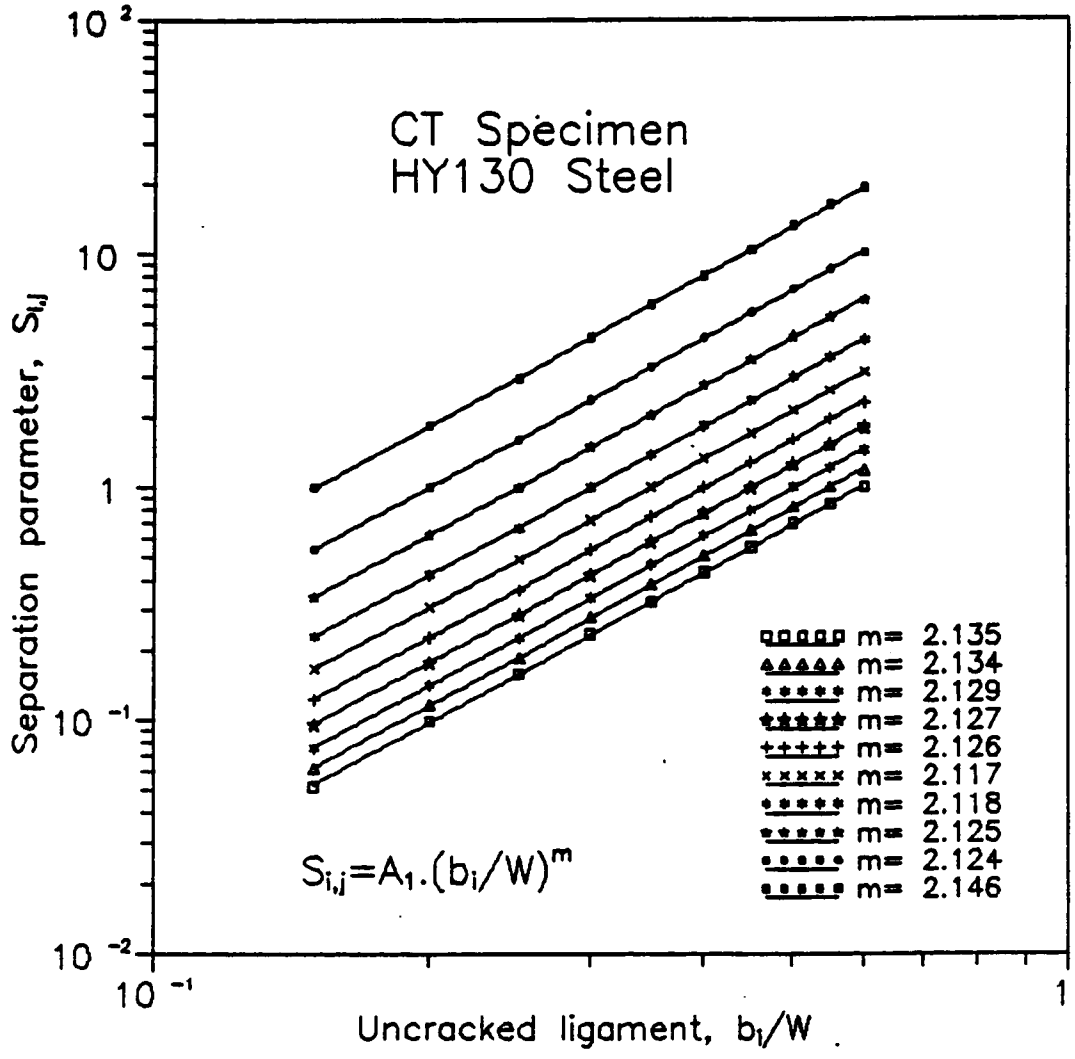


Fig. 3.2 - Power law fit of the $S_{i,j}$ versus b_i/W records for the HY130 CT set.

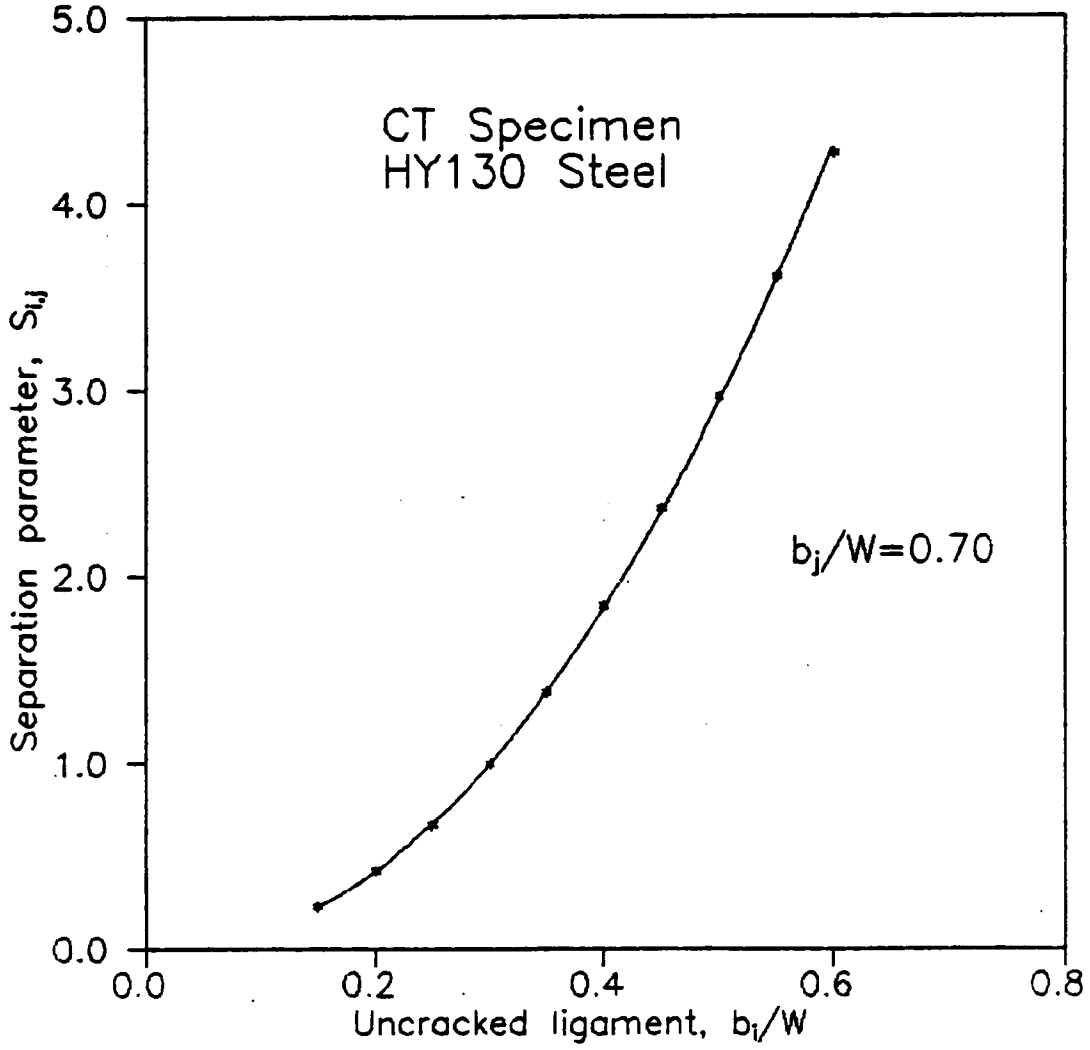


Fig. 3.3 - Sample of the power law fit of one of the $\bar{S}_{i,j}$ versus b_i/W records in the HY130 CT set.

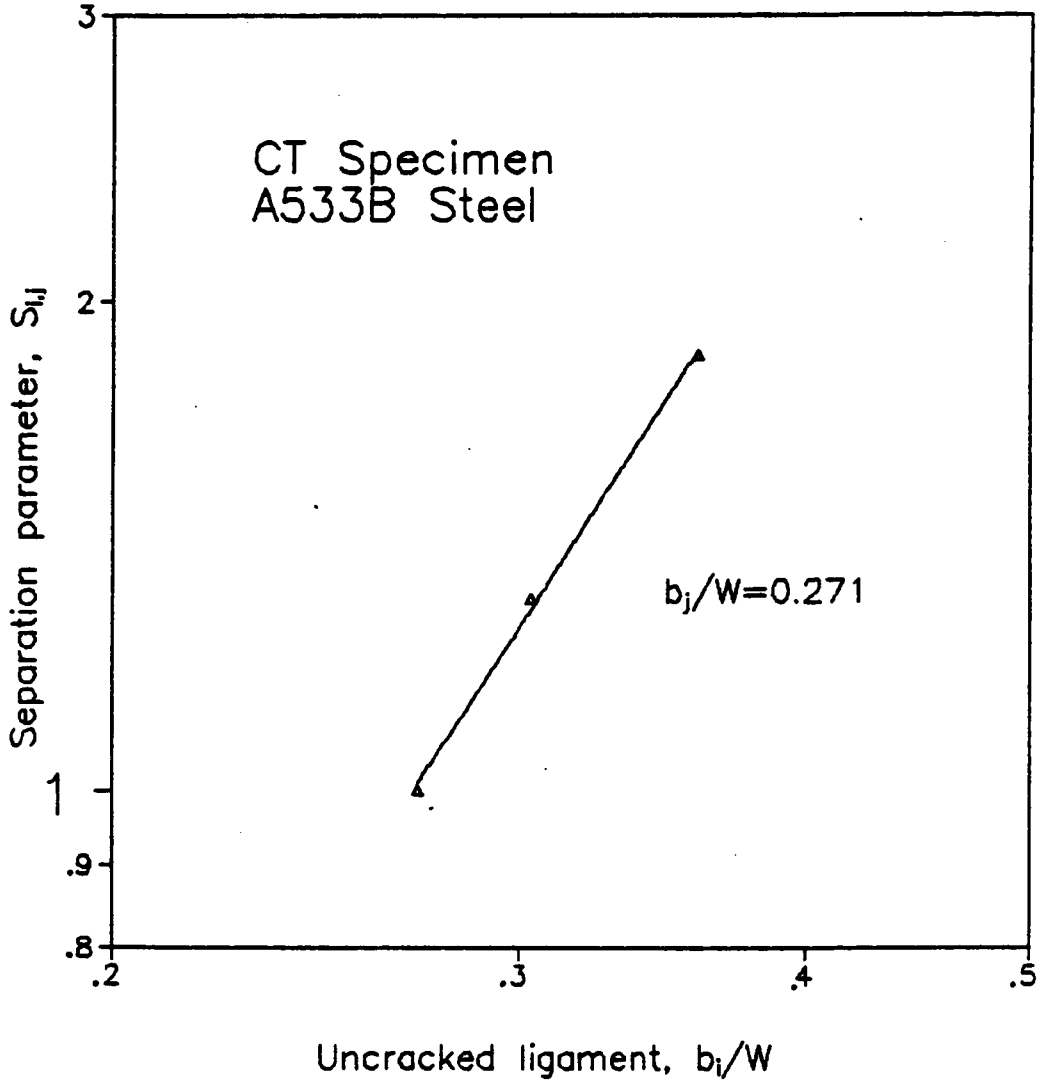


Fig. 3.4 - Power law fit of the $S_{i,j}$ versus b_i/W record for the A533B CT set.

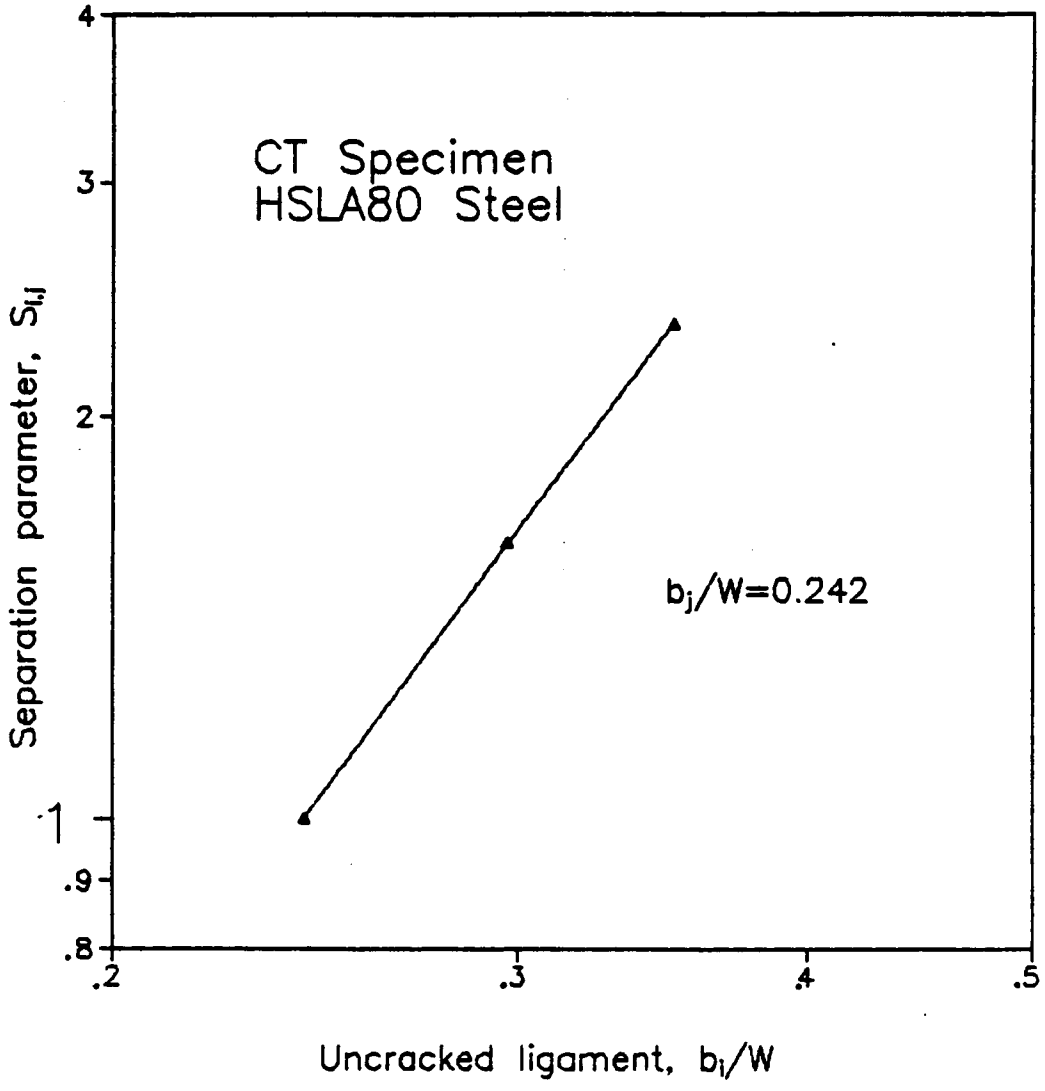


Fig. 3.5 - Power law fit of the $S_{i,j}$ versus b_i/W record for the HSLA80 CT set.

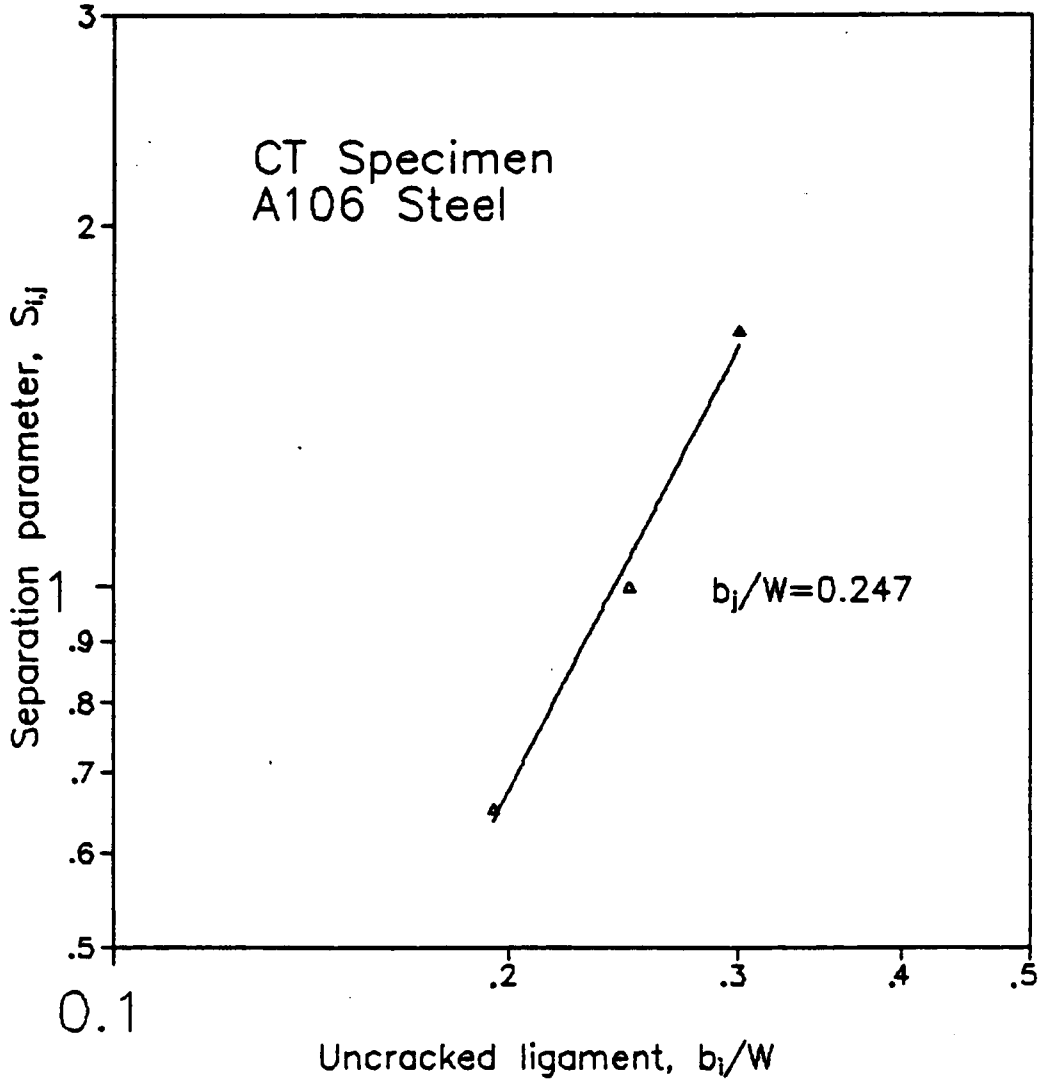


Fig. 3.6 - Power law fit of the $S_{i,j}$ versus b_i/W record for the A106 CT set.

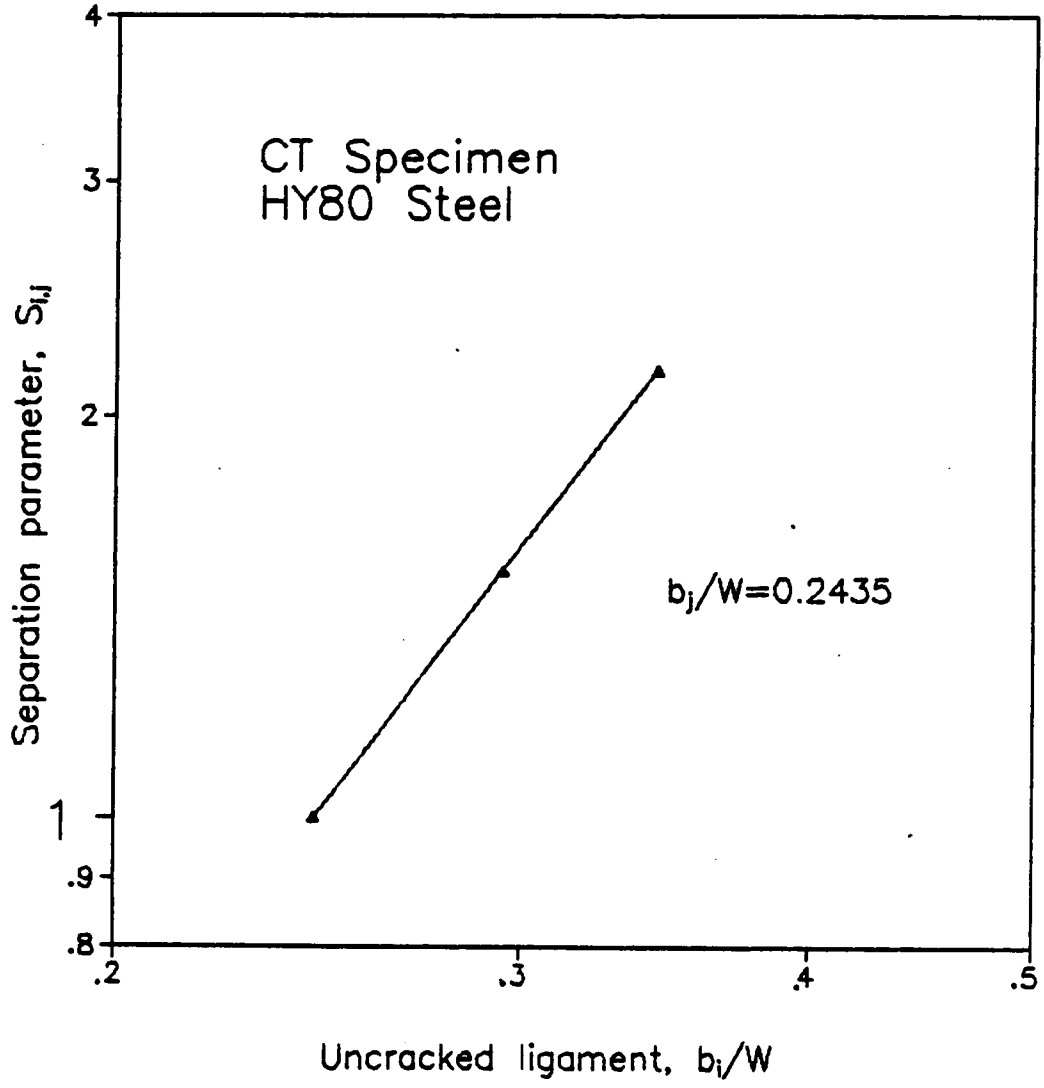


Fig. 3.7 - Power law fit of the $S_{i,j}$ versus b_i/W record for the HY80 CT set.

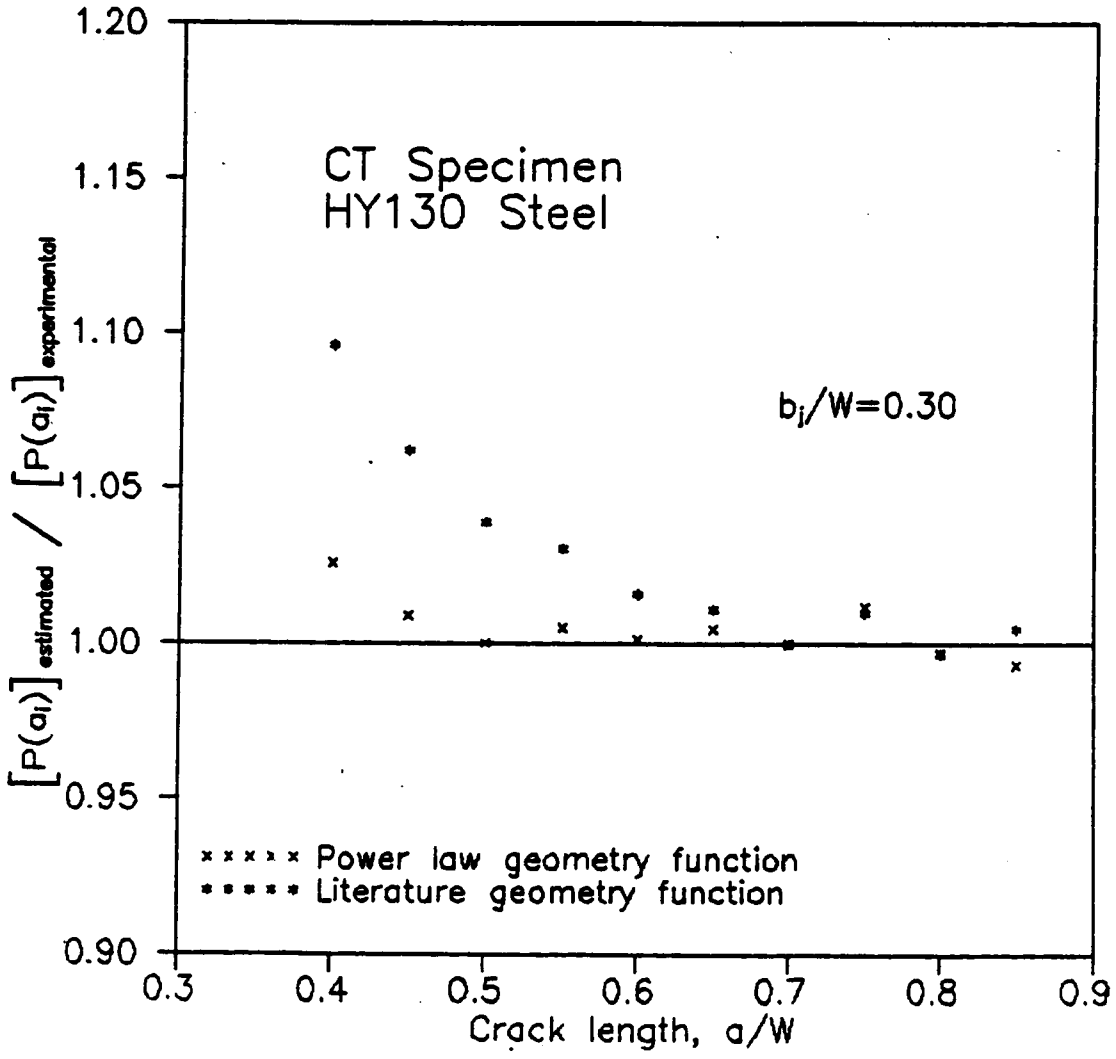


Fig. 3.8 - Load estimation errors using the power law geometry function and the literature geometry function.

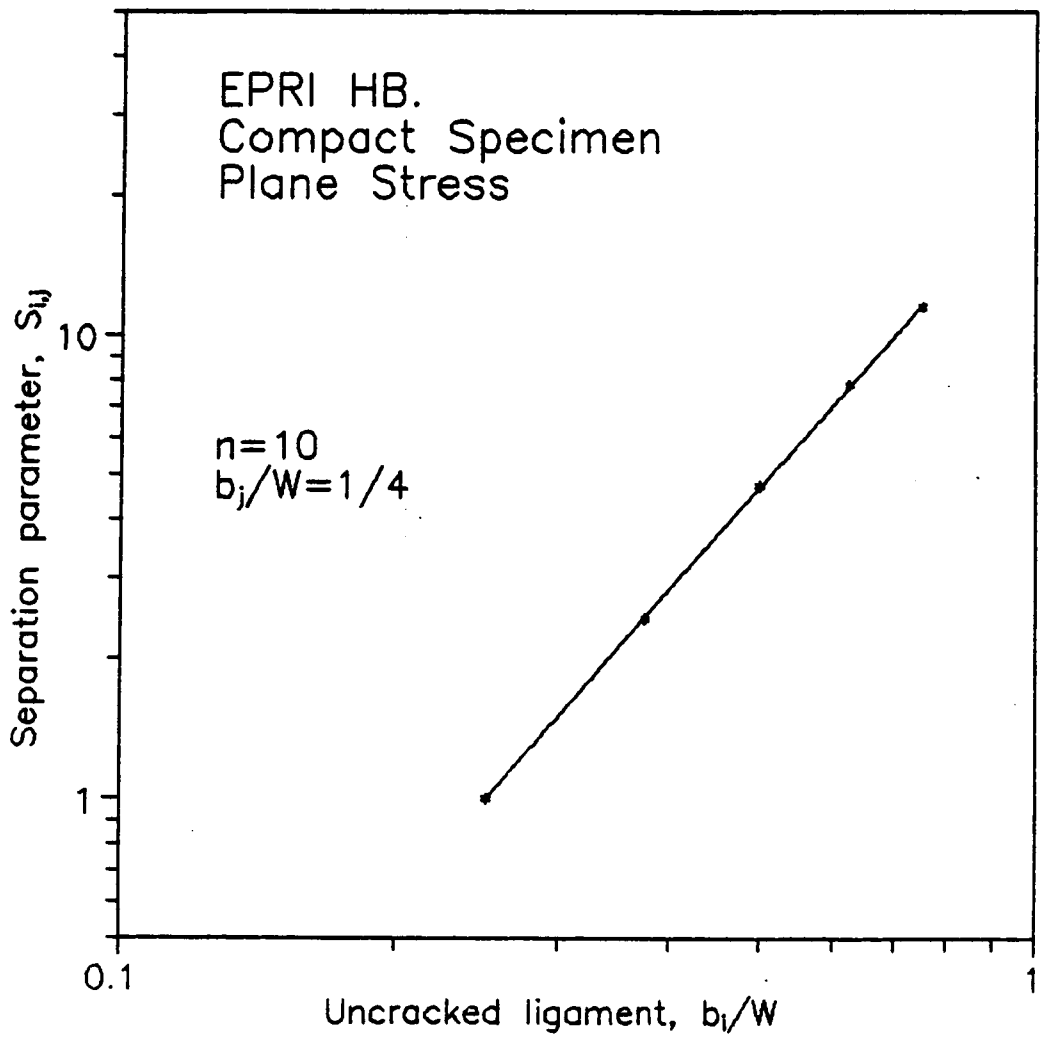


Fig. 3.9 - Power law fit of the $S_{i,j}$ versus b_i/W record obtained using the Handbook numerical solutions for the compact geometry with plane stress constraint.

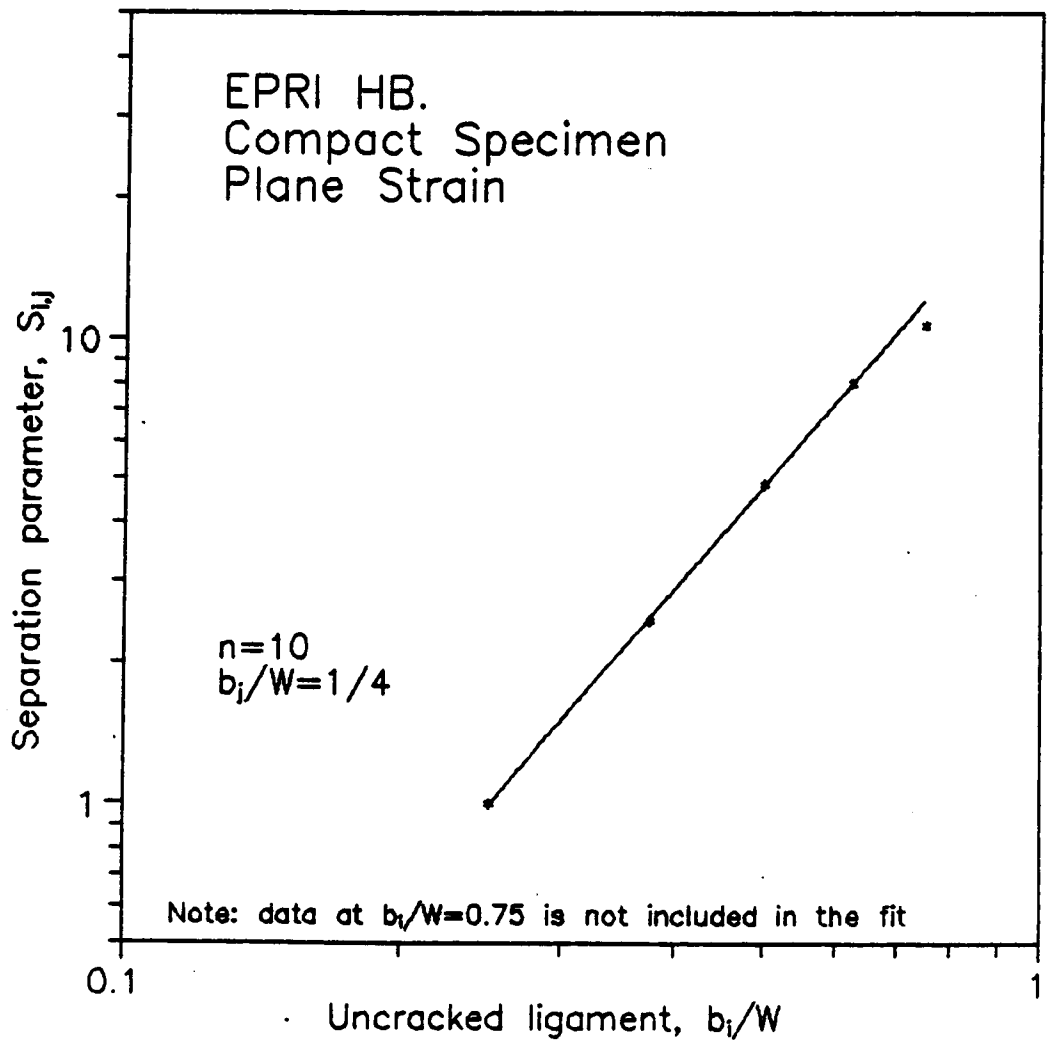


Fig. 3.10 - Power law fit of the $S_{i,j}$ versus b_i/W record obtained using the Handbook numerical solutions for the compact geometry with plane strain constraint.

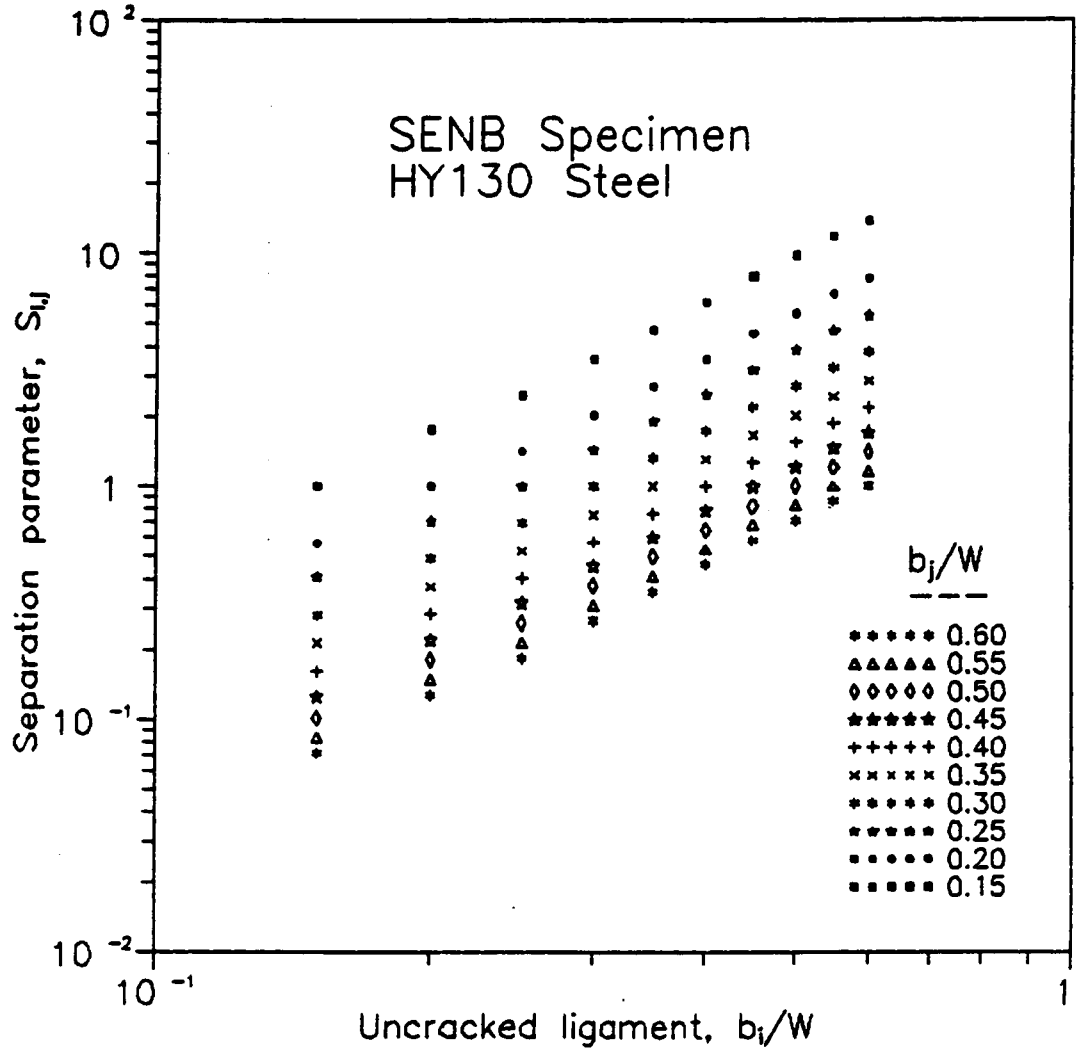


Fig. 3.11 - Variation of the separation parameters, $S_{i,j}$, with respect to uncracked ligament, b_i/W, on logarithmic coordinates for the HY130 SENB set.

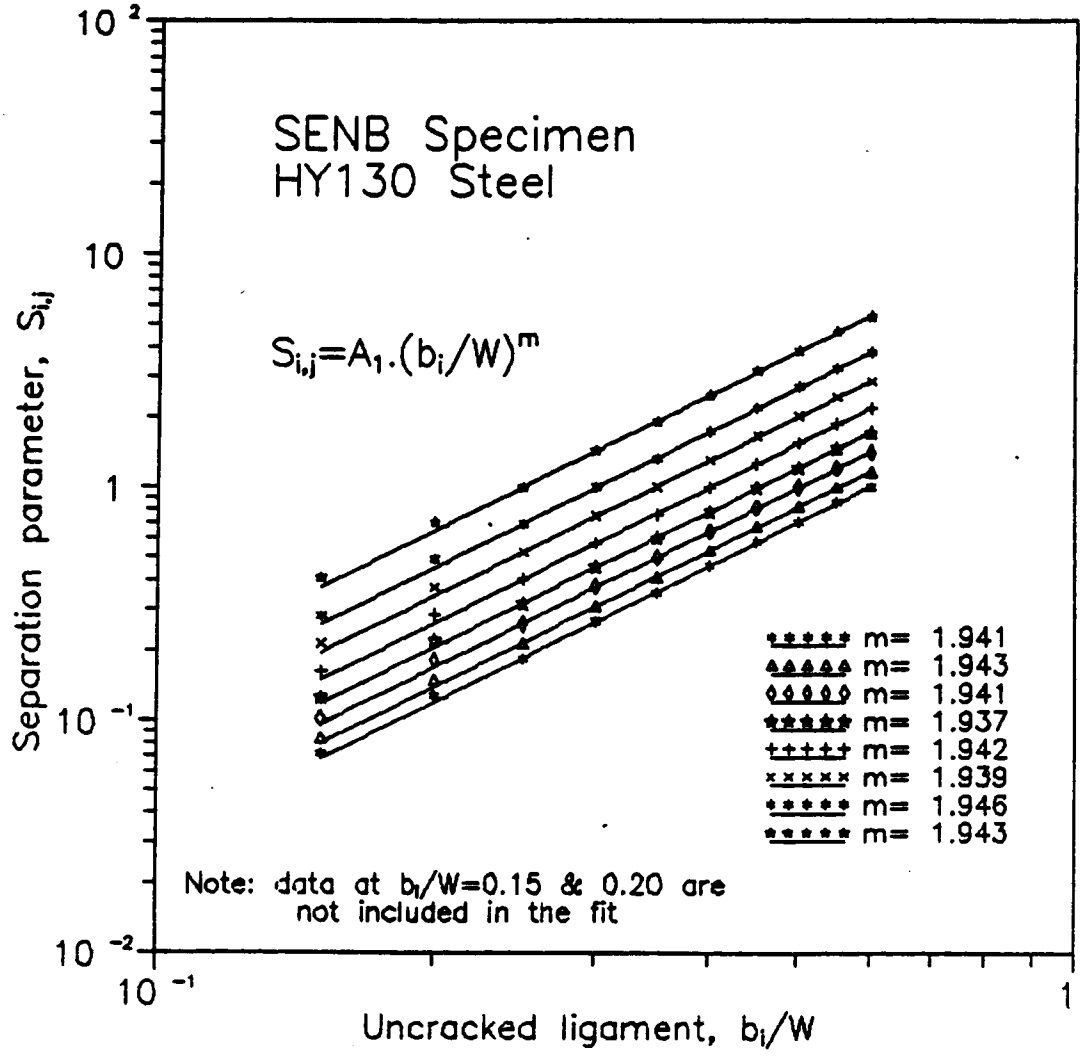


Fig. 3.12 - Power law fit of the $S_{i,j}$ versus $b_i/\bar{W}$ records for the HY130 SENB set.

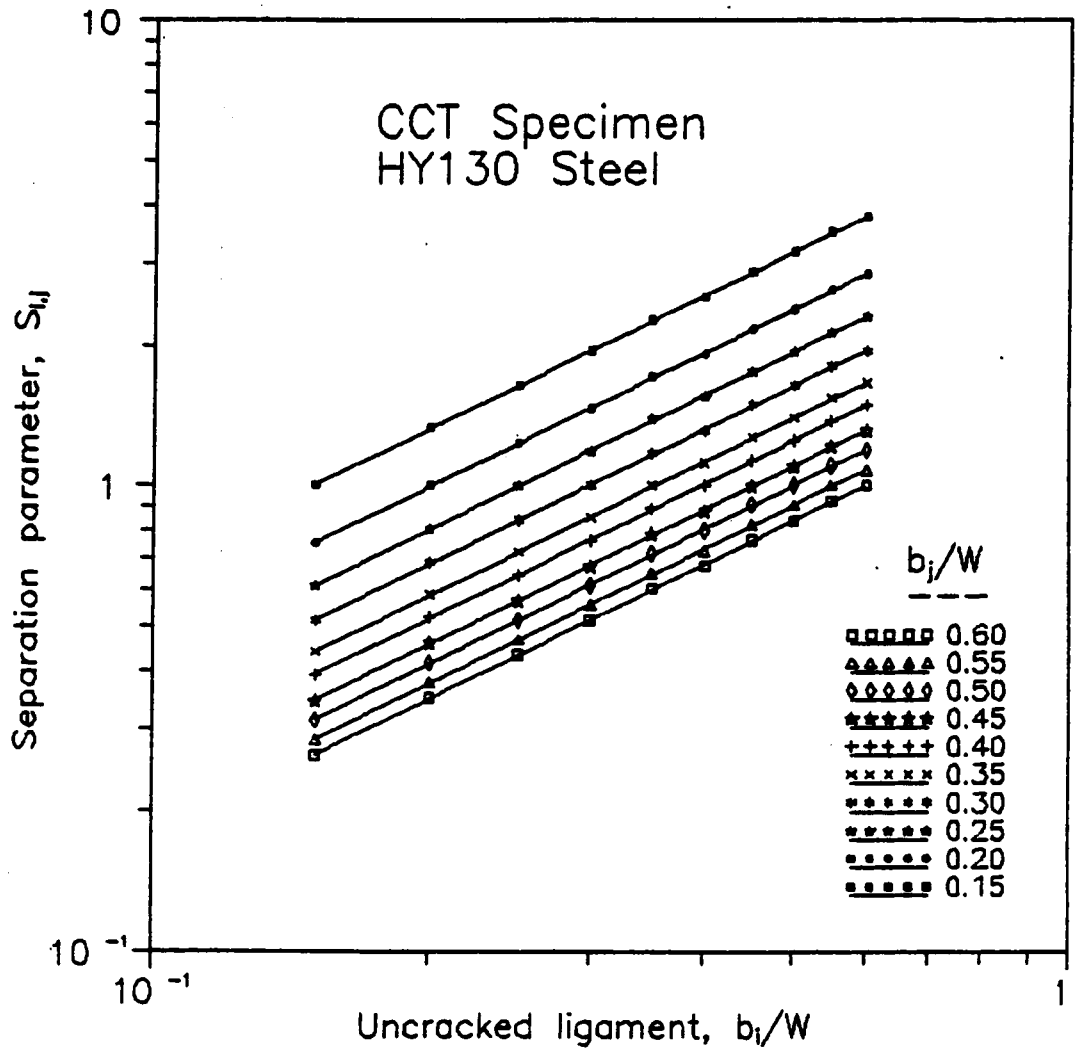


Fig. 3.13 - Power law fit of the $S_{i,j}$ versus $b_i/\bar{W}$ records for the HY130 CCT set.

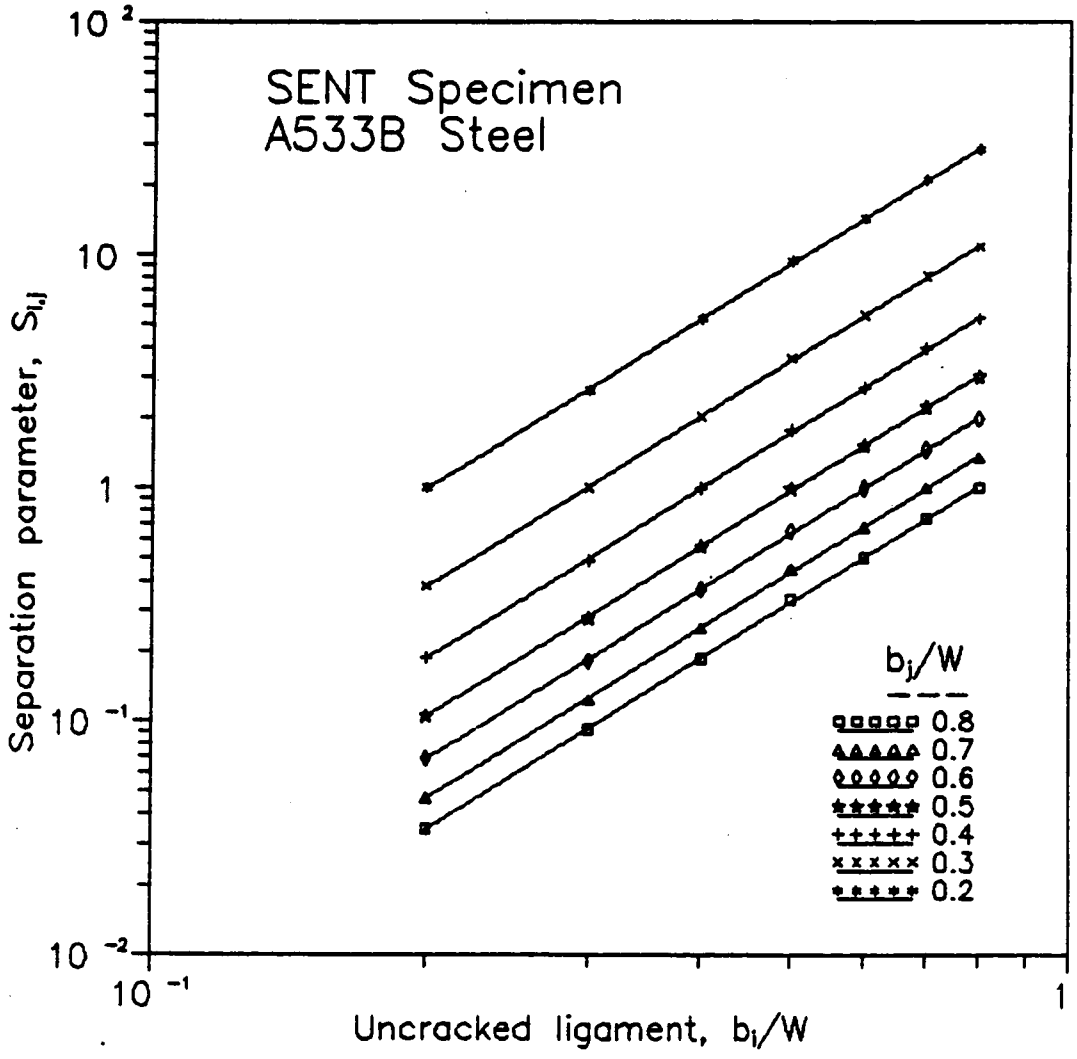


Fig. 3.14 - Power law fit of the $S_{i,j}$ versus b_i/W records for the A533B SENT set.

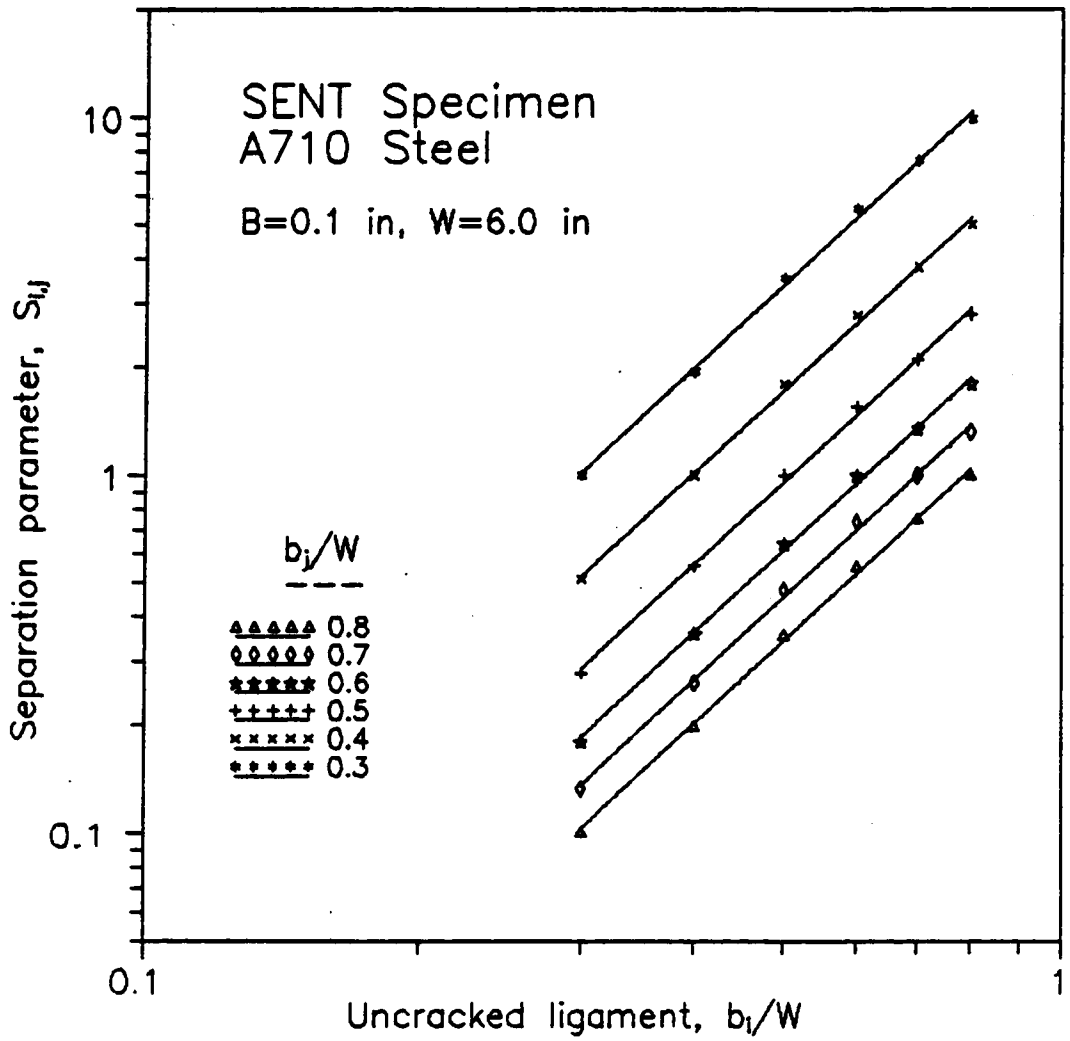


Fig. 3.15 - Power law fit of the $S_{i,j}$ versus b_i/W records for the A710 SENT thin specimens set.

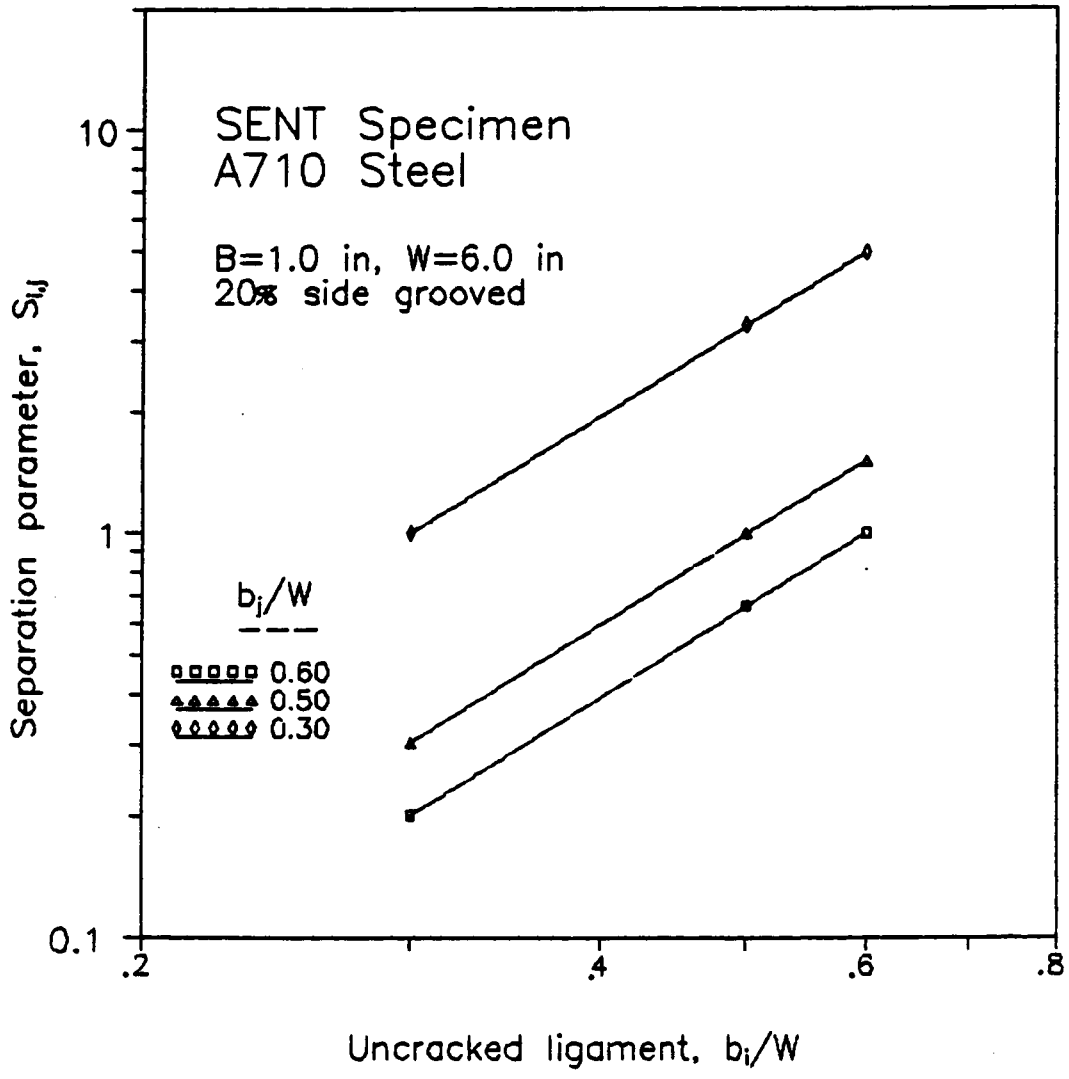


Fig. 3.16 - Power law fit of the $S_{i,j}$ versus b_i/W records for the A710 SENT 1.0 in. thick specimens with 20% side grooving.

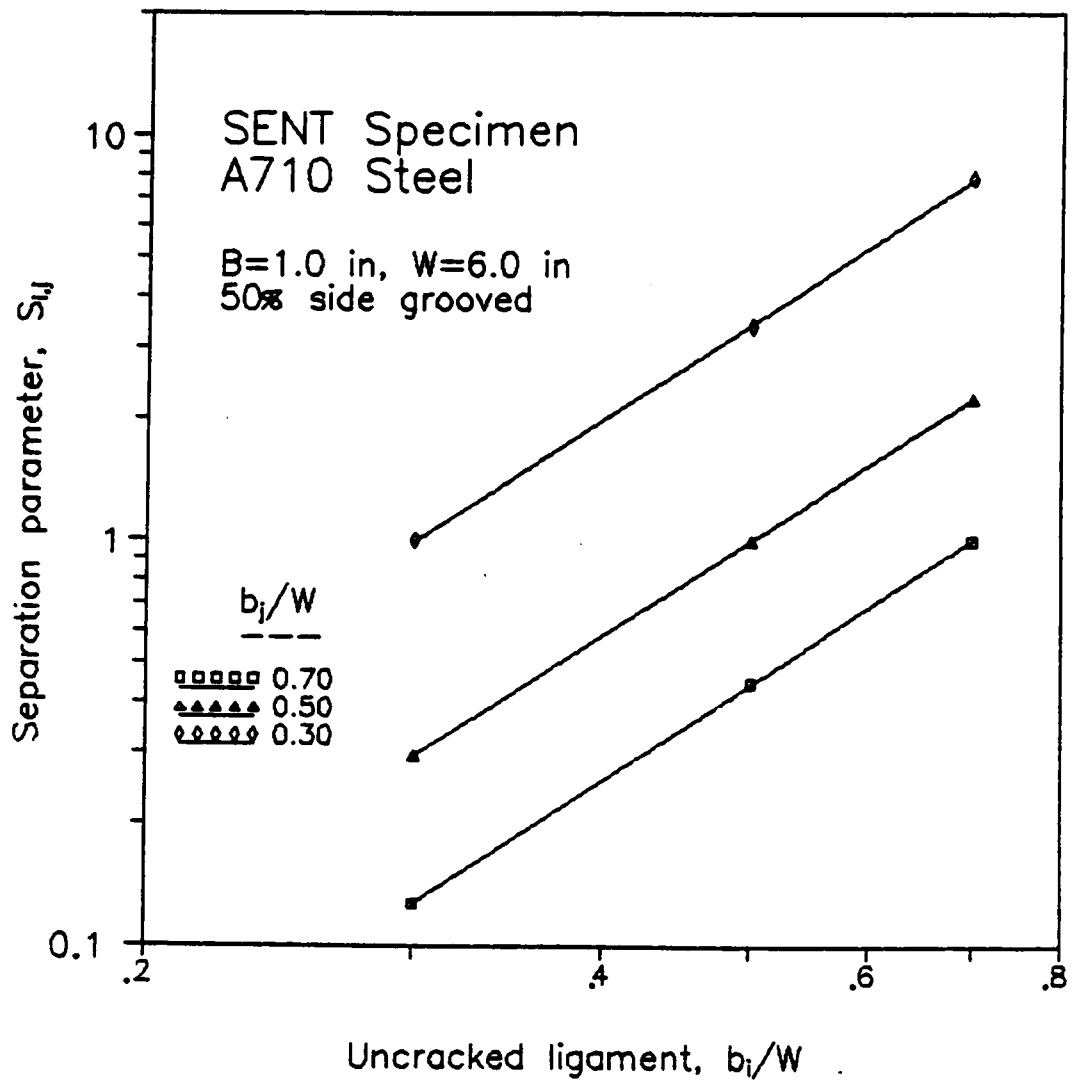


Fig. 3.17 - Power law fit of the $S_{i,j}$ versus b_i/W records for the A710 SENT 1.0 in. thick specimens with 50% side grooving.

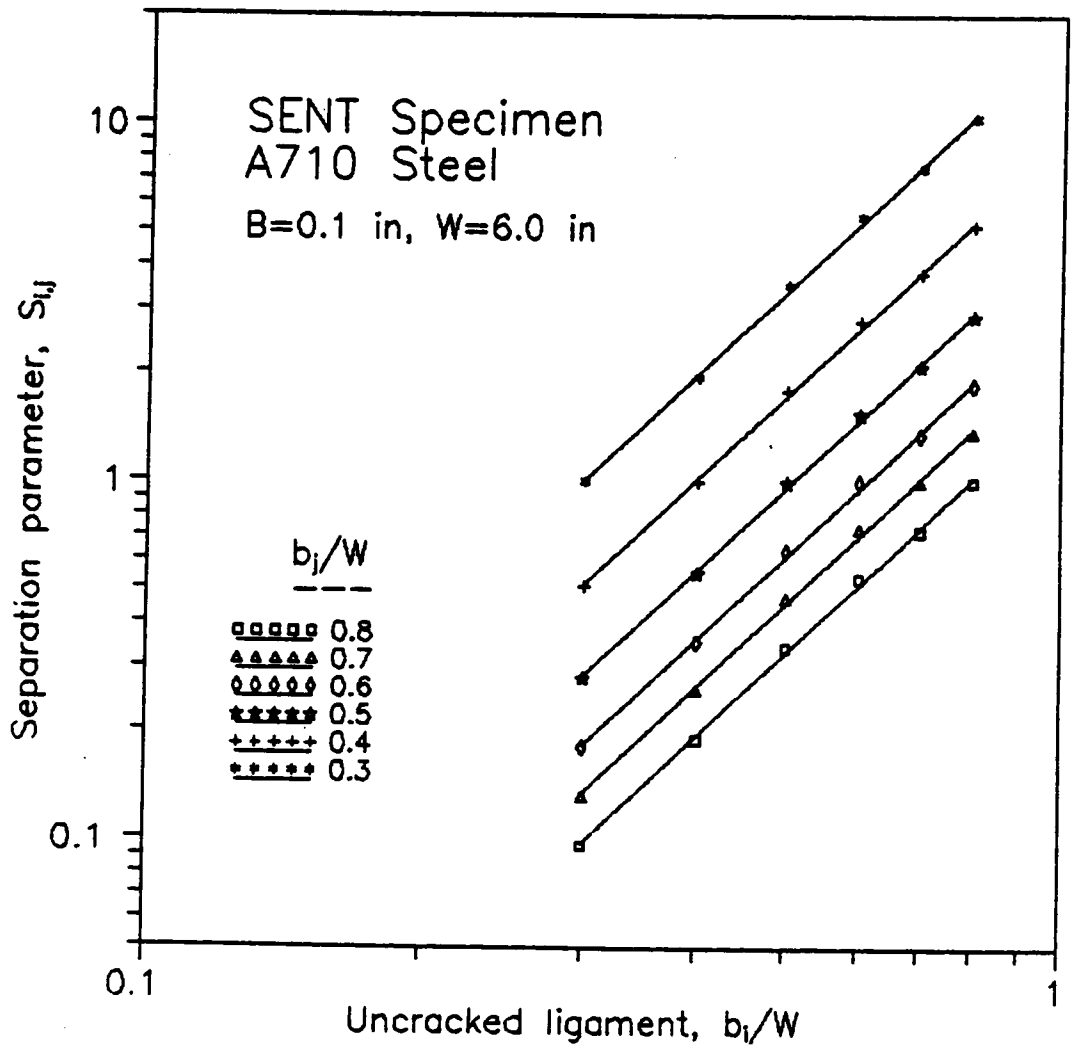


Fig. 3.18 - Power law fit of the $S_{i,j}$ versus b_i/W records obtained using load versus crack mouth opening displacement records for the A710 SENT thin specimens set.

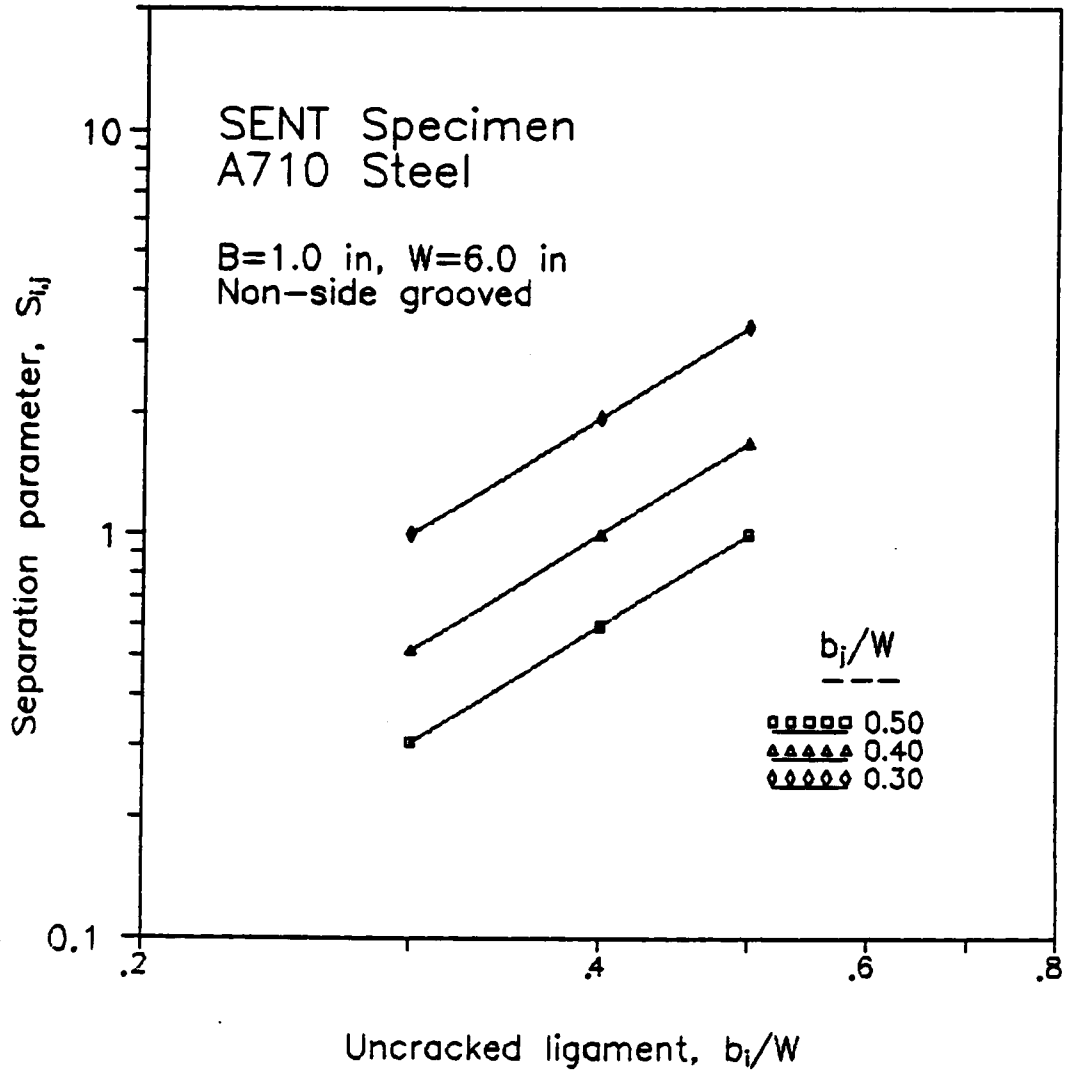


Fig. 3.19 - Power law fit of the $S_{i,j}$ versus b_i/W records obtained using the load versus crack mouth opening displacement records for the A710 SENT 1.0 in. thick specimens with no side grooving.

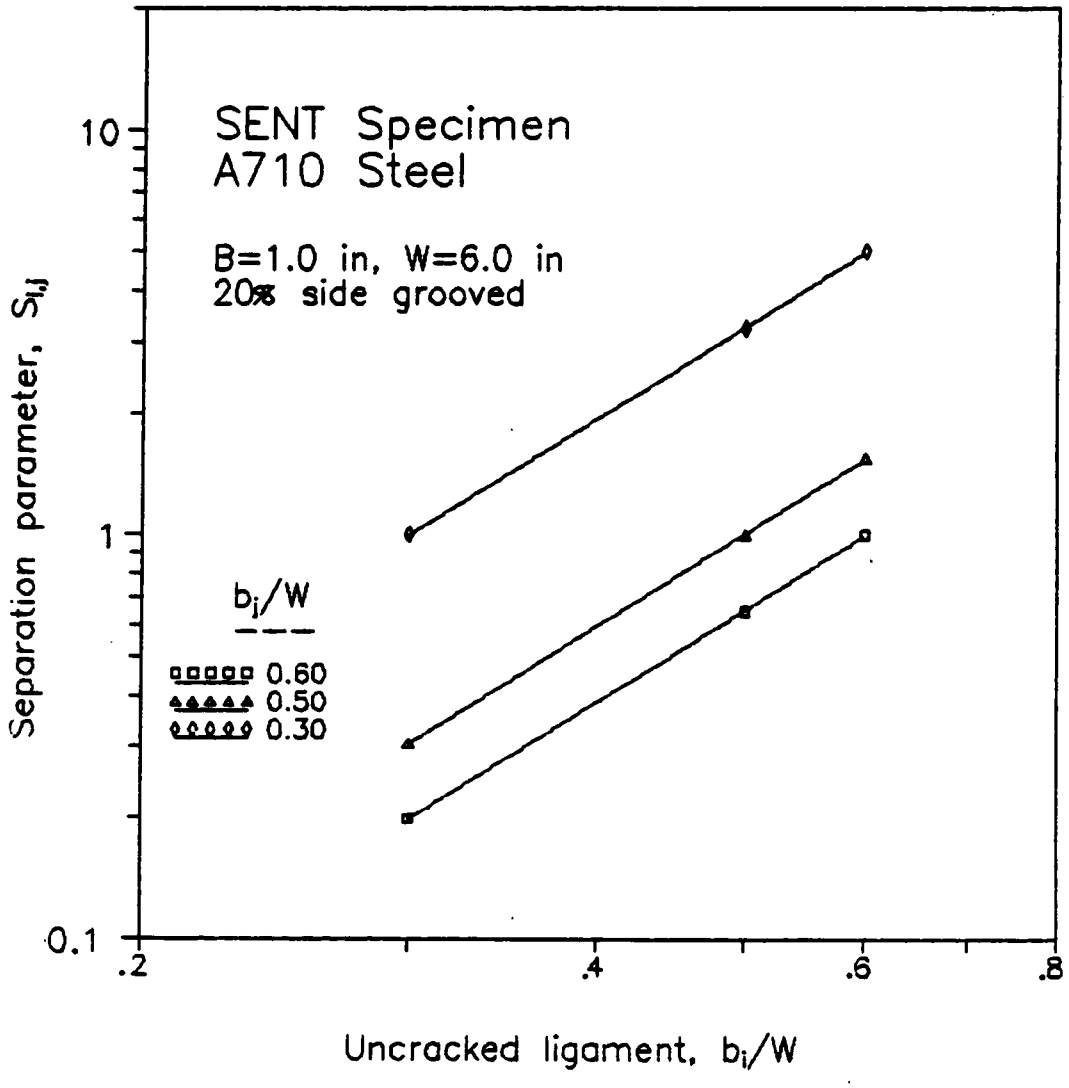


Fig. 3.20 - Power law fit of the $S_{i,j}$ versus b_i/W records obtained using the load versus crack mouth opening displacement records for the A710 SENT 1.0 in. thick specimens with 20% side grooving.

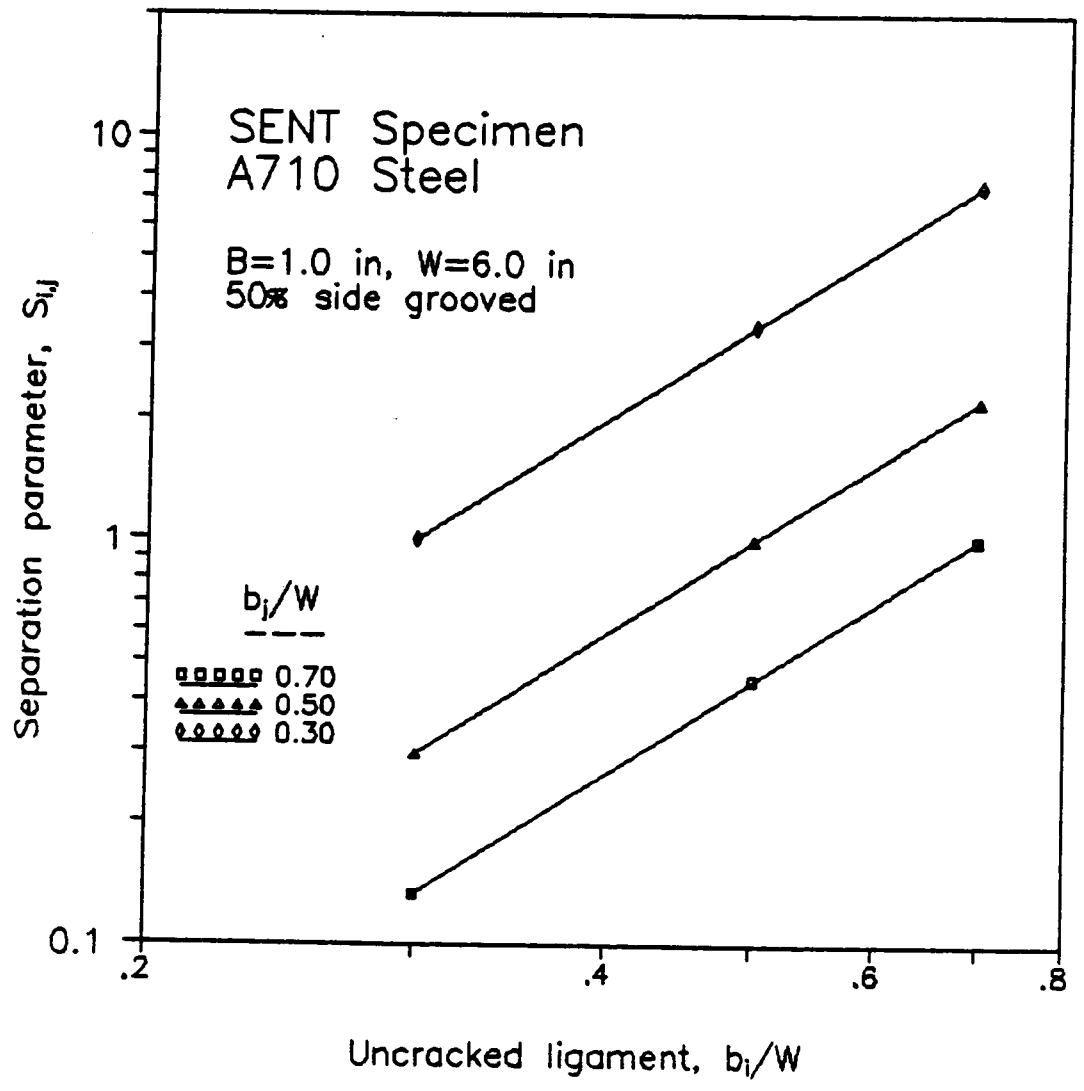


Fig. 3.21 - Power law fit of the $S_{i,j}$ versus b_i/W records obtained using the load versus crack mouth opening displacement records for the A710 SENT 1.0 in. thick specimens with 50% side grooving.

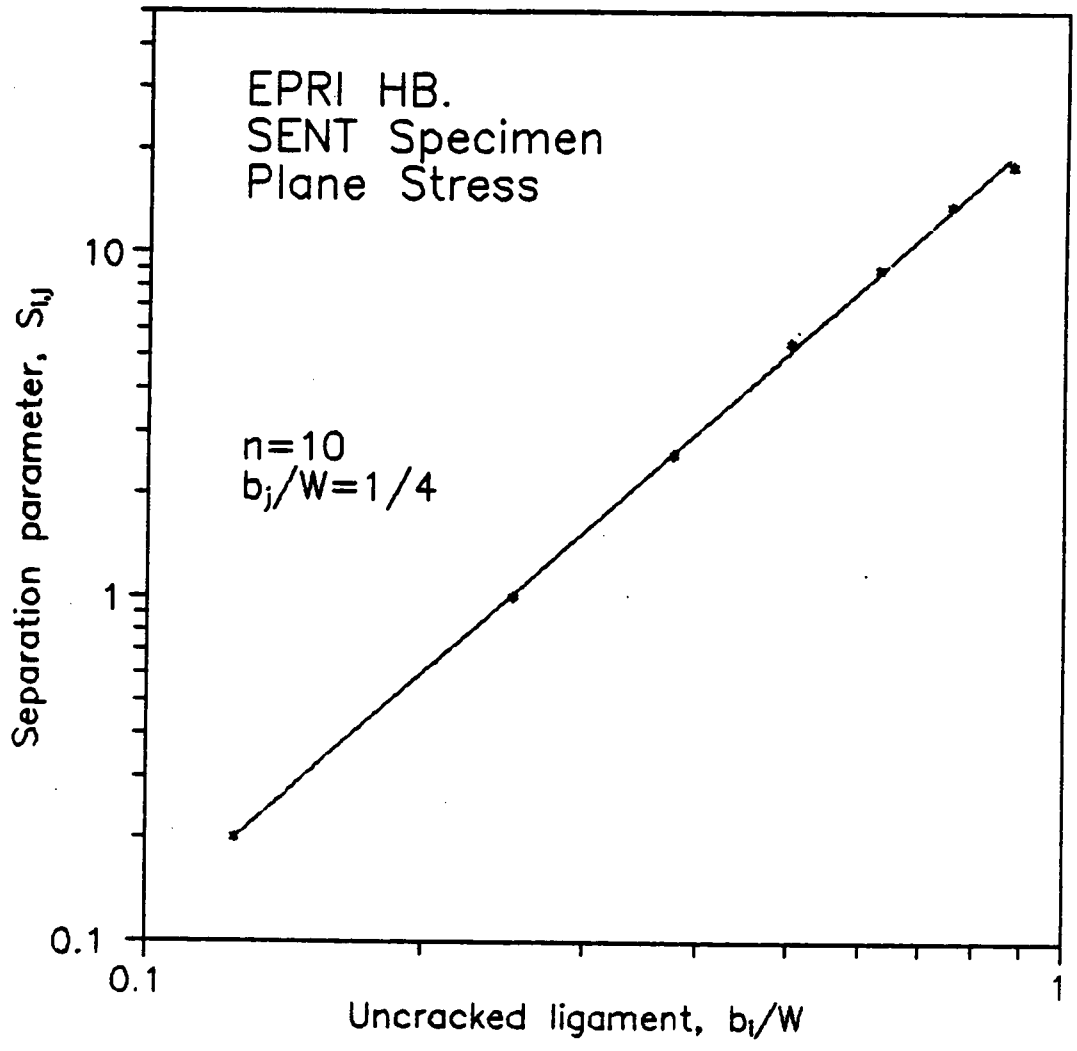


Fig. 3.22 - Power law fit of the $S_{i,j}$ versus b_i/W record obtained using the Handbook numerical solutions of the load versus crack mouth opening displacement relationship for the SENT geometry with plane stress constraint.

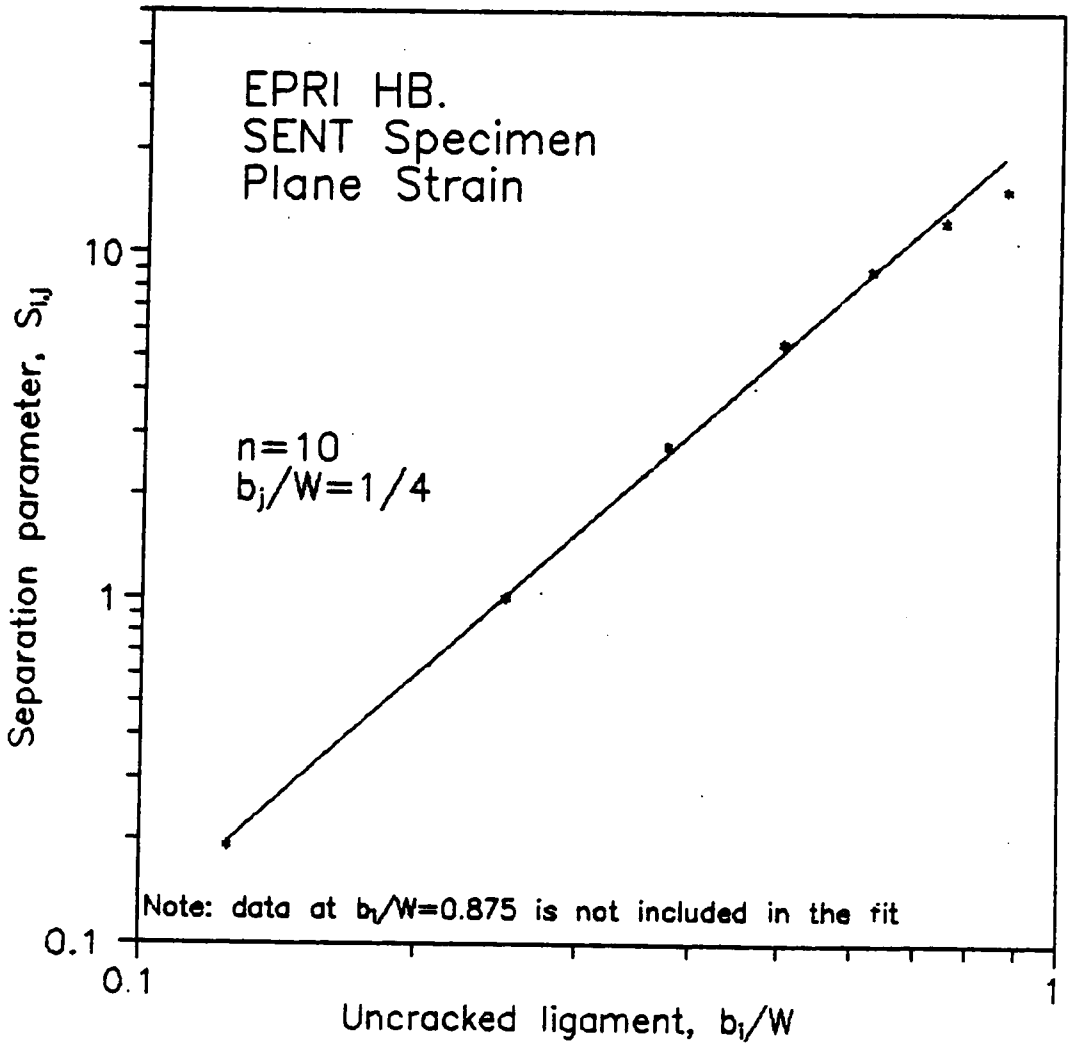


Fig. 3.23 - Power law fit of the $S_{i,j}$ versus b_i/W record obtained using the Handbook numerical solutions of the load versus crack mouth opening displacement relationship for the SENT geometry with plane strain constraint.

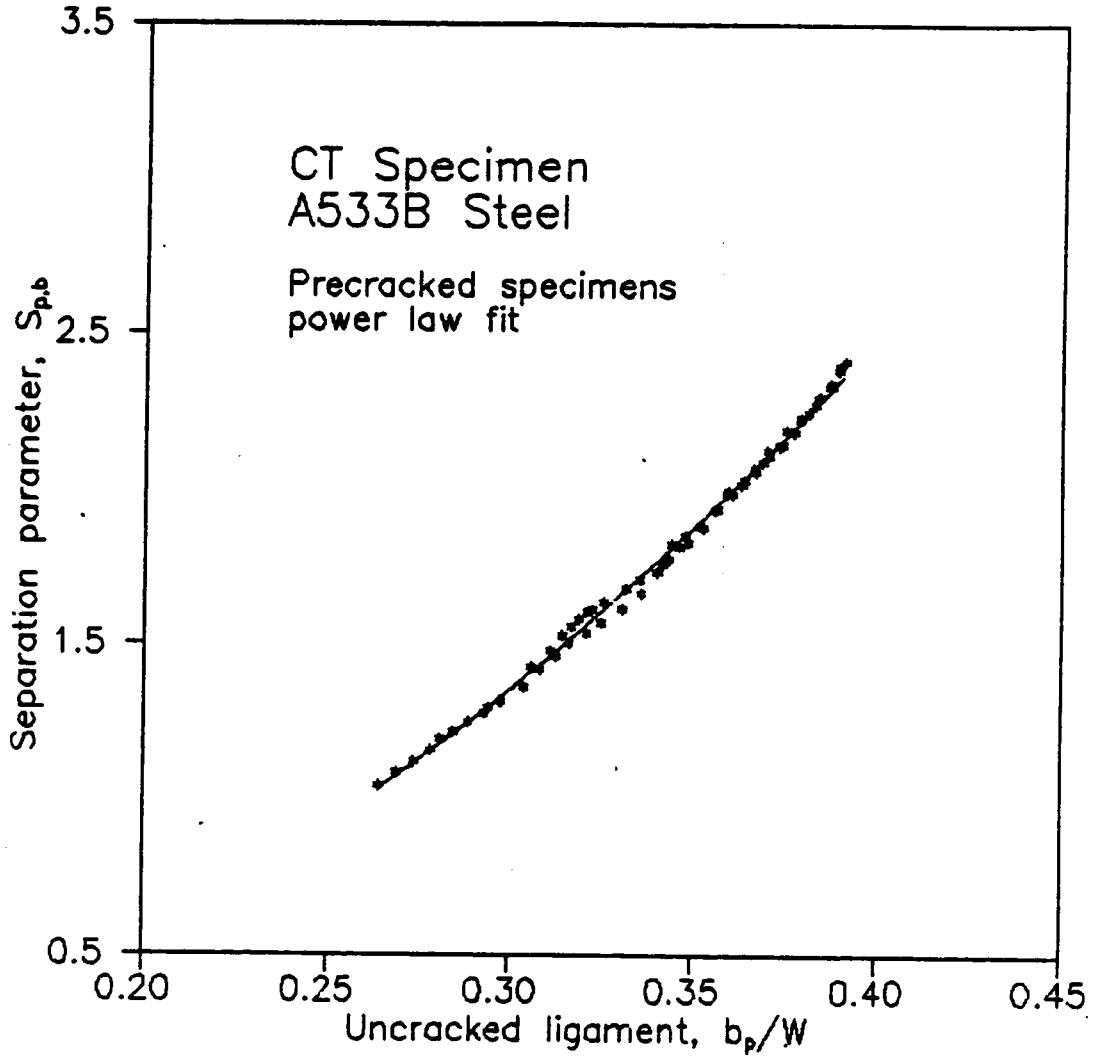


Fig. 3.24 - Power law fit of the $S_{i,j}$ versus b_i/W records for the A533B CT precracked specimens set.

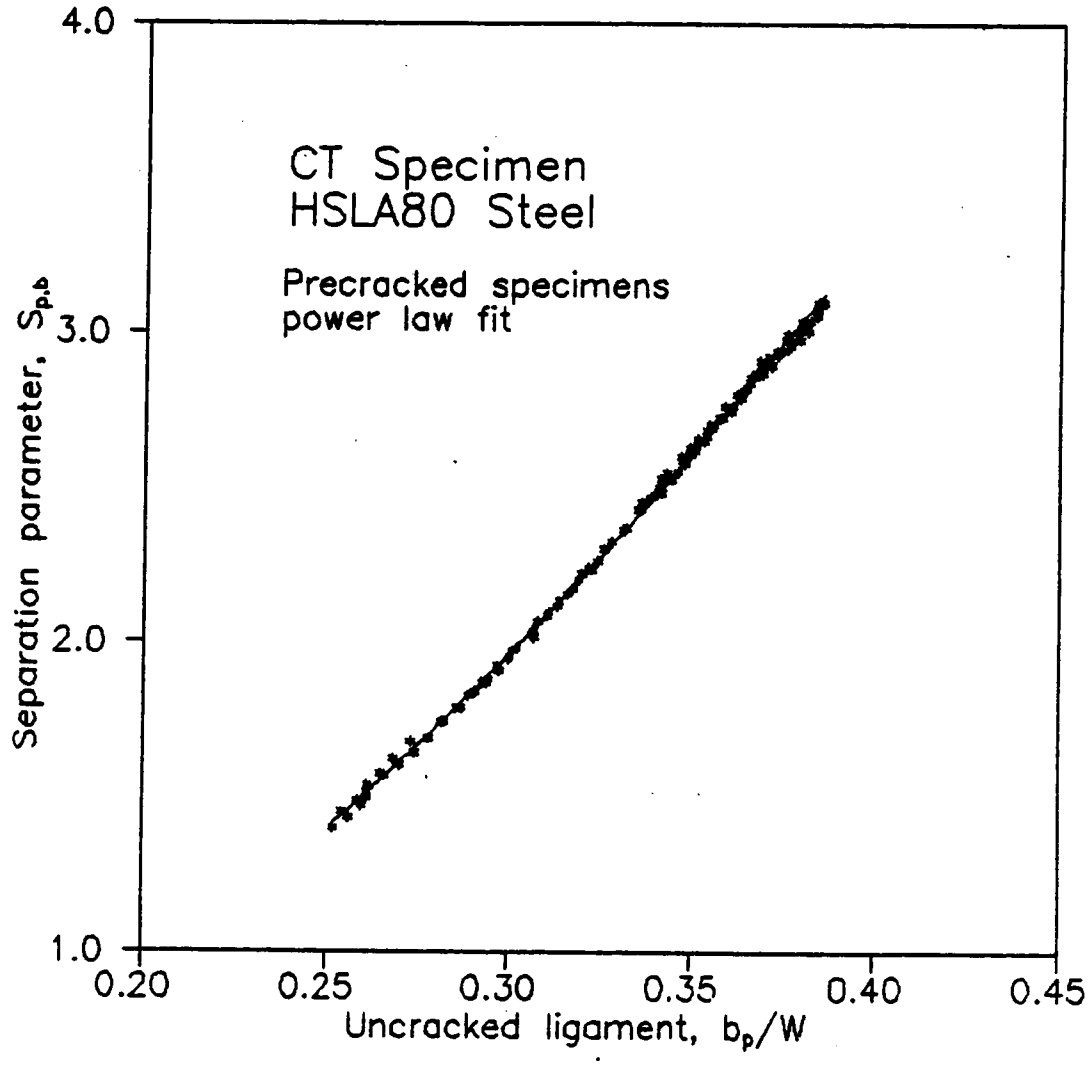


Fig. 3.25 - Power law fit of the $S_{i,j}$ versus $b_i/\bar{W}$ records for the HSLA80 CT precracked specimens set.

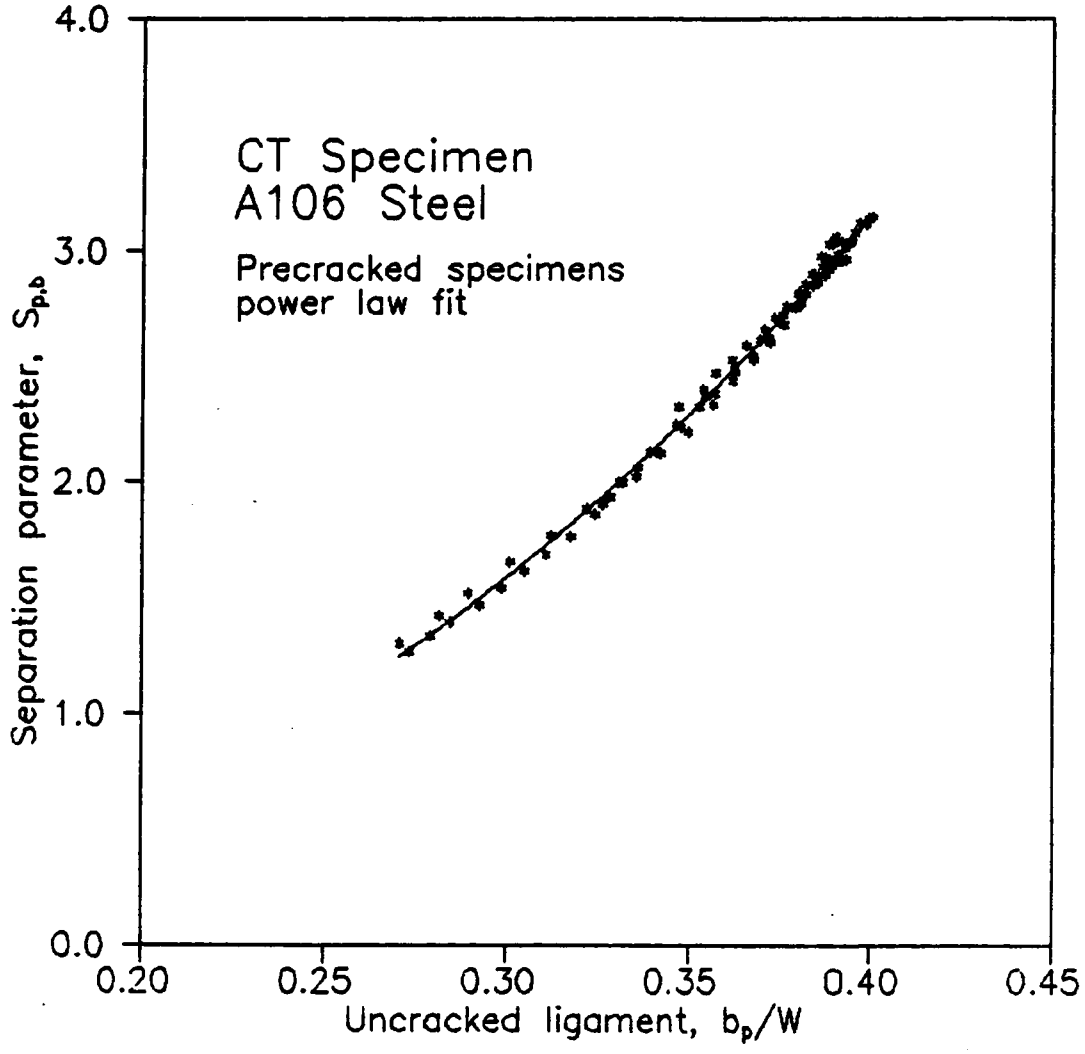


Fig. 3.26 - Power law fit of the $S_{i,j}$ versus b_i/W records for the A106 CT precracked specimens set.

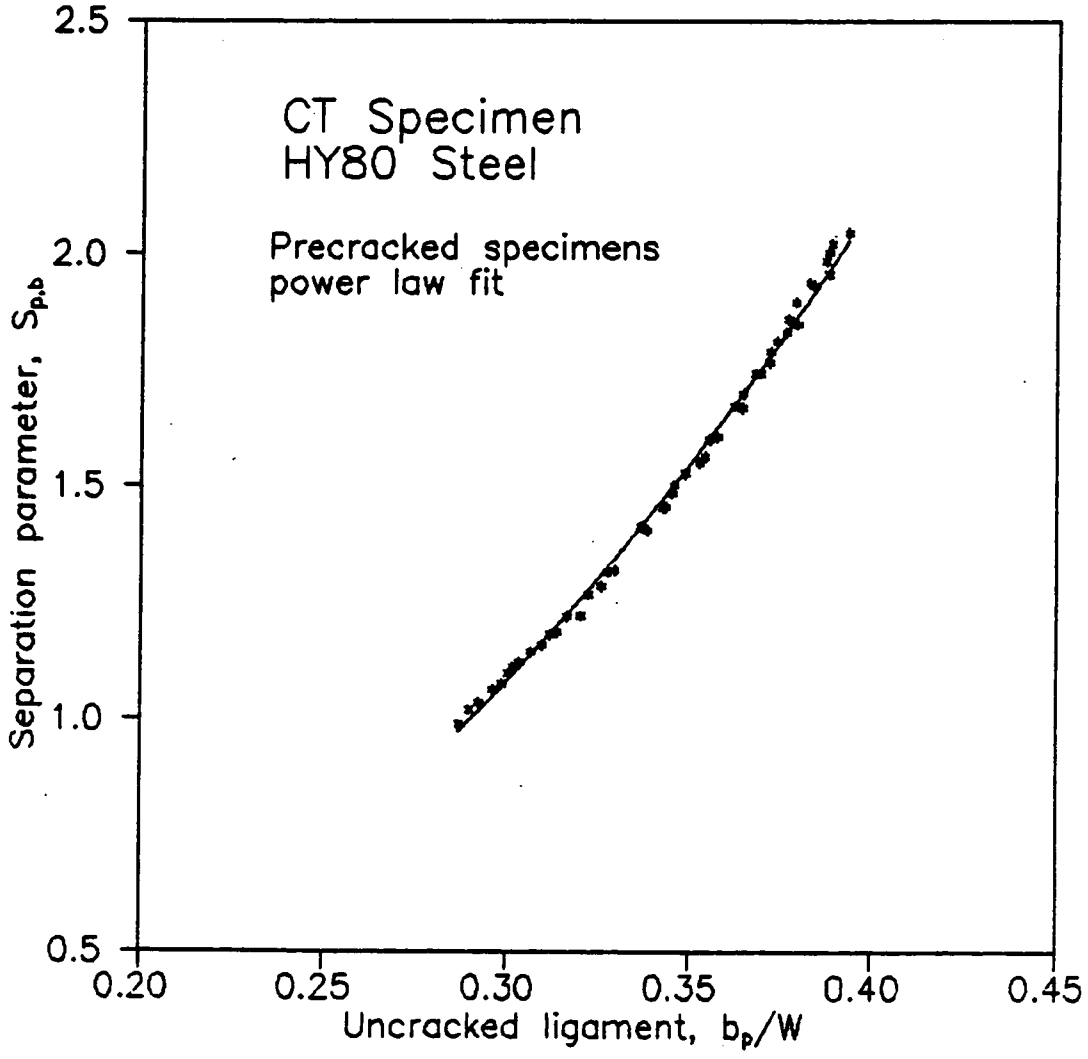


Fig. 3.27 - Power law fit of the $S_{i,j}$ versus b_i/W records for the HY80 CT precracked specimens set.

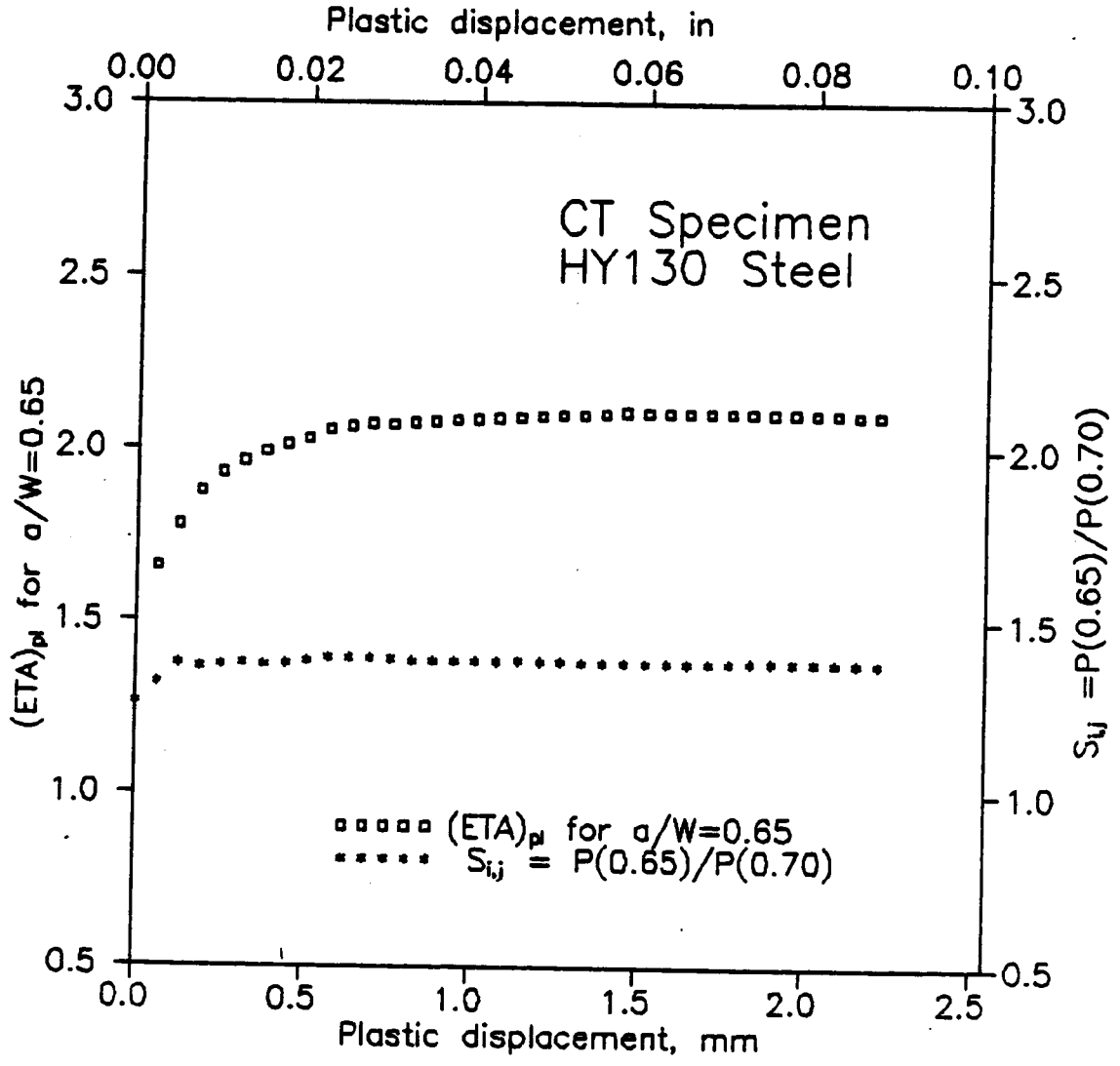


Fig. 3.28 - Variation of η_{pl} obtained using classical method versus plastic displacement for one of the HY130 CT test records.

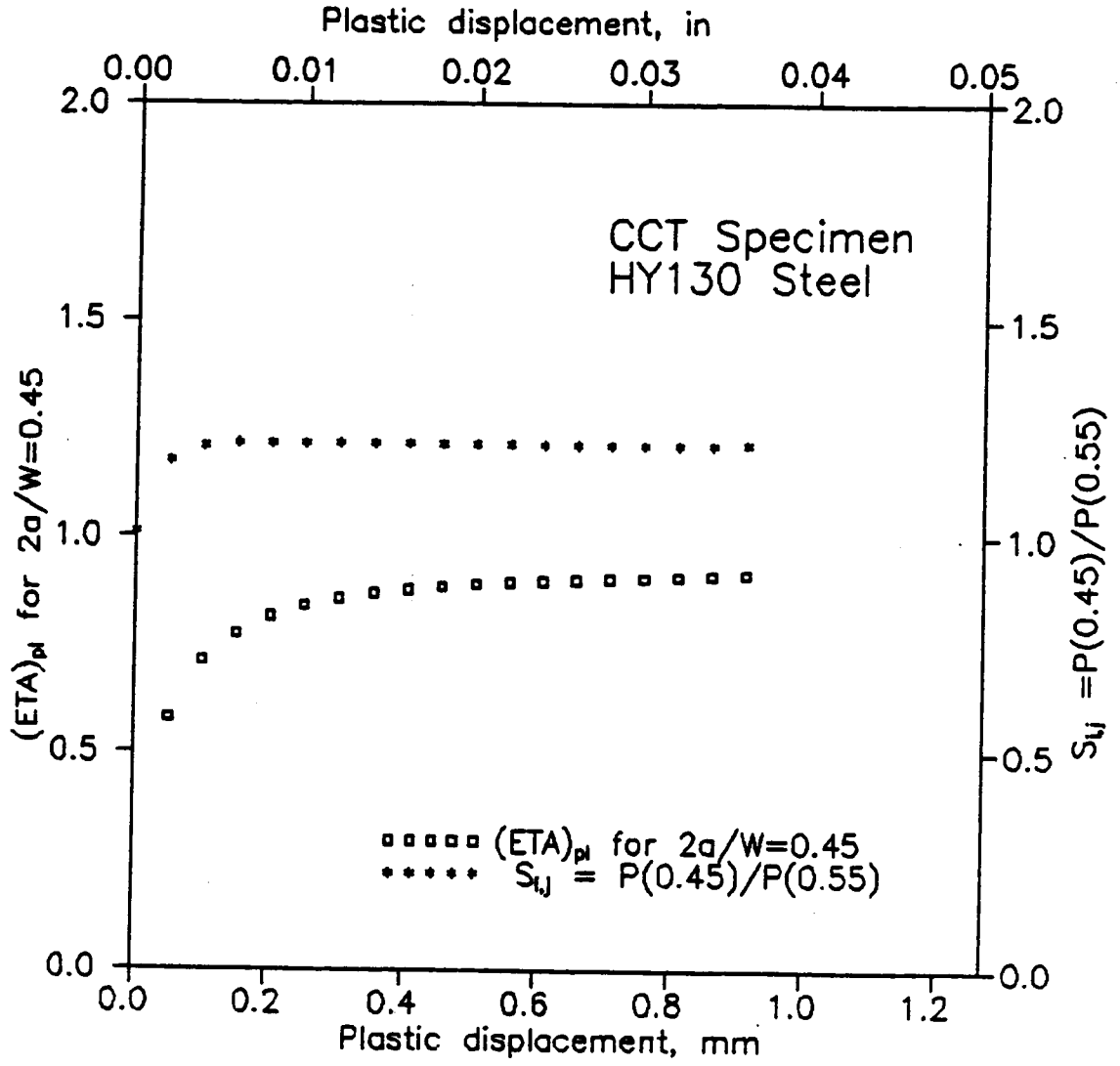


Fig. 3.29 - Variation of η_{pl} obtained using classical method versus plastic displacement for one of the HY130 CCT test records.

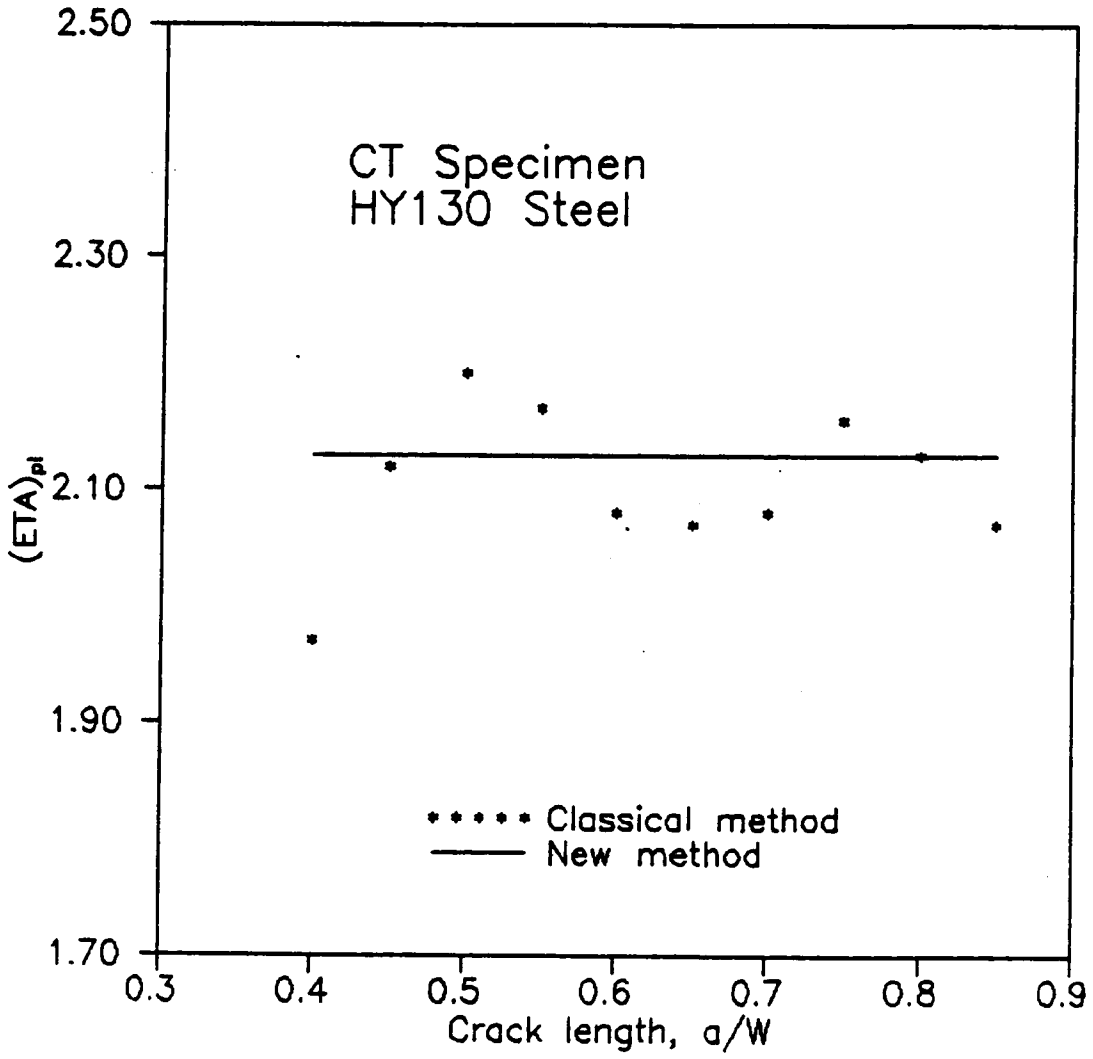


Fig. 3.30 - η_{pl} values obtained using both classical and new methods for the HY130 CT set.

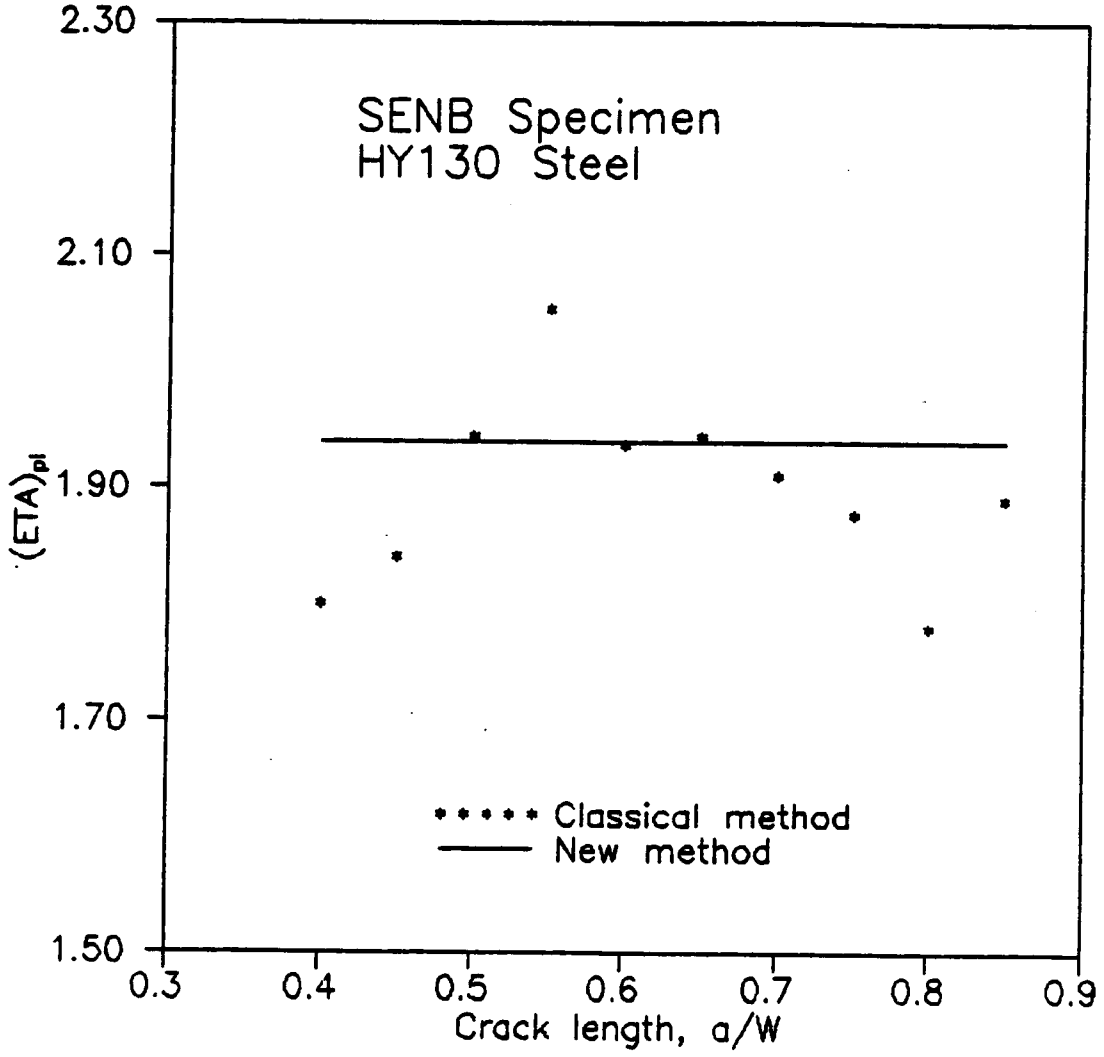


Fig. 3.31 - η_{pl} values obtained using both classical and new methods for the HY130 SENB set.

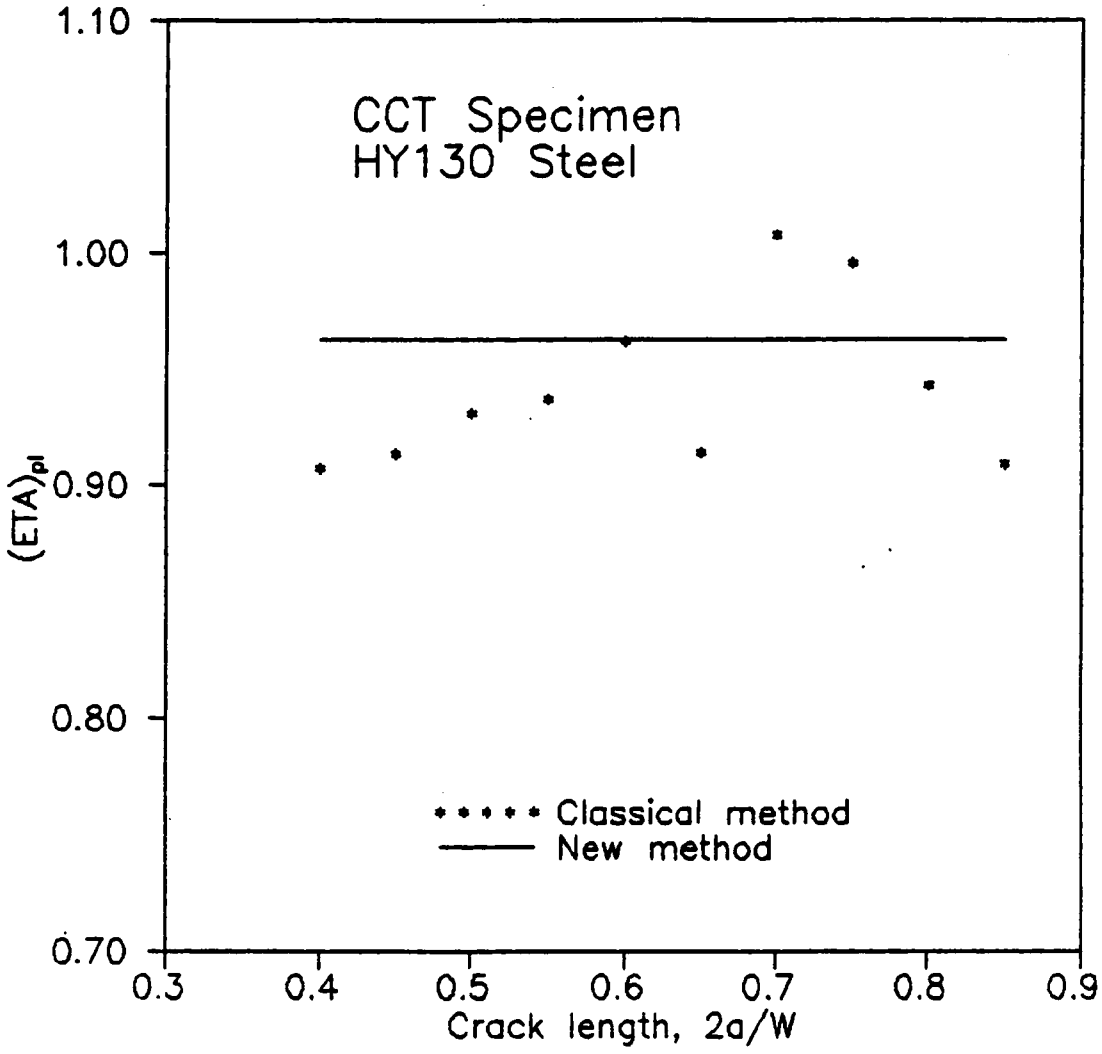


Fig. 3.32 - η_{pl} values obtained using both classical and new methods for the HY130 CCT set.

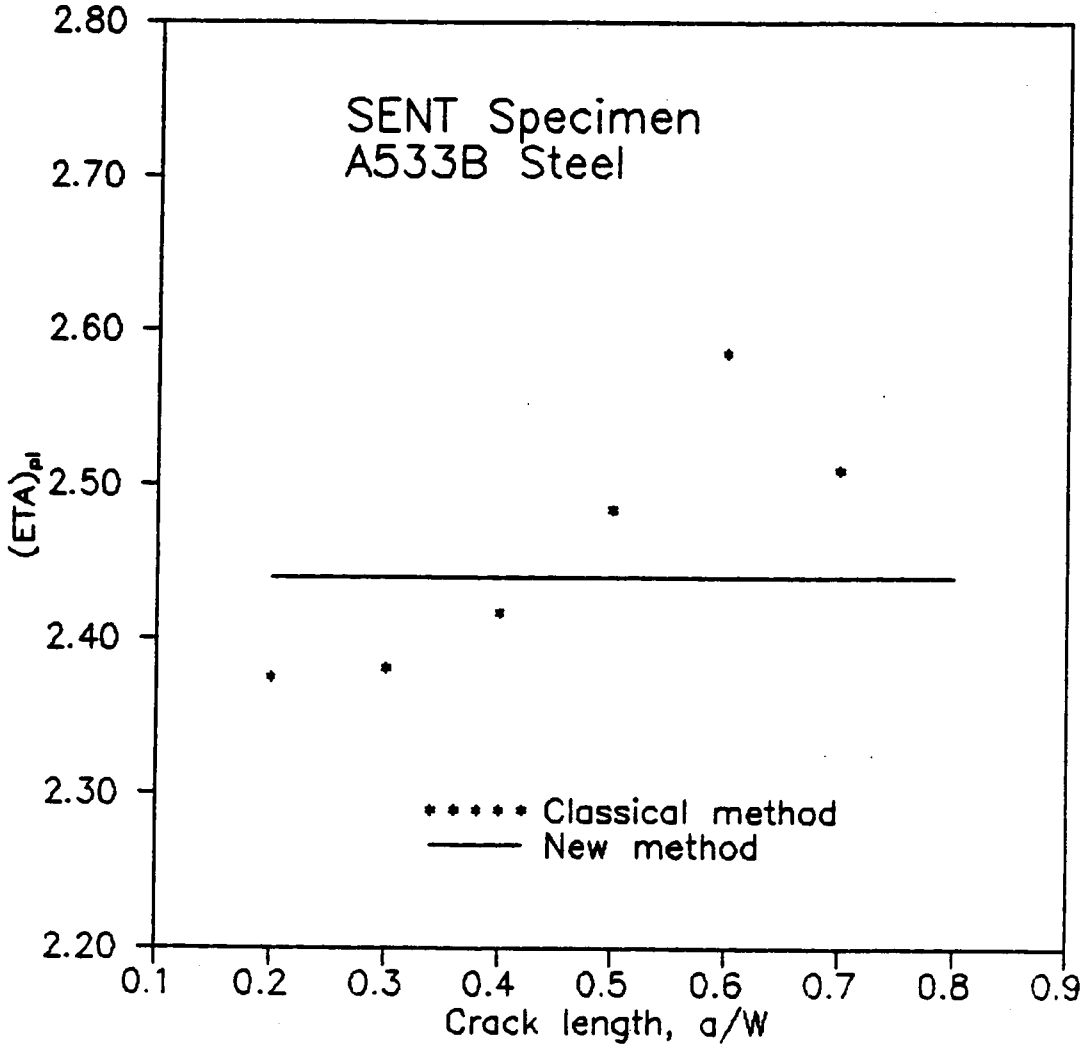


Fig. 3.33 - η_{pl} values obtained using both classical and new methods for the A533B SENT set.

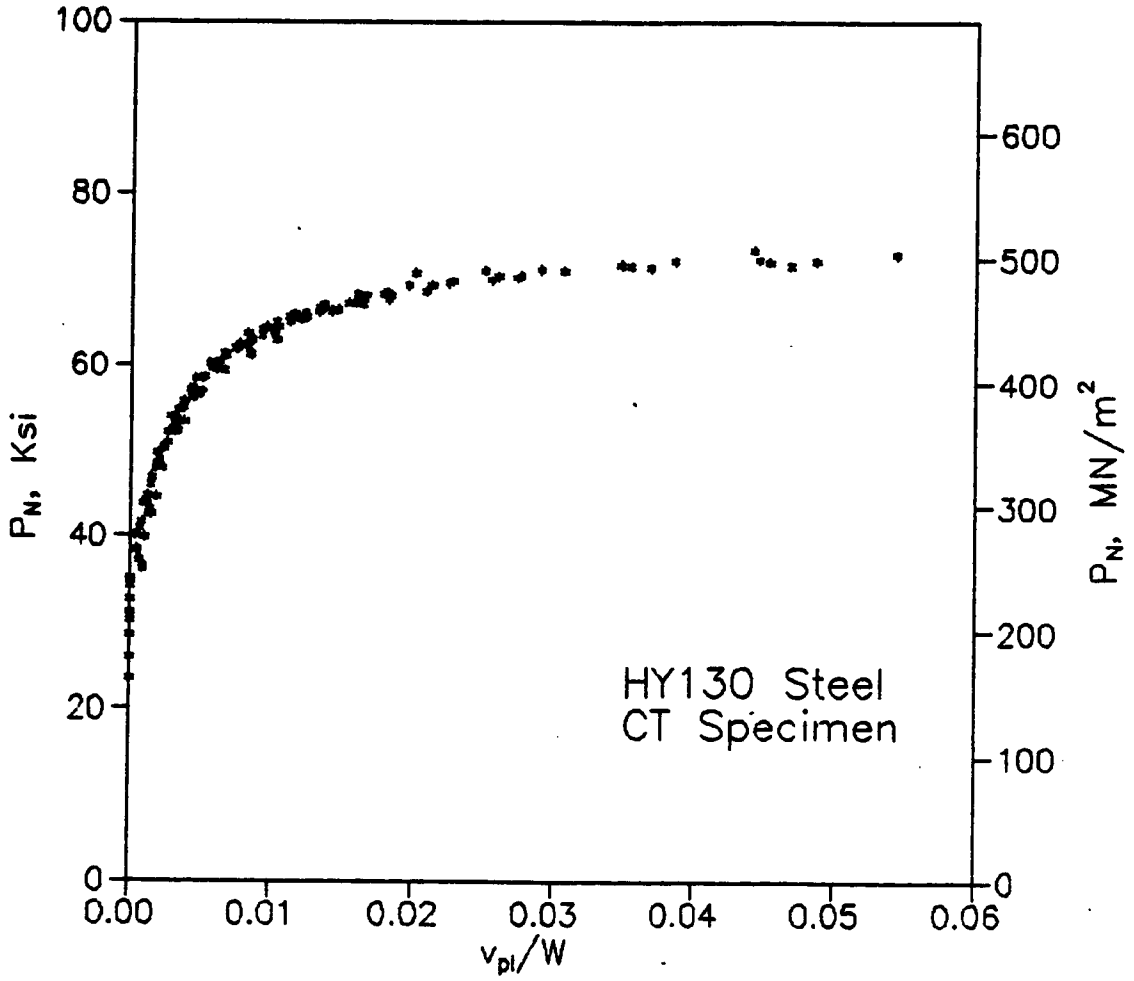


Fig. 4.1 - Deformation function for the HY130 CT set developed by load normalization using a power law geometry function with a power law exponent of 2.13.

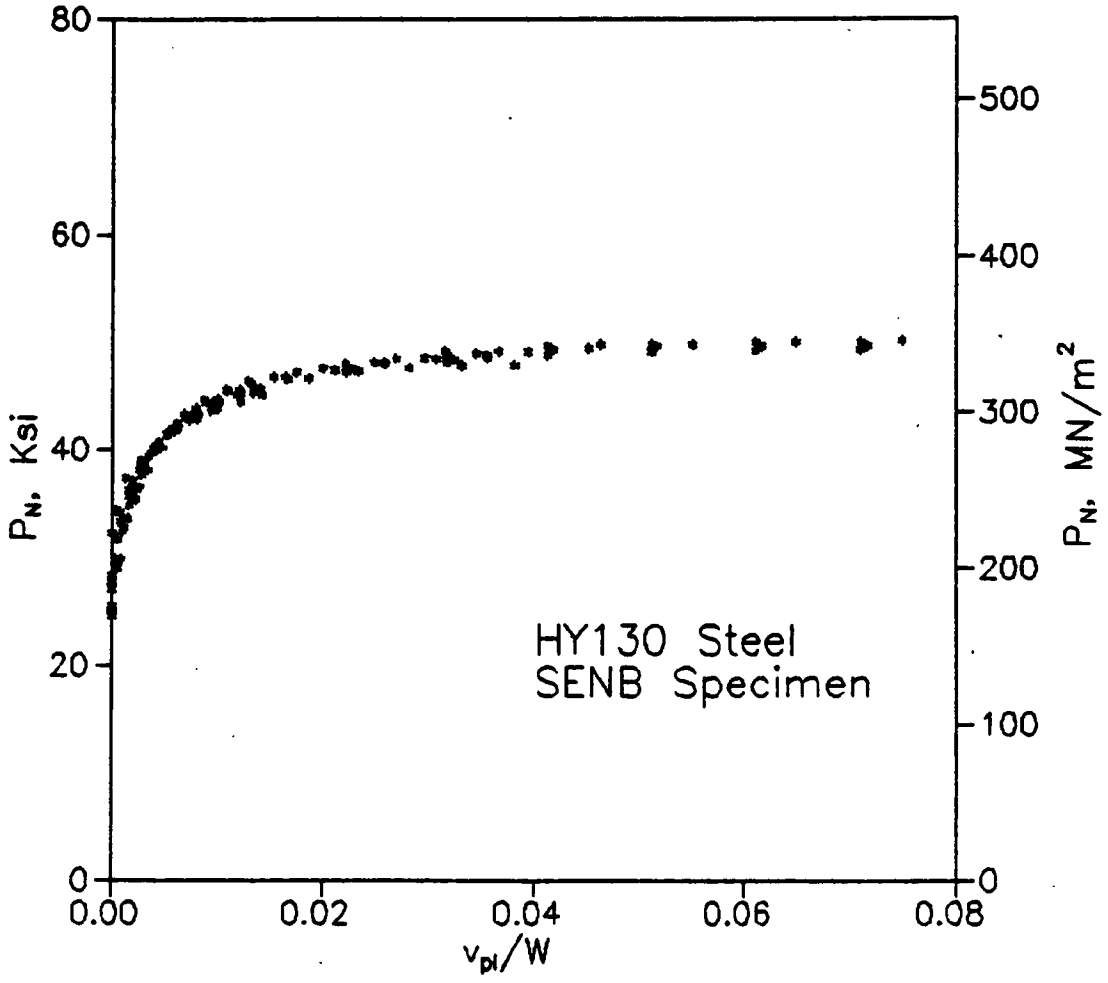


Fig. 4.2 - Deformation function for the HY130 SENB set developed by load normalization using a power law geometry function with a power law exponent of 1.96.

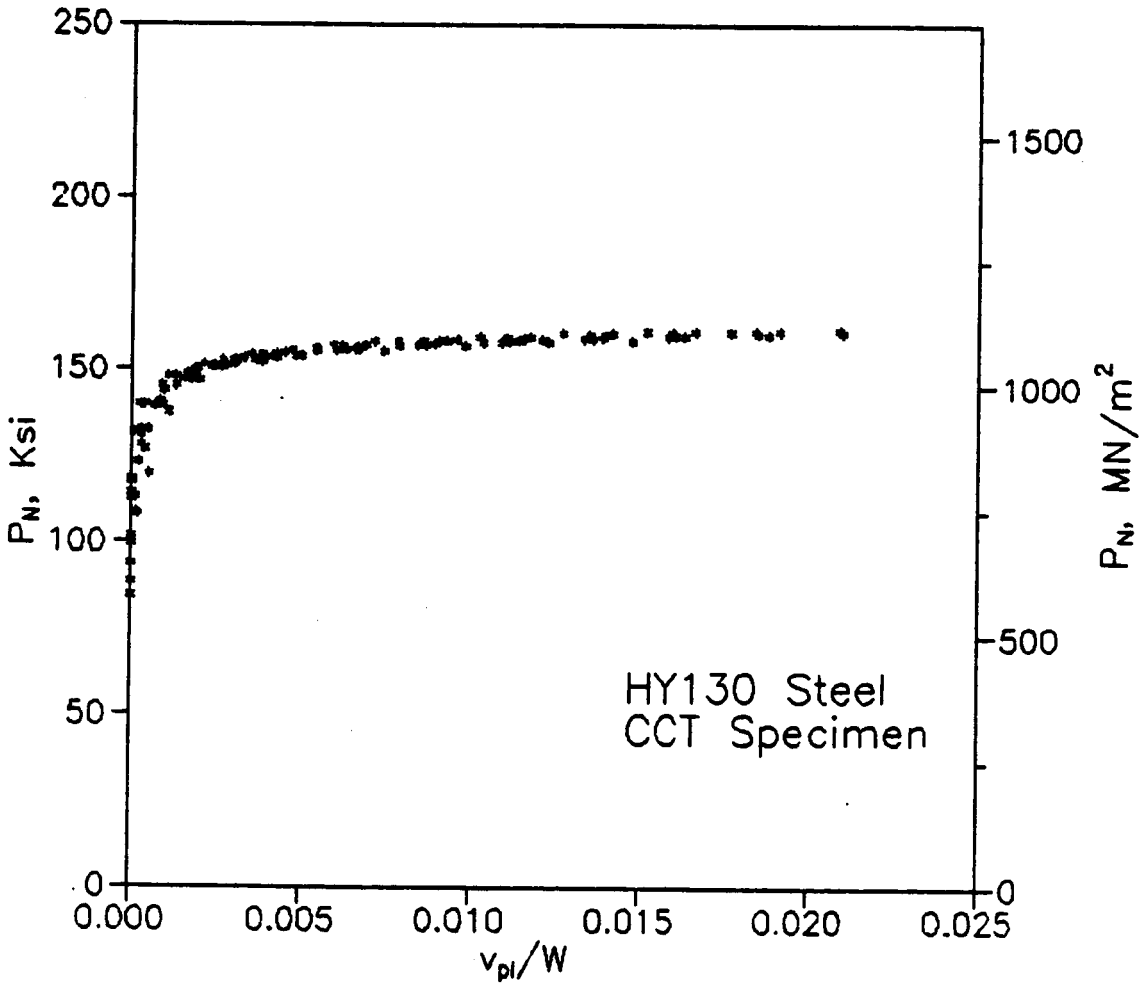


Fig. 4.3 - Deformation function for the HY130 CCT set developed by load normalization using a power law geometry function with a power law exponent of 0.963.

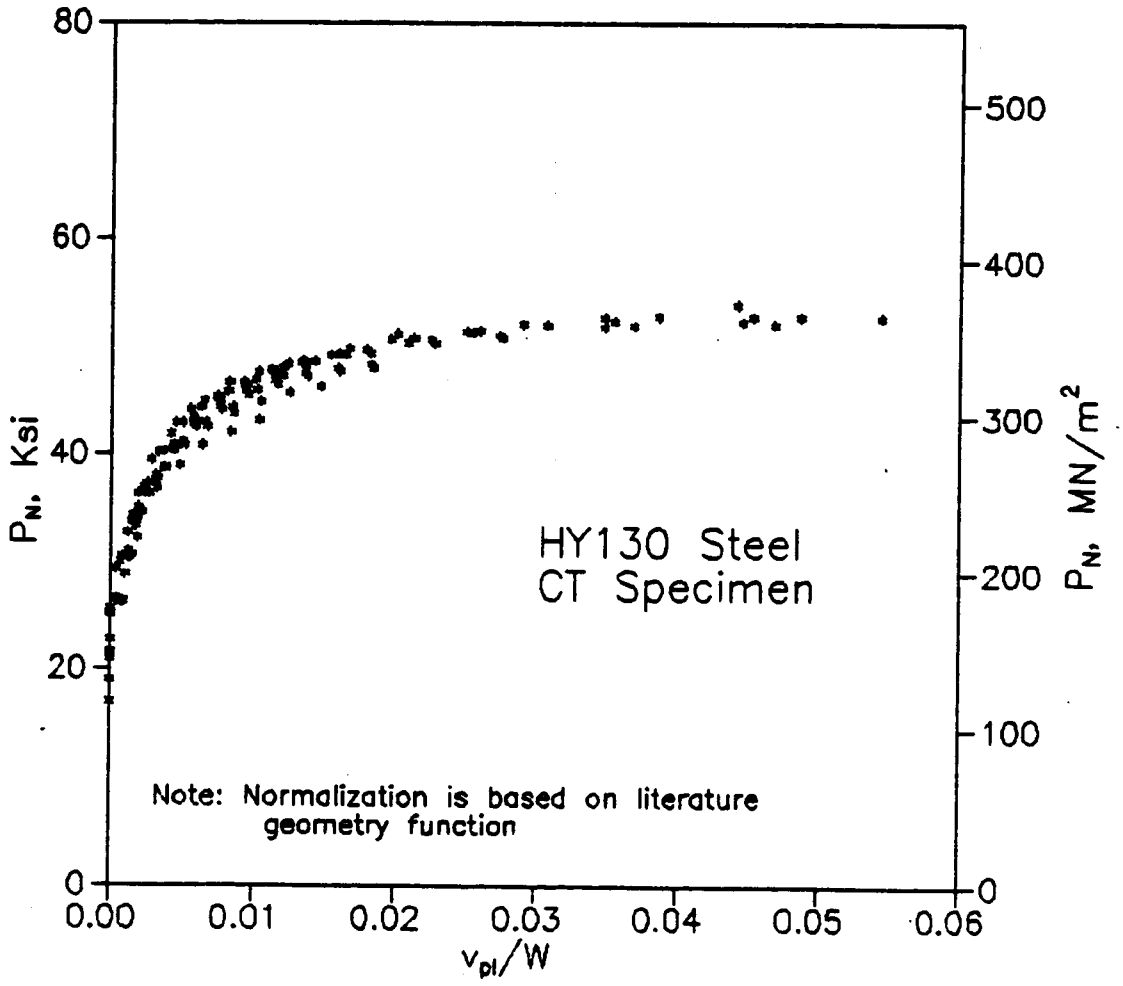


Fig. 4.4 - Deformation function for the HY130 CT set developed by load normalization using the geometry function expression given in Eq [3.7].

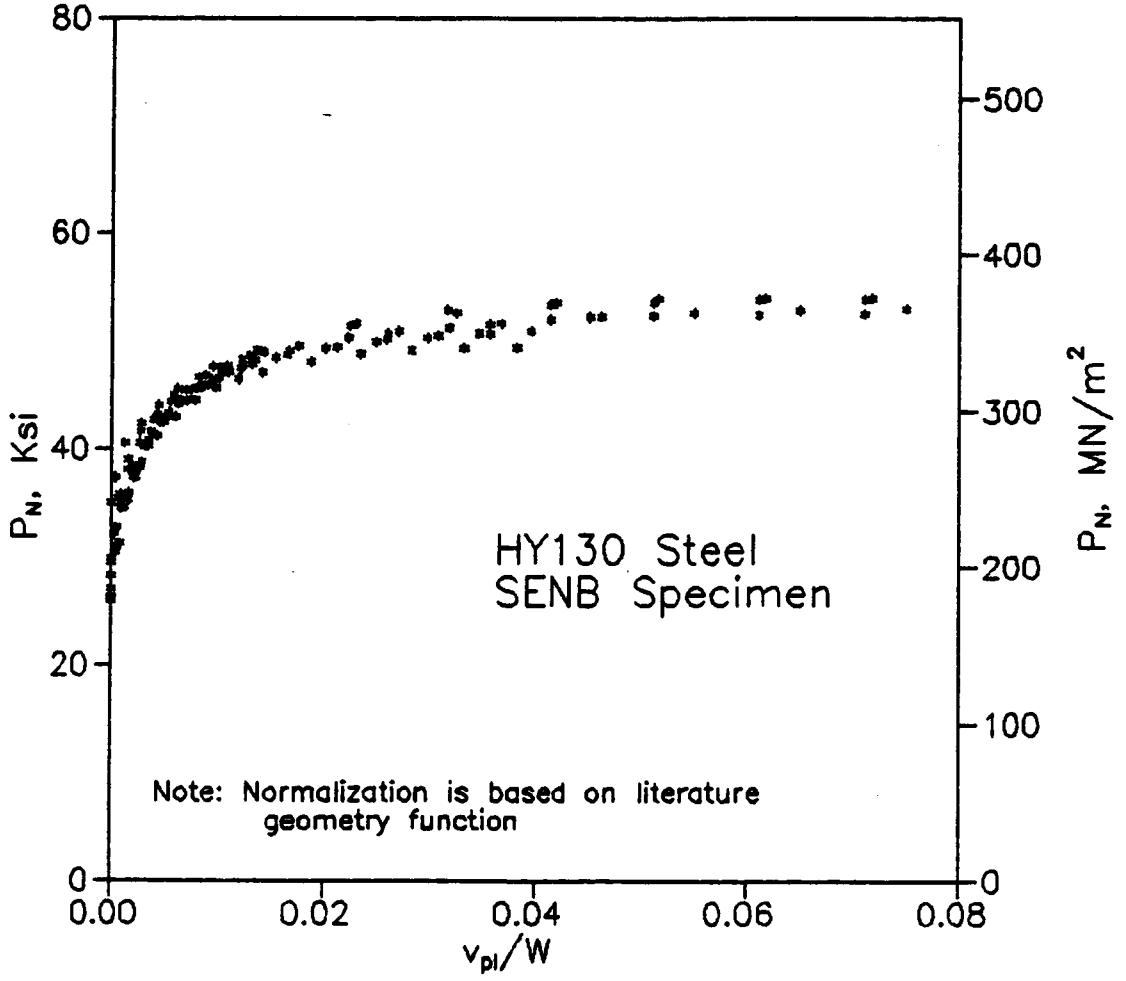


Fig. 4.5 - Deformation function for the HY130 SENB set developed by load normalization using a power law geometry function with a power law exponent of 2.0.

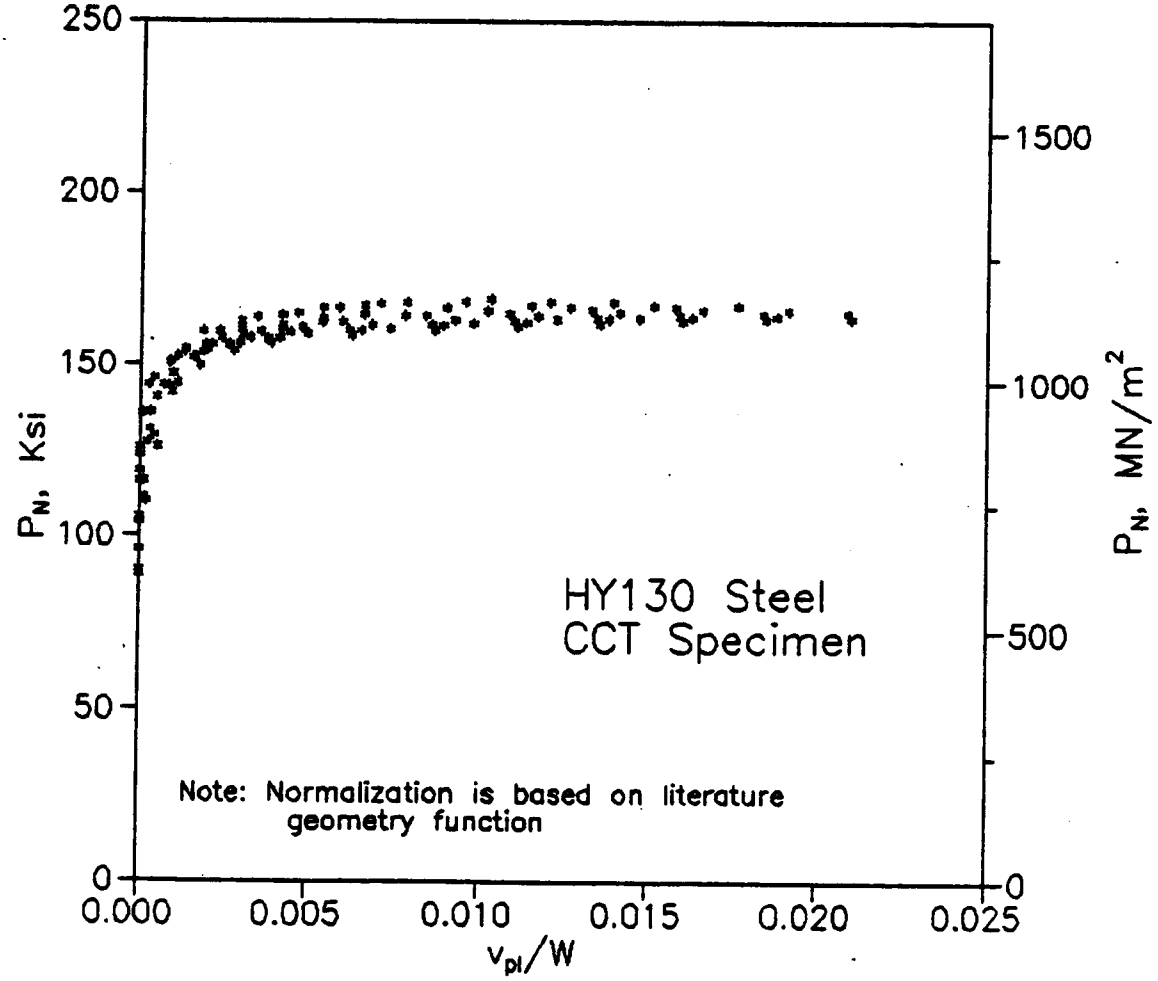


Fig. 4.6 - Deformation function for the HY130 CCT set developed by load normalization using a power law geometry function with a power law exponent of 1.0.

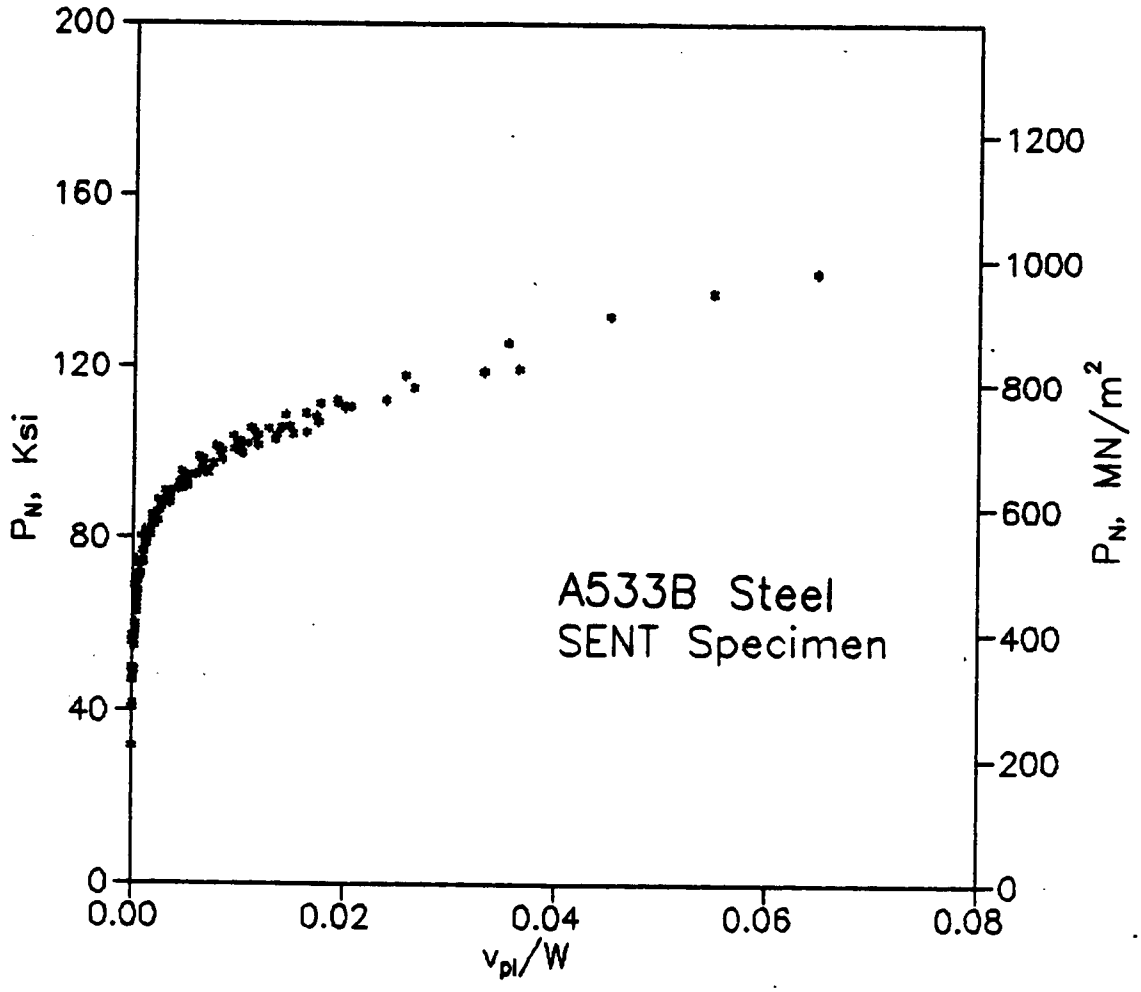


Fig. 4.7 - Deformation function for the A533B SENT set developed by load normalization using a power law geometry function with a power law exponent of 2.44.

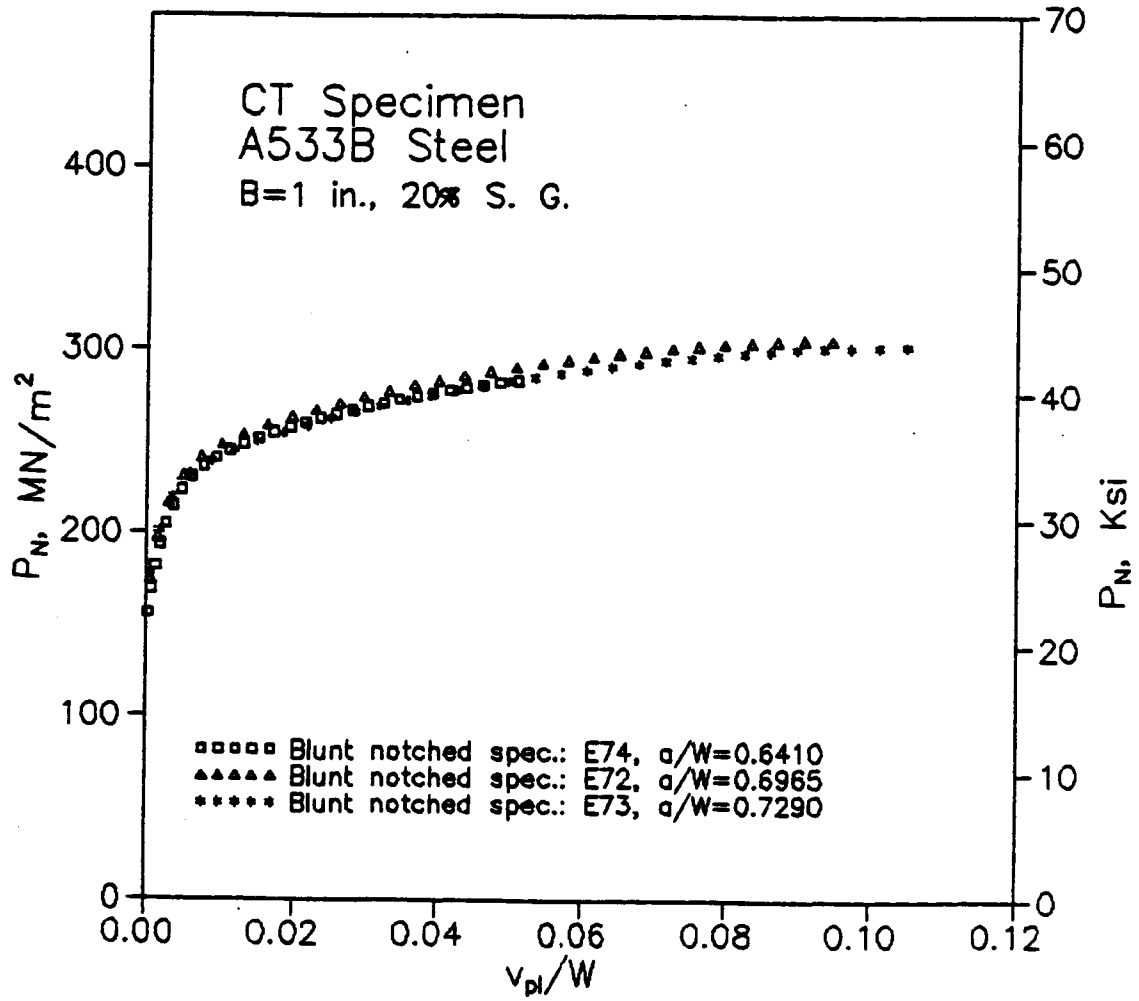


Fig. 4.8 - Deformation function for the A533B blunt notched CT specimens developed by load normalization using a power law geometry function with a power law exponent of 2.19.

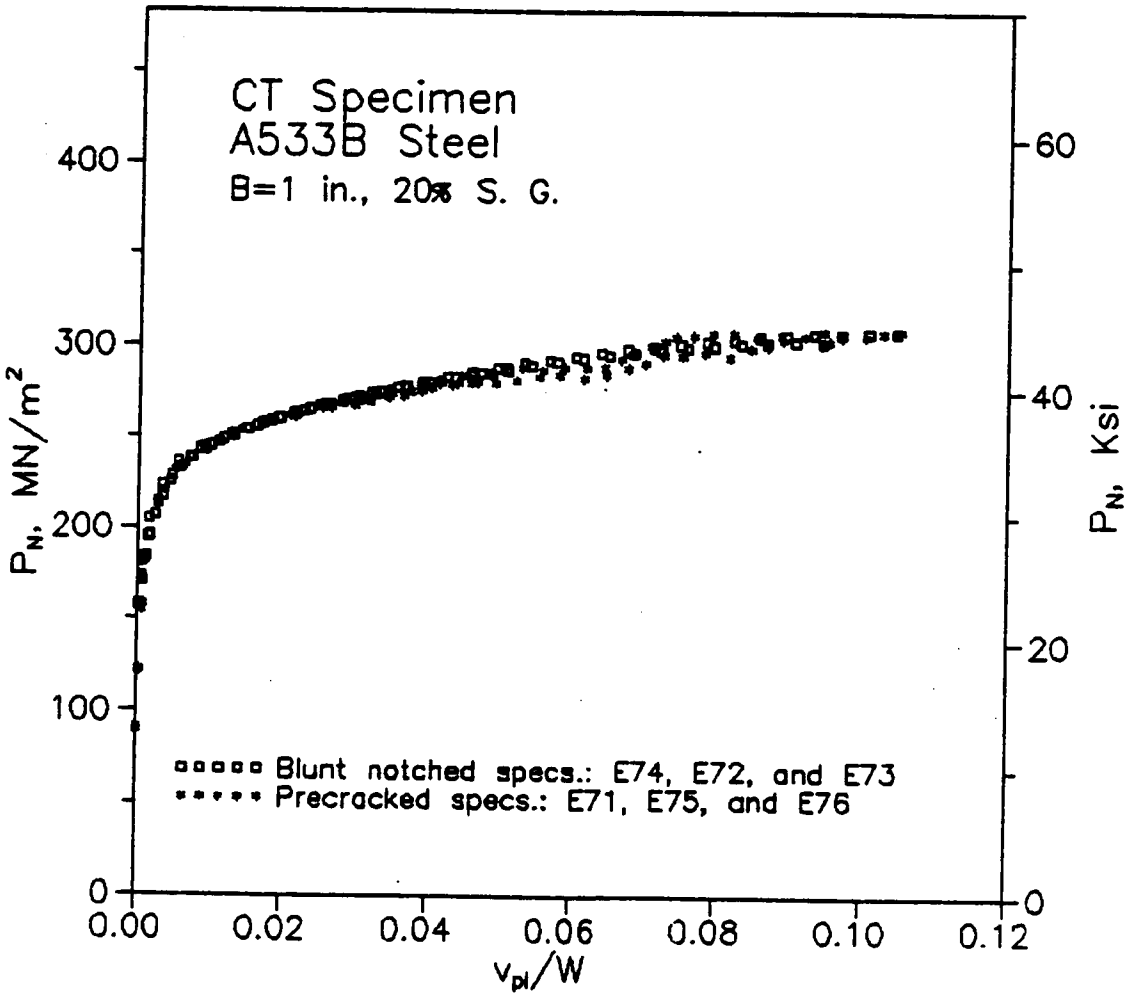


Fig. 4.9 - Deformation functions for both blunt notched and precracked A533B CT specimens sets developed by load normalization using a power law geometry function with a power law exponent of 2.12.

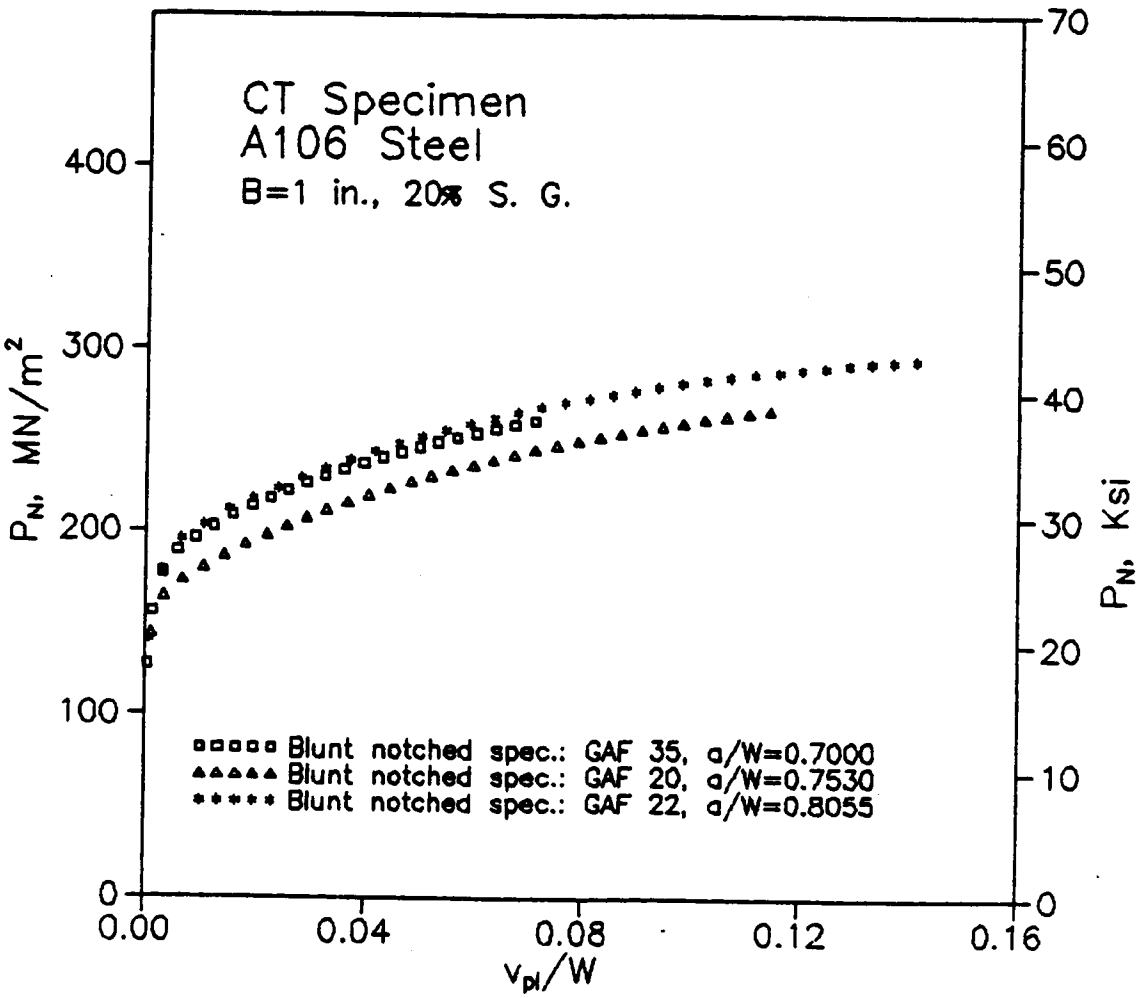


Fig. 4.10 - Deformation function for the A106 blunt notched CT specimens developed by load normalization using a power law geometry function with a power law exponent of 2.11.

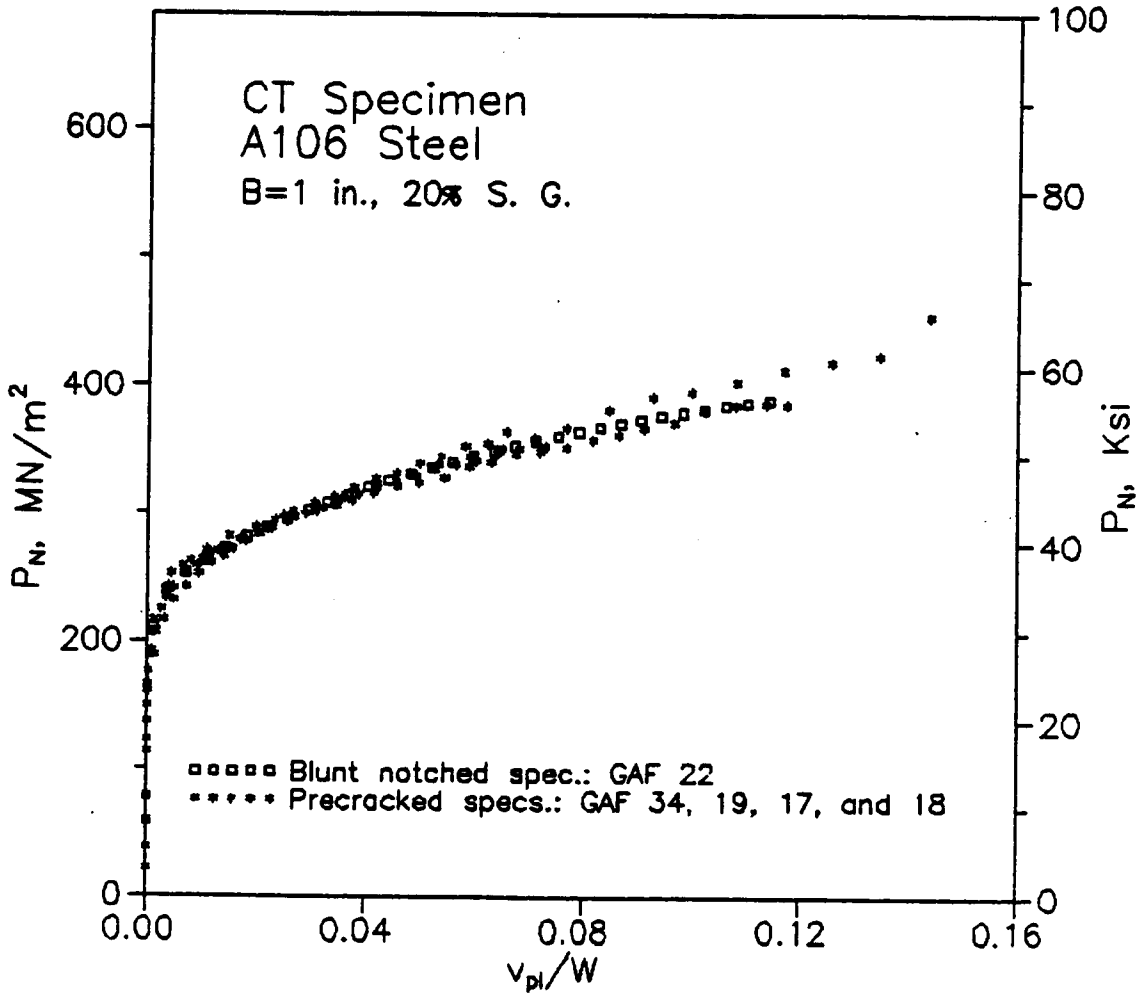


Fig. 4.11 - Deformation function for one blunt notched and four precracked A106 CT specimens developed by load normalization using a power law geometry function with a power law exponent of 2.38.

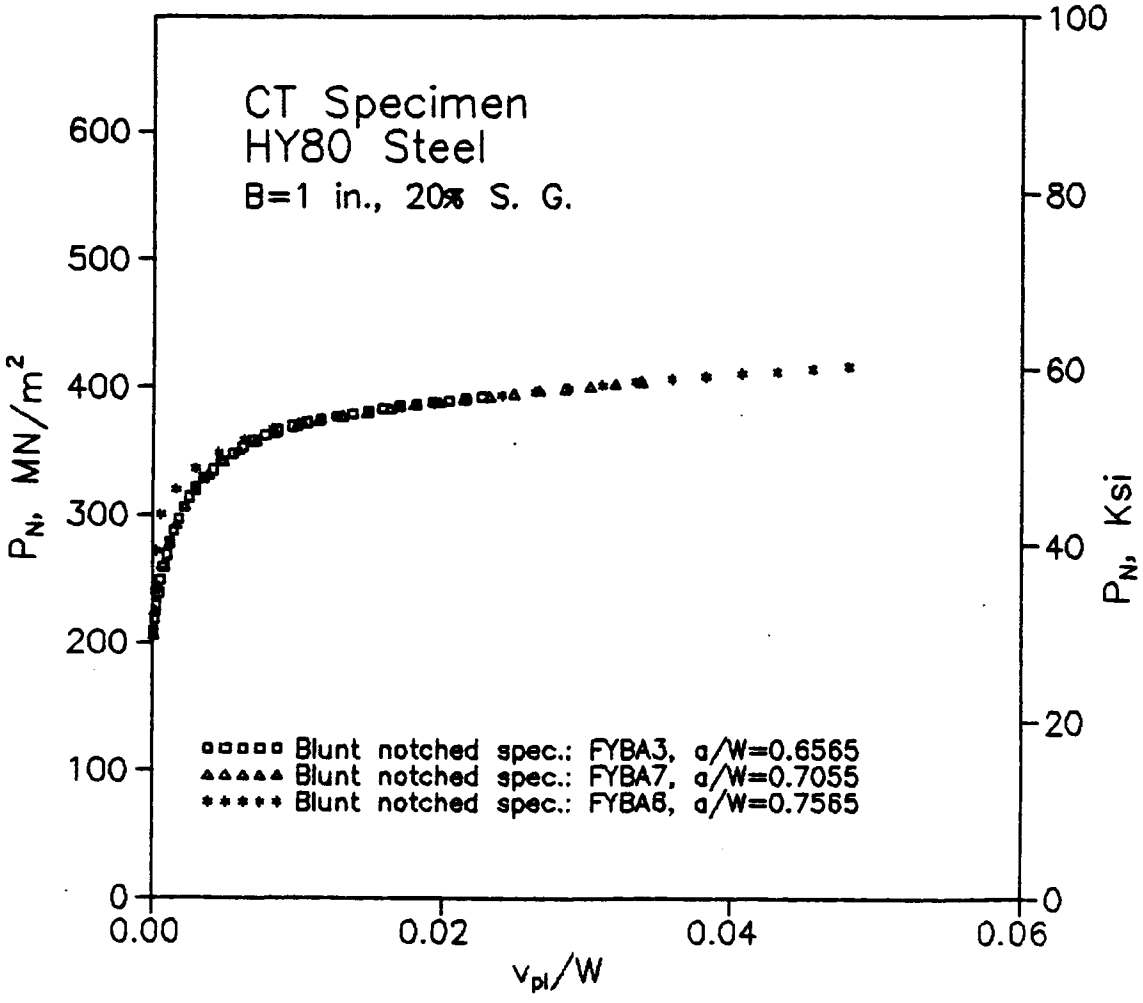


Fig. 4.12 - Deformation function for the HY80 blunt notched CT specimens developed by load normalization using a power law geometry function with a power law exponent of 2.25.

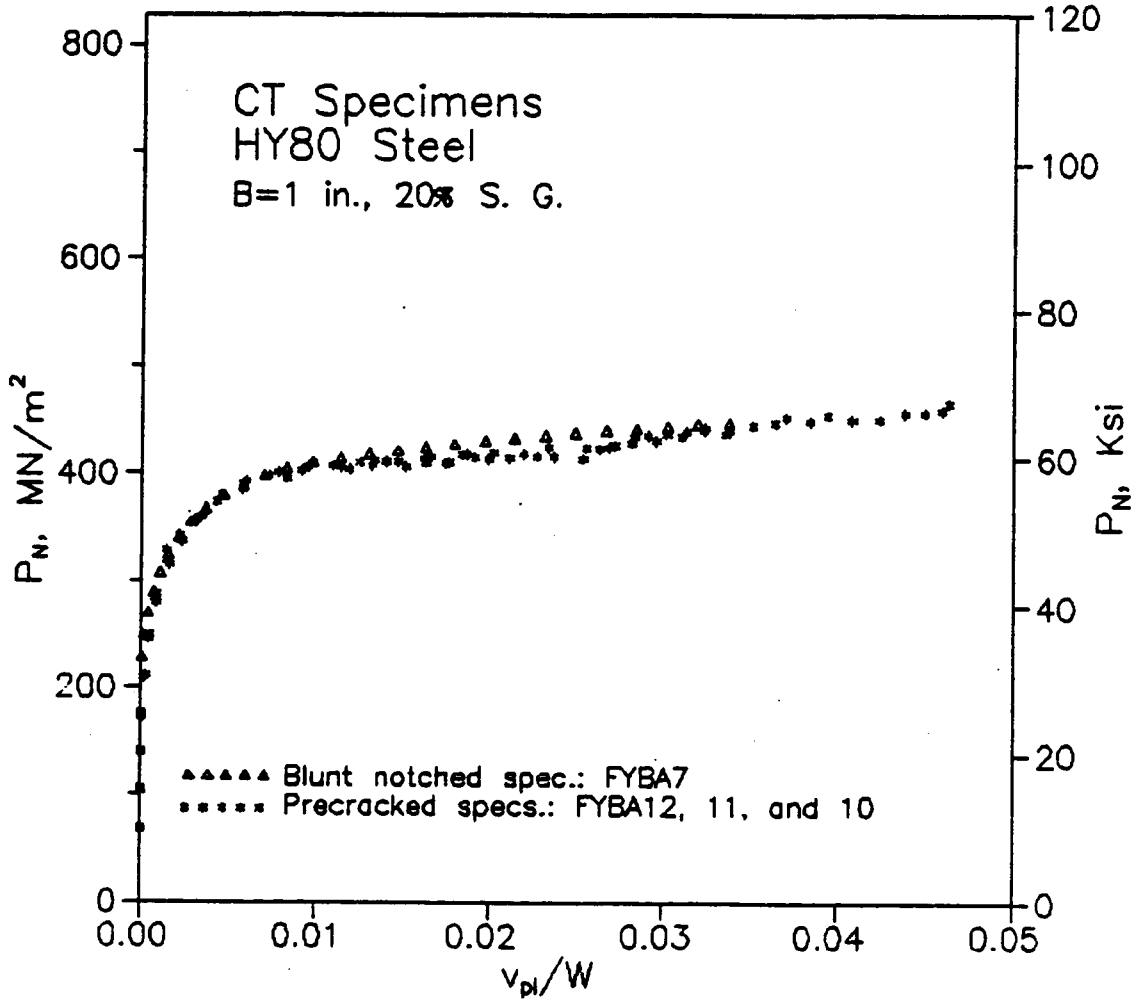


Fig. 4.13 - Deformation function for one blunt notched and three precracked HY80 CT specimens developed by load normalization using a power law geometry function with a power law exponent of 2.28.

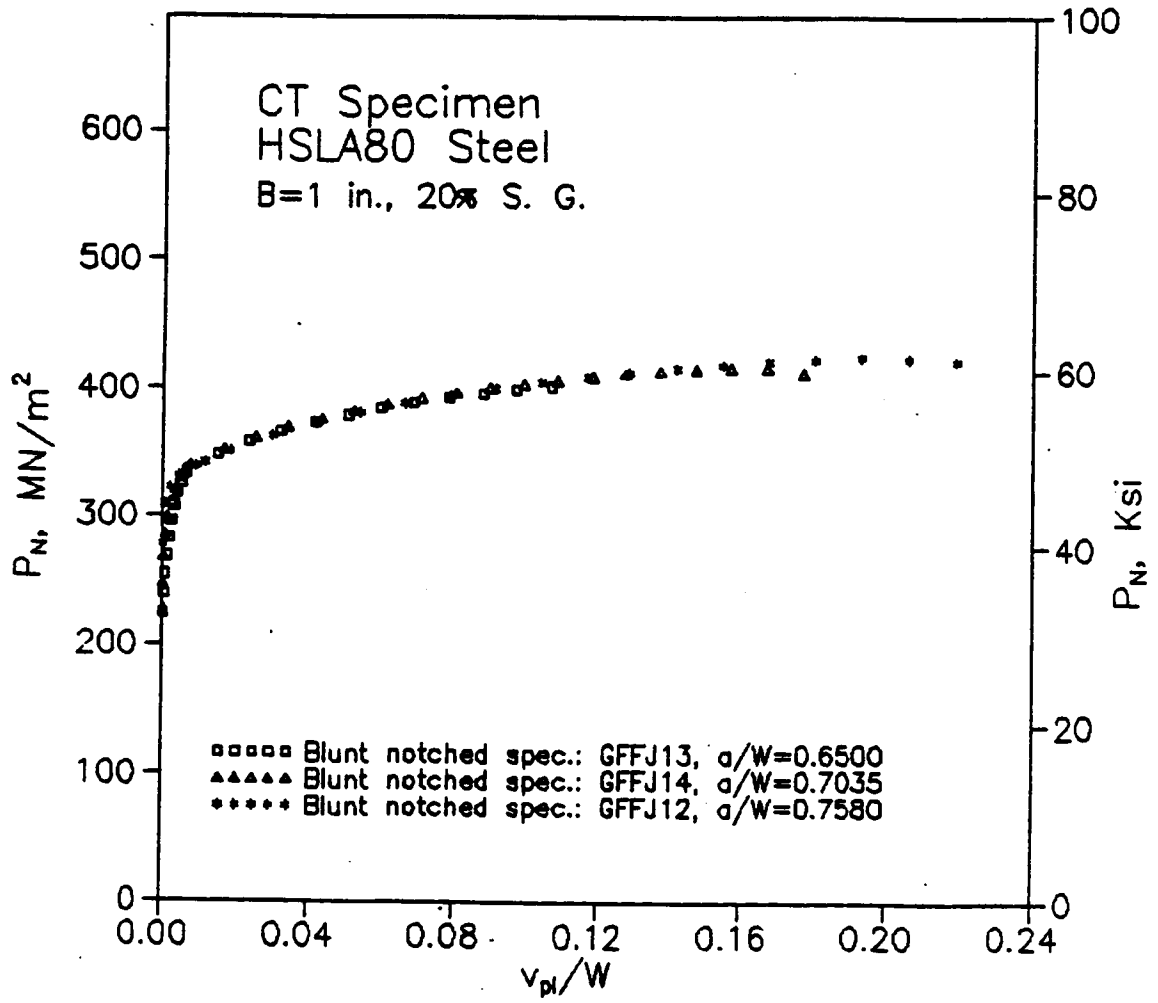


Fig. 4.14 - Deformation function for the HSLA80 blunt notched CT specimens developed by load normalization using a power law geometry function with a power law exponent of 2.32.

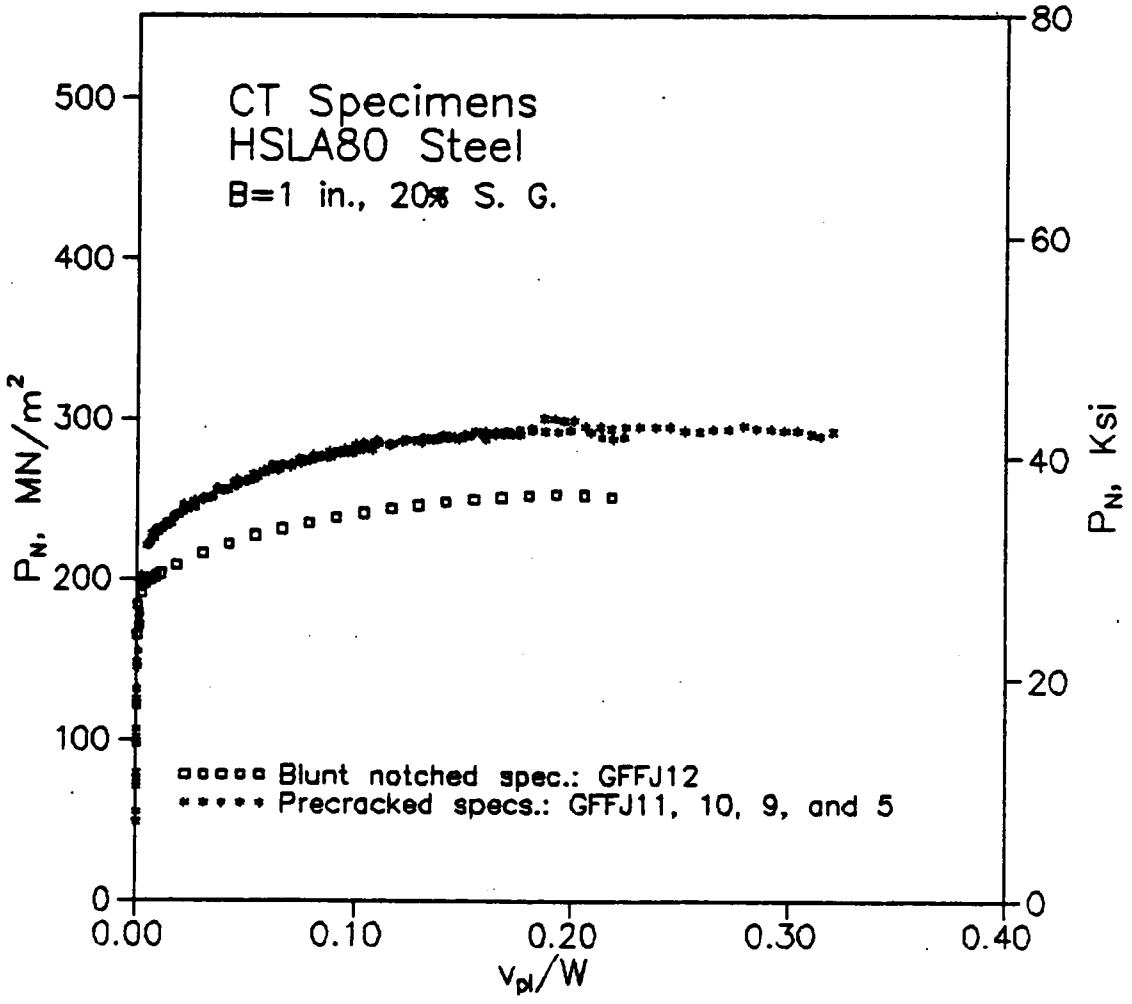


Fig. 4.15 - Deformation function for one blunt notched and four precracked HSLA80 CT specimens developed by load normalization using a power law geometry function with a power law exponent of 1.87.

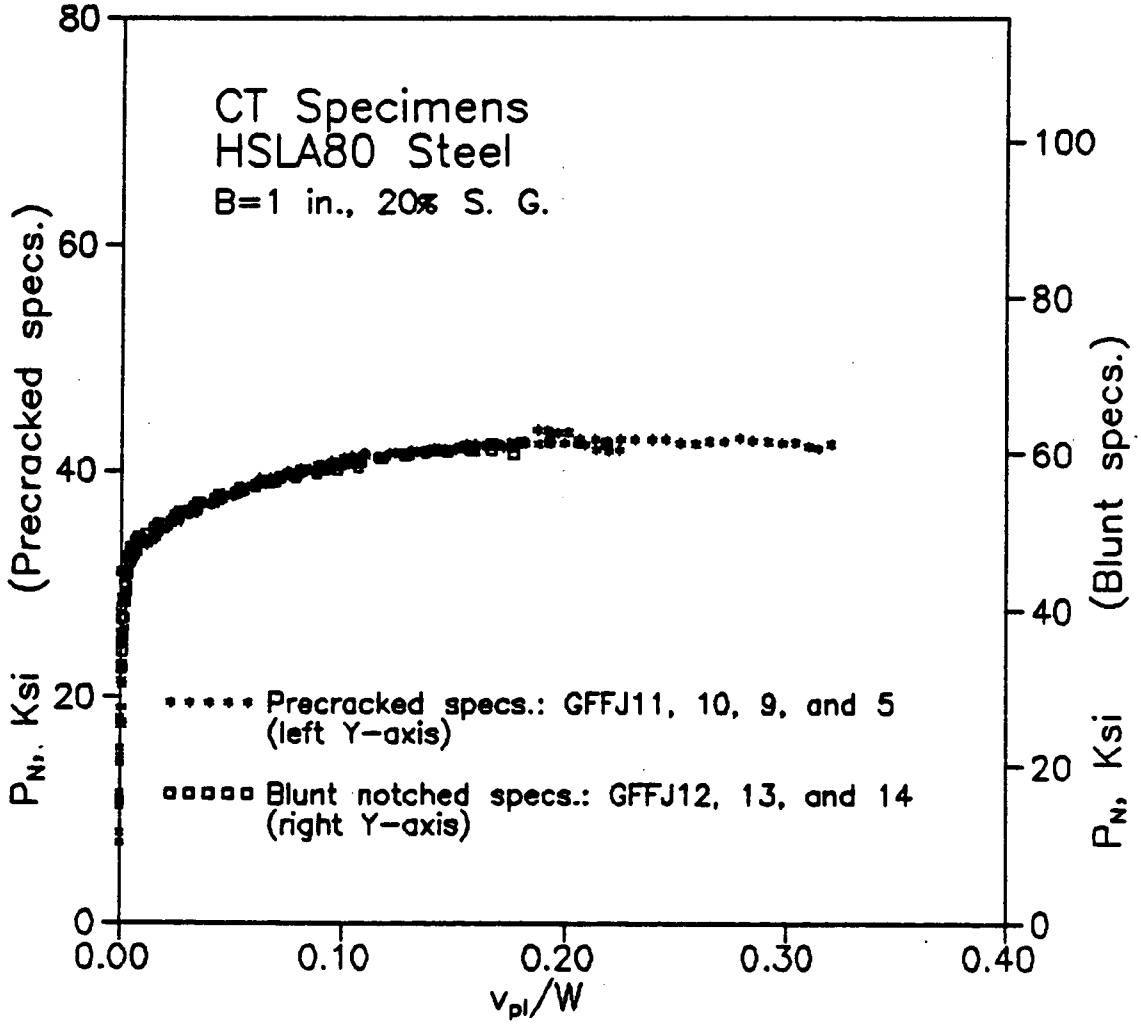


Fig. 4.16 - Deformation functions for both blunt notched and precracked HSLA80 CT specimens sets using different Y-axes.

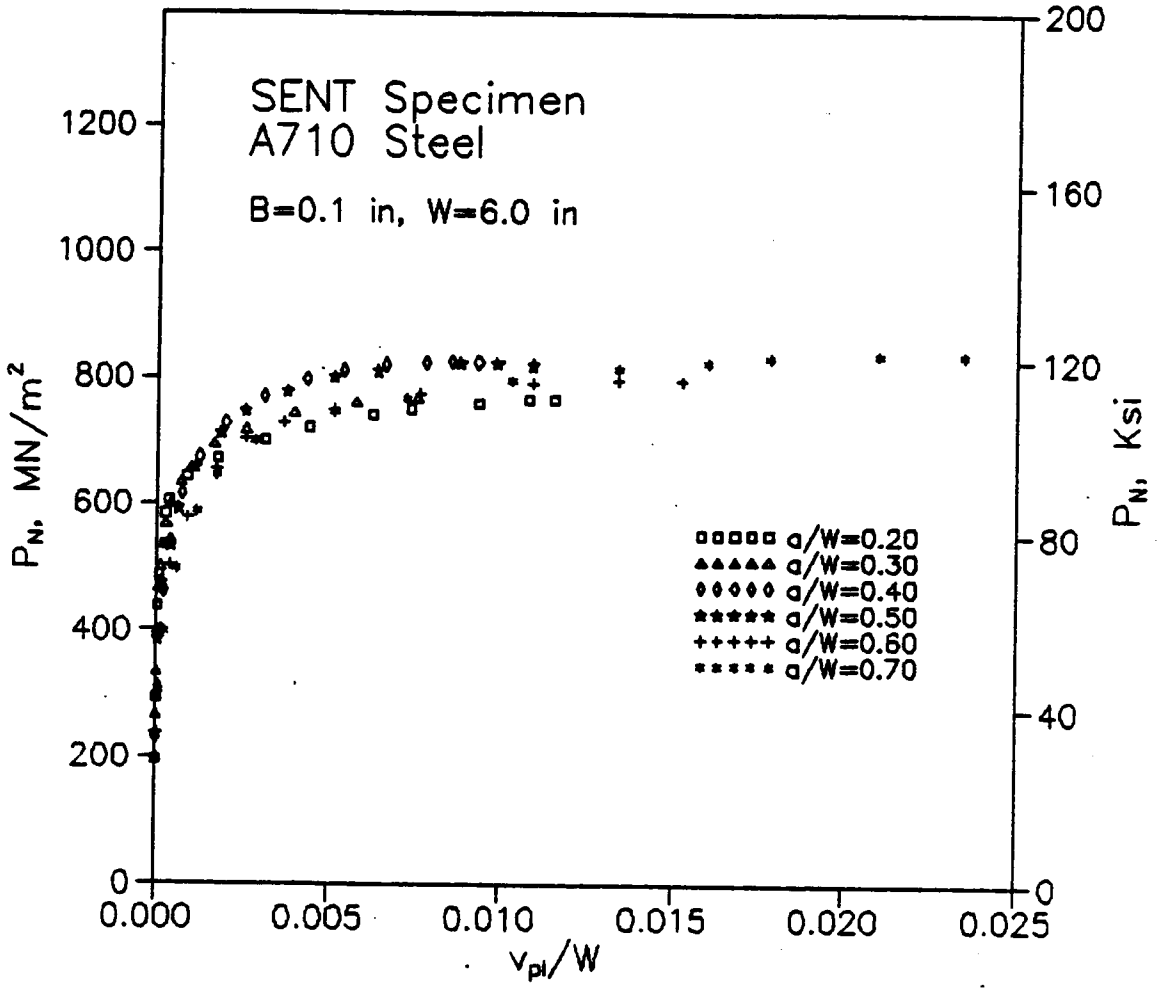


Fig. 4.17 - Deformation function for the load versus load line displacement test records of the A710 SENT thin specimens.

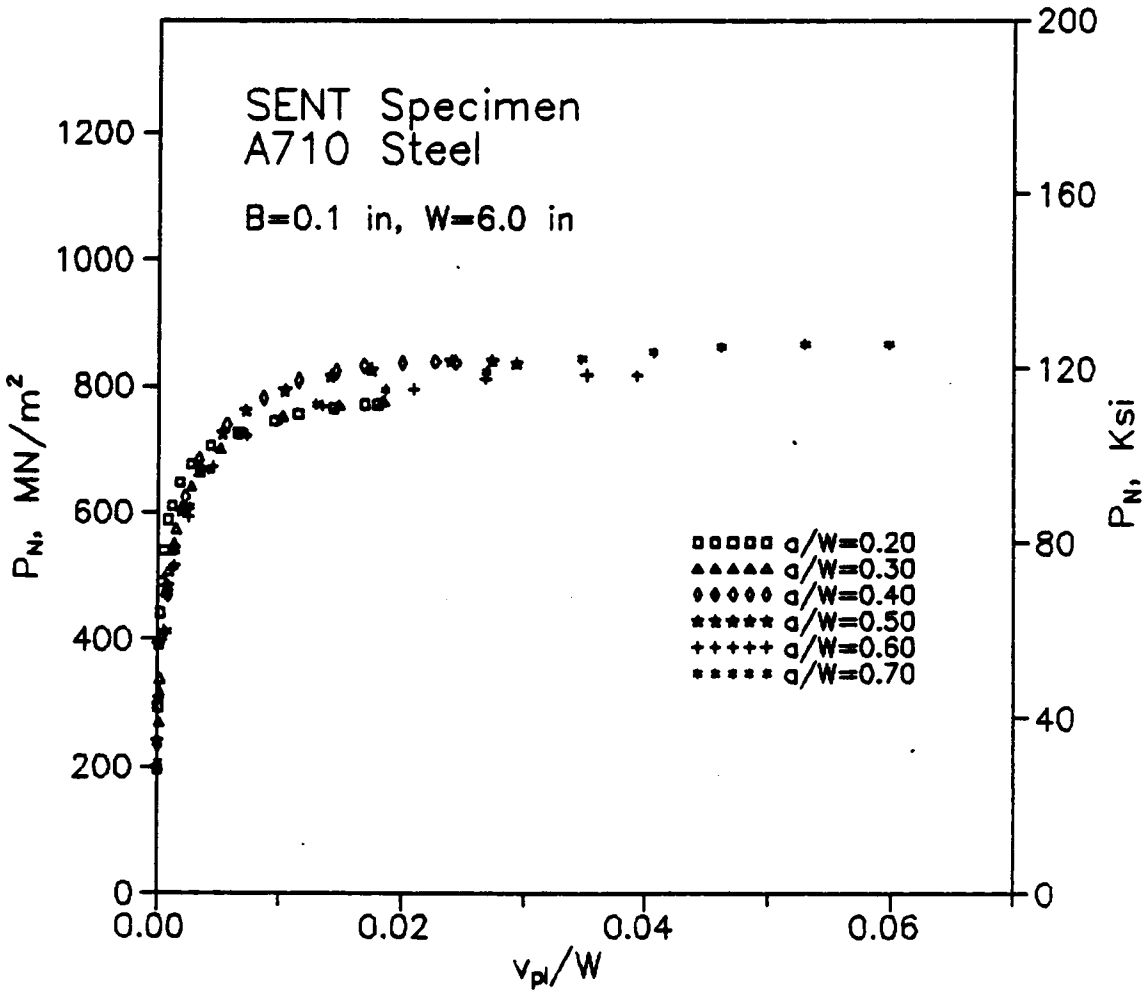


Fig. 4.18 - Deformation function for the load versus crack mouth opening displacement test records of the A710 SENT thin specimens.

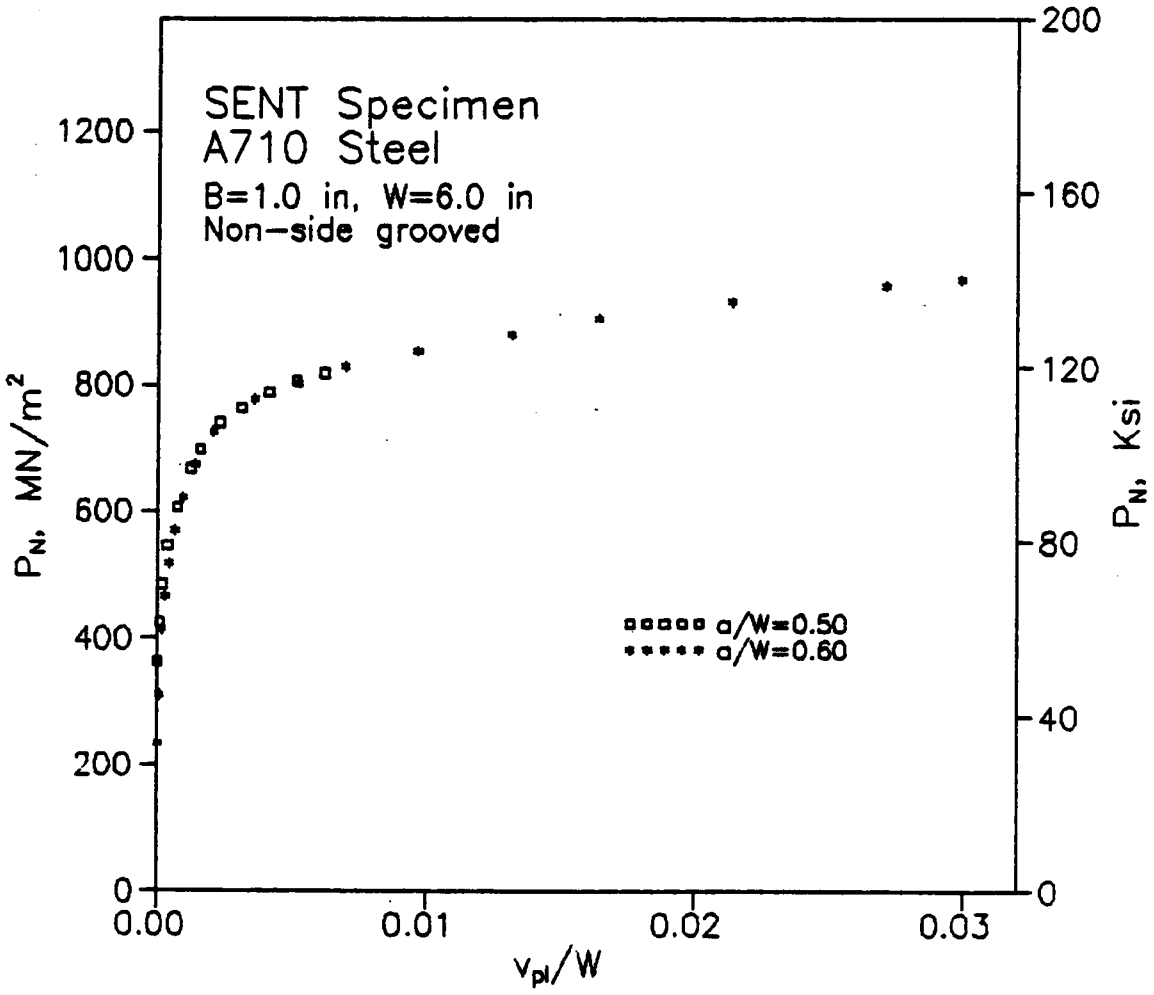


Fig. 4.19 - Deformation function for the load versus load line displacement test records of the A710 SENT specimens of 1.0 in. thickness with no side grooving.

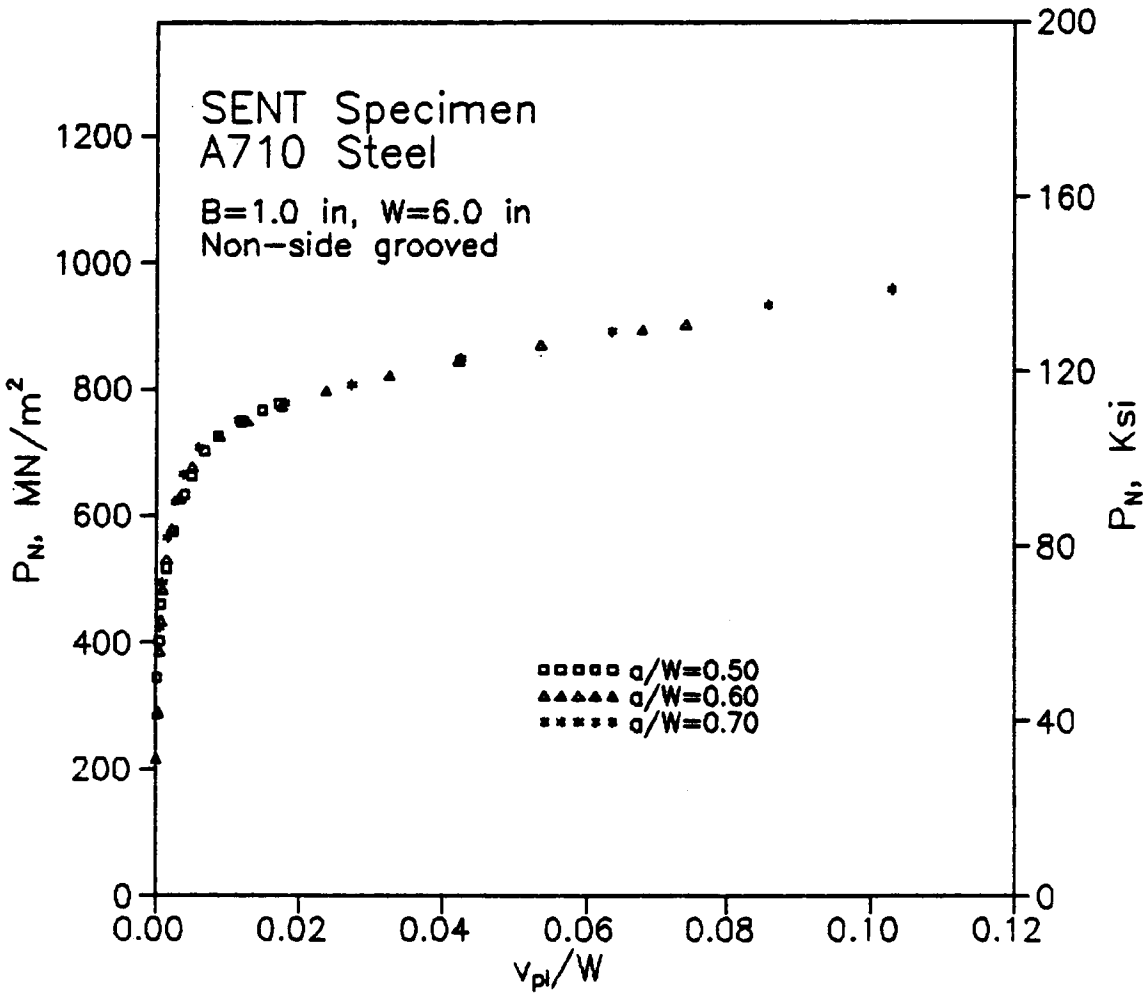


Fig. 4.20 - Deformation function for the load versus crack mouth opening displacement test records of the A710 SENT specimens of 1.0 in. thickness with no side grooving.

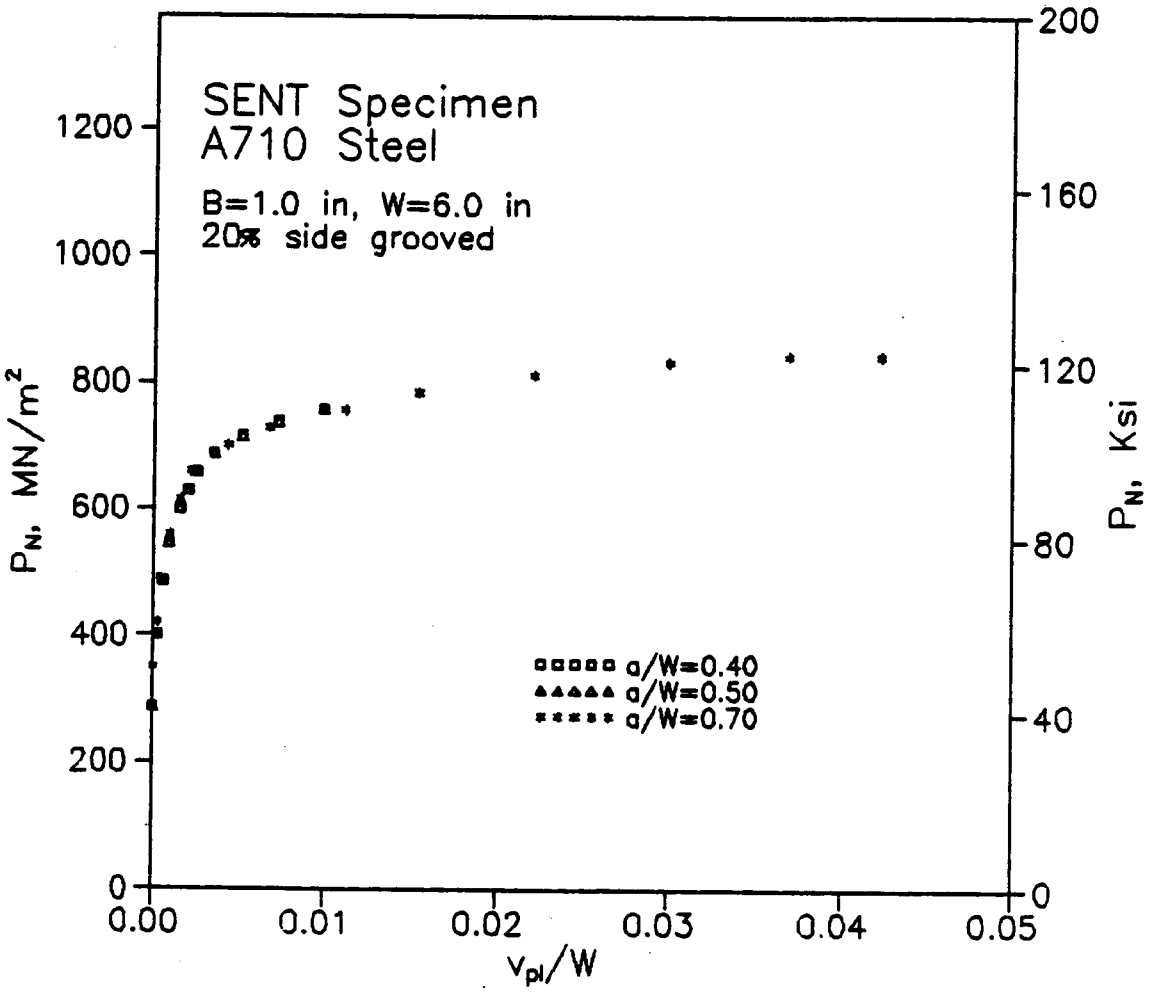


Fig. 4.21 - Deformation function for the load versus load line displacement test records of the A710 SENT specimens of 1.0 in. thickness with 20% side grooving.

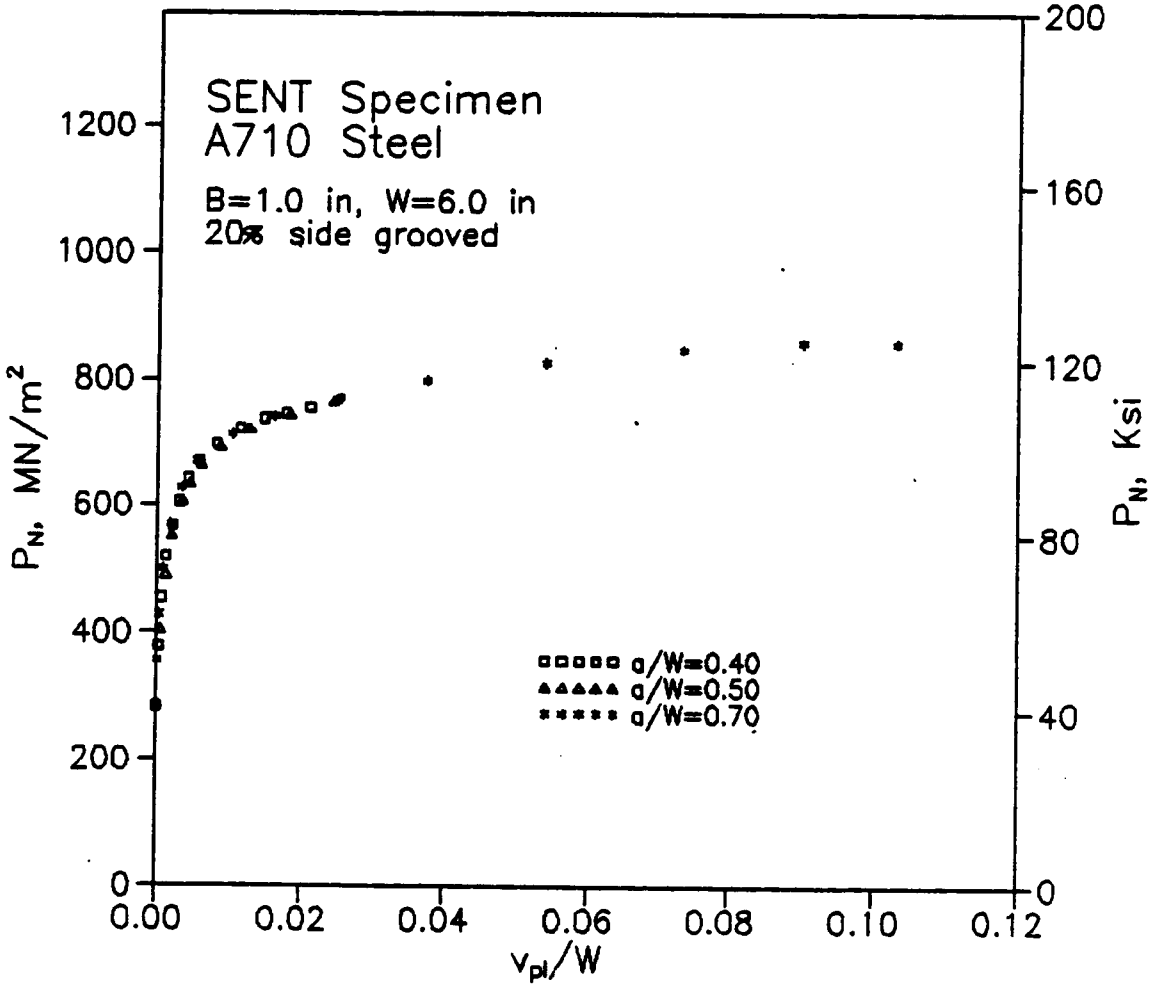


Fig. 4.22 - Deformation function for the load versus crack mouth opening displacement test records of the A710 SENT specimens of 1.0 in. thickness with 20% side grooving.

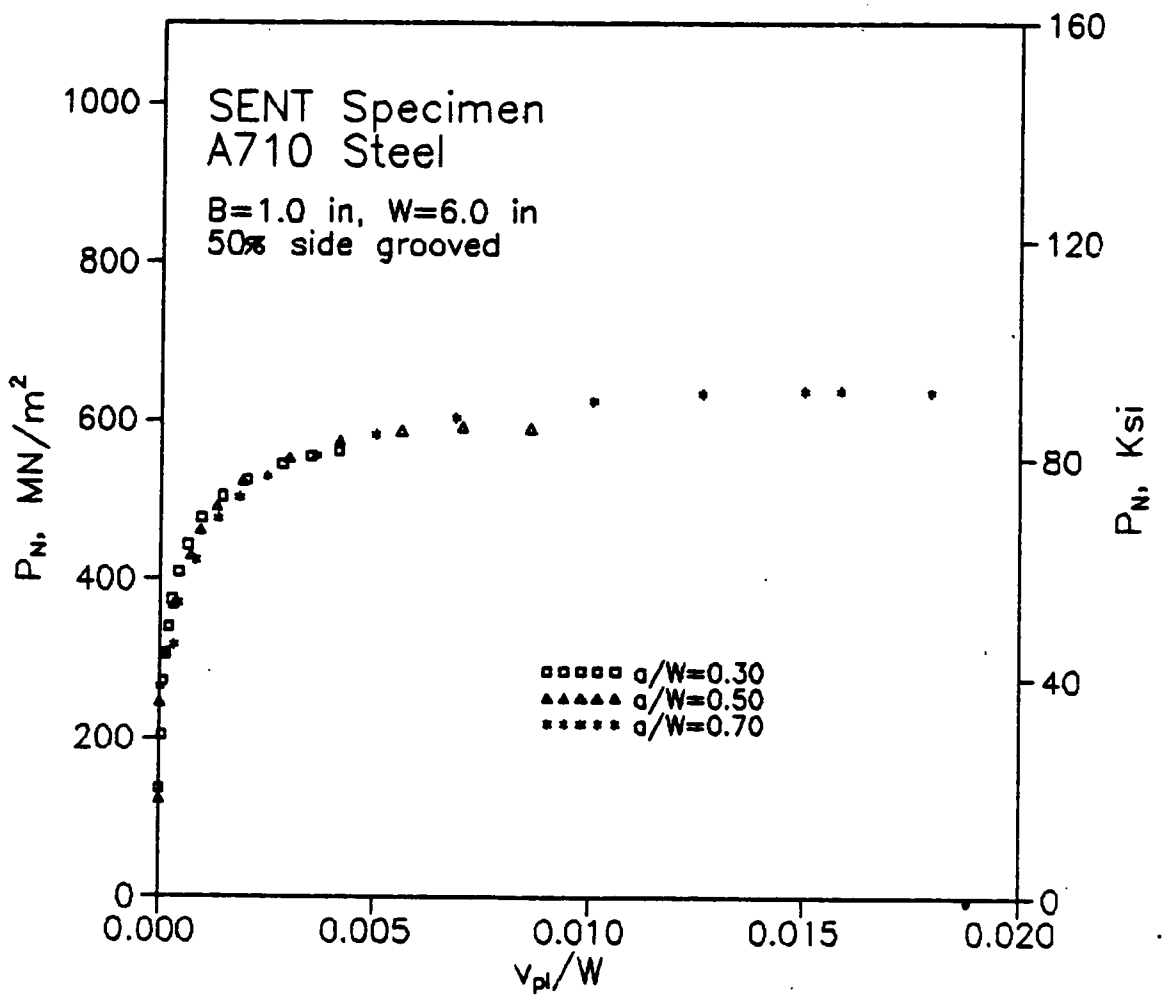


Fig. 4.23 - Deformation function for the load versus load line displacement test records of the A710 SENT specimens of 1.0 in. thickness with 50% side grooving.

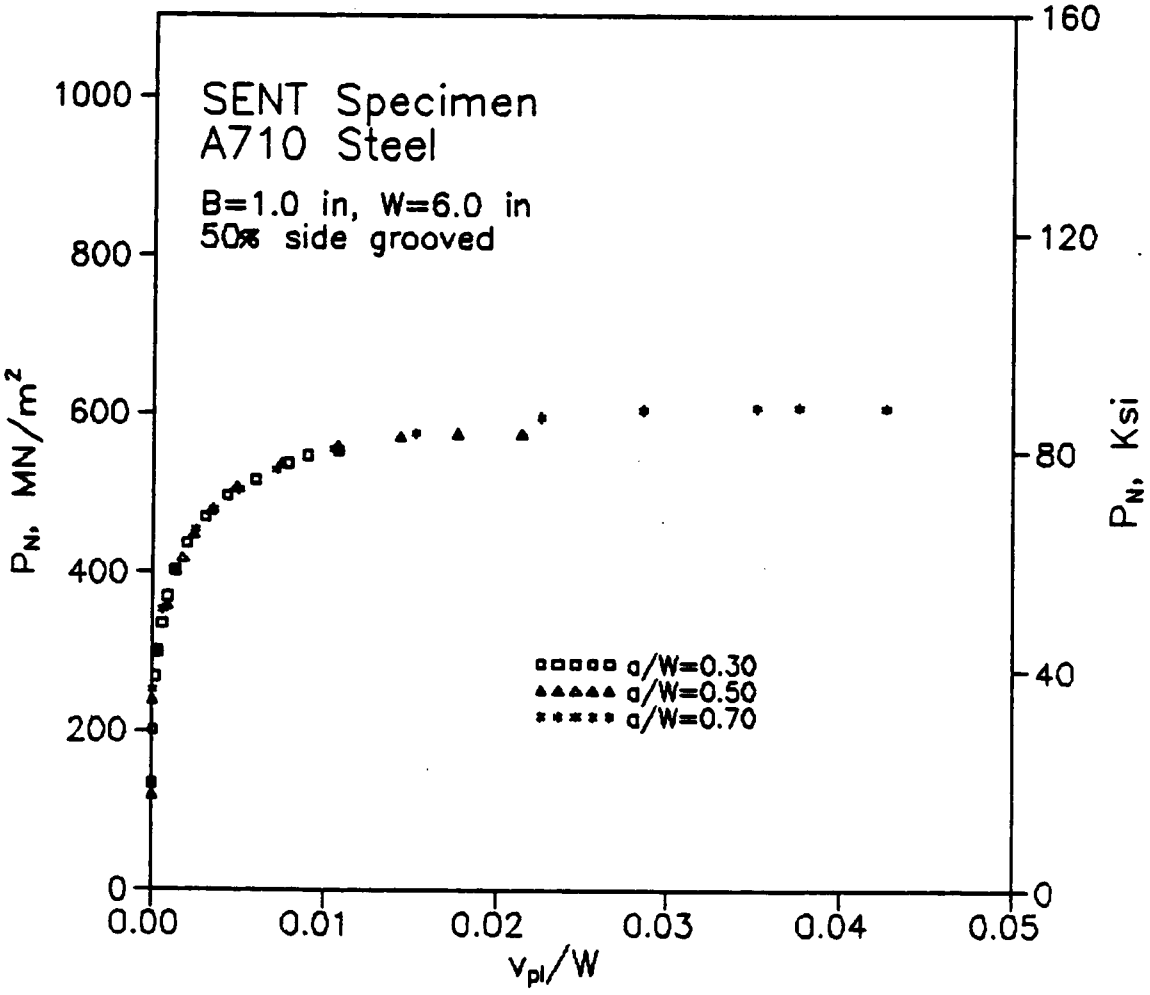


Fig. 4.24 - Deformation function for the load versus crack mouth opening displacement test records of the A710 SENT specimens of 1.0 in. thickness with 50% side grooving.

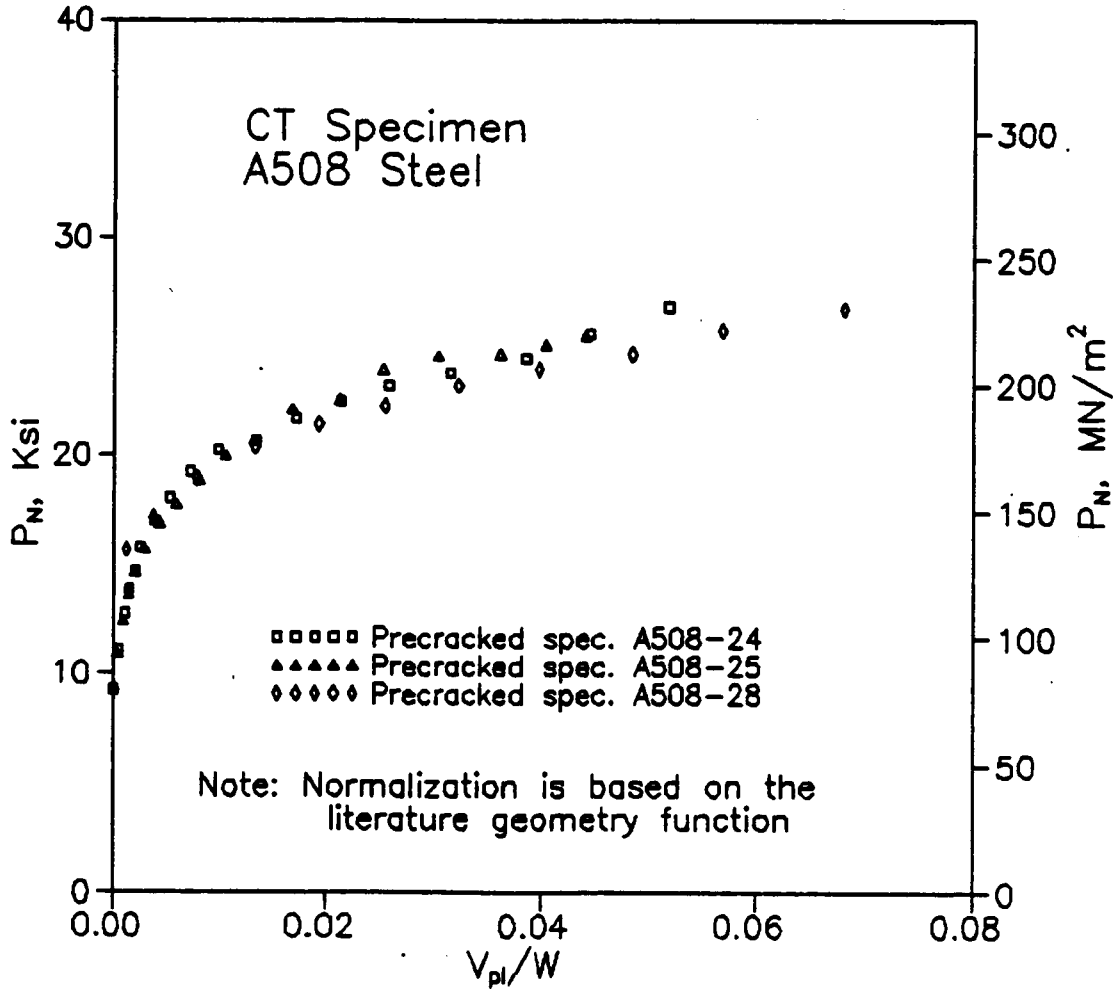


Fig. 4.25 - Load normalization in the A508 precracked specimens using the literature geometry function expression, Eq [3.7].

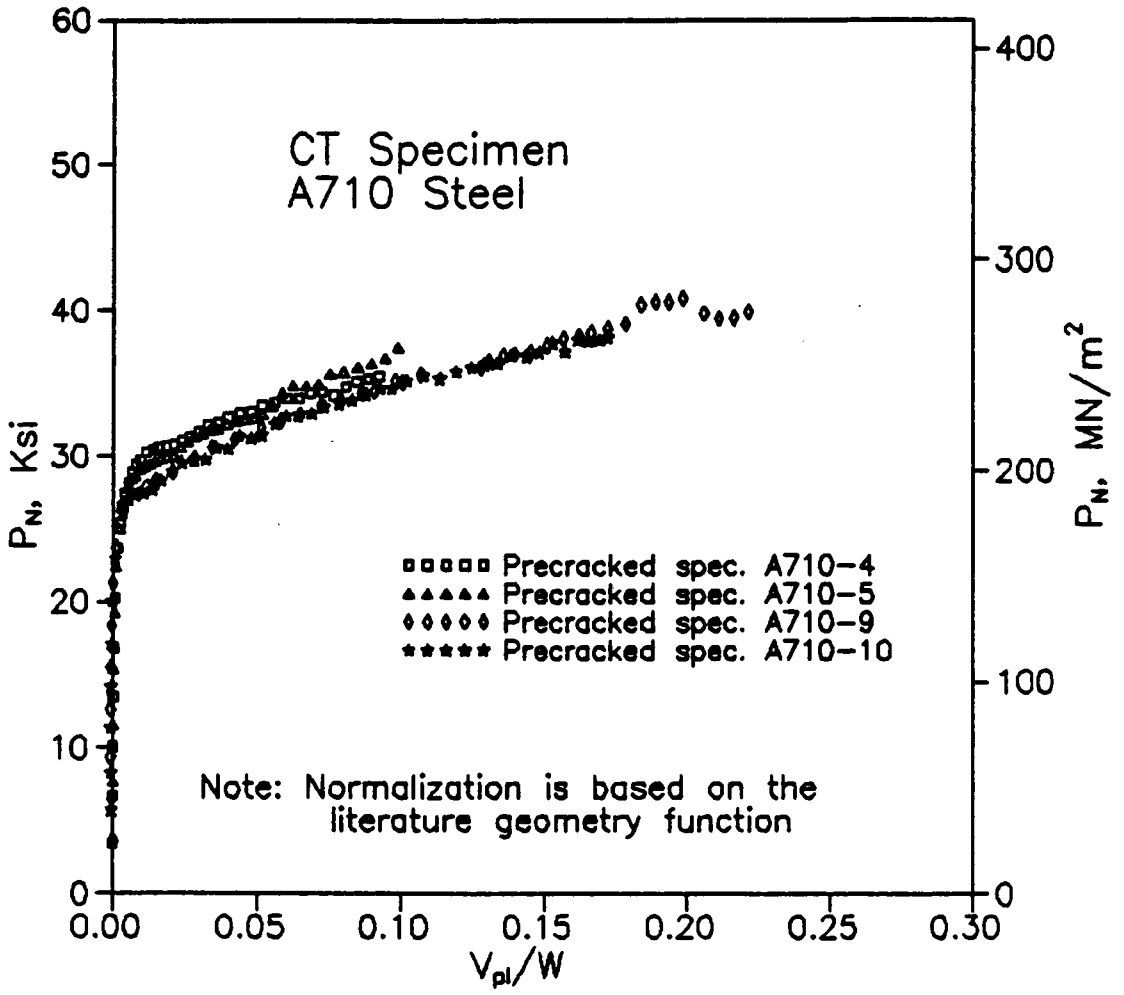


Fig. 4.26 - Load normalization in the A710 precracked specimens using the literature geometry function expression, Eq [3.7].

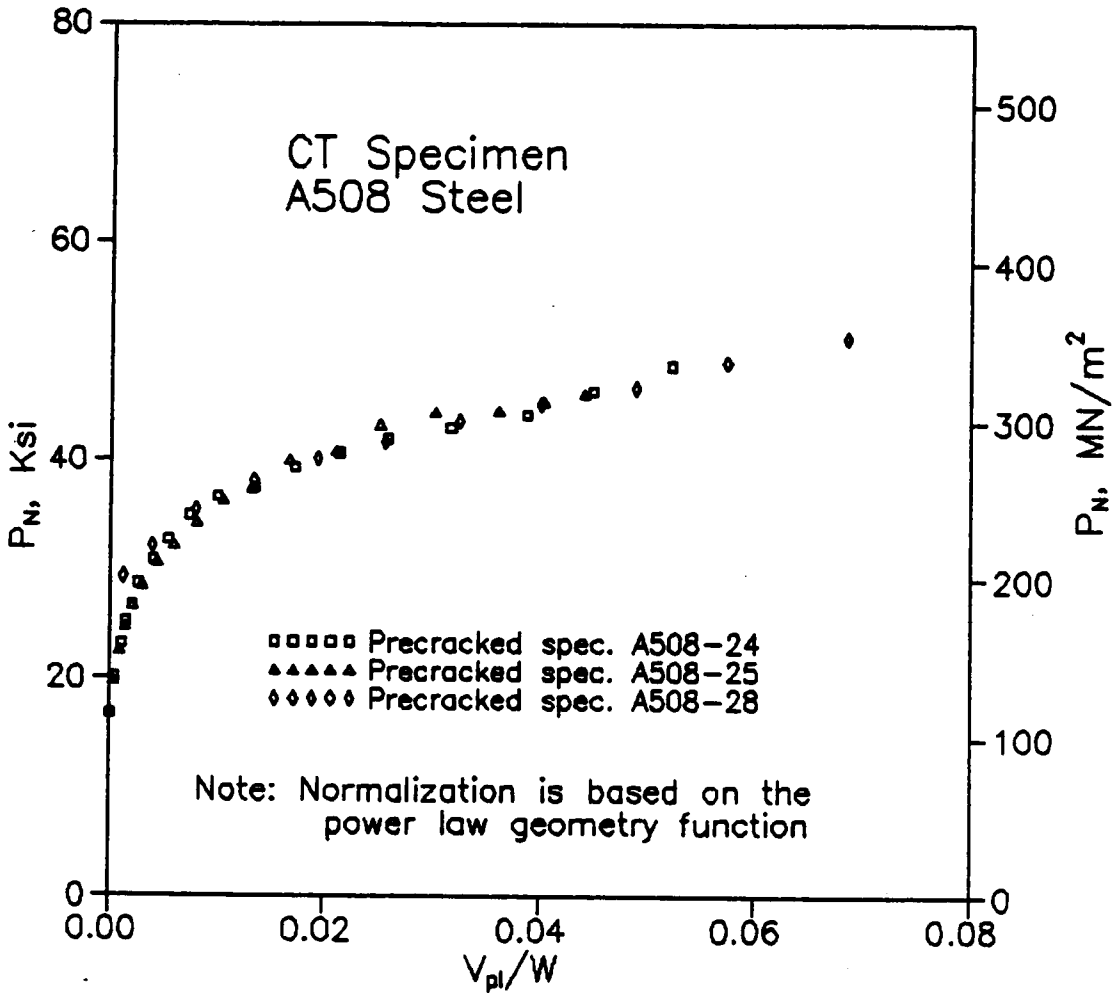


Fig. 4.27 - Load normalization in the A508 precracked specimens using a power law geometry function with a power law exponent of 2.22.

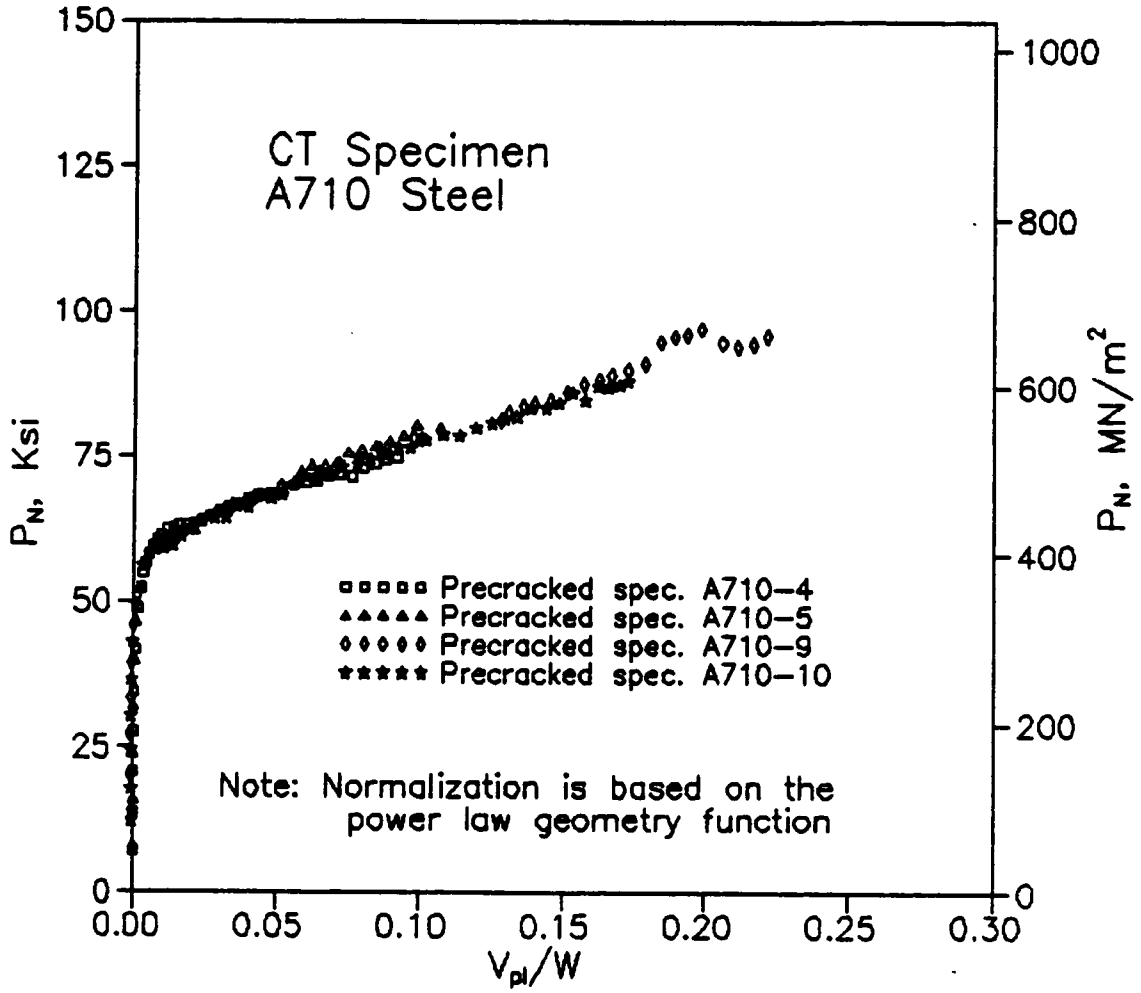
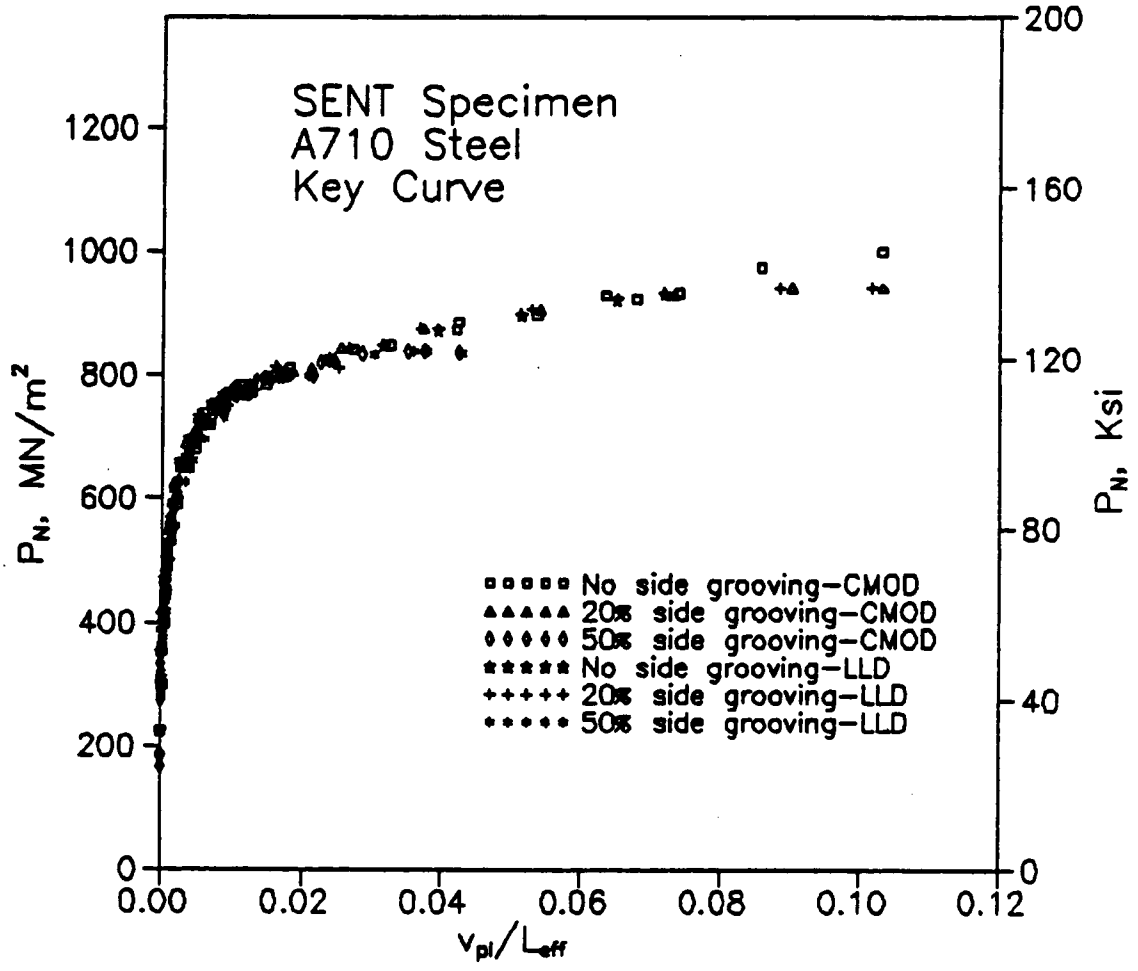


Fig. 4.28 - Load normalization in the A710 precracked specimens using a power law geometry function with a power law exponent of 2.40.



CMOD : load-crack mouth opening displacement test record.

LLD : load-load line displacement test record.

Fig. 4.29 - Key curve for the different 1.0 in. thickness A710 specimens.

VITA

Monir Hanna Sharobeam was born in Fayoom, Egypt, on February 3, 1954. He received the Bachelor of Science degree in Mechanical Engineering from Cairo University in 1976. He worked as a teaching assistant in Cairo University. In 1981, he received his Master of Science degree in Machine Design and Production from Cairo University. He continued working in Cairo University as an assistant lecturer. In Fall 1986, he accepted a graduate assistantship at the University of Tennessee and began to work toward a Doctoral degree in Engineering Science and Mechanics. This degree will be awarded in December 1990.

He is a member of "Phi Kappa Phi" Honor Society, and "Tau Beta Pi" Engineering Honor Society. He is married to Nahed Emil Ayad.